Ana Isabel Bento Rovisco

Mestre em Engenharia Física

Solution-based Zinc-Tin Oxide nanostructures: from synthesis to applications

Dissertação para obtenção do Grau de Doutor em Nanotecnologias e Nanociências

Orientador: Doutor Pedro Miguel Cândido Barquinha, Professor Associado, Faculdade de Ciências e Tecnologia da Universidade Nova de Lisboa FCT-UNL

Co-orientador: Doutora Rita Maria Mourão Salazar Branquinho, Professora Auxiliar Convidada, Faculdade de Ciências e Tecnologia da Universidade Nova de Lisboa FCT-UNL

Júri:

Presidente: Prof. Doutora Elvira Maria Correia Fortunato

Arguente(s): Prof. Doutor Paulo Jorge Matos Fernandes Martins Ferreira
Prof. Doutora Eulália Fernanda Alves de Carvalho Pereira

Vogais: Prof. Doutora Florinda Mendes da Costa
Prof. Doutor Pedro Miguel Cândido Barquinha
Doutor João Oliveira Ventura

FACULDADE DE CIÊNCIAS E TECNOLOGIA
UNIVERSIDADE NOVA DE LISBOA

Outubro 2019

Ana Isabel Bento Rovisco

Mestre em Engenharia Física

Solution-based Zinc-Tin Oxide nanostructures: from synthesis to applications

Dissertação para obtenção do Grau de Doutor em

Nanotecnologias e Nanociências

Orientador:	Doutor Pedro Miguel Cândido Barquinha, Professor Associado, Faculdade de Ciências e Tecnologia da Universidade Nova de Lisboa FCT-UNL
Co-orientador:	Doutora Rita Maria Mourão Salazar Branquinho, Professora Auxiliar Convidada, Faculdade de Ciências e Tecnologia da Universidade Nova de Lisboa FCT-UNL

	Júri:
Presidente:	Prof. Doutora Elvira Maria Correia Fortunato
Arguente(s):	Prof. Doutor Paulo Jorge Matos Fernandes Martins Ferreira
	Prof. Doutora Eulália Fernanda Alves de Carvalho Pereira
Vogais:	Prof. Doutora Florinda Mendes da Costa
	Prof. Doutor Pedro Miguel Cândido Barquinha
	Doutor João Oliveira Ventura

FACULDADE DE CIÊNCIAS E TECNOLOGIA
UNIVERSIDADE NOVA DE LISBOA

Outubro 2019

Solution-based Zinc-Tin Oxide nanostructures: from synthesis to applications

Acknowledgments

I would like to thank my supervisors, Prof. Pedro Barquinha, for giving me the opportunity to work in this interesting field, and Prof. Rita Branquinho, for the support with the chemistry related aspect of this work, and to both for helping me with the planning of the work, giving new ideas and discussing the results. Thank you for all your support and enthusiasm throughout these years.

I am very thankful to Prof. Elvira Fortunato and Prof. Rodrigo Martins for giving me the opportunity of doing this PhD, as well as all the conditions for developing the work.

To my current and past colleagues in CENIMAT that share the work and the lab with me, and directly or indirectly contributed to this work: Dr. Joana Pinto, for your time and help with everything but specially teaching me the XRD; MSc. Andreia dos Santos, whom I really enjoyed working with; MSc. Maria João Oliveira, Dr. Asal Kiazadeh, Dr. Jonas Deuermeier, Dr. Joana Neto, Prof. Daniela Gomes, Prof. Rui Igreja and MSc. Tiago Carvalho, for your contribution and help to in the different fields/techniques; MSc. Sónia Pereira, MSc. Alexandra Gonçalves and Dr. Ana Pimentel for helping me in all that it was necessary in the lab concerning equipments and resources; Dr. Diana Gaspar; Ricardo Ferreira; MSc. Ana Santa; MSc. Sofia Ferreira; Prof. Pydi Bahubalindruni; Dr. Andreia Araújo; MSc. Emanuel Carlos; Susana Mendes for your help and support in all the bureaucratic issues and for being always so patient and kind; and all the rest of the group that I did not mentioned.

To Dr. Tobias Cramer from the University of Bologna for the AFM/PFM measurements, which were highly important for this work.

To Fundação para a Ciência e Tecnologia for the fellowship (SFRH/BD/131836/2017) that assured me these years of work experience. This work was funded by FEDER funds through the COMPETE 2020 Programme and National Funds through FCT - Portuguese Foundation for Science and Technology under the project number POCI-01-0145-FEDER-007688, Reference UID/CTM/50025. This work also received funding from the European Community's H2020 program under grant agreement No. 716510 (ERC-2016-STG TREND) and No. 685758 (1D-Neon), and from the 7th Framework Programme under Grant Agreement No. ICT- 2013-10-611070 (i-FLEXIS Project) and No. NMP3-LA-2010-246334 (ORAMA project).

To my friends Rita (with Tiago and João) and Leila for our old friendship, for being comprehensive and for giving me support in the last months. And, Carolina even far away you always have a funny and positive word. To "Jorge's friends" (Luis Paulo, Iola and Miguel, Marco and Mariana, João Lourenço, Fininho and others), that received me as their friend.

To my family, my brother and my parents who always did everything that they could to make it possible. Thank you for everything, including the soup and everything else in these last months, which was a great help. To Isis and Kaya, also part of my family, for the emotional support and

unconditional love. To my uncles and cousins, too numerous to nominate, that make this big, close and joyous (loud) family.

To Jorge's family, Luis, Catarina, Night, Ana, Cristina, Gaspar and Celeste, for the support and for making me feel part of your family. These last years were hard but we are all finishing it!

And most specially, thank you Jorge for all your support, patience, love, taking care of me and everything you always do for me and for letting us adopt two new family members, Ambrósio and Juju, which helped us to make it through. Without you it would not be achievable.

Abstract

Over the last decade the demand for low cost materials/methods increased significantly. Due to its high electrical conductivity, high mobility and absence of critical raw materials, zinc-tin oxide (ZTO) appears as an ideal candidate for several applications, such as electronics, energy, sensors and photocatalysis.

ZTO nanowires have been fabricated essentially by vapor-phase methods, however these methods are expensive and require high temperatures (>700 °C). In contrast, hydrothermal processing was explored in this work to synthesize ZTO nanowires, aiming at a maximum temperature of 200 °C. The synthesis was extensively studied regarding its chemical and physical parameters, aiming to achieve a well-controlled and reproducible process to achieve nanostructures with specific properties. A seed-layer free and one-step hydrothermal method at 200 °C was then optimized to produce $ZnSnO_3$ nanowires and Zn_2SnO_4 nanoparticles and octahedrons.

Although very challenging, due to the lower dimension of the nanowires, the resistivity of a single $ZnSnO_3$ nanowire was measured using a nanoprobe inside a scanning electron microscope.

Due to the excellent piezoelectric properties of $ZnSnO_3$, robust energy harvesters of a micro-structured composite of $ZnSnO_3$ nanowires and PDMS film were fabricated, resulting in a great performance regarding output voltage, current and instantaneous power density (>200 $\mu W \cdot cm^{-2}$).

Memristors were also fabricated using the $ZnSnO_3$ nanowires, showing an excellent on/off ratio (>10^7) and a retention time higher than 4×10^4 s.

The photocatalytic behavior of different ZTO nanostructures was studied under both UV and visible light for methylene blue and rhodamine B, allowing for complete degradation of both dyes in 90 min.

pH sensors were also fabricated using ZTO nanostructures as sensitive layer, revealing a sensitivity very close to the theoretical limit (-58.6 mV/pH).

These different applications highlight the multifunctionality of Zn:Sn:O nanostructures, demonstrating the potential of its low-cost synthesis for integration on environmentally friendly and self-sustainable smart surfaces.

Keywords: *Zinc-tin oxide; $ZnSnO_3$; Zn_2SnO_4; Nanostructures; Hydrothermal synthesis; Multifunctionality.*

Resumo

A necessidade de materiais/métodos de baixo-custo aumentou significativamente na última década. Devido à sua elevada condutividade elétrica, elevada mobilidade e ausência de matérias-primas críticas, o óxido de zinco e estanho (ZTO) aparece como um forte candidato para diferentes aplicações, como eletrónicas, energéticas, sensores e fotocatálise.

Nanofios de ZTO têm sido fabricados essencialmente por métodos de vapor, contudo, estes métodos apresentam elevados custos e requerem elevadas temperaturas (>700 °C). Neste trabalho foram explorados processos hidrotérmicos para sintetizar nanofios de ZTO, com uma temperatura máxima desejada de 200 °C. Os parâmetros químicos e físicos da síntese foram intensivamente estudados com o objetivo de obter um processo controlado e reprodutível para produzir nanoestruturas com propriedades específicas. Assim, foi otimizado um processo hidrotérmico de passo único, sem *seed-layer* a 200 °C, para produzir nanofios de $ZnSnO_3$, e nanopartículas e octaedros de Zn_2SnO_4.

Embora desafiante devido às pequenas dimensões dos nanofios, a resistividade de um nanofio individual de $ZnSnO_3$ foi medida com sucesso, usando pontas de prova no microscópio eletrónico de varrimento.

Devido às suas excelentes propriedades piezoelétricas, os fios foram utilizados para fabricar robustos nanogeradores de energia, constituídos por um filme microestruturado destes fios embebidos em PDMS, resultando numa excelente performance relativamente à resposta de tensão, corrente e densidade de potência instantânea (>200 $\mu W \cdot cm^{-2}$).

Este material foi também usado para produzir memórias, resultando numa excelente razão *on*/*off* ($>10^7$) e um tempo de retenção superior a 4×10^4 s.

O comportamento fotocatalítico de diferentes nanoestruturas de ZTO foi estudado sob luz UV e visível em metileno azul e em rodamina B, tendo sido obtida uma completa degradação de ambos os corantes em 90 minutos.

Sensores de pH foram ainda produzidos usando nanoestruturas de ZTO como material ativo, revelando uma performance muito próxima do limite teórico (-58.6 mV/pH).

Estas aplicações realçam a multifuncionalidade deste material, mostrando o potencial de uma síntese de baixo custo de nanoestruturas de Zn:Sn:O para integração em superfícies amigas do ambiente e autossustentáveis.

Termos-chave: *Óxido de Zinco e Estanho; $ZnSnO_3$; Zn_2SnO_4; Nanoestruturas; Síntese hidrotermal; Multifuncionalidade.*

Table of Contents

List of Figures

List of Tables

Abbreviations

0D – Zero dimensions

1D – One dimension

2D – Two dimensions

3D – Three dimensions

AFM – Atomic force microscopy

ATR – Attenuated Total Reflectance

BNT – Barium neodymium titanate

CC – Current compliance

CEMOP – Centre of Excellence in Microelectronics Optoelectronics and Processes

CENIMAT – Centro de Investigação de Materiais

CPU – Central process unit

CVD – Chemical vapor deposition

DSSCs – Dye-sensitized solar cells

DRAM – Dynamic random-access memory

EBL – E-beam lithography

EDS – Energy dispersive X-ray spectroscopy

Fcc – Face-centered cubic

FE-SEM – Field Emission Scanning Electron Microscopy

FET – Field effect transistor

FTIR – Fourier-transform infrared

FTO – Fluorine doped tin oxide

HRS – High resistive state

ICDD – International Centre for Diffraction Data

IGZO – Indium gallium zinc oxide

IoT – Internet of things

IPA – Isopropyl alcohol

IR – Infra red

ITO – Indium tin oxide

I(V) – Current-voltage

KPFM – Kelvin probe force microscope

LED – Light-emitting diode

LRS – Low resistive state

MB – Methylene blue

NIL – Nanoimprint lithography

NCs – Nanocubes

NPs – Nanoparticles

NWs – Nanowires

Orth – Orthorhombic

PDMS – Polydimethylsiloxane

PENG – Piezoelectric nanogenerator

PEN – Polyethylene naphthalate

PET – Polyethylene terephthalate

PFM – Piezoresponse force microscopy

PSC – Perovskite solar cell

PVD – Physical vapor deposition

PZT – Lead zirconate titanate

SC – Supercapacitor

SEM – Scanning electron microscopy

sccm – Standard cubic centimeters per minute

SS – Stainless Steel

Re-RAM – Resistive random-access memory

RhB – Rhodamine B

TEM – Transmission electron microscopy

TENG – Triboelectric nanogenerator

TCO – Transparent conductive oxide

TFT – Thin film transistor

UV – Ultra-violet

Vis. – Visible

XRD – X-ray diffraction

XPS – X-ray photoelectron spectroscopy

ZnAc – Zinc acetate

ZnO – Zinc oxide

ZTO – Zinc-tin oxide

Symbols

A – Optical absorption

C – Concentration

C_0 – Initial concentration

d – Film thickness

d_{hkl} – Interplanar spacing

d_{33} – Piezoelectric coefficient

e (or q) – elementary charge of a particle (1.6×10^{-19} C)

E_C – Conduction band

E_F – Fermi level

E_g – Band gap

E_K – Electron kinetic energy

E_B – Binding energy

E_{opt} – Optical band gap

E_{Ref} – Reference electrode potential

E^0 – Standard electrode potential

f – Frequency

h – Planck's constant (4.135×10^{-15} eV.s)

I – Current

I_{on} – On current

I_{off} – Off current

k – Degradation rate

P – Power

R – Resistance

t – Time

T – Temperature

V – Voltage

V_{Ref} – Reference voltage

Z – Impedance

α – Absorption coefficient

ε_0 – Vacuum permittivity

θ – Bragg angle

ϕ – Work function

λ – Wavelength of electromagnetic wave

μ – Mobility

v – Frequency of electromagnetic wave

ρ – Electrical resistivity

Introduction

Motivation and Objectives

The motivation of this thesis is related with the demand for a new generation of sustainable nanostructured oxide materials, fabricated by low-temperature solution routes and able to be integrated in a wide range of applications. Owing to the multiple phases and morphologies achievable with multicomponent oxides of different compositions, they seem to be ideal for this multifunctional concept, allowing to combine in the same surface different devices such as sensors, energy harvesters, transistors and memories, all based in the same material system. It is also imperative to combine these concepts with sustainability, searching for materials that are abundant in the earth, with low-cost and that can be recyclable and preferentially non-toxic. Additionally, when considering concepts as the IoT, which demand for material/device integration in a plethora of objects, with different shapes and surface properties, it is desirable that the nanostructured materials being developed are compatible with multiple deposition/integration methods. A good example is that they would not rely on a specific seed layer or substrate to grow with the desired properties.

In the Chapter 1 it will be possible to verify that zinc-tin oxide (ZTO) is one the most promising multicomponent oxide materials for achieving this desired multifunctionality. Its multifunctionality comes essentially from the great electrical and optical properties of its two crystalline phases, $ZnSnO_3$ and Zn_2SnO_4 and the wide range of shapes in which this material is possible to obtain. While the different nanostructures can be advantageous for different applications, 1D morphologies such as nanowires are specially interesting. They have a high surface area but also very efficient electron transport properties which is relevant for several applications but specifically for electronics, which is always a significant drive for the development of materials.

Table 1 summarizes several reports on ZTO nanowires, their fabrication method and targeted applications. The lack of low-cost processes to synthesize ZTO nanowires is made clear and, moreover, reports on solution-based processing always require the use of seed-layers.

Thus, this work intends to address those problems, by developing ZTO nanowires by low-cost and low-complexity processes, based on hydrothermal methods below 200 °C. Seed-layer free synthesis is primary considered due to the higher flexibility allowed for the integration of the nanostructures, while also imposing less constraints during the synthesis process itself. Due to the complexity of this synthesis an extensive investigation covering the different physical and

chemical synthesis parameters is intended. A proper control of not only the phase but also the morphology of the nanostructures is expected, since this is known to be determinant for their electrical and optical properties.[1,2]

Afterwards, implementation of the produced nanostructures in devices through transfer or direct growth methodologies was intended, with the major goal of demonstrating that the low-cost multifunctional materials developed have great potential to conceive self-sustainable smart surfaces.

Table 1. Summary of ZTO ($ZnSnO_3$ and Zn_2SnO_4) nanowires, their synthesis methods and applications. Abbreviations: FTO – fluorine-doped tin oxide; SS – stainless steel; fcc - face centered; orth – orthorhombic. *(for ethanol, hydrogen and methane)

Phase	Synthesis Method	Application	References
$ZnSnO_3$ microwires and microbelts	Carbon-thermal reaction (900 °C)	Energy harvesting	3–6
$ZnSnO_3$ nanowires	Thermal evaporation (990 °C)	Photoconductors	7,8
$ZnSnO_3$ nanowires	Thermal evaporation (990 °C)	Ethanol sensors	9
$ZnSnO_3$ nanowires	Seed-layered (FTO) hydrothermal synthesis	Piezophotocatalysis	10,11
R3C - $ZnSnO_3$ nanowires	Seed-layered (ZnO thin-film) hydrothermal synthesis	Hydrogen generation	12
Zn:Sn:O nanowires	Thermal evaporation (700 °C – 850 °C)	Transistors	13,14
Zn_2SnO_4 nanowires	Thermal evaporation (800 °C – 950 °C)	Gas sensors*	15,16
Zn_2SnO_4 nanowires	Thermal evaporation (500 °C – 900 °C)	Photosensors	17–19
Zn_2SnO_4 nanowires	Thermal evaporation (800 °C)	Resistive switching memory	20
Zn_2SnO_4 nanowires	Thermal evaporation (900 °C)	Dye-sensitized solar cells	21
Zn_2SnO_4 nanowires	Thermal evaporation (900 °C)	Li-batteries	22
Zn_2SnO_4 nanowires	Seed-layered (SS) hydrothermal synthesis	Dye-sensitized solar cells	23

Thesis structure

This thesis is mainly structured in an article-based format, as most of the chapters are based on either already published manuscripts or manuscripts that are submitted or under submission. Nevertheless, all of these were edited as to keep the dissertation consistency, with the respective supporting information being merged into the main text, as well as any other additional information considered relevant.

Chapter 1 starts with an overview of green multicomponent oxide semiconductor nanostructures, their fabrication methods and applications, as well as the characterization techniques typically involved under this scope.

Chapter 2 describes the optimization of the hydrothermal synthesis of $ZnSnO_3$ nanowires using a conventional oven. For this optimization, the chemical and physical parameters of the synthesis were extensively studied with the aim of properly controlling the synthesis process to achieve the desired nanostructures with good reproducibility.

Chapter 3 shows other synthesis routes that were explored besides that presented in chapter 2. Herein, the knowledge previously acquired was used for reducing the time of the reaction synthesis by using a microwave system and, in order to have nanostructures directly grown on substrates, the influence of different seed layers in the ZTO nanostructures growth was studied.

In **Chapter 4** energy harvesting and optoelectronic applications employing the synthetized $ZnSnO_3$ nanowires are presented. Their characteristic piezoelectricity is explored and a work consisting on energy harvesters made using a film of PDMS with embedded $ZnSnO_3$ nanowires is presented. In the same chapter, the electrical characterization of the $ZnSnO_3$ nanowires is then provided. Lastly, their application for memristor and light sensing devices is shown.

In **Chapter 5** the photocatalytic activity of three different synthetized ZTO nanostructures is presented, in the degradation of two dyes: methylene blue and rhodamine B, and under both UV and visible light.

Chapter 6 presents electrodeposition as an integration method for the nanostructures in devices and the application of several ZTO-based nanostructures as sensitive layer for pH sensing.

In **Chapter 7** the main conclusions drawn from the developed work are presented. Future perspectives as well as suggestions for the continuation of the work under the scope of this project are also presented.

Outputs

The work performed in this PhD project resulted in several oral and poster presentations in national and international conferences and also peer-reviewed papers published in international scientific periodicals. The work developed in this PhD was also very useful to achieve the objectives of multiple tasks of the European Community's H2020 project 1D-Neon (No. 685758) and of the ERC starting grant TREND (No. 716510).

The outputs are presented below.

Publications

1. **A. Rovisco**, R. Branquinho, J. Martins, M. J. Oliveira, D. Gomes, E. Fortunato, R. Martins and P. Barquinha, Seed-layer free zinc tin oxide tailored nanostructures for nanoelectronic applications: effect of chemical parameters, ACS Appl. Nano Mater., 1, 3986–97, 2018, DOI: 10.1021/acsanm.8b00743
2. **A. Rovisco**, R. Branquinho, J. Martins, E. Fortunato, R. Martins and P. Barquinha, Growth mechanism of seed-layer free $ZnSnO_3$ nanowires: effect of physical parameters, Nanomaterials, 9(7), 1002, 2019, DOI: 10.3390/nano9071002
3. **A. Rovisco**, A. dos Santos, T. Cramer, J. Martins, R. Branquinho, H. Águas, B. Fraboni, E. Fortunato, R. Martins, R. Igreja and P. Barquinha, Piezoelectricity Enhancement of Nanogenerators based on PDMS and $ZnSnO_3$ Nanowires through Micro-structuration, under revision ACS Applied Materials and Interfaces 2019
4. **A. Rovisco**, R. Branquinho, J. Deuermeier, J. Martins, T. Freire, E. Fortunato, R. Martins and P. Barquinha, Photocatalytic behavior of solution-based Zn:Sn:O nanostructures, under submission 2019
5. **A. Rovisco**, R. Branquinho, J. Martins, E. Fortunato, R. Martins and P. Barquinha, Literature review on green multicomponent oxide semiconductor nanostructures, under preparation 2019
6. **A. Rovisco**, J. Neto, R. Branquinho, J. Martins, E. Fortunato, R. Martins and P. Barquinha, pH sensors based on electrodeposited ZTO nanostructures, under preparation 2019
7. **A. Rovisco**, J. Martins, A Kiazadeh, R. Branquinho, E. Fortunato, R. Martins and P. Barquinha, $ZnSnO_3$ nanowires resistive switching memories, under preparation 2019

Oral presentations

1. **Ana Rovisco**, Rita Branquinho, Jorge Martins, Maria João Oliveira, Daniela Nunes, Elvira Fortunato, Rodrigo Martins and Pedro Barquinha, Seed-layer free zinc tin oxide tailored nanostructures: effect of chemical parameters, 15th International Conference on Nanosciences & Nanotechnologies (NN18), 3-6 July 2018, Thessaloniki, Greece

2. **Ana Rovisco**, Rita Branquinho, Jorge Martins, Elvira Fortunato, Rodrigo Martins and Pedro Barquinha, Seed-layer free zinc tin oxide tailored nanostructures for nanoelectronic applications produced by low-temperature hydrothermal synthesis, 2018 MRS Fall Meeting, November 25 - 30, 2018 Hynes Convention Center, Boston, Massachusetts, USA

3. **A. Rovisco**, R. Branquinho, J. Martins, E. Fortunato, R. Martins and P. Barquinha, $ZnSnO_3$ nanowires by hydrothermal synthesis, Materiais 2019, 14-17 April 2019, Lisbon, Portugal

4. **Ana Rovisco**, Zinc tin oxide nanostructures characterization using a SEM workstation, Seminário Hitachi: Os limites da microscopia, CENIMAT (UNL), Caparica, 16th May 2019

5. **A. Rovisco,** J. Martins, A.d.Santos, J. Neto, R. Branquinho, E.Fortunato, R. Martins and P. Barquinha, Multifunctional Zinc Tin Oxide Nanostructures: From Photocatalysis to Electronic Applications, Nanotech France 2019, 26 - 28 June, Paris, France

Contribution in oral presentations

1. P. Barquinha, C. Fernandes, A. Santos, E. Carlos, R. Branquinho, A. Kiazadeh, J. Martins, **A. Rovisco**, R. Martins, E. Fortunato, "Sustainable, multifunctional and flexible electronics platform based on oxides", NanoPT 2017, Porto, February 2017 – ***invited***

2. Pedro Barquinha, **Ana Rovisco**, Soumen Maiti, Rita Branquinho, Zinc-tin oxide tailored nanostructures produced by solution-based methods: a vehicle towards sustainable and multifunctional oxide nanoelectronics, XVII Brazilian MRS Meeting, September 16-20, 2018, Natal, Brasil – ***invited***

3. S. Nandy, S. Goswami, **A. Rovisco**, P. Barquinha, R. Martins, E. Fortunato, "Electro-typing" Data Storage Device by Probe Induced Charge Injection Method, Materiais 2019, 14-17 April 2019, Lisbon, Portugal

4. Pedro Barquinha, Daniela Nunes, Ana Pimentel, Lídia Santos, **Ana Rovisco**, Rita Branquinho, Suman Nandy, Elvira Fortunato and Rodrigo Martins, Oxides and the challenges of the future, Nanotech France 2019, 26 - 28 June, Paris, France – ***invited***

Posters

1. **A. Rovisco**, R. Branquinho, J. Martins, E. Fortunato, R. Martins and P. Barquinha, Solution-based multicomponent oxide semiconductor nanowires for electronic applications**,** EMRS Spring Meeting, 1-5th May, Lille, France, 2016

2. **A. Rovisco**, A. Pimentel, D. Nunes, P. Barquinha, E. Fortunato and R. Martins, Metal-oxide nanostructures synthesized under microwave irradiation, Jornadas do CENIMAT 2016, July 2016

3. **A. Rovisco**, R. Branquinho, J. Martins, E. Fortunato, R. Martins and P. Barquinha, Solution-based multicomponent oxide semiconductor nanowires for electronic applications, Encontro Ciência 2016, Centro de Congressos de Lisboa, 4-6 July, Portugal

4. **A. Rovisco**, R. Branquinho, E. Fortunato, R. Martins and P. Barquinha, Solution-based multicomponent oxide semiconductor nanowires for electronic applications, Encontro Ciência 2017, Centro de Congressos de Lisboa, 3-5 July, Portugal

5. **Ana Rovisco**, Rita Branquinho, Elvira Fortunato, Rodrigo Martins and Pedro Barquinha, Zinc-tin Oxide Nanowires: Electrical Characterization inside SEM, 5th Dresden Nanoanalysis Symposium, Dresden, September 1st, Germany, 2017

6. **Ana Rovisco**, Rita Branquinho, Jorge Martins, Maria João Oliveira, Daniela Nunes, Elvira Fortunato, Rodrigo Martins and Pedro Barquinha, $ZnSnO_3$ Nanowires: Synthesis and Electrical Characterization inside SEM, 17th International Conference on Nanoimprint and Nanoprint Technologies, September 18-20, INL | Braga, Portugal, 2018

7. **Ana Rovisco**, Rita Branquinho, Jonas Deuermeier, Elvira Fortunato, Rodrigo Martins and Pedro Barquinha, $ZnSnO_3$ phase identification by XRD, EDS and XPS analyzes, Spring School and Workshop on Quantitative methods in X-ray spectrometry, May 2019, Lisbon, Portugal

8. **Ana Rovisco**, Rita Branquinho, Jorge Martins, Elvira Fortunato, Rodrigo Martins and Pedro Barquinha, Seed-layer free $ZnSnO_3$ nanowires by hydrothermal synthesis: effect of physical parameters, 6th Nano Today Conference, 16-20 June 2019, Lisbon, Portugal

9. **A. Rovisco**, R. Branquinho, Jonas Deuermeier, E. Fortunato, R. Martins and P. Barquinha, $ZnSnO_3$ phase identification by XRD, EDS and XPS analyzes, Encontro Ciência 2019, Centro de Congressos de Lisboa, 8-10 July, Portugal

10. **A. Rovisco,** A.d.Santos, R. Igreja, R. Branquinho, E.Fortunato, R. Martins and P. Barquinha, Micro-structured composite of PDMS and $ZnSnO_3$ nanowires for energy harvesting, E-MRS Fall Meeting, 16-19th September 2019, Warsaw, Poland

Contribution in posters:

1. J.V. Pinto, **A. Rovisco**, T. Calmeiro, S. Nandy, P. Barquinha, R. Martins, E. Fortunato, Electrical Characterization of ZTO NWs by Electrical Mode AFM, 5th Euro AFM Forum, University of Geneva, 22-24 June 2016

2. D. Nunes, A. Pimentel, **A. Rovisco**, A. Gonçalves, A.C. Marques, S. Pereira, L. Santos, P. Barquinha, E. Fortunato and R. Martins, Metal-oxide nanostructures synthesized under microwave irradiation, I3N Annual Meeting 2017, Lisboa, February 2017

3. Suman Nandy, Sumita Goswami, **Ana Rovisco**, Pedro Barquinha, Rodrigo Martins, Elvira Fortunato, Atomic force microscopy: Impact on nanoscale charge-transport dynamics, 6th Dresden Nanoanalysis Symposium, Dresden, August 31st, Germany, 2018

Awards

1. Second Place in the Science as Art Competition, 2018 MRS Fall Meeting
2. Cover image in Nano Today (Volume 21) – Winner of Cover Competition 2018 (Chapter 8 - Appendix 1)
3. Cover image in Nano Today (Volume 26) – Winner of Cover Competition 2019 (Chapter 8 - Appendix 2)

References

1. Baruah, S. & Dutta, J. Zinc stannate nanostructures: hydrothermal synthesis. *Sci. Technol. Adv. Mater.* **12**, 013004 (2011).
2. Zeng, J. *et al.* Transformation process and photocatalytic activities of hydrothermally synthesized Zn2SnO4 nanocrystals. *J. Phys. Chem. C* **112**, 4159–4167 (2008).
3. Wu, J. M., Xu, C., Zhang, Y. & Wang, Z. L. Lead-free nanogenerator made from single ZnSnO3 microbelt. *ACS Nano* **6**, 4335–40 (2012).
4. Wu, J. M., Chen, K.-H., Zhang, Y. & Wang, Z. L. A self-powered piezotronic strain sensor based on single ZnSnO3 microbelts. *RSC Adv.* **3**, 25184 (2013).
5. Wu, J. M. *et al.* Ultrahigh Sensitive Piezotronic Strain Sensors Based on a ZnSnO3 Nanowire/Microwire. *ACS Nano* **6**, 4369–4374 (2012).
6. Wu, J. M. *et al.* Flexible and transparent nanogenerators based on a composite of lead-free ZnSnO3 triangular-belts. *Adv. Mater.* **24**, 6094–6099 (2012).
7. Xue, X. Y. *et al.* Electronic transport characteristics through individual ZnSnO3 nanowires. *Appl. Phys. Lett.* **88**, 182102 (2006).
8. Xue, X. Y., Guo, T. L., Lin, Z. X. & Wang, T. H. Individual core-shell structured ZnSnO3 nanowires as photoconductors. *Mater. Lett.* **62**, 1356–1358 (2008).
9. Xue, X. Y., Chen, Y. J., Wang, Y. G. & Wang, T. H. Synthesis and ethanol sensing properties of ZnSnO3 nanowires. *Appl. Phys. Lett.* **86**, 1–3 (2005).

10. Wang, Y.-T. & Chang, K.-S. Piezopotential-Induced Schottky Behavior of Zn 1− x SnO 3 Nanowire Arrays and Piezophotocatalytic Applications. *J. Am. Ceram. Soc.* **99**, 2593–2600 (2016).

11. Lo, M.-K., Lee, S.-Y. & Chang, K.-S. Study of ZnSnO 3 -Nanowire Piezophotocatalyst Using Two-Step Hydrothermal Synthesis. *J. Phys. Chem. C* **119**, 5218–5224 (2015).

12. Chang, Y. T. *et al.* Performance of hydrogen evolution reaction of R3C ferroelectric ZnSnO 3 nanowires. *Nanotechnology* **30**, 455401 (2019).

13. Lim, T., Kim, H., Meyyappan, M. & Ju, S. Photostable Zn 2 SnO 4 Nanowire Transistors for Transparent Displays. *ACS Nano* **6**, 4912–4920 (2012).

14. Kim, S., Kim, H., Janes, D. B. & Ju, S. Interface studies of N2 plasma-treated ZnSnO nanowire transistors using low-frequency noise measurements. *Nanotechnology* **24**, 305201 (2013).

15. Chen, D. *et al.* Electric transport, reversible wettability and chemical sensing of single-crystalline zigzag Zn2SnO4 nanowires. *J. Mater. Chem.* **21**, 17236 (2011).

16. Tharsika, T., Haseeb, A. S. M. a., Akbar, S. a., Sabri, M. F. M. & Wong, Y. H. Gas sensing properties of zinc stannate (Zn2SnO4) nanowires prepared by carbon assisted thermal evaporation process. *J. Alloys Compd.* **618**, 455–462 (2015).

17. Karthik, K. R. G. *et al.* Physical and Electrical Properties of Single Zn2SnO4 Nanowires. *Electrochem. Solid-State Lett.* **14**, K5 (2011).

18. Tien, L.-C., Yang, S.-J., Chen, Y.-H. & Ho, C.-H. Observation of near-band-edge photoluminescence and UV photoresponse in near-stoichiometric Zn 2 SnO 4 nanowires. *Mater. Res. Express* **3**, 066201 (2016).

19. Zhang, Y. *et al.* High performance ultraviolet photodetectors based on an individual Zn2SnO4 single crystalline nanowire. *J. Mater. Chem.* **20**, 9858 (2010).

20. Dong, H. *et al.* High performance bipolar resistive switching memory devices based on Zn2SnO4 nanowires. *Nanoscale* **4**, 2571 (2012).

21. Chen, J., Lu, L. & Wang, W. Zn2SnO4 nanowires as photoanode for dye-sensitized solar cells and the improvement on open-circuit voltage. *J. Phys. Chem. C* **116**, 10841–10847 (2012).

22. Cherian, C. T., Zheng, M., Reddy, M. V, Chowdari, B. V. R. & Sow, C. H. Zn2SnO4 Nanowires versus Nanoplates: Electrochemical Performance and Morphological Evolution during Li-Cycling. *ACS Appl. Mater. Interfaces* **5**, 6054–6060 (2013).

23. Li, Z. *et al.* Vertically building Zn2SnO4 nanowire arrays on stainless steel mesh toward fabrication of large-area, flexible dye-sensitized solar cells. *Nanoscale* **4**, 3490–4 (2012).

Chapter 1 – Literature review on green multicomponent oxide semiconductor nanostructures

The first chapter presents itself as a framing of the work in this thesis under the field of nanotechnology. It starts by presenting the state of the art concerning the relevance of multicomponent semiconductor oxide nanostructures, including the properties of the nanomaterials that are relevant for this work and its applications. Special attention is given to green materials, due to the importance of avoiding critical raw materials.

The contents of this Chapter are adapted from the following paper:

- **A. Rovisco**, R. Branquinho, J. Martins, E. Fortunato, R. Martins and P. Barquinha, Literature review on green multicomponent oxide semiconductor nanostructures, under preparation 2019

1.1. Abstract

Herein, a comprehensive review of the literature on green multicomponent oxide semiconductor nanostructures is presented. This review pretends to highlight the importance of these materials for the post-Si era, as their properties can be appropriately tuned by either changing the cations or the cationic ratio. The demand for environmentally friendly materials, as well as the need for reducing the costs in the industry increases the demand for novel materials and simpler methods. Thus, potential materials for meeting these requirements, while still enabling good performances, are here explored and summarized. The importance of these materials further increases with their potential to be implemented in future smart and self-sustainable surfaces, where their multifunctionality, derived from their varied excellent properties, allows the combined integration of multiple devices such as sensors, harvesters and electronic components. In this context, the viability of the different oxide nanostructure materials and morphologies for specific applications is also described.

1.2. Introduction

Nanotechnology attracted a very high attention over the last decades, leading to a very fast development of materials and processing routes. Different areas such as electronics, chemical sensors, medicine/biology, optoelectronics, energy, and others, have profited from this rapid growth. Particularly, for electronic and sensors applications there is an increasing demand for flexible and transparent devices and also for miniaturization to meet near-future concepts such as internet-of-things and smart surfaces where low-cost, sustainability and high-integration level are crucial.[1] Having in mind the environmental issues that we are facing in the modern era, the importance of searching for environmentally friendly, recyclable and low-cost nanomaterials and fabrication processes is essential.[2]

Oxide materials have been widely used in thin-film technology, since they allow not only for good electrical properties but also for transparency, large area uniformity and good mechanical flexibility.[3,4] This is well aligned with the requirements highlighted above for smart surfaces. Depending on the metal cations (and on the metal to oxygen ratio), metal oxides can be considered as dielectrics, semiconductors or even conductors.[5–8] Dielectrics are usually based on the metal ions of Si, Ta, Al and Hf, while semiconductors and conductors typically contain In, Zn, Cd and Sn metal ions.[9]

One of the very interesting properties of oxide (semi)conductors composed of multiple post-transition-metal cations is that their carrier transport is fairly insensible to structural randomness. Unlike conventional covalent semiconductors where carrier transport paths are composed of strongly directive sp3 orbitals, in multicomponent oxides neighboring metal 4s or 5s orbitals largely overlap and constitute the bottom of the conduction band, and this is not severally affected

even in an amorphous state.[10] Indium-gallium-zinc oxide (IGZO) thin films are perhaps the most striking example of this: while single crystalline films prepared at temperatures exceeding 1000 °C exhibit hall mobility (μ_H) in the range of 10-20 cm^2/Vs, very similar values are obtained for polycrystalline or even amorphous films, even if processed at room temperature.[10,11]

Owing to their remarkable electrical properties, In-based materials are currently the multicomponent oxide conductors and semiconductors with larger market relevance in large area electronics.[5,12] Indium-tin oxide (ITO) is traditionally seen as the reference transparent conductor, with low electrical resistivity of ≈ 10^{-4} Ω·cm and optical transmittance in visible range of ≈ 85 - 90 %.[13,14] IGZO enables high field-effect mobility >10 cm^2/Vs and low off-current <100 fA in thin-film transistors, TFTs) and excellent large area uniformity, being currently one of the dominant semiconductor technologies for display applications.[15,16] However, indium is an expensive material, due to its scarcity and high market value, appearing in the current (2017) list of the critical raw materials for the European Commission (**Figure 1.1**).[17] While slightly less critical, the same can be said for Gallium, another element of IGZO. This way, the replacement of these materials is imperative to assure long-term sustainability.[2]

Figure 1.1. List of critical raw materials for the EU in 2017, adapted from the European Commission report.[17]

The considerations mentioned above for thin-film oxide electronics are also important when heading towards oxide nanostructures. Indeed, while oxide materials such as SnO_2, ZnO and In_2O_3, have been extensively explored as semiconductor nanostructures, multicomponent oxide materials have great potential to enhance properties and enlarge the range of applications of oxide materials. The properties of these multicomponent oxide nanostructures can be tuned by adjusting the cationic ratio.[9,15,18,19] Therefore, several structures can be achieved, such as perovskites (ABO_3), spinel structures (AB_2O_4) and other $A_xB_yO_z$ structures, allowing different electrical, optical, mechanical, chemical and physical properties.[20–22] Materials properties such as ferroelectricity, superconductivity, magnetism and piezoelectricity have been demonstrated.[16] A good demonstration of the potential of a multicomponent approach for oxide nanostructures is the significant enhancement of piezoelectric response reported for $ZnSnO_3$ compared to ZnO, owing to the larger displacement of the Zn atom in the ZnO_6 octahedral cell compared to the one of the Sn atom in the SnO_6 octahedral cell, resulting in large spontaneous polarization in the crystal structure along the c-axis.[23]

However, the synthesis of these multicomponent nanomaterials is significantly more complex due to the presence of two (or more) cations.[15] Thus, achieving a well-controlled reaction with the desired stoichiometry at the nanoscale can be very challenging, especially when considering low-complexity and low-cost methods.

The literature review presented in the next sections will cover the different multicomponent oxide semiconductor nanostructures, the methods for their fabrication and characterization and finally their applications. Especial attention will be held to materials and methods which are environmentally friendly and with low complexity and associated costs.

1.3. Nanostructures of green multicomponent oxide semiconductors

A nanostructure is, by definition, a structure for which at least one of its dimensions is less than 100 nm. Nevertheless, materials with dimensions in the range of 1 nm to 250 nm are governed either by the quantum effects of atoms and molecules or the bulk properties of materials.[24] Materials with structures at the nanoscale have unique optical, electronic, or mechanical properties when compared to the respective bulk materials, which arise from the quantum effects or from the much more significant contribution from the surface in comparison to the bulk. Additionally, these properties are dependent on the size of the structures, unlike in bulk materials, and can then be adjusted.

Depending on their morphologies, nanostructures can be considered as having zero, one, two or three dimensions (**Figure 1.2**), and each type of nanostructures can be suitable for different applications as their properties vary with shape and size. In the next sub-sections, nanostructures

having each of these dimensions will be described in more detailed, as well as the main green multicomponent oxides semiconductors that have been produced in the latter years for each.

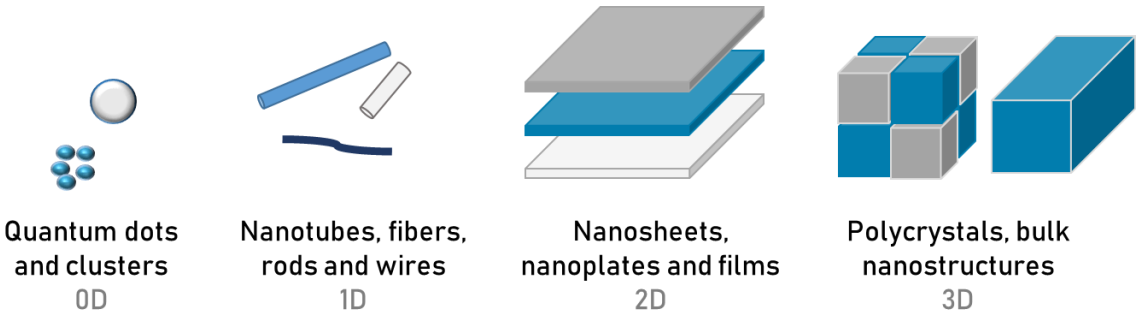

Figure 1.2. Schematic of the nanomaterials according to their different dimensions: 0D, 1D, 2D and 3D.

1.3.1. 0D nanostructures

The 0D nanostructures generally consist in small spherical nanoparticles with diameters lower than 100 nm, consequently, all their dimensions are in the nanometers range. These nanostructures are normally called quantum dots or clusters, which are isotropic structures, due to the electron confinement in all the 3 dimensions.[25]

Regarding multicomponent oxide semiconductors, several materials can be produced with zero dimensions being that Zn, Ca, Ti, Sn, Fe and Cu are some of the most common cations used.

Zn_2SnO_4 is one of the most reported ternary oxides as 0D nanostructures. Lehnen *et al.* reported very small Zn_2SnO_4 quantum dots (with diameters below 30 nm), produced with a microwave-assisted hydrothermal synthesis, followed by high-temperature annealing.[20] Numerous other reports on Zn_2SnO_4 nanoparticles have been shown, either using standard hydrothermal synthesis or solvothermal synthesis.[26–33]

Another Zn-based ternary oxide is the $ZnCr_2O_4$.[34,35] Nanoparticles of this material were reported by Mousavi *et al.*, and they were produced by a precipitation method, followed by a calcination at 700 °C for 3 h.[35] $ZnMn_2O_4$ nanoparticles were also reported, by Morán-Lázaro *et al.*, which used a microwave-assisted colloidal method to produce $ZnMn_2O_4$ nanoparticles (**Figure 1.3**a).[36]

Such as $ZnCr_2O_4$ and $ZnMn_2O_4$, spinel structure nanospheres of $CuFe_2O_4$ were also shown.[37,38] In 2013, Zhu *et al.* reported a hydrothermal method to produce $CuFe_2O_4$ nanospheres with an average size of 60 nm, as shown in **Figure 1.3**b.[39]

Perovskites from ABO_3 class are also commonly reported as 0D structures, with $SrTiO_3$ and $ZnSnO_3$ being a few examples of these materials.[40]

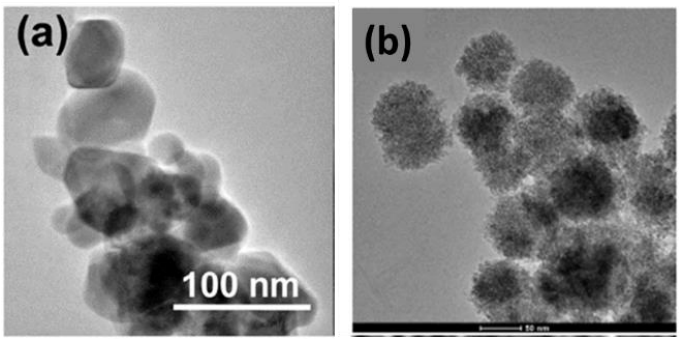

Figure 1.3. TEM images of: (a) $ZnMn_2O_4$ nanoparticles from ref. [36] and (b) $CuFe_2O_4$ nanospheres from ref. [39].

$SrTiO_3$ nanoparticles have also been synthesized by hydrothermal synthesis, for example, Shen et al. reported a hydrothermal synthesis of the material at 120 °C for 36 h.[41]

Regarding $ZnSnO_3$ nanoparticles, several hydro and solvothermal routes have been reported for its synthesizes.[42–45] For instance, Beshkar *et al.* reported the use of the Pechini method at 80 °C to synthesize fcc-$ZnSnO_3$ nanoparticles, followed by a calcination at 700 °C for 2 h.[46] **Figure 1.4** shows $ZnSnO_3$ nanoparticles from different synthesis routes.

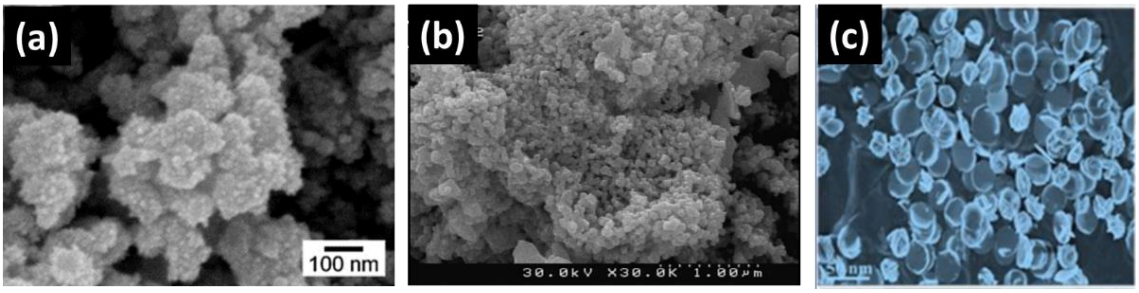

Figure 1.4. SEM images of fcc-$ZnSnO_3$ nanoparticles produced (a) at CENIMAT by hydrothermal synthesis; (b) by Pechini method using gelling agent, from ref. [46]; and (c) FE-SEM image of fcc-$ZnSnO_3$ nanoparticles annealed at 400 °C from ref. [47].

Other ternary structures, such as ABO_4, have been reported in the form of 0D nanostructures. Hu *et al.* reported $CaWO_4$ and $Ca_{1-x}Zn_xWO_4$ nanocrystals produced by a solution chemistry at room temperature.[48]

In summary, several multicomponent oxide semiconductor materials have been reported as 0D nanostructures. These materials are essentially based on Zn, Sn and Ti, metals. Besides the simple hydrothermal synthesis, a combination of a chemical method followed by a calcination (at high temperature) has shown to be a very common and efficient route to produce 0D nanostructures.

1.3.2. 1D nanostructures

The 1D nanostructures can have different forms such as wires, tubes, belts, and rods. In these structures only one of its dimensions (the length) is not in the nanometer range, with diameters normally being tens of nanometers. Nanowires and nanorods are distinguished by their length to diameter ratio: while ratios of 100-1000 are usually reported as nanowires, nanorods are typically thicker and have length to diameter ratios between 3 and 5.[49]

These structures have raised high interest in the scientific community, as they are the smallest structures showing an efficient transport of electrons and optical excitations.[16] They present large surface to volume ratio resulting in spatial confinement of electrons, phonons and electric fields around the particles. These properties make them suitable for applications such as catalysis, optoelectronic and sensors.[25]

The synthesis of multicomponent oxide nanostructures is complex, and the complexity further increases when the desired morphology is not very stable or not the structure with the faster nucleation.[1] 1D morphologies are seldom the most favorable, thus 1D nanostructures are normally hard to achieve. Nevertheless a few multicomponent materials have been reported in the form of nanowires so far, with a few review papers having been published on the topic.[15,16,21,50,51] Vapor phase methods are often used to produce 1D nanostructures, by suppling enough energy to induce the desired growth. Alternatively, nanoscale patterning methods, such as e-beam lithography, nanoimprint lithography and focused-ion-beam (FIB) writing, can be combined with conventional deposition methods to pattern materials at a nanoscale level, for instance in the form of nanowires.[1,52]

The AB_2O_4 class of materials is one of the most reported for 1D materials. In 2009, Fan *et al.* reviewed the Zn-based ternary oxide nanotubes and nanowires.[21] Several Zn-based materials were reported by the authors, such as Zn_2TiO_4, $ZnMn_2O_4$ and Zn_2SnO_4.

Kim *et al.* reported the synthesis and application of $ZnMn_2O_4$ nanowires (**Figure 1.5**a).[53] The α-MnO_2 nanowires were firstly synthetized by hydrothermal reaction and were then mixed with $Zn(CH_3COO)_2$ in high purity ethanol and diethylamine, for several hours. Finally, the $ZnMn_2O_4$ nanowires are formed with a calcination at 480 °C in an O_2 atmosphere for 12 h.

While several reports on Zn_2SnO_4 nanowires also exist, these consist essentially in vapor phase methods, more specifically in thermal evaporation at high temperature,[54] showing the difficulty in obtaining the nanowire form as mentioned before.[55] This Zn_2SnO_4 phase theoretically requires 750 °C for its formation, making it rather complex to obtain nanowires with this phase. This is emphasized by the fact that there are only a few reports for Zn_2SnO_4 nanowires from solution processes, mostly assisted by seed-layers. For example, Zn_2SnO_4 nanowires were grown on a stainless steel seed-layer and from Mn_3O_4 nanowires.[56,57]

Chen *et al*. produced nanowires with an interesting "zig zag" form by thermal evaporation (catalyst-free method) at 920 °C.[58] Similar structures of Zn_2TiO_4 were reported by Yang *et al.*, (called twinned nanowires by the authors), produced by vapor-phase transport (VPT) at 950 °C.[59]

$CuFe_2O_4$ was also reported as a 1D material, for example, Zhao *et al.* showed a simple electrospinning method, followed by a high temperature annealing, to produce hollow fibers of this material (**Figure 1.5**b).[60]

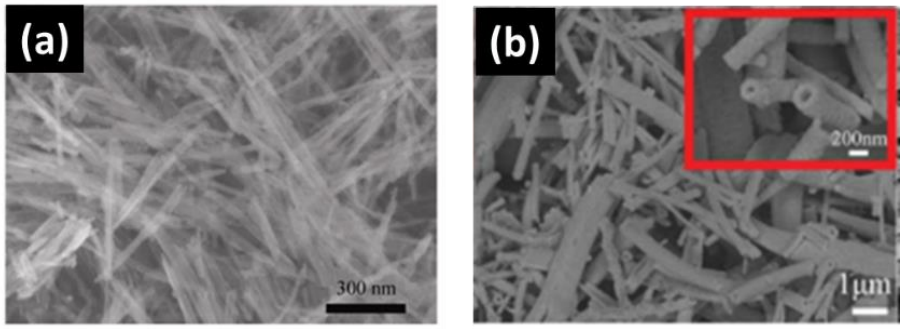

Figure 1.5. SEM images of: (a) $ZnMn_2O_4$ nanowires from ref. [53]; (b) $CuFe_2O_4$ hollow fibers fabricated by simple electrospinning after an annealing at 700 °C for 2 h, from ref. [60].

Regarding the ABO_3 perovskite materials, the Zn:Sn:O system can result in the $ZnSnO_3$ phase. Nevertheless, being a metastable phase, only a few reports for nanowires from these structures exist, consisting typically in carbon-thermal reaction, thermal evaporation or CVD processes [18,61] Regarding reports on solution processing of $ZnSnO_3$ nanowires, there are reports employing FTO seed-layers,[62–64] and an interesting approach where ZnO nanowires are transformed into $ZnSnO_3$ nanowires[65]. Recently, $ZnSnO_3$ nanowires were produced by a one-step solution process without any seed-layer, under the context of the present dissertation work.[45,66] Electrospinning also started to be widely used for producing nanofibers, and $ZnSnO_3$ nanofibers is one the materials already reported.[67,68]

Other 1D perovskites have been reported, being actually very commonly reported one-dimension nanostructured materials.[16,69,70] As early as 2011, Rørvik *et al.* made a review of one-dimensional nanostructures of ferroelectric perovskites.[69] Titanites such as $SrTiO_3$, $CaTiO_3$ are also very often reported as 1D nanostructures.[16,69,71,72] For example, **Figure 1.6** shows $CaTiO_3$ nanofibers produced by electrospinning used for drug release.[73]

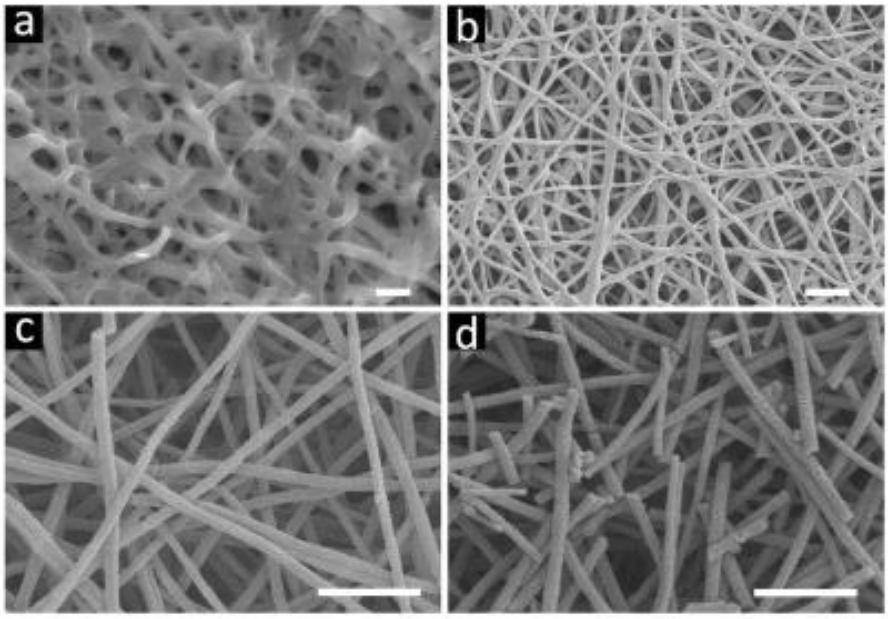

Figure 1.6. SEM images (a-d) of $CaTiO_3$ nanofibers with different conditions of synthesis. The images' scale bar is 1 μm.[73]

An alternative approach for producing 1D perovskites was reported by Barrocas *et al.*, showing the fabrication of $CaMn_3O_6$ nanorods by RF-sputtering film deposition, using an unconventional nanopowder target of the same material produced by combustion, followed by a post-annealing treatment at 800 °C for 6 h in an air atmosphere.[70]

Concerning ABO_4 structures, this class has also been reported in one-dimensional form. For example, $NiMoO_4$ nanowires were reported by several groups, with Guo *et al.*[74] showing the hydrothermal synthesis of these structures on carbon cloths (**Figure 1.7**), while Cai *et al.* presented the hydrothermal synthesis of $NiMoO_4$ nanowires on a Ni foam.[75]

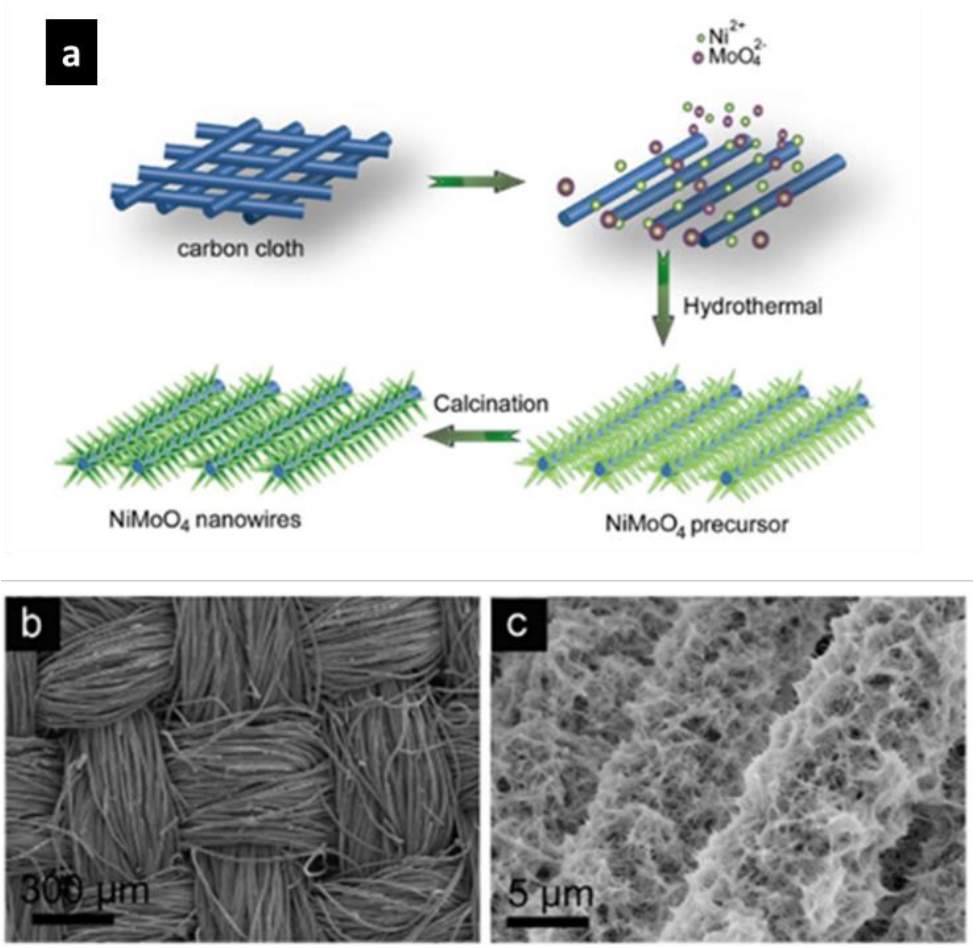

Figure 1.7. (a) Schematic and (b and c) SEM images of the hydrothermal synthesis of $NiMoO_4$ nanowires on carbon cloths.[74]

In summary, a wide range of green multicomponent oxide materials 1D structure were already reported. Nevertheless, these are often synthesized using expensive methods (vapor-phase methods) associated with elevated temperatures, whereas a much harder task is achieving 1D nanostructures by solution processes, with reports typically presenting a much higher degree of complexity. This way the fabrication of this type of structures through simpler and low-cost methods is still a challenging goal to be achieved.

1.3.3. 2D nanostructures

The 2D nanostructures have only one dimension confined at the nanoscale. These structures present a very high surface to volume ratio.[76] Different 2D structures have been reported, such as nanosheets, thin films, nanowalls, nanoprisms, nanoflakes, nanoplates and nanodisks.[77]

Regarding thin films, it is a technology that has been widely developed, for which amorphous films are typically used. Usually they involve either vapor phase methods or other cumbersome techniques. In-based materials are the most common for thin films, as mentioned before.[6] Nevertheless, due to environmental issues and the scarcity of the material, In-free thin films have

been increasingly explored. For example, ZTO thin-films have gained high attention in the last years, especially as semiconductor layer in electronic devices, due to their great electrical performance, and have been produced not only by physical processes (such as sputtering) but also by solution processes (as combustion).[78–80]

Concerning 2D nanocrystals, some of the most common multicomponent oxide materials are based-on Co, Bi or V. Nevertheless, environmentally friendly materials such as Zn-based materials are also very common. Recently, 2D $ZnSnO_3$ nanostructures, produced by hydrothermal synthesis, were reported.[81,82] Particularly interesting are the face-centered $ZnSnO_3$ flakes (**Figure 1.8**) synthesized by a hydrothermal method at only 100 °C.[83] **Figure 1.8** presents 2D $ZnSnO_3$ nanostructures (nanoplates and nanosheets).

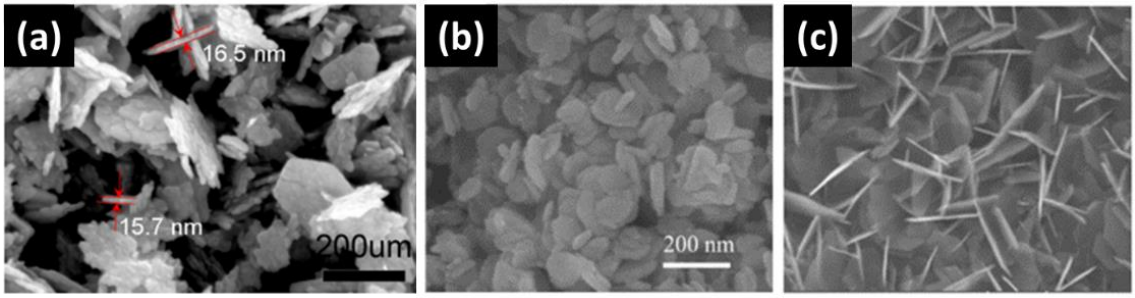

Figure 1.8. SEM images of: (a) $ZnSnO_3$ nanosheets;[81] (b) $ZnSnO_3$ nanoplates;[82] and (c) face centered $ZnSnO_3$ nanoflakes.[83]

Also a ABO_3 material, $SrTiO_3$ nanosheets were reported as well, synthesized via solvothermal route with ethylene glycol, for example.[84]

Nanoplates with Zn_2SnO_4 structure were also already reported, with Cherian *et al.* showing its production by hydrothermal synthesis.[55] Concerning spinel materials, Zhang *et al.* reported $CuFe_2O_4$ nanodisks produced by hydrothermal synthesis at 180 °C for 24 h.[38]

In the previously mentioned report by Cai *et al.* regarding $NiMoO_4$ nanowires, the hydrothermal synthesis of ultrathin mesoporous $NiMoO_4$ nanosheets on Ni foam is also shown.[75]

Furthermore, Guo *et al.* reported orthorhombic $Ho_2Cu_2O_5$ nanoplates produced via coordination-complex methods with and without N_2 environment, showed in **Figure 1.9**, both employing high temperatures (≥ 800 ºC).[85]

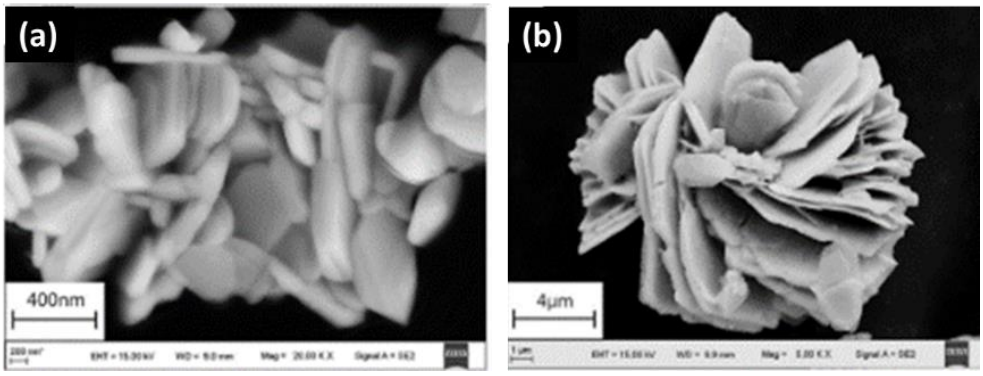

Figure 1.9. (a) SEM images of $Ho_2Cu_2O_5$ nanoplates produced by coordination-complex method under N_2; (b) High-contrast SEM images of $Ho_2Cu_2O_5$ nanoplates produced by coordination-complex method.[85]

As 2D nanostructures have received increased attention in the last years, due to their high surface area, many materials have been developed in different 2D structures. While a very common technique to produce nanosheets is the exfoliation of layered materials, to the authors best knowledge there are no reports using this method to produce 2D nanostructures of environmentally friendly multicomponent oxide materials.[86] For these materials the hydrothermal method is the most employed for 2D nanostructures, unlike the case for 1D structures where the vapor-phase methods are predominantly used.

1.3.4. 3D structures

In 3D nanostructures, there is no confinement in any of the dimensions, with all of them being larger than 100 nm. There are several forms of 3D nanostructures reported, such as nanoflowers, nanocones, octahedrons, nanoballs, nanocubes, nanocoils and nanopillars.[77]

Hollow spheres are an interesting example, with application in drug delivery, but the complexity of both composition and morphology make it very hard to synthesize.[87] Nevertheless, there are a few examples of multicomponent oxide hollow spheres. $SrTiO_3$ hollow spheres were synthesized through a simple and rapid "TEG-sol" method, by Hao *et al.*.[88] Also, Gao *et al.* reported the synthesis of $ZnSnO_3$ hollow spheres (**Figure 1.10**a) by hydrothermal synthesis at 120 °C for 3 h.[89]

A very common 3D structure is a nanocube shape. For instance, Chen et al. reported a synthesis which could result in $ZnSnO_3$ nanocubes (**Figure 1.10**b) or $ZnSnO_3$ nanosheets, depending on the processing temperature.[81] Other example was shown by Zhang *et al.*, who reported $CuFe_2O_4$ nanocubes, produced by hydrothermal synthesis at 180 °C for 24 h.[38]

Another common 3D structure is the octahedron shape. Octahedrons of Zn_2SnO_4 have been reported by several different groups, and this was identified as the most stable phase and shape for ZTO (**Figure 1.10**c). Zn_2SnO_4 octahedrons constituted by nanoplates, as shown in **Figure**

1.10d, can also be formed.[90,91] Another example of octahedrons was shown by Sato *et al.*, who reported the hydrothermal synthesis of delafossite $CuAlO_2$.[92]

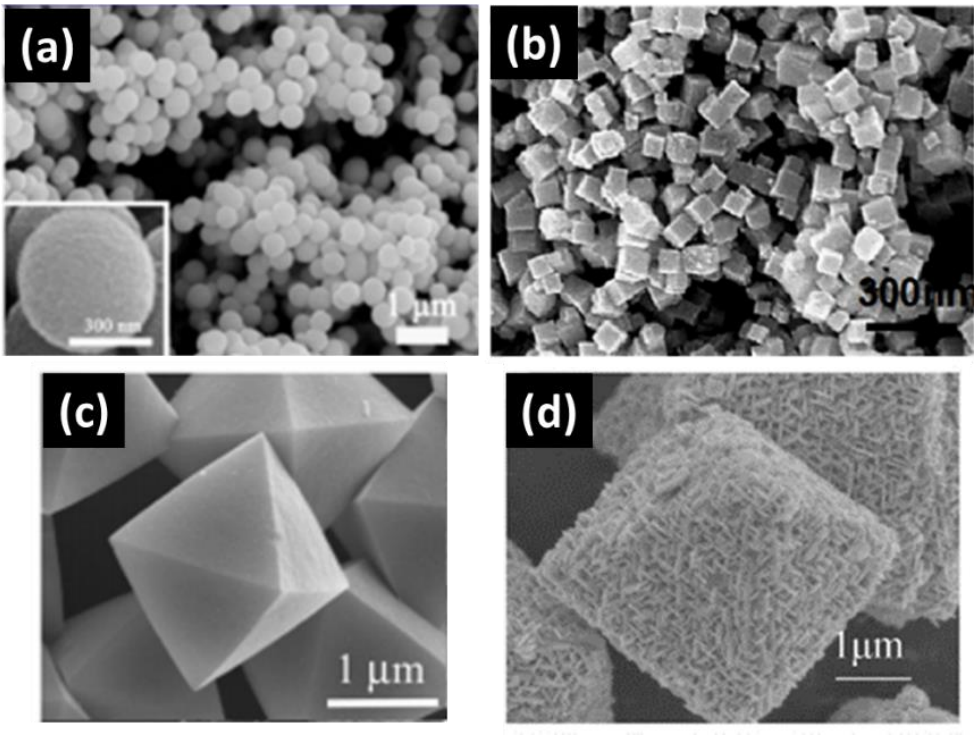

Figure 1.10. SEM images of: (a) orthorhombic $ZnSnO_3$ hollow spheres from ref [89] and (b) Face-centered $ZnSnO_3$ nanocubes from ref. [81] (c) Fe-SEM images of Zn_2SnO_4 octahedrons from ref. [93]; and (d) SEM image of Zn_2SnO_4 octahedrons formed from nanoplates from ref. [90].

Another common example for 3D nanostructures is the nanoflower-like, which are very common for Co-based materials. Still, Zn_2SnO_4 nanoflowers have also been reported. Jaculine *et al.* showed Zn_2SnO_4 nanoflowers produced by hydrothermal synthesis for 48 h at 220 °C.[94] Another example is $ZnMn_2O_4$ nanoflowers that were produced via template-free hydrothermal synthesis.[95] This type of nanostructures is very interesting due to their high surface area, an important characteristic for applications such as sensing or catalysis.

In summary, like was shown for 0D, 1D and 2D nanostructures, several multicomponent semiconductor oxide 3D nanostructures have already been reported, with Zn-based materials being once again the most commonly reported. Some of the crystalline structures for these nanostructures are complex and consequently a well-controlled process for their production is hard to achieve.

1.4. Synthesis methods

Different approaches can be followed in order to induce the desired nanostructures' formation. The nanostructures can be obtained by chemical reaction or by nanomanipulation

techniques, such as template membranes or (nano)lithography processes.[15,96,97] Thus, they can be produced in the form of powder or directly grown on substrates, the latter often involving the use of seed-layers to induce the nanostructures' growth.[25]

Nevertheless, whichever the followed approach, there are several chemical and physical methods based on either vapor phase or solution phase processes, for synthesizing the multicomponent oxide nanostructures.[98]

1.4.1. Vapor phase methods

Vapor phase (VP) methods are the most common processes to synthesize metal-oxide nanostructures. These methods can be categorized by either a vapor–liquid–solid (VLS) mechanism or a vapor–solid (VS) mechanism, with the most common VP processes being chemical vapor deposition (CVD), laser ablation (pulsed laser deposition), thermal evaporation and sputtering.[18,54,99]

Briefly, in VLS methods a catalyst is used to direct the nanostructures' growth, being that these catalysts are formed at high temperatures, followed by the adsorption and dissolution of a gaseous precursor and finally the precipitation of the nanostructures. This process is very common to produce nanowires, where the size is easily controllable by adjusting the catalyst size. Nevertheless, catalyst remains are usually left attached to the nanowires. Regarding VS processes, catalysts are not required, with the growth of the nanostructures being controlled both by the materials' crystalline structure and the employed reaction parameters (temperature, pressure, etc.).[98]

The advantages of these VP methods over solution-based ones are related with excellent crystallinity and uniformity.[98] However, these techniques are cumbersome, expensive, and generally demand high temperatures (>700 °C).[100] Thereby, solution-based methods are imperative for decreased complexity, cost and temperature, requirements of most of the industrial applications.

1.4.2. Solution-based methods

Solution synthesis of nanostructures consists in the mixture of well-defined quantities of different ions, which are then submitted to controlled conditions of heat, pressure and temperature, resulting in a precipitate formed by insoluble compounds. This resultant precipitate (the nanostructures) is collected and usually cleaned and dried.[24] In some cases additional annealing treatments of the nanopowders are performed in order to obtain the desired crystallinity. Furthermore, by varying the different synthesis parameters it is possible to control the morphology, size and crystalline structure of the synthesized nanostructures. In these methods a wide array of chemical precursors (which supply the desired ions to the solution) as well as several types of solvents and additives can constitute the solution.[101]

Solution methods present themselves as a great alternative for the synthesis of nanostructures: they permit a decrease of complexity, cost and temperature (being compatible with different technologies such as flexible substrates [98] and paper electronics [102]), while also enabling very satisfactory levels of performance. Moreover, these methods have a high yield (product ratio to reagent), allow the fabrication of a wide variety of compounds and can be easily scaled in volume, a fundamental advantage when considering their industrial prodution.[15,24,96]

Nevertheless, there are some drawbacks concerning these solution-based processes. For example, concerning the synthesis of 1D metal oxide nanostructures, directing the growth of the structures may require additional aspects to be considered such as the use of surfactants, templates or seeds (thin films, 1D structures, etc.). This is even more relevant when aiming for 1D nanostructures of complex materials, such as perovskites.[101]

The main challenge of the solution processes is to well-understand and control the reaction kinetics, often being hard to achieve a good reproducibility and to have a perfect control over the obtained nanostructures' crystallinity and morphology. This is especially true for the syntheses of multicomponent oxides, for which the complexity is significantly higher.[15,16] Nevertheless, there are several solution-based processes that have been reported as nanostructures' fabrication methods, such as combustion, electrospinning, spray pyrolysis, sol-gel, electrochemical deposition, and hydro/solvothermal methods.[15,103] The latter are the most frequently used and they are described next.[98,100,104]

Hydro/solvothermal methods

The hydrothermal methods have been widely explored and developed in the last years.[100,101,104] This method consists in a chemical reaction in an aqueous solution, under high pressure (> 1 atm) and at temperatures usually ranging between 100 °C and 300 °C. In case of using non-aqueous solvents, the method is called solvothermal.[100,101] Typically, the solution is kept inside an autoclave and a conventional oven is used as heat source. The pressure inside the autoclave is dependent both on the temperature and the volume used, and very high values can typically be supported. This allows for an elevated energy supply for the reactions even at relatively low temperatures.

While the typical nucleation and growth mechanism of the oxide nanostructures in these reactions is thought to consist mainly in dissolution–reprecipitation, these mechanisms are often not well understood. The mechanism consists on the precursors' dissolution followed by the diffusion of their species and their reaction/precipitation resulting in the final compound. Both dissolution and diffusion of the species during the synthesis are strongly determined by the solvent (as well as the employed hydrothermal parameters) playing then a very important role in this process. When the precursors' solubility is not high enough, precluding an efficient reaction, mineralizer agents can be used (NaOH, KOH, etc.) to increase the solubility of the species.[100,101]

While inexpensive and simple, this technique still allows for a well-controlled obtention of the desired nanostructures' shape and structure with a high reproducibility, thus presenting as an excellent alternative to the conventional physical methods.[32,105]

Additionally, while conventional ovens are typically used as the heat source, recently microwave-assisted synthesis have been widely explored and have shown to allow to reduce the synthesis duration due to its more efficient (and more homogeneous) heat transfer process.[106–108]

1.5. Characterization techniques

To properly identify the synthesized material and study its properties, a wide range of techniques can been used to analyze either the crystallinity, morphology, size, element concentration, and the electrical, optical and mechanical properties.[109] In this review special emphasis will be given to the techniques usually employed for identification of the nanomaterials, which normally are used in complement to each other. A sub-section will be dedicated to the most common techniques for determination of the optical, mechanical and electrical properties.

1.5.1. Scanning electron microscopy (SEM)

The scanning electron microscopy (SEM) is the one of the most used techniques to analyze the morphology of the nanostructures, by imaging the samples surfaces. The basis of this technique consists in the incidence of a highly energetic and focused electron beam in a surface, consequently emitting primary electrons from the interaction while the materials emit secondary electrons, backscattered electrons (BSE) and X-rays being that some electrons are also transmitted. High resolution images (presently at atomic scale, 1-5 nm) of the sample's surface are created by the secondary and backscattered electrons.[110] The electron beam can be generated either using a tungsten filament cathode, by thermionic emission, or by a field-emission gun, with the electron energy typically in a range between 1 to 30 keV. In the electron column the beam is oriented by a pair of scanning coils or deflector plates for scanning a specific area of the sample. As the emission of secondary electrons is dependent on the angle of incidence between the beam and the sample, an image generated by these electrons presents contrast between flat and steep regions of the material, thus giving information about the surface topography. On the other hand, the electron backscattering is dependent on the atomic weight of an element, thus, images obtained through these electrons show contrast according to elemental composition of the material, providing useful information about the chemical composition of the sample.

1.5.2. X-ray diffraction (XRD)

X-ray diffraction (XRD) is commonly used to investigate the crystallinity of materials, allowing to identify the structure, phase, lattice parameters and crystalline grain size for crystalline materials.[109,111,112] As so, this technique one of the most employed for the nanostructures' characterization.[109] It should be noted that material identification using this technique is only possible for crystalline materials, whereas amorphous materials result in no identifiable patterns.

The qualitative and quantitative analysis is based on the Bragg's law of diffraction, represented by the following equation:

$$n\lambda = 2d_{hkl}\sin\theta \quad (1)$$

Where n is the order of diffraction, λ the X-ray's wavelength, d_{hkl} the interplanar spacing, and θ the incident and diffraction angle, which is swept during the measurement. According to this relation, peaks observed in the pattern formed from the collected x-ray intensity provide structural information about the analyzed material. This technique can also be performed under temperatures up to 1200 °C, allowing to study phase changes under temperature. Nevertheless, similar patterns often exist for different materials, and thus other techniques are usually combined with XRD for the proper identification a material.

1.5.3. Energy-dispersion X-ray spectroscopy (EDS)

Energy-dispersive X-ray spectroscopy (EDS) is a very useful technique that provides qualitative and quantitative surface element analysis. This technique is often integrated in SEM systems where an X-ray detector is integrated. This technique is based on the detection of secondary X-rays emitted from a material as a result of the interaction between a highly energetic electron beam (10-20 keV) with its surface. This X-ray emission is generated up to a depth about 2 µm and is dependent on the elemental composition of the material. Scanning the sample thus results in an elemental mapping. While a quantitative analyzes by peak-height ratio comparison to known standards can be made, the energy peaks correspond to different energy-level shells that often coincide between different elements and so this technique is usually combined with others for a proper material identification.[110,113]

1.5.4. X-ray photoelectron spectroscopy (XPS)

The X-ray photoelectron spectroscopy (XPS) is based-on the photoelectric effect. This technique can provide information about the surface of the sample, namely electronic structure, elemental composition, oxidation state and ligand binding (surface-sensitive), with most of the signal arising from the top 1-10 nm.[109] In XPS, photoelectrons are emitted from the sample after it is stricken by soft monochromatic X-rays with energies between 200 and 2000 eV. The kinetic

energy of the ejected electrons is determined by a spectrometer and is related to the binding energy of the atom from which it was ejected. This relation is given by:

$$h\upsilon = E_K + E_B + \phi \quad (2)$$

where h is the Planck constant, υ the frequency of the incident X-ray, E_K the electron kinetic energy, E_B the binding energy of the electron to the nucleus relative to the Fermi level and ϕ the work function of the material (in case of being a solid).[114]

1.5.5. Fourier-transformed infrared spectroscopy (FTIR)

While the Fourier-transformed infrared spectroscopy (FTIR) was initially used in the investigation of organic materials, it is now very commonly used to analyze inorganic materials. By detecting the presence of OH groups its very suitable for the identify of hydroxides.[111] Moreover, the technique can be realized with materials in the different matter phases: liquid, solid or gas.[111] In this technique, a sample is irradiated with electromagnetic radiation with wavelengths within the mid-infrared region (4000-400 cm^{-1}), and by deducing the transmitted radiation from the total irradiated the absorbed fraction is measured. Molecules absorb frequencies that are characteristic of their structure, being that these resonant frequencies matching the vibrational frequencies allowed in the molecule. As these energies dependent on the shape of the molecular potential energy surfaces, the masses of the atoms, and the associated vibrionic coupling, the method thus provide information on molecular structures and interactions. In inorganic materials, such as the case of the nanomaterials in this scope, oxide bonds between constituents of the material result in absorption bands that can be used as fingerprints for identification.[111]

1.5.6. Raman spectroscopy

Raman spectroscopy is a technique based on the inelastic scattering of photons at the electrode cloud of a molecule. The samples (solid, liquid or vapor) are irradiated with a monochromatic light (typically a laser) with wavelength either in the near-IR, visible or near-UV range, and the light emitted from the sample is collected in a monochromator. The difference in energy between incident photons and emitted photons (Raman shift) gives the energy shift between rotational-vibrational-electronic (rovibronic) states in the molecule. The intensity of this effect is proportional to the electric dipole-electric dipole polarizability of the molecules, and thus depends its rovibronic states. As these states are specific to chemical bonds, they are a fingerprint for material identification, and provide information about the chemical structure and physical form of the materials.[115,116]

1.5.7. UV-visible spectroscopy

This technique is used to measure optical parameters such as the absorption coefficient, refractive index, optical band gap and transparency of a material. Furthermore, the technique is very interesting for nanostructures as it allows to determine the size and concentration, while being capable of also giving information on agglomeration state as well as some information on the nanoparticles shape.[109] In this technique a UV/visible light beam irradiates the sample and both the transmitted as well as the reflected light (with the help of an integrating sphere) are collected, from which the absorbed light can then be inferred. The absorption spectra can then be constructed which is related to the electronic structure of the material.[115]

1.5.8. Photoluminescence (PL) spectroscopy

This technique is used for characterization of the electronic structure of materials. PL can be used to quantify optical emission efficiencies and other material properties such as composition, impurity content and thickness.[117] The technique consists in using a fixed wavelength excite electrons in the sample material (photo-excitation), and then measure the different wavelengths emitted from the relaxation of these electrons to lower energy states. These corresponding energy levels can give information on material imperfections and impurities, e.g. in the case of the metal oxide materials defect levels associated to oxygen vacancies can be observed.[118]

1.5.9. Atomic force microscopy (AFM)

This technique consists in the physical scanning of a surface by a probe with an atomic-scale tip, producing a high-resolution image of the material surface. While this technique pictures the topography of the sample, several other modules are available for properties' such as electrostatic force microscopy (EFM), Kelvin probe (KPFM), conductive AFM (C-AFM), piezoresponse (PFM) which can provide further morphological, electrical and mechanical information. This technique can provide valuable information for nanomaterials such as size, shape, structure, dispersion, and aggregation.[110]

1.6. Integration and applications

The numerous nanostructure types in which multicomponent oxide materials can be grown result in a varied array of properties which can be tuned regarding the nanostructures' morphology (shape, size, structure) and composition (oxygen content, defects, material stoichiometry, etc.). As so, these nanostructures have been explored for a wide range of applications. Regarding their implementation, the nanostructures can either be directly produced in the desired substrates (for which seed-layers can be employed to induce specific structures in specific substrate areas) or

in the form of powder for which post-processing transfer methods are then required for device integration.

The transfer of the nanostructures presents as one of the main challenges in their application, as these transfer methods are often either difficult to perform or inefficient. Still, these methods are typically associated with low costs and allow for a greater flexibility to obtain different phases within a material system during the synthesis process itself. Additionally, when increasingly more demanding substrates (e.g, conformal and transparent) are required by concepts such as the IoT, the flexibility in integration given by transfer methods gains even more importance.[119]

Several transfer methods have already been explored, the most common being drop-casting and spin-coating, spray-coating, printing and dielectrophoresis (electrodeposition).[120–123] While challenging, the further development of these methods to a point where they permit a reliable nanostructure integration is key, as the multicomponent oxide nanostructures' wide range of applications demands for significantly different approaches and architectures to be explored.

The most common applications for these nanostructures will be presented next, referencing the main materials that have been used for each application, with the focus being maintained on multicomponent materials containing non-critical elements.

1.6.1. Electronic Applications

Due to market implications, electronics applications are always a relevant drive for materials. The multicomponent semiconductor nanostructures are particularly interesting for these applications, with wide band gap semiconductors allowing for high-power and high-frequency operations.[100]

In **Figure 1.11** the electronic density of states for semiconductors with different dimensions is presented. As observed, the electronic confinement alters the shape of the density of states which, in the case of no confinement effects, presents the typical parabolic distribution known for most semiconductors. As previously mentioned, the designation of the nanostructures relates to the number of dimensions in which the electrons are not confined: in a 0D nanostructure the electrons are confined in all dimensions, in a 1D nanostructures the electrons are confined in 2 dimensions (and move in one dimension), in 2D nanostructures the electrons are confined in 1 dimension (and move in 2 dimensions) while for 3D nanostructures the electrons are not confined in any dimension.

The size-dependency of properties is a very interesting phenomena for the tuning of nanostructures for specific applications and while this dependency is higher the more confined the nanostructures are, 1D nanostructures still present several advantages over 0D nanostructures, being in fact the more commonly sought for electronic aplications.[124] In these structures, the quantum confinement results in high density of electronic states near the edges of the conduction and valence bands, with the discretization of the energy states beginning to dictate

the material's properties.[124] Additionally, the carriers' movement is limited to a single dimension, leading to a reduction of the low-angle scattering. All this results in efficient charge transport characteristics with high electrical mobilities being found for these materials, which is desirable for different applications but especially for electronics.[98] Furthermore, the high aspect ratio of these structures facilitates the electrical contacting.

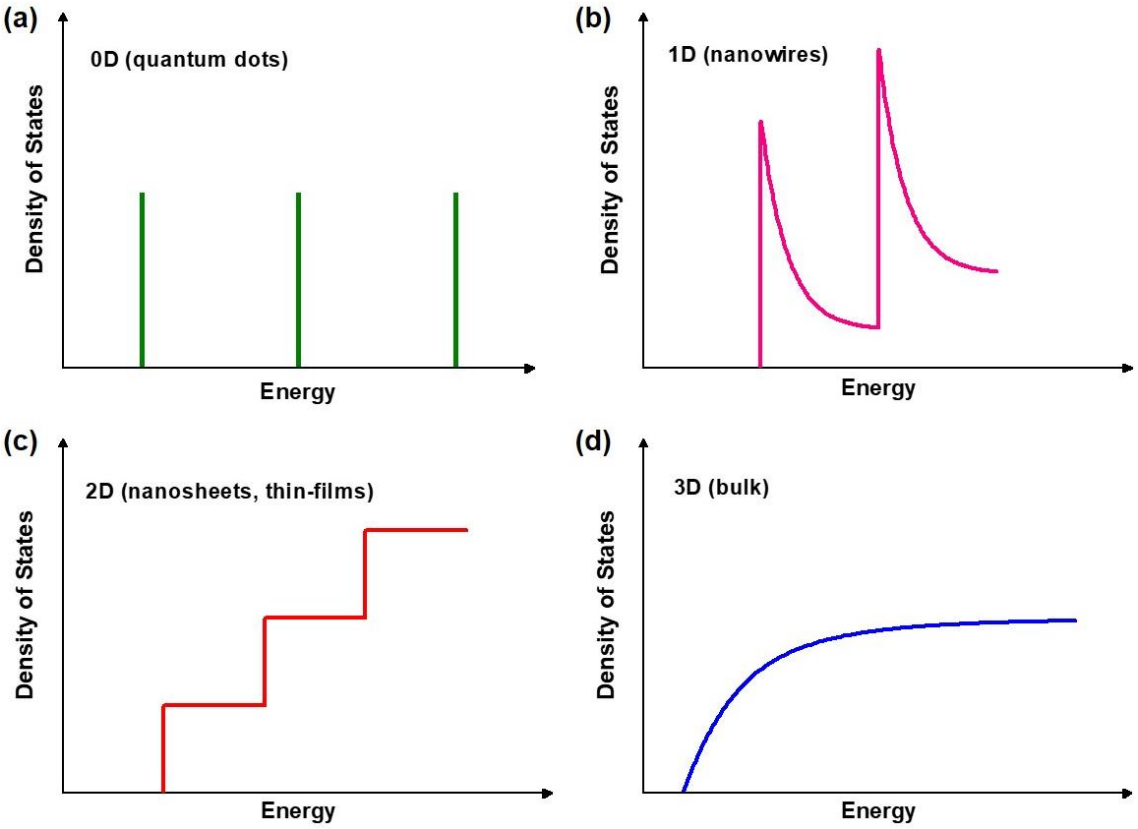

Figure 1.11. Density of states of a semiconductor with a: (a) 0D structure (quantum dots), (b) 1D structure (nanowire), (c) 2D structure (nanosheets, thin films) and (d) 3D (bulk) structure.

Field effect Transistors

Field effect transistors are the key element in today's electronics. Its miniaturization is always pursued, and for the Si technology transistors fabricated in 7 nm-nodes are already a reality. With nanoelectronics demanding for a new generation of materials to circumvent the limitations of conventional Si technology, multicomponent metal oxide semiconductor nanostructures appear as interesting candidates. Due to their excellent electrical properties, as previously discussed, 1D structures are the most interesting in this regard, having already shown a great applicability as a semiconductor material in field-effect transistors.[50,98,125,126] A few transistors based on multicomponent oxide nanostructures have been reported lately, however, as with the thin film technology, most consist in In-based materials.[5–7,98,120,127–130]

For the thin film technology, promising In-free multicomponent oxide materials have already been shown. A prime example is ZTO, a candidate for the replacement of IGZO, for which devices produced both by physical and solution processes have been reported by several groups.[131–134] For instance, in CENIMAT (our research group) ZTO produced both by sputtering and by solution based processes was already demonstrated has having great potential: Fernandes *et al.* showed the use of amorphous ZTO TFTs produced with low thermal budgets (≤ 180 º C) for inverters and amplifiers, while Salgueiro *et al.* showed ZTO TFTs by solution combustion synthesis.[78,80] As in thin film technology, ZTO is also one of the most promising multicomponent metal oxides for transistors with nanostructures.[58,126,135] Demonstrations of discrete Zn_2SnO_4 nanotransistors were already made using nanotransfer moulding of ZTO inks followed by annealing at 500 °C, or by simple pick-and-place approach of drop-casted ZTO nanowires prepared by CVD above 700 °C (**Figure 1.12**) and by thermal evaporation at 1000 °C.[18,52,99]

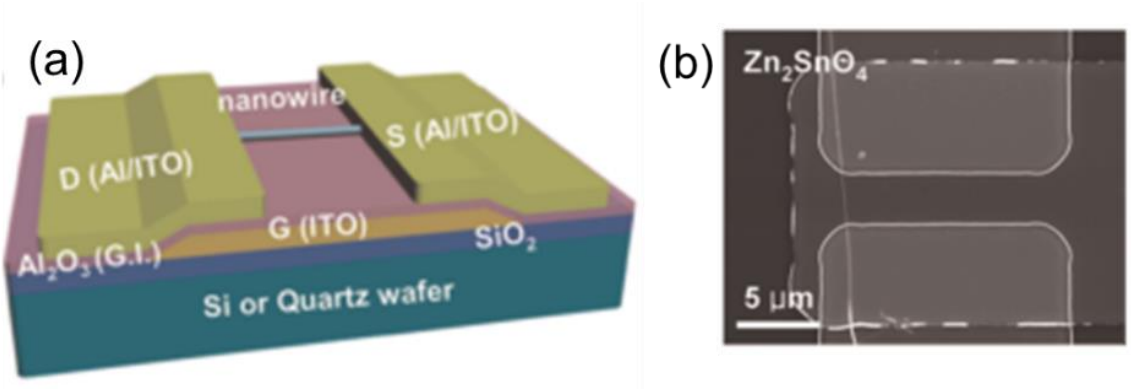

Figure 1.12. (a) Cross-sectional view of a bottom-gated nanowire transistor structure. (b) FE-SEM image of the nanowire channel region for a Zn_2SnO_4 nanowire transistor. Adapted from ref. [99].

Different architectures can be considered for single nanowire transistors, as shown in **Figure 1.13**. As the simpler approach, a typical TFT structure can be emulated by replacing the usual semiconductor film by a horizontal nanowire using either a simple pick-and-place method or another transfer method. Nevertheless, architectures such as those employing gate-all-around the 1D nanostructures are very interesting approaches as the excellent gate control they provide allows for very high on/off ratios, steep subthreshold slopes and low threshold voltages.[136] Moreover, vertical architectures trough aligning the nanowires perpendicularly to the substrate enable increased device density.

An alternative approach are transistors employing random nanowire networks. While resulting in poorer performance than single wire architectures, these are considerably less demanding in terms of manufacture and have the potential to bring a significant boost to the field-effect mobility achieved with oxide semiconductor thin films.[126,137]

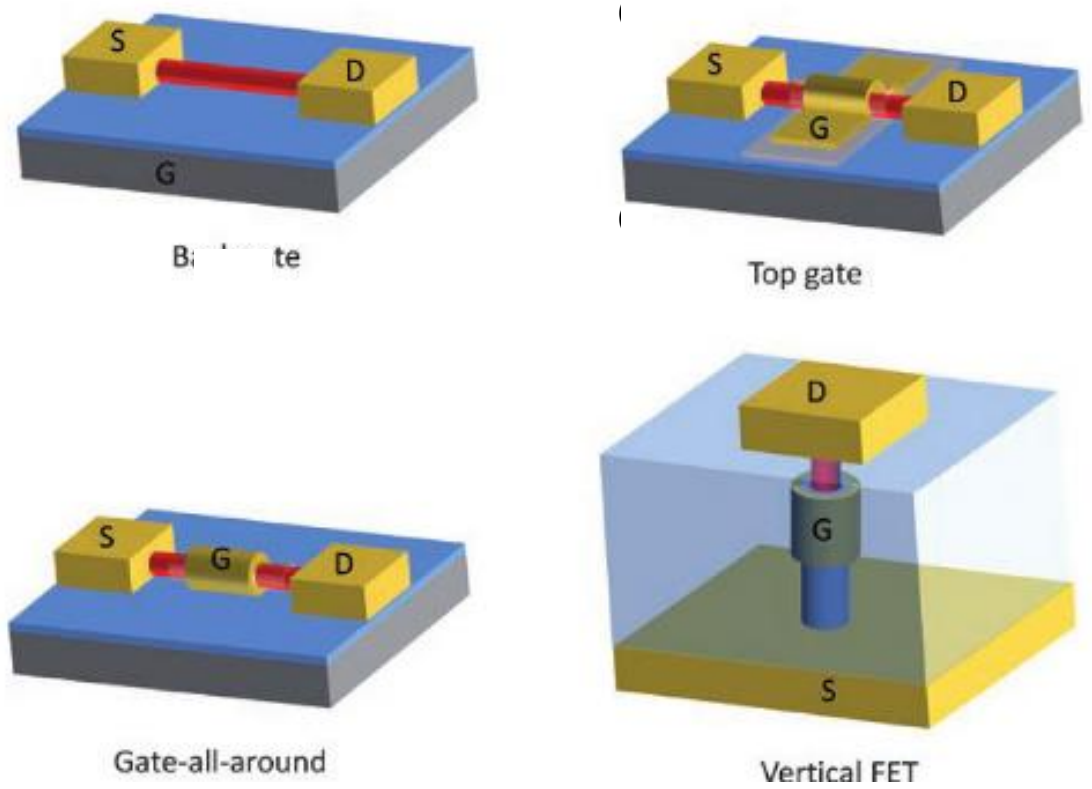

Figure 1.13. Schematic of nanowire transistor structures: horizontal nanowire FET with a (a) back-gate, (b) top-gate (c) gate-all-around geometry and (d) vertical nanowire FET with gate-all-around geometry. Adapted from ref.[138].

Resistive Switching Memories

Other electronic devices than transistors can greatly benefit from the properties of semiconductor nanostructures. For instance, these materials have also been used for the resistive switch layer in an emerging type of memory devices known as memristors. Resistive switching memories (or memristors) have been proposed as a superior alternative to conventional memories by possessing both elevated integration capability (higher than flash) and non-volatility, while enabling access speeds close to that of dynamic random-access memory (DRAM). Memristors are typically composed by a metal-oxide-metal structure, where the modification of the resistance state is due to the change of an internal state variable in the oxide layer.[139] Wide band gap semiconductors are good candidates for this application due to its highly mobile Fermi level, allowing for a strong modulation of the resistance state.[6] From the various oxide materials that have been explored for this application, TiO_2 and ZnO have attracted the most attention due to their high dielectric constant, wide band gap and fast resistive switching behavior.[140] Additionally, ferroelectric materials have been reported as active layers in these devices, with nanostructured ferroelectric materials presenting better performance than film-based ones.[136] Concerning nanostructures, reports show ZTO as the active material in memristors in different forms, such as amorphous thin films, Zn_2SnO_4 nanowires and $ZnSnO_3$ nanocubes, being the latter a known ferroelectric material, and thus specially relevant for this application.[141–148]

Circuits integration

Several nanocircuits using these electronic devices were implemented in the last years, and **Figure 1.14** shows a schematic of the devices that can be integrated in the same nanowire-based chip.[149] For example, Yan *et al.* developed programmable nanowire circuits for processors, using Ge/Si core/shell nanowires, while Ju *et al.* reported AMOLED displays driven exclusively by ZnO/In_2O_3 nanowire electronics and showed that such displays can be optically transparent.[150–152] To the authors' best knowledge, there is no demonstrations of circuits integration using environmentally friendly multicomponent oxide semiconductor nanomaterials. Also, a demonstration of high-density integration with oxide nanotransistors with controlled properties on large areas is yet to be seen, owing mostly to the inefficient transfer or direct grow methods of these materials.

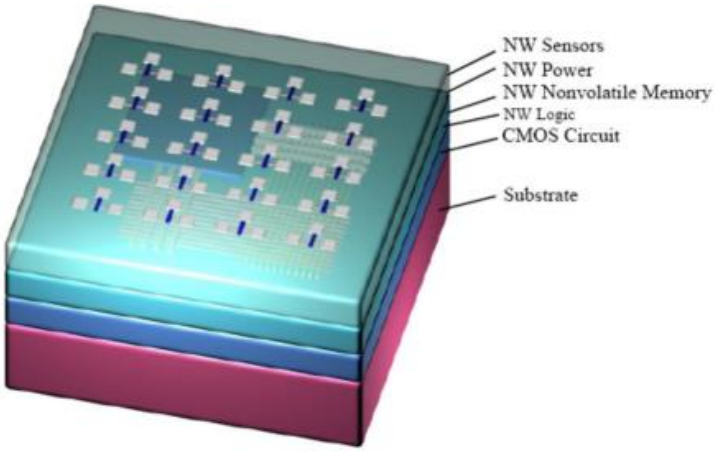

Figure 1.14. Schematic of a 3-D multifunctional nanowire-based chip.[149]

1.6.2. Sensors

Multicomponent oxides nanostructures are very interest for sensor applications. Their smaller crystallite size, high surface-to-volume ratios and surface reactivity result in enhanced sensitivities/selectivity with multicomponent materials typically presenting smaller response times and superior stabilities compared to binary oxides.[153] Moreover, the implementation of these nanostructures in sensors allows miniaturization of the devices, as well as cost reduction. Several types of nanostructures have been employed in sensor devices, such as nanoparticles (0D), nanowires (1D), nanosheets (2D) and nanocubes (3D).[119] Different sensing application have been explored using multicomponent oxide nanostructures such as gas sensors, humidity sensors, photosensors and biosensors, as described next.

Gas sensors

Environmental issues coming from the use of insecticides and pesticides in agriculture, combustion of fossil fuels, and others, are a concern nowadays.[154] Under this scope, gas sensors are the most commonly reported application for oxide nanostructures. Besides the typically high surface-to-volume ratio of nanostructures another important aspect regarding the metal oxides nanostructures is their surface defect density which results in a high conductance change as carriers are activated from their trapped states to the conduction band when exposed to the target gases.[155] This results in an increased response by the sensors, given by the resistance change of the material.[36,154,156] Additionally, catalytic activity as that known for transition metal oxides has been related to increase gas adsorption capability.[154,157] ZnO was shown to be capable of detecting a variety of gases (CO_2, H_2S, NO_2, NO, NH_3, C_3H_8 and CH_4), and studies on the influence of morphology showed that changing the nanostructures' shape allows to enhance the sensors' sensibility to different gases.[119] $ZnMn_2O_4$ nanoparticles were already used as gas sensors for propane and carbon monoxide detection.[36] $ZnTiO_3$ nanoparticles were used on a sodium super ionic conductor for detection of toluene.[158] Zn_2SnO_4 and $ZnSnO_3$ nanostructures of different forms, such as nanoparticles, nanofibers and nanowires have also been widely used for gas sensing applications.[67,159] Notably, 1D nanostructures are specially advantageous when FET architectures are considered for the gas sensing.[155]

Humidity sensors

Multicomponent oxide nanostructures have also been used as active layer for humidity sensors. Their surface reactivity provides the humidity sensing properties, as the interaction between their surface and water molecules generates an electrical resistance change.[42] Therefore the nanostructures' morphology, surface defects and interfacial properties control their sensing performance.[47] In comparison to binary oxides, multicomponent oxides present a higher stability in aqueous environments, increasing their reliability for these applications.[160] $ZnSnO_3$ has been reported as an excellent humidity sensor, in different nanostructure forms such as nanoparticles or in a composite of $ZnSnO_3$ nanocubes and Ag nanowires.[42,47]

Photosensors

Oxide semiconductors are known to be great light sensors due to their photoconductivity.[161,162] Most of the multicomponent oxides being considered here have wide band gaps being well suited for UV detection.[163] UV photodetectors play an important role in biological applications, space exploration, environmental sensors, and also in fire monitoring.[164] Additionally, photoconductors are important for concepts such as light-wave communication, binary switches in imaging techniques, optoelectronic circuits and next-generation memories. For the latter, it is expected that light-sensitive memristive devices can be used to overcome the processor-memory communication bottleneck, with oxide materials being a prime candidate due to their properties. 1D nanomaterials have already shown high sensitivity to light in experimental devices, attributed to their high surface-to-volume ratio and Debye length comparable to their

size.[165] Nevertheless, the most common multicomponent oxide materials for photosensors are also based on indium, gallium and germanium, as verified for other electronic applications.[100] ZTO appears as the most promising environmentally friendly 1D multicomponent oxide material for photosensing applications.[163] Zn_2SnO_4 has been widely explored for this, with different shapes such as nanoparticles, nanowires and nanocubes having been reported.[28,166–169] $ZnSnO_3$ nanostructures were also reported as photoconductors.[161] While the optical band gap of these materials is typically in the UV energy levels (hence their transparency), quantum confinement effects or even defect levels near the band edges can be explored to increase the absorption for lower energy levels.

Biosensors

The metal oxides' strong electron-transfer kinetics and adsorption capability make them interesting materials for biosensing devices. Thus, multicomponent oxides have also been used for biosensing applications. For instance, $SrTiO_3$ nanoparticles were used for label-free capacitive biosensors for Escherichia coli detection, $ZnSnO_3$ nanoparticles were used as electrochemical biosensors for label free sub-femtomolar detection of cardiac biomarker troponin T and a composite of Zn_2SnO_4 nanoparticles and graphene was used for morphine and codeine detection.[170–172]

1.6.3. Catalysis

Industrial actions and human activities play a negative environmental impact, raising high water pollution, among other issues.[173] Metal oxide nanostructures are being used for photoelectrochemical (PEC) water splitting, production of hydrogen, CO_2 reduction and photocatalysis for pollutant degradation.[174–176] Regarding the breakdown of water pollutants, these materials present great advantages for this application as their band gaps are close to the visible light range and they have high surface-to-volume ratios.[177] Titanium oxide, zinc-based oxides and manganites are some of the most common materials for this application.[160,175,178–182] As multicomponent oxides present a higher stability in aqueous environments when compared with binary oxides, they have a significant advantage for the photocatalytic applications.[160] Different forms of these materials, such as normal spinel, inverse spinel and perovskite structures have been employed.[174,176,183] In fact, piezoelectricity and ferroelectricity (associated with perovskite structures) have shown to play an important role in photocatalysis, since the photogeneration of electron-hole pairs is enhanced by the dipole moment formed by the polarization electric field across the polar materials.[184,185] Several spinel structures have been reported as showing excellent photocatalytic activities, namely ZnM_2O_4 (with M = Fe, Mn or Al), and $CuFe_2O_4$.[38,186–188] $ZnMn_2O_4$ nanoparticles were shown to have high photocatalytic activity, degrading both 96 % of Congo red dye and 45 % of organic carbon in just 15 min.[187] The same material was used for degradation of rhodamine B under visible-light.[186] Inverse spinel structures such as Zn_2SnO_4 nanostructures have also been widely used.[189,190] For instance, Zn_2SnO_4

nanocrystals were used for the degradation of 50 % of reactive red 141 dye in 270 min under sunlight.[189]

Regarding perovskites (ABO_3) nanostructures, different $ZnSnO_3$ structures such as nanowires and nanoplates were already used as photocatalysts for organic pollutants (for example, methylene blue and rhodamine B).[46,191,192] Due to its high optical band gap (3.6-3.9 eV) UV light is usually required to photoactivate this material. Nevertheless, fcc-$ZnSnO_3$ nanoparticles were already reported with a very satisfactory photocatalytic behavior on methylene blue degradation under visible light (0.0156 min^{-1}).[177] $SrTiO_3$ nanoparticles synthesized by hydrothermal synthesis were used for degradation of methyl orange, with a rate of 0.01013 min^{-1}.[41] Recently, an alternative photocatalytic approach has been explored, with piezoelectric materials such as $ZnSnO_3$ (nanowires and nanoplates) and $BaTiO_3$ (nanoparticles, nanoplates and nanowires) being used for piezophotocatalysis.[62,64,193–196] Regarding photocatalytic hydrogen generation, Zieliñska *et al.* showed the performance of alkaline-earth titanates ($CaTiO_3$, $BaTiO_3$ and $SrTiO_3$) in the presence of electron donors, with the best performance being achieved for $SrTiO_3$.[197] Other materials such as $CaMn_3O_6$ nanorods were also successfully applied as photocatalysts for rhodamine 6G under visible light, showing a degradation ratio of 0.3926 h^{-1}.[70]

Not only the phase but also the morphology has been reported as controlling the photocatalytic properties. Dong *et al.* showed the influence of $CaTiO_3$ nano/microstructures' morphology in the degradation of several organic pollutants, finding an optimal activity for butterfly-like dendrites to degrade rhodamine B (2.069 min^{-1}).[198] Other interesting applications of photocatalytic properties have been reported, such as the photocatalytic inactivation of Escherichia Coli using ZTO nanocubes under visible light. Only a 10 % surviving rate was found for the bacteria, whereas the absorption of the visible light was attributed to the inherent surface defects enhancing the absorption edge in the visible region.[160] With this in mind, lower cost methods for nanostructure production (as hydrothermal methods), which typical result in more defective structures, might be advantageous for this applications as defect levels near the band edges may increasing the absorption for lower energy levels.

1.6.4. Energy applications

Energy Harvesting – nanogenerators

Nanogenerators are devices that can convert mechanical vibrations into electrical energy, being highly interesting for smart and self-sustainable surfaces and for the IoT, as they can be used for sustainable energy sources, biomedical systems and smart sensors.[199] Vibration energy is a great renewable electricity source and can be harvested by three effects: piezoelectric, electrostatic and electromagnetic transduction.[200,201] While lead zirconate titanate (PZT) is the material with the highest piezoelectric constant, it is environmentally harmful.[82] Several metal oxides have been explored for this application, with $BaTiO_3$ and $ZnSnO_3$ being the most common

due to their piezoelectric properties.[23,202–204] Nanostructures of these materials are often incorporated in polymers, enabling the robustness required for device practicality.[82,205] Several $BaTiO_3$ nanostructures were already explored for this application (being the most employed material in this regard), an example being shown in **Figure 1.15** where a nanogenerator based-on $BaTiO_3$ nanowires is depicted.[204] Nevertheless, with Ba being a critical material, alternative materials such as $ZnSnO_3$ are pursued and, in fact, several nanostructures from this material (such as nanocubes, nanowires, and nanoplates) have already been reported for energy harvesting devices.[23,82,202,203,206–212]

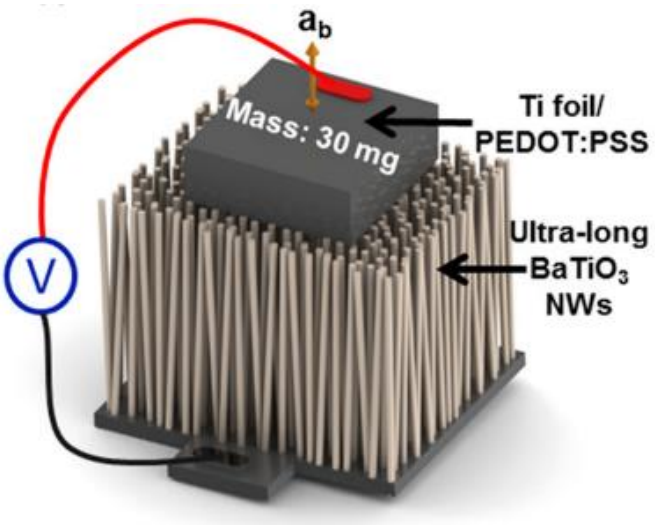

Figure 1.15. Vibration sensing and energy harvesting device with ultra-long $BaTiO_3$ nanowires.[204]

Solar Cells

While solar cell devices allow for a conversion process of solar light (energy) into electric energy, they often demand expensive methods and materials.[54] Multicomponent metal oxides have been used for dye-sensitized solar cells (DSSCs). DSSCs present high efficiency and low fabrication costs, and demand for wide band gap porous semiconductor materials as electrode, with long electron diffusion length, for supporting dye molecules and transporting the photoinjected electrons.[26] These requirements can be met by multicomponent semiconductor oxides, as their properties can be tuned for them to function as transparent conductive oxides (TCOs), and the control of the size/morphology of nanostructures can ensure high surface area for dye adsorption.[26] For instance, Zn_2SnO_4 has been widely used as photoanode for dye solar cells in different nanostructure morphologies as nanoparticles and nanowires.[26,56,213,214]

Electrochemical energy devices: Li-batteries and supercapacitors

Electrochemical capacitors (supercapacitors), rechargeable lithium-ion batteries are promising candidates regarding energy storage and conversion. Li-batteries are one of the most commonly reported systems for electrochemical energy storage employing ternary oxide nanomaterials.[77,215] Several multicomponent oxide nanostructures have been used for this

application, specially ZnO-based compounds such as $ZnFe_2O_4$, Zn_2SnO_4, and $ZnAl_2O_4$ as shown in different reviews.[21,77,216] For instance, Cherian *et al.* compared the performance of nanowires and nanoplates of Zn_2SnO_4 for Li-batteries.[55]

Supercapacitors (SC) can also be considered for this technology. Redox SCs are one type of SC where the charge storage is given by fast redox reactions of active species on the surface of electroactive materials.[217] Metal oxides have been widely used for this application due to their high specific capacitance and energy density, being that ternary metal oxides have shown higher supercapacitive performance than binary metal oxides due to their multiple oxidation states.[217] In 2015, Chen *et al.* published a review on ternary oxide nanostructures for supercapacitors, in which most of the reported materials contained the critical raw material cobalt (Co), whereas only 3 nanostructures without critical elements where shown: $NiMoO_4$ nanosheets (with a capacitance of 2840 $F \cdot g^{-1}$), $CuFe_2O_4$ nanospheres (334 $F \cdot g^{-1}$) and $MnFe_2O_4$ with graphene nanosheets (120 $F \cdot g^{-1}$).[39,75,217] Recently, holey C@$ZnFe_2O_4$ nanoflakes growth on carbon soot were also applied for supercapacitors resulting in a capacitance of 1452 $F \cdot g^{-1}$.[218] $NiMoO_4$ nanowires supported on carbon cloth were also tested as supercapacitor resulting in a capacitance of 1587 $F \cdot g^{-1}$.[74] Additionally, Zn_2SnO_4/MnO_2 core shell in carbon fibers showed a capacitance of 621.6 $F \cdot g^{-1}$.[219]

1.7. Conclusions

Near-future concepts such as the internet-of-things (IoT) require an increasing number of objects to have embedded electronics, sensors and connectivity, driving a demand for compact, smart, multifunctional and self-sustainable technology with low associated costs. While nanomaterials are thought to be able to meet these requirements, playing an important role in the future technological world, low-cost and sustainable technologies are a demand. For this, both low cost methods of fabrication and sustainable materials must be considered. In this regard, multicomponent oxide nanostructures appear as prime candidates, due to their wide array of excellent properties and compatibility with low-cost fabrication methods even when considering only available and sustainable materials. An overview on these materials was here presented, along with their synthesis methods, and their wide applicability was made clear by showcasing some of the several examples of their application in relevant areas such as energy, electronics and sensing.

From the broad range of multicomponent metal oxide semiconductor materials that have been synthesized in different nanostructures (often Zn, Sn and Ti-based), zinc-tin oxide appears as one of the most promising. In the Table 1.1 the optical, electrical and piezoelectric properties of some of the more employed oxide semiconductor nanostructures are presented. These properties show the potential of zinc-tin oxide compared with other binary and ternary oxides, to

achieve the desired multifunctionality to meet the concepts of IoT and smart surfaces while avoiding the use of critical raw materials.

Table 1.1. Optical, electrical and piezoelectric properties of some of the more employed oxide semiconductor nanostructures. The properties marked with * are referent to the bulk materials and with ** to theoretical calculations. Abbreviations: n/a – not applicable; n/f – not found.

Properties / Material	Band gap (eV)	Resistivity or Conductivity	Piezoelectric constant or Polarization	References
SnO_2	3.60	0.46 $(\Omega \cdot cm)^{-1}$	n/a	220
TiO_2	3.00 - 3.40	1.09 Ω·cm	n/a	178,221
ZnO	3.37	1.4 - 2 × 10^{-4} Ω·cm *	14.3–26.7 pm/V	222–224
IGZO	3.67	>10^6 – 10^{-3} Ω·cm *	n/a	120,225,226
$BaTiO_3$	3.47	1.6×10^{-13} – 4.3×10^{-12} S·m^{-1}	31.1 pm/V	227–230
$CaMnO_3$	5.30	n/f	4 μC/cm^2 **	70,231
$NiMoO_4$	2.20	10^7 Ω·cm *	n/a	232,233
$ZnSnO_3$	3.90	~73 Ω·cm	59 nC/cm^2	234,235
Zn_2SnO_4	3.30 - 3.60	1.6 Ω·cm	n/a	183,234

1.8. References

1. Xia, Y. N. *et al.* One-dimensional nanostructures: Synthesis, characterization, and applications. *Adv. Mater.* **15**, 353–389 (2003).
2. Mancini, L. *et al.* Potential of life cycle assessment for supporting the management of critical raw materials. *Int. J. Life Cycle Assess.* **20**, 100–116 (2015).
3. Bahubalindruni, P. G. *et al.* High-Gain transimpedance amplifier for flexible radiation dosimetry using ingazno tfts. *IEEE J. Electron Devices Soc.* **6**, 760–765 (2018).
4. He, Y., Wang, X., Gao, Y., Hou, Y. & Wan, Q. Oxide-based thin film transistors for flexible electronics. *J. Semicond.* **39**, (2018).
5. Martins, J. *et al.* Bias Stress and Temperature Impact on InGaZnO TFTs and Circuits. *Materials (Basel).* **10**, 680 (2017).
6. Fortunato, E., Barquinha, P. & Martins, R. Oxide semiconductor thin-film transistors: a review of recent advances. *Adv. Mater.* **24**, 2945–86 (2012).
7. Bahubalindruni, P. G. *et al.* Influence of Channel Length Scaling on InGaZnO TFTs Characteristics: Unity Current-Gain Cutoff Frequency, Intrinsic Voltage-Gain, and On-

Resistance. *J. Disp. Technol.* **12**, 515–518 (2016).

8. Minami, T. Transparent conducting oxide semiconductors for transparent electrodes. *Semicond. Sci. Technol.* **20**, (2005).

9. Facchetti, A., Marks, T. J. & Wiley InterScience (Online service). *Transparent electronics : from synthesis to applications*. (Wiley, 2010).

10. Nomura, K. *et al.* Room-temperature fabrication of transparent flexible thin-film transistors using amorphous oxide semiconductors. *Nature* **432**, 488–492 (2004).

11. Nomura, K. *et al.* Carrier transport in transparent oxide semiconductor with intrinsic structural randomness probed using single-crystalline InGaO3(ZnO)5 films. *Appl. Phys. Lett.* **85**, 1993–1995 (2004).

12. Baraton, M.-I. The Future of TCO Materials: Stakes and Challenges. *MRS Proc.* **1209**, 1209-P03-06 (2009).

13. Farhan, M. S., Zalnezhad, E., Bushroa, A. R. & Sarhan, A. A. D. Electrical and optical properties of indium-tin oxide (ITO) films by ion-assisted deposition (IAD) at room temperature. *Int. J. Precis. Eng. Manuf.* **14**, 1465–1469 (2013).

14. Ali, A. H., Hassan, Z. & Shuhaimi, A. Enhancement of optical transmittance and electrical resistivity of post-annealed ITO thin films RF sputtered on Si. *Appl. Surf. Sci.* **443**, 544–547 (2018).

15. Shankar, K. S. & Raychaudhuri, A. K. Fabrication of nanowires of multicomponent oxides: Review of recent advances. *Mater. Sci. Eng. C* **25**, 738–751 (2005).

16. Mao, Y., Park, T.-J. & Wong, S. S. Synthesis of classes of ternary metal oxide nanostructures. *Chem. Commun.* 5721 (2005).

17. European Commission. *COMMUNICATION FROM THE COMMISSION TO THE EUROPEAN PARLIAMENT, THE COUNCIL, THE EUROPEAN ECONOMIC AND SOCIAL COMMITTEE AND THE COMMITTEE OF THE REGIONS*. (2017).

18. Pang, C. *et al.* Synthesis, characterization and opto-electrical properties of ternary Zn2SnO4 nanowires. *Nanotechnology* **21**, 465706 (2010).

19. Baruah, S. & Dutta, J. Zinc stannate nanostructures: Hydrothermal synthesis. *Sci. Technol. Adv. Mater.* **12**, (2011).

20. Lehnen, T., Zopes, D. & Mathur, S. Phase-selective microwave synthesis and inkjet printing applications of Zn2SnO4 (ZTO) quantum dots. *J. Mater. Chem.* **22**, 17732 (2012).

21. Fan, H. J., Yang, Y. & Zacharias, M. ZnO-based ternary compound nanotubes and nanowires. *J. Mater. Chem.* **19**, 885 (2009).

22. Rajeshwar, K. *et al.* Review—Copper Oxide-Based Ternary and Quaternary Oxides: Where Solid-State Chemistry Meets Photoelectrochemistry. *J. Electrochem. Soc.* **165**, H3192–H3206 (2018).

23. Wu, J. M. *et al.* Flexible and transparent nanogenerators based on a composite of lead-free ZnSnO3 triangular-belts. *Adv. Mater.* **24**, 6094–6099 (2012).

24. Pitkethly, M. J. Nanomaterials – the driving force. *Mater. Today* **7**, 20–29 (2004).

25. Sajanlal, P. R., Sreeprasad, T. S., Samal, A. K. & Pradeep, T. Anisotropic nanomaterials: structure, growth, assembly, and functions. *Nano Rev.* **2**, 5883 (2011).

26. Tan, B., Toman, E., Li, Y. & Wu, Y. Zinc Stannate (Zn2SnO4) Dye-Sensitized Solar Cells. *J. Am. Chem. Soc.* **129**, 4162–4163 (2007).

27. Joseph, L. A., Jeronsia, J. E., Jaculine, M. M. & Das, S. J. Investigations on Structural and Optical Properties of Hydrothermally Synthesized Zn2SnO4 Nanoparticles. *Phys. Res. Int.* **2016**, 1–6 (2016).

28. Wang, Y. F. *et al.* Optimized Zn2SnO4 nanoparticles with enhanced performance for photodetectors and photocatalysts. *RSC Adv.* **6**, 69191–69195 (2016).

29. Dimitrievska, M. *et al.* Eu3+-Doped Wide Band Gap Zn2SnO4 Semiconductor Nanoparticles: Structure and Luminescence. *J. Phys. Chem. C* **120**, 18887–18894 (2016).

30. Šepelák, V. *et al.* Nonequilibrium structure of Zn2SnO4 spinel nanoparticles. *J. Mater. Chem.* **22**, 3117 (2012).

31. Wu, Y. S., Chang, W. K. & Jou, M. Photocatalytic Analysis and Characterization of Zn_2SnO_4 Nanoparticles Synthesized via Hydrothermal Method with Na_2CO_3 Mineralizer. *Adv. Mater. Res.* **97**–**101**, 19–22 (2010).

32. Annamalai, A., Carvalho, D., Wilson, K. C. & Lee, M.-J. Properties of hydrothermally synthesized Zn2SnO4 nanoparticles using Na2CO3 as a novel mineralizer. *Mater. Charact.* **61**, 873–881 (2010).

33. Sun, G., Zhang, S. & Li, Y. Solvothermal Synthesis of Zn2SnO4 Nanocrystals and Their Photocatalytic Properties. *Int. J. Photoenergy* **2014**, 1–7 (2014).

34. Naz, S., Durrani, S. K., Mehmood, M. & Nadeem, M. Hydrothermal synthesis, structural and impedance studies of nanocrystalline zinc chromite spinel oxide material Studies of nanocrystalline zinc chromite spinel oxide material. *J. Saudi Chem. Soc.* **20**, 585–593 (2016).

35. Mousavi, Z., Soofivand, F., Esmaeili-Zare, M., Salavati-Niasari, M. & Bagheri, S. ZnCr2O4 Nanoparticles: Facile Synthesis, Characterization and Photocatalytic Properties. *Sci. Rep.* **6**, 20071 (2016).

36. Morán-Lázaro, J. *et al.* Synthesis of ZnMn2O4 Nanoparticles by a Microwave-Assisted Colloidal Method and their Evaluation as a Gas Sensor of Propane and Carbon Monoxide. *Sensors* **18**, 701 (2018).

37. Rani, B. J. *et al.* Structural, optical and magnetic properties of CuFe2O4 nanoparticles. *J. Mater. Sci. Mater. Electron.* **29**, 1975–1984 (2018).

38. Zhang, E., Wang, L., Zhang, B., Xie, Y. & Wang, G. Shape-controlled hydrothermal synthesis of CuFe2O4 nanocrystals for enhancing photocatalytic and photoelectrochemical performance. *Mater. Chem. Phys.* **235**, 121633 (2019).

39. Zhu, M., Meng, D., Wang, C. & Diao, G. Facile fabrication of hierarchically porous CuFe2O4 nanospheres with enhanced capacitance property. *ACS Appl. Mater. Interfaces* **5**, 6030–6037 (2013).

40. Hayashi, H. & Hakuta, Y. Hydrothermal Synthesis of Metal Oxide Nanoparticles in Supercritical Water. *Materials (Basel).* **3**, 3794–3817 (2010).

41. Shen, H. *et al.* Low temperature hydrothermal synthesis of SrTiO 3 nanoparticles without alkali and their effective photocatalytic activity. *J. Adv. Ceram.* **5**, 298–307 (2016).

42. Singh, R., Yadav, A. K. & Gautam, C. Synthesis and Humidity Sensing Investigations of Nanostructured ZnSnO3. *J. Sens. Technol.* **01**, 116–124 (2011).

43. Modeshia, D. R. & Walton, R. I. Solvothermal synthesis of perovskites and pyrochlores: crystallisation of functional oxides under mild conditions. *Chem. Soc. Rev.* **39**, 4303 (2010).

44. Mageshwari, K., Kim, T. G. & Park, J. Effect of alkaline concentration on the structural and luminescence properties of ZnSnO3 nanoparticles obtained by facile reflux method. *J. Mater. Sci. Mater. Electron.* **27**, 4093–4097 (2016).

45. Rovisco, A. *et al.* Seed-Layer Free Zinc Tin Oxide Tailored Nanostructures for Nanoelectronic Applications: Effect of Chemical Parameters. *ACS Appl. Nano Mater.* **1**, 3986–3997 (2018).

46. Beshkar, F., Amiri, O. & Salehi, Z. Synthesis of ZnSnO3 nanostructures by using novel

gelling agents and their application in degradation of textile dye. *Sep. Purif. Technol.* **184**, 66–71 (2017).

47. Sharma, A., Kumar, Y. & Shirage, P. M. Structural, optical and excellent humidity sensing behaviour of ZnSnO3nanoparticles: effect of annealing. *J. Mater. Sci. Mater. Electron.* **29**, 10769–10783 (2018).

48. Hu, W., Tong, W., Li, L., Zheng, J. & Li, G. Cation non-stoichiometry in multi-component oxide nanoparticles by solution chemistry: a case study on CaWO4 for tailored structural properties. *Phys. Chem. Chem. Phys.* **13**, 11634 (2011).

49. Sadeghi, B. Synthesis and Application of Nanorods. in *Nanorods* (InTech, 2012).

50. Dasgupta, N. P. *et al.* Semiconductor Nanowires - Synthesis, Characterization, and Applications. *Adv. Mater.* **26**, 2137–2184 (2014).

51. Jie, J. *et al.* Growth of Ternary Oxide Nanowires by Gold-Catalyzed Vapor-Phase Evaporation. *J. Phys. Chem. B* **108**, 8249–8253 (2004).

52. Hwang, J. K. *et al.* Direct nanoprinting by liquid-bridge-mediated nanotransfer moulding. *Nat. Nanotechnol.* **5**, 742–748 (2010).

53. Kim, S. W. *et al.* Electrochemical performance and ex situ analysis of ZnMn2O4 nanowires as anode materials for lithium rechargeable batteries. *Nano Res.* **4**, 505–510 (2011).

54. Sun, S. & Liang, S. Morphological zinc stannate: synthesis, fundamental properties and applications. *J. Mater. Chem. A* **5**, 20534–20560 (2017).

55. Cherian, C. T., Zheng, M., Reddy, M. V, Chowdari, B. V. R. & Sow, C. H. Zn2SnO4 Nanowires versus Nanoplates: Electrochemical Performance and Morphological Evolution during Li-Cycling. *ACS Appl. Mater. Interfaces* **5**, 6054–6060 (2013).

56. Li, Z. *et al.* Vertically building Zn2SnO4 nanowire arrays on stainless steel mesh toward fabrication of large-area, flexible dye-sensitized solar cells. *Nanoscale* **4**, 3490–4 (2012).

57. Zhou, T., Liu, X., Zhang, R., Wang, Y. & Zhang, T. Shape control and selective decoration of Zn2SnO4 nanostructures on 1D nanowires: Boosting chemical–sensing performances. *Sensors Actuators B Chem.* **290**, 210–216 (2019).

58. Chen, D. *et al.* Electric transport, reversible wettability and chemical sensing of single-crystalline zigzag Zn2SnO4 nanowires. *J. Mater. Chem.* **21**, 17236 (2011).

59. Yang, Y. *et al.* Twinned Zn2TiO4 spinel nanowires using ZnO nanowires as a template. *Adv. Mater.* **19**, 1839–1844 (2007).

60. Zhao, J. *et al.* Magnetic and electrochemical properties of CuFe2O4 hollow fibers fabricated by simple electrospinning and direct annealing. *CrystEngComm* **14**, 5879 (2012).

61. Xue, X. Y., Chen, Y. J., Wang, Y. G. & Wang, T. H. Synthesis and ethanol sensing properties of ZnSnO3 nanowires. *Appl. Phys. Lett.* **86**, 1–3 (2005).

62. Lo, M.-K., Lee, S.-Y. & Chang, K.-S. Study of ZnSnO3-Nanowire Piezophotocatalyst Using Two-Step Hydrothermal Synthesis. *J. Phys. Chem. C* **119**, 5218–5224 (2015).

63. Chang, Y. T. *et al.* Performance of hydrogen evolution reaction of R3C ferroelectric ZnSnO 3 nanowires. *Nanotechnology* **30**, 455401 (2019).

64. Wang, Y.-T. & Chang, K.-S. Piezopotential-Induced Schottky Behavior of Zn1−xSnO3 Nanowire Arrays and Piezophotocatalytic Applications. *J. Am. Ceram. Soc.* **99**, 2593–2600 (2016).

65. Men, H. *et al.* Fast synthesis of ultra-thin ZnSnO3 nanorods with high ethanol sensing properties. *Chem. Commun.* **46**, 7581 (2010).

66. Rovisco, A. *et al.* Growth Mechanism of Seed-Layer Free ZnSnO3 Nanowires: Effect of

Physical Parameters. *Nanomaterials* **9**, 1002 (2019).

67. Chen, Q. *et al.* Enhanced acetone sensor based on Au functionalized In-doped ZnSnO3 nanofibers synthesized by electrospinning method. *J. Colloid Interface Sci.* **543**, 285–299 (2019).

68. Haq, M. ul *et al.* A two-step synthesis of microsphere-decorated fibers based on NiO/ZnSnO3 composites towards superior ethanol sensitivity performance. *J. Alloys Compd.* **777**, 73–83 (2019).

69. Rørvik, P. M., Grande, T. & Einarsrud, M. A. One-dimensional nanostructures of ferroelectric perovskites. *Adv. Mater.* **23**, 4007–4034 (2011).

70. Barrocas, B., Sério, S. & Melo Jorge, M. E. Hierarchically Grown CaMn3O6 Nanorods by RF Magnetron Sputtering for Enhanced Visible-Light-Driven Photocatalysis. *J. Phys. Chem. C* **118**, 24127–24135 (2014).

71. Rørvik, P. M. *et al.* Influence of volatile chlorides on the molten salt synthesis of ternary oxide nanorods and nanoparticles. *Inorg. Chem.* **47**, 3173–3181 (2008).

72. Fu, Q., He, T., Li, J. L. & Yang, G. W. Band-engineered SrTiO3 nanowires for visible light photocatalysis. *J. Appl. Phys.* **112**, 104322 (2012).

73. Zhang, Q., Li, X., Ren, Z., Han, G. & Mao, C. Synthesis of CaTiO3 Nanofibers with Controllable Drug-Release Kinetics. *Eur. J. Inorg. Chem.* **2015**, 4532–4538 (2015).

74. Guo, D., Luo, Y., Yu, X., Li, Q. & Wang, T. High performance NiMoO4 nanowires supported on carbon cloth as advanced electrodes for symmetric supercapacitors. *Nano Energy* **8**, 174–182 (2014).

75. Cai, D. *et al.* Enhanced performance of supercapacitors with ultrathin mesoporous NiMoO4 nanosheets. *Electrochim. Acta* **125**, 294–301 (2014).

76. Sun, Z. *et al.* Generalized self-assembly of scalable two-dimensional transition metal oxide nanosheets. *Nat. Commun.* **5**, 1–9 (2014).

77. Tiwari, J. N., Tiwari, R. N. & Kim, K. S. Zero-dimensional, one-dimensional, two-dimensional and three-dimensional nanostructured materials for advanced electrochemical energy devices. *Prog. Mater. Sci.* **57**, 724–803 (2012).

78. Fernandes, C. *et al.* A Sustainable Approach to Flexible Electronics with Zinc-Tin Oxide Thin-Film Transistors. *Adv. Electron. Mater.* **4**, 1800032 (2018).

79. Branquinho, R. *et al.* Towards environmental friendly solution-based ZTO/AlOx TFTs. *Semicond. Sci. Technol.* **30**, 24007 (2015).

80. Salgueiro, D. *et al.* Solution based zinc tin oxide TFTs: the dual role of the organic solvent. *J. Phys. D. Appl. Phys.* **50**, 065106 (2017).

81. Chen, Y. *et al.* An evolution from 3D face-centered-cubic ZnSnO3 nanocubes to 2D orthorhombic ZnSnO3 nanosheets with excellent gas sensing performance. *Nanotechnology* **23**, 415501 (2012).

82. Guo, R., Guo, Y., Duan, H., Li, H. & Liu, H. Synthesis of Orthorhombic Perovskite-Type ZnSnO3 Single-Crystal Nanoplates and Their Application in Energy Harvesting. *ACS Appl. Mater. Interfaces* **9**, 8271–8279 (2017).

83. Joseph, J., Saseendran, S. B., Achary, S. R., Sukumaran, A. A. & Jayaraj, M. K. Zinc stannate flakes for optoelectronic and antibacterial applications. *Dae Solid State Phys. Symp. 2018* **2115**, 030026 (2019).

84. Xu, G. *et al.* Self-assembly and formation mechanism of single-crystal SrTiO3 nanosheets via solvothermal route with ethylene glycol as reaction medium. *CrystEngComm* **15**, 7206 (2013).

85. Guo, R. *et al.* Controlled synthesis, formation mechanism, and carbon oxidation properties

of Ho2Cu2O5 nanoplates prepared with a coordination-complex method. *Appl. Surf. Sci.* **396**, 1076–1084 (2017).

86. Osada, M. & Sasaki, T. Exfoliated oxide nanosheets: new solution to nanoelectronics. *J. Mater. Chem.* **19**, 2503 (2009).

87. Wang, Z., Zhou, L. & Lou, X. W. Metal oxide hollow nanostructures for lithium-ion batteries. *Adv. Mater.* **24**, 1903–1911 (2012).

88. Hao, Y., Zhang, J., Bi, M., Feng, Z. & Bi, K. Hollow-sphere SrTiO3 nanocube assemblies with enhanced room-temperature photoluminescence. *Mater. Des.* **155**, 257–263 (2018).

89. Wang, Y. *et al.* One Pot, Two Phases: Individual Orthorhombic and Face-Centered Cubic ZnSnO3 Obtained Synchronously in One Solution. *Inorg. Chem.* **53**, 12289–12296 (2014).

90. Ji, X. *et al.* Hydrothermal synthesis of novel Zn2SnO4 octahedron microstructures assembled with hexagon nanoplates. *J. Alloys Compd.* **503**, L21–L25 (2010).

91. Xia, J. *et al.* 3D composites of ZnSnO3 nanoplates/reduced graphene oxide aerogels as an advanced lithium-ion battery anode. *J. Mater. Sci. Mater. Electron.* **0**, 0 (2018).

92. Sato, T. *et al.* Hydrothermal synthesis of CuAlO2 with the delafossite structure in supercritical water. *J. Supercrit. Fluids* **46**, 173–177 (2008).

93. Cai, P. *et al.* Conversion of ternary Zn2SnO4 octahedrons into binary mesoporous SnO2 and hollow SnS2 hierarchical octahedrons by template-mediated selective complex extraction. *J. Mater. Chem. A* **1**, 5217 (2013).

94. Mary Jaculine, M., Justin Raj, C. & Jerome Das, S. Hydrothermal synthesis of highly crystalline Zn2SnO4 nanoflowers and their optical properties. *J. Alloys Compd.* **577**, 131–137 (2013).

95. Javed, Q. *et al.* Preparation, Characterizations and Optical Property of Single Crystalline ZnMn2O4 Nanoflowers via Template-Free Hydrothermal Synthesis. *J. Nanosci. Nanotechnol.* **13**, 2937–2942 (2013).

96. Law, M., Goldberger, J. & Yang, P. Semiconductor Nanowires and Nanotubes. *Annu. Rev. Mater. Res.* **34**, 83–122 (2004).

97. Sun, Z., Liao, T. & Kou, L. Strategies for designing metal oxide nanostructures. *Sci. China Mater.* **60**, 1–24 (2017).

98. Chen, D., Liu, Z., Liang, B., Wang, X. & Shen, G. Transparent metal oxide nanowire transistors. *Nanoscale* **4**, 3001 (2012).

99. Lim, T., Kim, H., Meyyappan, M. & Ju, S. Photostable Zn2SnO4 Nanowire Transistors for Transparent Displays. *ACS Nano* **6**, 4912–4920 (2012).

100. Zhou, Z., Lan, C., Wei, R. & Ho, J. C. Transparent metal-oxide nanowires and their applications in harsh electronics. *J. Mater. Chem. C* **7**, 202–217 (2019).

101. Einarsrud, M.-A. & Grande, T. 1D oxide nanostructures from chemical solutions. *Chem. Soc. Rev.* **43**, 2187–2199 (2014).

102. Araújo, A. *et al.* Direct growth of plasmonic nanorod forests on paper substrates for low-cost flexible 3D SERS platforms. *Flex. Print. Electron.* **2**, 014001 (2017).

103. Para, T. A., Reshi, H. A. & Shelke, V. Synthesis of ZnSnO3 nanostructure by sol gel method. *AIP Conf. Proc.* **1731**, 1–4 (2016).

104. Baruah, S. & Dutta, J. Zinc stannate nanostructures: hydrothermal synthesis. *Sci. Technol. Adv. Mater.* **12**, 013004 (2011).

105. Rabenau, A. The Role of Hydrothermal Synthesis in Preparative Chemistry. *Angew. Chemie Int. Ed. English* **24**, 1026–1040 (1985).

106. Nunes, D. *et al.* Tailoring Upconversion and Morphology of Yb/Eu Doped Y2O3

Nanostructures by Acid Composition Mediation. *Nanomaterials* **9**, 234 (2019).

107. Nunes, D. *et al.* Photocatalytic behavior of TiO2 films synthesized by microwave irradiation. *Catal. Today* **278**, 262–270 (2016).

108. Pimentel, A. *et al.* Microwave Synthesized ZnO Nanorod Arrays for UV Sensors: A Seed Layer Annealing Temperature Study. *Materials (Basel).* **9**, 299 (2016).

109. Mourdikoudis, S., Pallares, R. M. & Thanh, N. T. K. Characterization techniques for nanoparticles: Comparison and complementarity upon studying nanoparticle properties. *Nanoscale* **10**, 12871–12934 (2018).

110. Salame, P. H., Pawade, V. B. & Bhanvase, B. A. Characterization Tools and Techniques for Nanomaterials. in *Nanomaterials for Green Energy* 83–111 (Elsevier, 2018).

111. Nasrazadani, S. & Hassani, S. Modern analytical techniques in failure analysis of aerospace, chemical, and oil and gas industries. in *Handbook of Materials Failure Analysis with Case Studies from the Oil and Gas Industry* 39–54 (Elsevier, 2016).

112. Iwashita, N. X-ray Powder Diffraction. in *Materials Science and Engineering of Carbon* 7–25 (Elsevier, 2016).

113. Barquinha, P. Transparent oxide thin-film transistors: production, characterization and integration (Doctoral Thesis). (Faculdade de Ciências e Tecnologia, 2010).

114. Konno, H. X-ray Photoelectron Spectroscopy. in *Materials Science and Engineering of Carbon* 153–171 (Elsevier, 2016).

115. Kranz, C. & Mizaikoff, B. Nanomaterials: Characterization Methods. in *Reference Module in Chemistry, Molecular Sciences and Chemical Engineering* 1–10 (Elsevier, 2018).

116. Kaburagi, Y., Yoshida, A. & Hishiyama, Y. Raman Spectroscopy. in *Materials Science and Engineering of Carbon* **2**, 125–152 (Elsevier, 2016).

117. Gilliland, G. D. Photoluminescence spectroscopy of crystalline semiconductors. *Mater. Sci. Eng. R Reports* **18**, 99–399 (1997).

118. Kalantar-zadeh, F. Chapter 5 : Characterization Techniques for Nanomaterials. *Nanotechnology-Enabled Sensors* 211–281 (2008).

119. Nunes, D. *et al.* Metal oxide nanostructures for sensor applications. *Semicond. Sci. Technol.* **34**, 043001 (2019).

120. Santos, L. *et al.* Solvothermal Synthesis of Gallium–Indium-Zinc-Oxide Nanoparticles for Electrolyte-Gated Transistors. *ACS Appl. Mater. Interfaces* **7**, 638–646 (2015).

121. Xie, S., Ouyang, Z., Jia, B. & Gu, M. Large-size, high-uniformity, random silver nanowire networks as transparent electrodes for crystalline silicon wafer solar cells. *Opt. Express* **21**, A355 (2013).

122. Grey, P. *et al.* Handwritten Oxide Electronics on Paper. *Adv. Mater. Technol.* **2**, 1–7 (2017).

123. Maijenburg, a. W. *et al.* Dielectrophoretic alignment of metal and metal oxide nanowires and nanotubes: A universal set of parameters for bridging prepatterned microelectrodes. *J. Colloid Interface Sci.* **355**, 486–493 (2011).

124. Khan, Z. H., Kumar, A., Husain, S. & Husain, M. *Advances in Nanomaterials*. **79**, (Springer India, 2016).

125. Liu, Z., Xu, J., Chen, D. & Shen, G. Flexible electronics based on inorganic nanowires. *Chem. Soc. Rev.* **44**, 161–92 (2015).

126. Huang, H. *et al.* Metal oxide nanowire transistors. *J. Mater. Chem.* **22**, 13428 (2012).

127. Kiazadeh, A. *et al.* Improving positive and negative bias illumination stress stability in parylene passivated IGZO transistors. *Appl. Phys. Lett.* **109**, 051606 (2016).

128. Rosa, J. *et al.* Memristors Using Solution-Based IGZO Nanoparticles. *ACS Omega* **2**, 8366–8372 (2017).

129. Dasgupta, S., Kruk, R., Mechau, N. & Hahn, H. Inkjet Printed, High Mobility Inorganic-Oxide Field Effect Transistors Processed at Room Temperature. *ACS Nano* **5**, 9628–9638 (2011).

130. Yu, X., Marks, T. J. & Facchetti, A. Metal oxides for optoelectronic applications. *Nat. Mater.* **15**, 383–396 (2016).

131. Mullings, M. N. *et al.* Thin film characterization of zinc tin oxide deposited by thermal atomic layer deposition. *Thin Solid Films* **556**, (2014).

132. Dutta, S. & Dodabalapur, A. Zinc tin oxide thin film transistor sensor. *Sensors Actuators B Chem.* **143**, 50–55 (2009).

133. Kim, C. H., Rim, Y. S. & Kim, H. J. Chemical stability and electrical performance of dual-active-layered zinc-tin-oxide/indium-gallium-zinc-oxide thin-film transistors using a solution process. *ACS Appl. Mater. Interfaces* **5**, 6108–12 (2013).

134. Hong, S., Park, J. W., Kim, H. J., Kim, Y. & Kim, H. J. A review of multi-stacked active-layer structures for solution-processed oxide semiconductor thin-film transistors. *J. Inf. Disp.* **17**, 93–101 (2016).

135. Kim, S., Kim, H., Janes, D. B. & Ju, S. Interface studies of N2 plasma-treated ZnSnO nanowire transistors using low-frequency noise measurements. *Nanotechnology* **24**, 305201 (2013).

136. Huang, H. *et al.* Metal oxide nanowire transistors. *J. Mater. Chem.* **22**, 13428 (2012).

137. Unalan, H. E. *et al.* Zinc oxide nanowire networks for macroelectronic devices. *Appl. Phys. Lett.* **94**, 163501 (2009).

138. Xiang, J., Kim, J. H. & Lu, W. Chapter 2. High Performance, Low Power Nanowire Transistor Devices. in *RSC Smart Materials* 54–110 (2015).

139. Nagashima, K. *et al.* Intrinsic mechanisms of memristive switching. *Nano Lett.* **11**, 2114–2118 (2011).

140. Tripathi, S. K., Kaur, R. & Rani, M. Oxide Nanomaterials and their Applications as a Memristor. *Solid State Phenom.* **222**, 67–97 (2014).

141. Murali, S. *et al.* Resistive switching in zinc-tin-oxide. *Solid. State. Electron.* **79**, 248–252 (2013).

142. Ali, S., Bae, J. & Lee, C. H. Printed non-volatile resistive switches based on zinc stannate (ZnSnO3). *Curr. Appl. Phys.* **16**, 757–762 (2016).

143. Hsu, C. C., Chen, Y. T., Chuang, P. Y. & Lin, Y. S. Abnormal Volatile Memory Characteristic in Normal Nonvolatile ZnSnO Resistive Switching Memory. *IEEE Trans. Electron Devices* **65**, 2812–2819 (2018).

144. Cheng, B., Ouyang, Z., Chen, C., Xiao, Y. & Lei, S. Individual Zn2SnO4-sheathed ZnO heterostructure nanowires for efficient resistive switching memory controlled by interface states. *Sci. Rep.* **3**, 3249 (2013).

145. Dong, H. *et al.* High performance bipolar resistive switching memory devices based on Zn2SnO4 nanowires. *Nanoscale* **4**, 2571 (2012).

146. Siddiqui, G. U., Rehman, M. M. & Choi, K. H. Enhanced resistive switching in all-printed, hybrid and flexible memory device based on perovskite ZnSnO3 via PVOH polymer. *Polymer (Guildf).* **100**, 102–110 (2016).

147. Yang, Y. J., Rehman, M. M., Siddiqui, G. U., Na, K. H. & Choi, K. H. Effect of adding a polymer and varying device size on the resistive switching characteristics of perovskite nanocubes heterojunction. *Curr. Appl. Phys.* **17**, 1733–1741 (2017).

148. Siddiqui, G. U., Rehman, M. M. & Choi, K. H. Resistive switching phenomena induced by the heterostructure composite of ZnSnO3 nanocubes interspersed ZnO nanowires. *J. Mater. Chem. C* **5**, 5528–5537 (2017).

149. Lu, W., Xie, P. & Lieber, C. M. Nanowire Transistor Performance Limits and Applications. *IEEE Trans. Electron Devices* **55**, 2859–2876 (2008).

150. Yan, H. *et al.* Programmable nanowire circuits for nanoprocessors. *Nature* **470**, 240–244 (2011).

151. Ju, S. *et al.* Transparent active matrix organic light-emitting diode displays driven by nanowire transistor circuitry. *Nano Lett.* **8**, 997–1004 (2008).

152. Ju, S. *et al.* Fabrication of fully transparent nanowire transistors for transparent and flexible electronics. *Nat. Nanotechnol.* **2**, 378–84 (2007).

153. Wan, Sun, J. & Liu, H. Semiconducting Oxide Nanowires: Growth, Doping and Device applications. in *Nanowires - Implementations and Applications* 59–98 (InTech, 2011).

154. Galstyan, V. *et al.* Multicomponent Metal Oxide Nanostructures: Fabrication and Study of Core Issues to Improve Gas Sensing Performance. *Proceedings* **2**, 970 (2018).

155. Huang, J. & Wan, Q. Gas sensors based on semiconducting metal oxide one-dimensional nanostructures. *Sensors* **9**, 9903–9924 (2009).

156. Shingange, K. *et al.* 0D to 3D ZnO nanostructures and their luminescence, magnetic and sensing properties: Influence of pH and annealing. *Mater. Res. Bull.* **85**, 52–63 (2017).

157. Gentry, S. J. & Jones, T. A. The role of catalysis in solid-state gas sensors. *Sensors and Actuators* **10**, 141–163 (1986).

158. Zhong, T., Zhao, W., Jiang, F. & Liang, X. Toluene sensor combining NASICON with ZnTiO3 electrode. *Sensors Actuators, B Chem.* **202**, 1103–1108 (2014).

159. Chen, R., Zhou, W., Zhang, M., Wong, M. & Kwok, H. S. Self-aligned top-gate InGaZnO thin film transistors using SiO2/Al2O3 stack gate dielectric. *Thin Solid Films* **548**, 572–575 (2013).

160. Khan, M. N., Jaisai, M. & Dutta, J. Photocatalytic Inactivation of Escherichia Coli Using Zinc Stannate Nanostructures under Visible Light. *Adv. Mater. Res.* **1131**, 203–209 (2015).

161. Xue, X. Y., Guo, T. L., Lin, Z. X. & Wang, T. H. Individual core-shell structured ZnSnO3 nanowires as photoconductors. *Mater. Lett.* **62**, 1356–1358 (2008).

162. Lin, D., Wu, H. & Pan, W. Photoswitches and memories assembled by electrospinning aluminum-doped zinc oxide single nanowires. *Adv. Mater.* **19**, 3968–3972 (2007).

163. Lou, Z. & Shen, G. Z. Flexible photodetectors based on 1D inorganic nanostructures. *Adv. Sci.* **3**, 1–19 (2015).

164. Tian, W., Lu, H. & Li, L. Nanoscale ultraviolet photodetectors based on onedimensional metal oxide nanostructures. *Nano Res.* **8**, 382–405 (2015).

165. Zhai, T. *et al.* A comprehensive review of one-dimensional metal-oxide nanostructure photodetectors. *Sensors* **9**, 6504–6529 (2009).

166. Dong, Y. *et al.* Zinc Stannate Nanocrystal-Based Ultrarapid-Response UV Photodetectors. *Adv. Mater. Technol.* **3**, 1800085 (2018).

167. Zhang, Y. *et al.* High performance ultraviolet photodetectors based on an individual Zn2SnO4 single crystalline nanowire. *J. Mater. Chem.* **20**, 9858 (2010).

168. Li, L., Gu, L., Lou, Z., Fan, Z. & Shen, G. ZnO Quantum Dot Decorated Zn2SnO4 Nanowire Heterojunction Photodetectors with Drastic Performance Enhancement and Flexible Ultraviolet Image Sensors. *ACS Nano* **11**, 4067–4076 (2017).

169. Zhao, Y. *et al.* Band Gap Tunable Zn2SnO4 Nanocubes through Thermal Effect and Their Outstanding Ultraviolet Light Photoresponse. *Sci. Rep.* **4**, 6847 (2015).

170. Malvano, F. *et al.* Fabrication of SrTiO3 Layer on Pt Electrode for Label-Free Capacitive Biosensors. *Biosensors* **8**, 26 (2018).

171. Supraja, P., Sudarshan, V., Tripathy, S., Agrawal, A. & Singh, S. G. Label free electrochemical detection of cardiac biomarker troponin T using ZnSnO3 perovskite nanomaterials. *Anal. Methods* **11**, 744–751 (2019).

172. Bagheri, H., Khoshsafar, H., Afkhami, A. & Amidi, S. Sensitive and simple simultaneous determination of morphine and codeine using a Zn2SnO4 nanoparticle/graphene composite modified electrochemical sensor. *New J. Chem.* **40**, 7102–7112 (2016).

173. Kampouri, S. & Stylianou, K. C. Dual-Functional Photocatalysis for Simultaneous Hydrogen Production and Oxidation of Organic Substances. *ACS Catal.* **9**, 4247–4270 (2019).

174. Barrocas, B. *et al.* Characterization and electrochemical behaviour of nanostructured calcium samarium manganite electrodes fabricated by RF-Magnetron Sputtering. *Electrochim. Acta* **137**, 99–107 (2014).

175. Barrocas, B., Sério, S., Rovisco, A. & Melo Jorge, M. E. Visible-Light Photocatalysis in Ca0.6Ho0.4MnO3 Films Deposited by RF-Magnetron Sputtering Using Nanosized Powder Compacted Target. *J. Phys. Chem. C* **118**, 590–597 (2014).

176. Chandrasekaran, S. *et al.* Spinel photocatalysts for environmental remediation, hydrogen generation, CO2 reduction and photoelectrochemical water splitting. *J. Mater. Chem. A* **6**, 11078–11104 (2018).

177. Najam Khan, M., Al-Hinai, M., Al-Hinai, A. & Dutta, J. Visible light photocatalysis of mixed phase zinc stannate/zinc oxide nanostructures precipitated at room temperature in aqueous media. *Ceram. Int.* **40**, 8743–8752 (2014).

178. Nunes, D. *et al.* Photocatalytic TiO2 Nanorod Spheres and Arrays Compatible with Flexible Applications. *Catalysts* **7**, 60 (2017).

179. Barrocas, B., Monteiro, O. C., Jorge, M. E. M. & Sério, S. Photocatalytic activity and reusability study of nanocrystalline TiO2 films prepared by sputtering technique. *Appl. Surf. Sci.* **264**, 111–116 (2013).

180. Pimentel, A. *et al.* Synthesis of Long ZnO Nanorods under Microwave Irradiation or Conventional Heating. *J. Phys. Chem. C* **118**, 14629–14639 (2014).

181. Najam Khan, M. & Dutta, J. Comparison of photocatalytic activity of zinc stannate particles and zinc stannate/zinc oxide composites for the removal of phenol from water, and a study on the effect of pH on photocatalytic efficiency. *Mater. Sci. Semicond. Process.* **36**, 124–133 (2015).

182. Barrocas, B., Sério, S., Rovisco, A., Nunes, Y. & Jorge, M. E. E. M. Removal of rhodamine 6G dye contaminant by visible light driven immobilized Ca1-xLnxMnO3 (Ln=Sm, Ho; 0.1≤x≤0.4) photocatalysts. *Appl. Surf. Sci.* **360**, 798–806 (2015).

183. Lei, M. *et al.* A novel self-catalytic route to zinc stannate nanowires and cathodoluminescence and electrical transport properties of a single nanowire. *J. Alloys Compd.* **657**, 394–399 (2016).

184. Chen, F., Huang, H., Guo, L., Zhang, Y. & Ma, T. The Role of Polarization in Photocatalysis. *Angew. Chemie Int. Ed.* **58**, 10061–10073 (2019).

185. Liang, Z., Yan, C. F., Rtimi, S. & Bandara, J. Piezoelectric materials for catalytic/photocatalytic removal of pollutants: Recent advances and outlook. *Appl. Catal. B Environ.* **241**, 256–269 (2019).

186. Zhao, L., Li, X. & Zhao, J. Fabrication, characterization and photocatalytic activity of cubic-like ZnMn2O4. *Appl. Surf. Sci.* **268**, 274–277 (2013).

187. Taghavi Fardood, S., Moradnia, F. & Ramazani, A. Green synthesis and characterisation of ZnMn2O4 nanoparticles for photocatalytic degradation of Congo red dye and kinetic study. *Micro Nano Lett.* **14**, 986–991 (2019).

188. Juibari, N. M. & Eslami, A. Investigation of catalytic activity of ZnAl2O4 and ZnMn2O4 nanoparticles in the thermal decomposition of ammonium perchlorate. *J. Therm. Anal. Calorim.* **128**, 115–124 (2017).

189. Foletto, E. L. *et al.* Application of Zn2SnO4 photocatalyst prepared by microwave-assisted hydrothermal route in the degradation of organic pollutant under sunlight. *Ceram. Int.* **39**, 4569–4574 (2013).

190. Fu, X. *et al.* Hydrothermal synthesis, characterization, and photocatalytic properties of Zn2SnO4. *J. Solid State Chem.* **182**, 517–524 (2009).

191. Borhade, A. V. & Baste, Y. R. Study of photocatalytic asset of the ZnSnO3 synthesized by green chemistry. *Arab. J. Chem.* **10**, S404–S411 (2017).

192. Fang, C., Geng, B., Liu, J. & Zhan, F. d-fructose molecule template route to ultra-thin ZnSnO3 nanowire architectures and their application as efficient photocatalyst. *Chem. Commun.* 2350 (2009).

193. Biswas, A., Saha, S. & Jana, N. R. ZnSnO3 Nanoparticle-Based Piezocatalysts for Ultrasound-Assisted Degradation of Organic Pollutants. *ACS Appl. Nano Mater.* **2**, 1120–1128 (2019).

194. Lin, H. M. & Chang, K. S. Synergistic piezophotocatalytic and photoelectrochemical performance of poly(vinylidene fluoride)-ZnSnO3 and poly(methyl methacrylate)-ZnSnO3 nanocomposites. *RSC Adv.* **7**, 30513–30520 (2017).

195. Wu, J. *et al.* Insights into the Role of Ferroelectric Polarization in Piezocatalysis of Nanocrystalline BaTiO3. *ACS Appl. Mater. Interfaces* **10**, 17842–17849 (2018).

196. Wu, J., Qin, N. & Bao, D. Effective enhancement of piezocatalytic activity of BaTiO3 nanowires under ultrasonic vibration. *Nano Energy* **45**, 44–51 (2018).

197. Zieliñska, B., Borowiak-Palen, E. & Kalenczuk, R. J. Photocatalytic hydrogen generation over alkaline-earth titanates in the presence of electron donors. *Int. J. Hydrogen Energy* **33**, 1797–1802 (2008).

198. Dong, W., Zhao, G., Bao, Q. & Gu, X. Effects of morphologies on the photocatalytic properties of CaTiO3 nano/microstructures. *J. Ceram. Soc. Japan* **124**, 475–479 (2016).

199. Askari, H., Khajepour, A., Khamesee, M. B., Saadatnia, Z. & Wang, Z. L. Piezoelectric and triboelectric nanogenerators: Trends and impacts. *Nano Today* **22**, 10–13 (2018).

200. Chen, J. & Wang, Z. L. Reviving Vibration Energy Harvesting and Self-Powered Sensing by a Triboelectric Nanogenerator. *Joule* **1**, 480–521 (2017).

201. Rahimi, A., Zorlu, Ö., Muhtaroğlu, A. & Külah, H. A Compact Electromagnetic Vibration Harvesting System with High Performance Interface Electronics. *Procedia Eng.* **25**, 215–218 (2011).

202. Wu, J. M., Xu, C., Zhang, Y. & Wang, Z. L. Lead-free nanogenerator made from single ZnSnO3 microbelt. *ACS Nano* **6**, 4335–40 (2012).

203. Fu, Y. *et al.* Detecting Liquefied Petroleum Gas (LPG) at Room Temperature Using ZnSnO3/ZnO Nanowire Piezo-Nanogenerator as Self-Powered Gas Sensor. *ACS Appl. Mater. Interfaces* **7**, 10482–10490 (2015).

204. Koka, A., Zhou, Z., Tang, H. & Sodano, H. A. Controlled synthesis of ultra-long vertically aligned BaTiO3 nanowire arrays for sensing and energy harvesting applications. *Nanotechnology* **25**, 375603 (2014).

205. Malakooti, M. H., Julé, F. & Sodano, H. A. Printed Nanocomposite Energy Harvesters with Controlled Alignment of Barium Titanate Nanowires. *ACS Appl. Mater. Interfaces* **10**,

38359–38367 (2018).

206. Wu, J. M., Chen, K.-H., Zhang, Y. & Wang, Z. L. A self-powered piezotronic strain sensor based on single ZnSnO3 microbelts. *RSC Adv.* **3**, 25184 (2013).

207. Wu, J. M. *et al.* Ultrahigh Sensitive Piezotronic Strain Sensors Based on a ZnSnO3 Nanowire/Microwire. *ACS Nano* **6**, 4369–4374 (2012).

208. Choi, K. H., Siddiqui, G. U., Yang, B. & Mustafa, M. Synthesis of ZnSnO3 nanocubes and thin film fabrication of (ZnSnO3/PMMA) composite through electrospray deposition. *J. Mater. Sci. Mater. Electron.* **26**, 5690–5696 (2015).

209. Lee, K. Y., Gupta, M. K. & Kim, S. W. Transparent flexible stretchable piezoelectric and triboelectric nanogenerators for powering portable electronics. *Nano Energy* **14**, 139–160 (2015).

210. Yang, Y. J. *et al.* Highly Sensitive Flexible Human Motion Sensor Based on ZnSnO3/PVDF Composite. *J. Electron. Mater.* **46**, 4172–4179 (2017).

211. Alam, M. M., Ghosh, S. K., Sultana, A. & Mandal, D. Lead-free ZnSnO3/MWCNTs-based self-poled flexible hybrid nanogenerator for piezoelectric power generation. *Nanotechnology* **26**, 165403 (2015).

212. Lee, K. Y. *et al.* Unidirectional high-power generation via stress-induced dipole alignment from ZnSnO3 nanocubes/polymer hybrid piezoelectric nanogenerator. *Adv. Funct. Mater.* **24**, 37–43 (2014).

213. Chen, J., Lu, L. & Wang, W. Zn2SnO4 nanowires as photoanode for dye-sensitized solar cells and the improvement on open-circuit voltage. *J. Phys. Chem. C* **116**, 10841–10847 (2012).

214. Habibi, M. H., Mardani, M., Habibi, M. & Zendehdel, M. Enhanced photovoltage (Voc) of nano-structured zinc tin oxide (ZTO) working electrode prepared by a green hydrothermal route for dye-sensitized solar cell (DSSC). *J. Mater. Sci. Mater. Electron.* **28**, 3789–3795 (2017).

215. Rong, A. *et al.* Hydrothermal Synthesis of Zn2SnO4 as Anode Materials for Li-Ion Battery. *J. Phys. Chem. B* **110**, 14754–14760 (2006).

216. Wang, L., Zhang, G., Liu, Q. & Duan, H. Recent progress in Zn-based anodes for advanced lithium ion batteries. *Mater. Chem. Front.* **2**, 1414–1435 (2018).

217. Chen, D., Wang, Q. & Shen, G. Ternary oxide nanostructured materials for supercapacitors : a review. *J. Mater. Chem. A Mater. energy Sustain.* **3**, 10158–10173 (2015).

218. Vadiyar, M. M. *et al.* Holey C@ZnFe2O4 Nanoflakes by Carbon Soot Layer Blasting Approach for High Performance Supercapacitors. *ACS Appl. Energy Mater.* **2**, 6693–6704 (2019).

219. Bao, L., Zang, J. & Li, X. Flexible Zn2SnO4/MnO2 Core/Shell Nanocable−Carbon Microfiber Hybrid Composites for High-Performance Supercapacitor Electrodes. *Nano Lett.* **11**, 1215–1220 (2011).

220. Hernández-Ramírez, F. *et al.* Fabrication and electrical characterization of circuits based on individual tin oxide nanowires. *Nanotechnology* **17**, 5577–5583 (2006).

221. Fàbrega, C. *et al.* On the photoconduction properties of low resistivity TiO2 nanotubes. *Nanotechnology* **21**, (2010).

222. Pimentel, A. *et al.* Ultra-Fast Microwave Synthesis of ZnO Nanorods on Cellulose Substrates for UV Sensor Applications. *Materials (Basel).* **10**, 1308 (2017).

223. Ellmer, K. Resistivity of polycrystalline zinc oxide films: Current status and physical limit. *J. Phys. D. Appl. Phys.* **34**, 3097–3108 (2001).

224. Zhao, M., Wang, Z. & Mao, S. X. Piezoelectric Characterization of Individual Zinc Oxide Nanobelt Probed by Piezoresponse Force Microscope. *Nano Lett.* **4**, 587–590 (2004).

225. Barquinha, P., Pereira, L., Gonçalves, G., Martins, R. & Fortunato, E. Toward High-Performance Amorphous GIZO TFTs. *J. Electrochem. Soc.* **156**, H161 (2009).

226. Zan, H.-W., Tsai, W.-W., Chen, C.-H., Tsai, C.-C. & Meng, H.-F. 4.3: High Performance a-IGZO TFT with Nano-Dots Doping. *SID Symp. Dig. Tech. Pap.* **42**, 28–31 (2011).

227. Tang, H., Zhou, Z. & Sodano, H. A. Large-scale synthesis of BaxSr1−xTiO3 nanowires with controlled stoichiometry. *Appl. Phys. Lett.* **104**, 142905 (2014).

228. Huang, X., Xie, L., Jiang, P., Wang, G. & Liu, F. Electrical, thermophysical and micromechanical properties of ethylene-vinyl acetate elastomer composites with surface modified BaTiO3 nanoparticles. *J. Phys. D. Appl. Phys.* **42**, (2009).

229. Salehi, H., Shahtahmasebi, N. & Hosseini, S. M. Band structure of tetragonal BaTiO3. *Eur. Phys. J. B* **32**, 177–180 (2003).

230. Suzuki, K. & Kijima, K. Optical band gap of barium titanate nanoparticles prepared by RF-plasma chemical vapor deposition. *Japanese J. Appl. Physics, Part 1 Regul. Pap. Short Notes Rev. Pap.* **44**, 2081–2082 (2005).

231. Bhattacharjee, S., Bousquet, E. & Ghosez, P. Engineering multiferroism in CaMnO3. *Phys. Rev. Lett.* **102**, (2009).

232. De Moura, A. P. *et al.* Structural, optical, and magnetic properties of NiMoOnanorods prepared by microwave sintering. *Sci. World J.* **2015**, (2015).

233. Pandey, P. K., Bhave, N. S. & Kharat, R. B. Preparation and characterization of spray deposited NiMoO4 thin films for photovoltaic electrochemical studies. *Mater. Res. Bull.* **41**, 1160–1169 (2006).

234. Miyauchi, M., Liu, Z., Zhao, Z.-G., Anandan, S. & Hara, K. Single crystalline zinc stannate nanoparticles for efficient photo-electrochemical devices. *Chem. Commun.* **46**, 1529–1531 (2010).

235. Xue, X. Y. *et al.* Electronic transport characteristics through individual ZnSnO3 nanowires. *Appl. Phys. Lett.* **88**, 182102 (2006).

Chapter 2 – Synthesis and characterization of zinc-tin oxide nanowires

This chapter aims to present the results regarding the hydrothermal synthesis of seed-layer free ZTO nanostructures developed during this thesis project, with particular emphasis on the optimization of all the parameters leading to the achievement of $ZnSnO_3$ nanowires. The nanostructures syntheses and characterization were performed in the CENIMAT and CEMOP laboratory resources.

The contents presented in this chapter are adapted from the following publications:

- **A. Rovisco**, R. Branquinho, J. Martins, M. João Oliveira, D. Nunes, E. Fortunato, R. Martins and P. Barquinha, Seed-Layer Free Zinc Tin Oxide Tailored Nanostructures for Nanoelectronic Applications: Effect of Chemical Parameters. *ACS Appl. Nano Mater.* **1**, 3986–3997 (2018), DOI: 10.1021/acsanm.8b00743
- **A. Rovisco**, R. Branquinho, J. Martins, E. Fortunato, R. Martins and P. Barquinha, Growth Mechanism of Seed-Layer Free $ZnSnO_3$ Nanowires: Effect of Physical Parameters. *Nanomaterials* **9**, 1002 (2019), DOI: 10.3390/nano9071002

2.1. $ZnSnO_3$ nanowires synthesis: influence of the chemical parameters

2.1.1. Abstract

Semiconductor nanowires are mostly processed by complex, expensive and high temperature methods. In this work, with the intent of developing zinc tin oxide nanowires (ZTO nanowires) by low-cost and low-complexity processes, we show a detailed study on the influence of chemical parameters in the hydrothermal synthesis of ZTO nanostructures at temperatures of only 200 °C. Two different zinc precursors, the ratio between zinc and tin precursors, the concentration of the surfactant agent and of the mineralizer were studied. The type and the crystallinity of the nanostructures was found to be highly dependent on the used precursors and on the concentration of each reagent. Conditions for obtaining different ZTO nanostructures were achieved, namely Zn_2SnO_4 nanoparticles and $ZnSnO_3$ nanowires with length ≈ 600 nm, with the latter being reported for the first time ever by hydrothermal methods without the use of seed layers. The low-temperature hydrothermal methods explored here proved to be a low-cost, reproducible and highly flexible route to obtain multicomponent oxide nanostructures, particularly ZTO nanowires. The diversity of the synthetized ZTO structures have potential application in next-generation nanoscale devices such as field effect nanotransistors, nanogenerators, resistive switching memories, gas sensors and photocatalysis.

2.1.2. Introduction

The increasing demand to have smart and multifunctional surfaces on all sorts of objects and shapes is pushing flexible and transparent electronics to unprecedented performance and integration levels.[1] For this end, it is highly desirable a material system offering sustainability in terms of raw materials and processes to synthetize its low-dimensional structures, combined with a wide range of properties to enable its use on transistors, sensing or even energy-harvesting components. Metal oxides are one of the material classes with highest potential to fulfill all these needs. In fact, ZnO-based nanostructures have been widely explored over the last decade.[2,3] ZnO nanowires are a good example of the multifunctionality of oxides, enabling for instance nanogenerators to act as gas sensors and biosensors.[4,5] Moving from single to multicomponent oxides, e.g., from ZnO to zinc-tin oxide (ZTO), has been one of the current trends, enabling one to obtain different properties by adjusting the cationic ratio, resulting in a wider range of applications for a given material system.[6] Concerning sustainability, ZTO also has a great advantage over other multicomponent oxides as the well-established indium-gallium-zinc oxide (IGZO) in thin-film technologies, since it avoids the use of critical raw materials as In and Ga.[7]

ZTO can crystallize through solid-state reaction in the metastable perovskite (orthorhombic or ordered face centered, fcc)[8] or rhombohedral [9] forms ($ZnSnO_3$) and the more stable inverse

spinel orthostannate (Zn_2SnO_4).[10,11] In **Figure 2.1** the crystalline structure of both phases is presented.

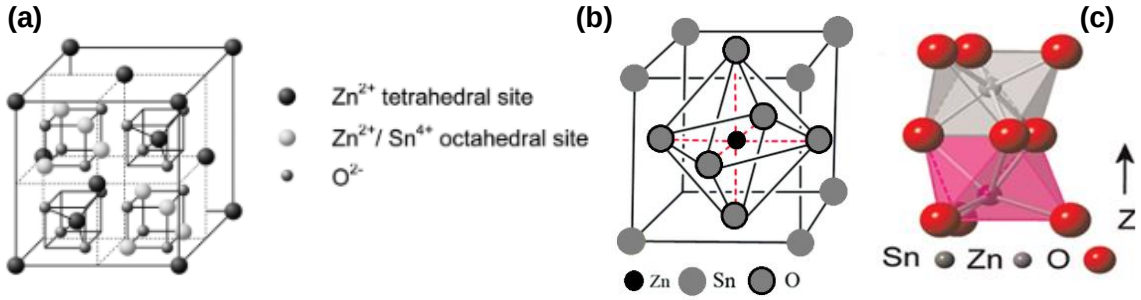

Figure 2.1. Crystal structure of (a) inverse spinel cubic Zn_2SnO_4 (reproduced from Ref [12] with permission of The Royal Society of Chemistry), (b) perovskite $ZnSnO_3$ adapted from Ref [13] with permission of The Royal Society of Chemistry. Perovskite $ZnSnO_3$ can be face-centered or orthorhombic (in which $a \neq b \neq c$). (c) Crystal structure of rhombohedral LN-type $ZnSnO_3$ reprinted with permission from Ref [14]. Copyright (2012) American Chemical Society.

Zn_2SnO_4 is an n-type semiconductor with mobilities higher than 112 $cm^2V^{-1}s^{-1}$ and a wide band gap of 3.6 eV being reported in nanostructures.[15,16] On the other hand, $ZnSnO_3$ has been reported as an excellent piezoelectric material, with a piezoelectric polarization along the c-axis ≈59 μC/cm^2, more than one order of magnitude higher than that of ZnO (≈5 μC/cm^2),[17–19] and also as a ferroelectric material.[20] Its band gap was reported as being 3.9 eV, higher than for Zn_2SnO_4.[21,22] These ZTO nanostructures can be synthetized by vapor phase processes as chemical vapor deposition (CVD)[23] and thermal evaporation,[6] which present high efficiency. However, these are cumbersome and expensive techniques, which demand high temperatures (>700 °C). Thereby, solution-based methods are imperative to decrease complexity, cost and temperature, while still enabling good performance of the synthesized nanostructures. Solution-based hydrothermal methods were already used to obtain ZTO nanostructures such as nanoparticles (NPs),[24] nanowires (NWs),[25] nanorods,[12] octahedrons,[26] nanocubes (NCs)[27,28] and nanoflowers[29]. These nanostructures have demonstrated interesting properties for numerous applications as photocatalysis,[30] sensors,[31–33] nanogenerators,[14,34,35] resistive switching memories[13,36] and solar cells,[37] reinforcing the multifunctionality of ZTO for next-generation nanoscale devices.

A proper control of the synthesis process to achieve the target structure and shape is crucial. As an example, for gas sensing it was already reported that within $ZnSnO_3$ structures an orthorhombic phase (as the one obtained in this study) possess a much higher sensitivity than the fcc. The dimension of the obtained structures also plays an important role, with higher specific surface areas resulting in improved gas sensing performance.[38]

However, two important drawbacks need to be solved: first, it is well known that obtaining a single phase ($ZnSnO_3$ or Zn_2SnO_4) and a single nanostructure shape (e.g. NP or NW), by solution

processes is quite challenging.[39,40] This can limit the usefulness of ZTO for different applications, as the properties are heavily dependent on phase and shape; also, low-cost hydrothermal methods, highly desirable from an upscaling perspective, always require seed-layers to achieve $ZnSnO_3$ nanowires.[39,41] While the use of a seed-layer can enable easier fabrication of vertical structures such as gate-all-around transistors,[42,43] synthesizing ZTO nanowires without a seed layer also brings multiple advantages: imposes less constrains to the synthesis conditions to be studied, which is crucial to investigate in detail the role of each synthesis parameter in controlling phase, shape and size of the nanostructures;[10,44] allows for less processing steps to obtain the nanostructures; provides higher degree of freedom to integration, by relying on a wide variety of available transfer methods to obtain random and aligned networks of nanowires on any substrate;[45] finally, the nanostructures do not incorporate on their final shape any undesired residuals from the seed layers.[46]

In these following sections, we present different multicomponent ZTO nanostructures produced by a seed-layer free, one-step hydrothermal method, at only 200 °C. The chemical and structural influence on the solution-based synthesis of the zinc salt, the ratio between zinc and tin precursors, the concentration of the surfactant agent (H_2O:EDA ratio), and the mineralizer (NaOH) concentration were studied with the aim of obtaining ZTO nanowires. We are particularly interested in 1D structures given their efficient charge transport, crucial for conceiving nanoelectronic devices.[47]

Herein we show a simple hydrothermal method where we can control the phase and shape of the nanostructures, by tuning the chemical parameters of the synthesis. $ZnSnO_3$ nanowires were successfully achieved, without the support of seed-layers and using two different zinc precursors.

2.1.3. Experimental Section

Nanostructures' synthesis

ZTO nanostructures were synthesized via hydrothermal method, using a modified version of the synthesis reported by Li *et al.*[15], without the use of a seed layer (in [15] a stainless steel mesh seed-layer is used). **Figure 2.2**a shows the schematic of the synthesis where the precursor concentrations used were 0.020 M of $SnCl_4 \cdot 5H_2O$ and 0.040 M of $Zn(CH_3COO)_2 \cdot 2H_2O$. The precursors were separately dissolved in 7.5 mL of water Millipore and were then mixed together. Afterwards, 7.5 mL of the surfactant etylenediamine (EDA) were added and the mixture was left stirring for 30 min. Finally, 0.240 M of NaOH were added. The precursors were smashed in a mortar before being added to water to help dissolution. The reagents used were all commercially available: zinc acetate dihydrate 99.0 % ($Zn(CH_3COO)_2 \cdot 2H_2O$), sodium hydroxide ≥98 % (NaOH) and etylenediamine 99 % (EDA) from Sigma-Aldrich, tin (IV) chloride 5-hydrate ($SnCl_4 \cdot 5H_2O$) extra pure from Riedel-de Haën and zinc chloride 98 % ($ZnCl_2$) from Merck.

To study the influence of the zinc precursor, zinc acetate was replaced by zinc chloride, maintaining the same concentration of zinc in the solution. Different Zn:Sn ratios (molar concentration) were studied, namely, 2:1, 1:1 and 1:2. The ratio between H_2O and EDA was variated (H_2O:EDA – 15:0, 9:6, 8:7, 7.5:7.5, 7:8, 6:9, 0:15), as well as the concentration of NaOH (0.100 M, 0.175 M, 0.240 M and 0.350 M). When the solution was ready, it was transferred into a 45 mL Teflon-lined stainless-steel autoclave, filling 33 % of the total autoclave volume. The mixture was kept in an electric oven (Thermo Scientific) at 200 °C for 24 hours, with a heating ramp of 200 °C/h. The autoclave was cooled to ambient temperature naturally. The resultant precipitate, comprising the nanostructures, was centrifuged at 4000 rpm and washed several times with de-ionized water and isopropyl alcohol, alternately. The nanostructures were finally dried at 60 °C, in vacuum, for 2 hours, as schematized in **Figure 2.2**b.

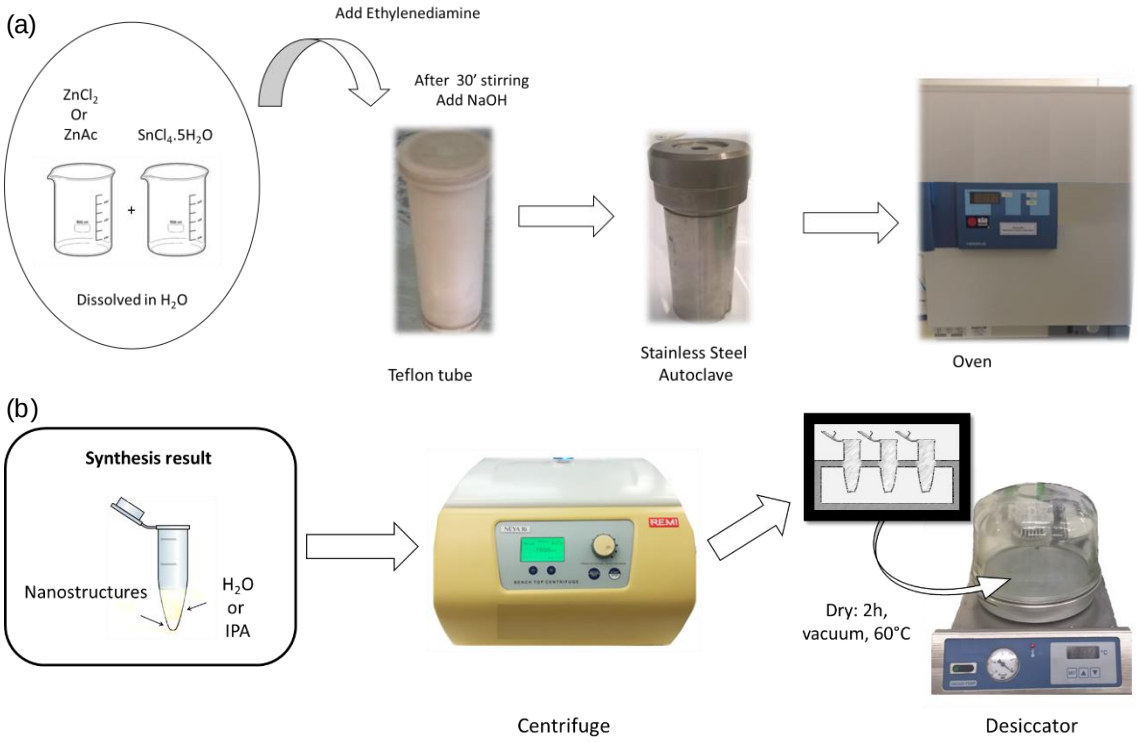

Figure 2.2. Schematic representation of (a) the hydrothermal synthesis process and (b) drying of the nanostructures.

Nanostructures' characterization

Structural characterization by X-Ray diffraction (XRD) was performed using a PANalytical's X'Pert PRO MRD diffractometer with Cu Ka radiation. The XRD data was acquired in the 10 – 90 ° 2θ range with a step size of 0.033 °, using the nanostructures in the form of powder. Fourier-transform infrared (FTIR) spectroscopy data was recorded using an Attenuated Total Reflectance (ATR) sampling accessory (Smart iTR) equipped with a single bounce diamond crystal on a Thermo Nicolet 6700 Spectrometer. The spectra were acquired with a 45° incident angle in the

range of 4000–525 cm^{-1} and with a 4 cm^{-1} resolution. Raman spectroscopy measurements were carried out in a Renishaw inVia Reflex micro-Raman spectrometer equipped with an air-cooled CCD detector and a HeNe laser operating at 50 mW of 532 nm laser excitation. The spectral resolution of the spectroscopic system is 0.3 cm^{-1}. The laser beam was focused with a 50× Leica objective lens (N Plan EPI) with a numerical aperture of 0.75. An integration time of 2 scans (10 s each) was used for all measurements to reduce the random background noise induced by the detector, without significantly increasing the acquisition time. The intensity of the incident laser was 50 μW. All spectra were obtained in triplicate for each sample at room temperature in the 100–1600 nm range. After measurements a baseline subtraction was performed in order to identify the different vibrational bands. The band gap of the ZTO nanostructures was estimated from reflectance spectra recorded in the 200–800 nm range with a PerkinElmer lambda 950 UV/VIS/NIR spectrophotometer using the Tauc plot method. The photoluminescence (PL) measurements were performed at room temperature, using a PerkinElmer LS.55 instrument with a Xenon lamp as excitation source with an excitation wavelength of 325 nm. The morphology and element analysis of the samples was performed using scanning electron microscopy (SEM) and energy dispersive X-ray spectroscopy (EDS) inside a Carl Zeiss AURIGA CrossBeam workstation.

2.1.4. Results and Discussion

Introduction: governing equations to obtain ZTO nanowires

In a typical hydrothermal method to achieve ZTO nanostructures, the synthesis product is seldom composed by a single crystalline phase. In fact, $ZnSnO_3$ nanowires, Zn_2SnO_4 nanoparticles, nanocubes and octahedrons with nanoplates, ZnO nanowires, SnO_2 nanoparticles and mixtures of them are usually obtained (**Figure 2.3**).[10]

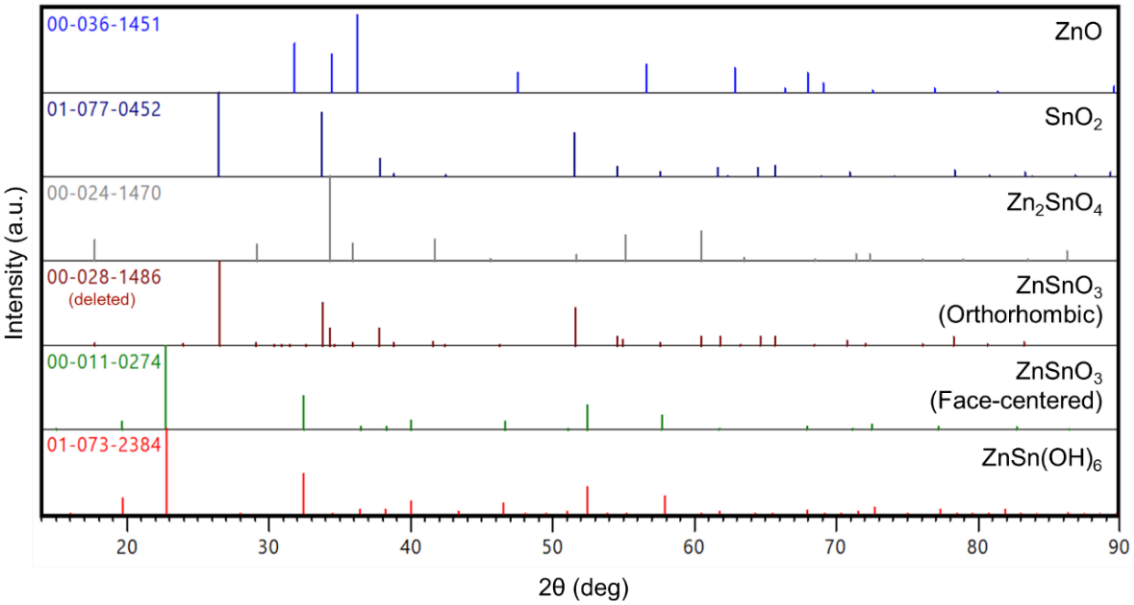

Figure 2.3. Representation of XRD peaks of ICDD cards of all the possible phases identified in the samples. The orth-$ZnSnO_3$ card 00-028-1486 is represented to show the similarity with $ZnSnO_3$ nanowires data. This card was however removed from inorganic crystal structure data.

It is thus imperative to revise the governing equations representing the chemical processes to achieve each of these phases when Zn and Sn precursors are present. The chemical reaction processes for the formation of $ZnSnO_3$ nanostructures can be represented by the equations:[48]

$$Zn^{2+} + Sn^{4+} + 6OH^- \rightarrow ZnSn(OH)_6 \quad (1)$$

$$ZnSn(OH)_6 \rightarrow ZnSnO_3 + 3H_2O \quad (2)$$

Concerning Zn_2SnO_4, its formation can be represented as follows:[15,44]

$$Zn^{2+} + Sn^{4+} + 6OH^- \rightarrow ZnSn(OH)_6 \downarrow \quad (3)$$

$$Zn^{2+} + 4OH^- \rightarrow Zn(OH)_4^{2-} \quad (4)$$

$$ZnSn(OH)_6 + Zn(OH)_4^{2-} \rightarrow Zn_2SnO_4 \downarrow + 4H_2O + 2OH^- \quad (5)$$

While these equations provide an ideal scenario to obtain $ZnSnO_3$ and Zn_2SnO_4 nanostructures, it has to be taken into account that the modification of the concentration of the precursors and the mineralizer during the reaction can promote the formation of other species/structures. Moreover, both ZTO phases have $ZnSn(OH)_6$ as an intermediate phase (**Figure 2.3**), which can also appear as an end product for synthesis with short durations and/or low temperatures. Given this, the detection of OH^- groups by FTIR spectroscopy reveals to be quite useful to infer about the completeness of the reaction (**Figure 2.4**).

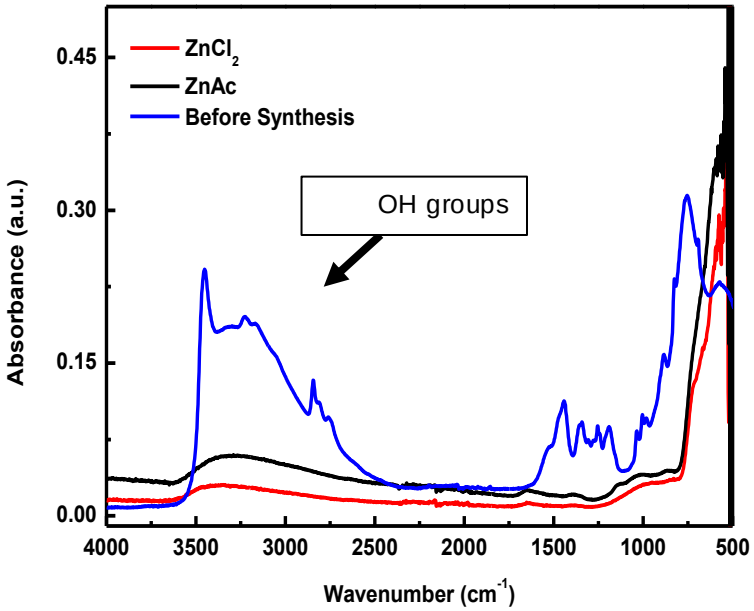

Figure 2.4. FTIR spectra of samples before the synthesis and after 24 h of synthesis for ZnAc and $ZnCl_2$ best conditions.

Regarding the formation of ZnO nanostructures, it is normally associated with a high alkaline concentration [44] and it can be represented by:

$$Zn(OH)_4^{2-} \rightarrow ZnO \downarrow + H_2O + 2OH^- \quad (6)$$

Where tin species are washed away after reaction.

Finally, in respect to the SnO_2 nanostructures,[44] its formation is favored by a lower alkaline concentration and can be represented by the following equation:

$$Sn^{4+} + 3H_2O \leftrightarrow H_2SnO_3 + 4H^+ \quad (7)$$

$$H_2SnO_3 \rightarrow SnO_2 \downarrow + H_2O \quad (8)$$

$$H^+ + OH^- \rightarrow H_2O \quad (9)$$

Similarly, to tin species in the case of a highly alkaline environment, the zinc species are washed away after synthesis.

While the cationic ratios and chemical parameters mentioned above dictate which nanostructures within the Zn-Sn-O system are obtained, understanding the growth mechanism for each nanostructure requires a detailed analysis on the effect of physical parameters such as time, temperature and pressure, which is presented in section 2.2.[44,49,50]

Influence of the Zn:Sn molar ratio

The type of precursor and the ratio between the metallic elements in the synthesis are crucial to define the nanostructures' shape, size and crystallinity. We first studied the different ratios between zinc and tin precursors (2:1, 1:1 and 1:2) using two different zinc sources, zinc acetate (ZnAc) and zinc chloride ($ZnCl_2$). For these studies a NaOH molar concentration of 0.240 M and a H_2O:EDA volume ratio of 7.5:7.5 mL:mL were used, based on the synthesis reported by Li *et al.*,[15] where Zn_2SnO_4 nanowires were grown on a stainless steel mesh for dye-sensitized solar cells application.

Synthesis using ZnAc as the Zn precursor, with a Zn:Sn molar ratio of 1:2, results in inconclusive XRD analysis, showing the possible presence of different phases, whose diffraction peaks overlap (**Figure 2.5**a): tetragonal phase of SnO_2 (ICDD card 01-077-0452), $ZnSnO_3$ orthorhombic perovskite phase and Zn_2SnO_4 inverse spinel phase (ICDD card 00-024-1470). For the $ZnSnO_3$ orthorhombic perovskite phase, peaks can be identified by the ICDD card 00-028-1486. It should be noted that although this card was removed from the ICDD database due to the similarities with a mixture of Zn_2SnO_4 and SnO_2 phases, several reports in literature still refer to it.[49,51–53] In fact, when we performed a peak indexation in different $ZnSnO_3$ nanowires samples, an orthorhombic phase was always determined. These findings are also supported by Raman analysis as will be discussed latter.

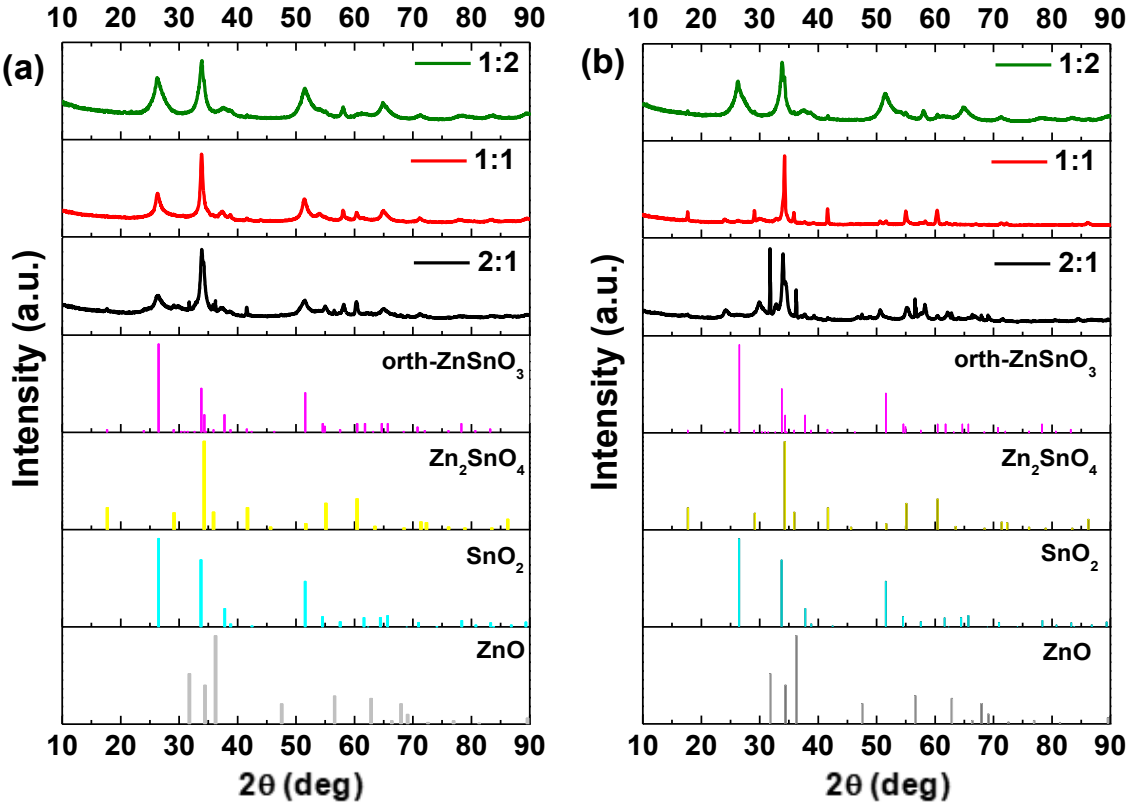

Figure 2.5. XRD patterns for three different Zn:Sn molar ratios (1:2, 1:1 and 2:1) using (a) ZnAc precursor and (b) $ZnCl_2$ precursor. Identification following ICDD card 00-028-1486 (deleted), 00-024-1470 and 01-077-0452 (**Figure 2.3**).

SEM analysis (**Figure 2.6**a) supports the argument that some ZTO ($ZnSnO_3$ and/or Zn_2SnO_4) nanowires are starting to form. This is reinforced by Raman spectroscopy analysis (**Figure 2.7**a), which shows the predominance of the vibrational band at 631 cm^{-1} associated with the expansion and contraction of the Sn-O bond peak,[54] but also that peaks at 538 and 676 cm^{-1} start to appear, corresponding to internal vibrations of the oxygen tetrahedron in Zn_2SnO_4 and to the characteristic Raman M-O bonds stretching vibration mode in the MO_6 octahedron of $ZnSnO_3$ and/or Zn_2SnO_4, respectively.[44]

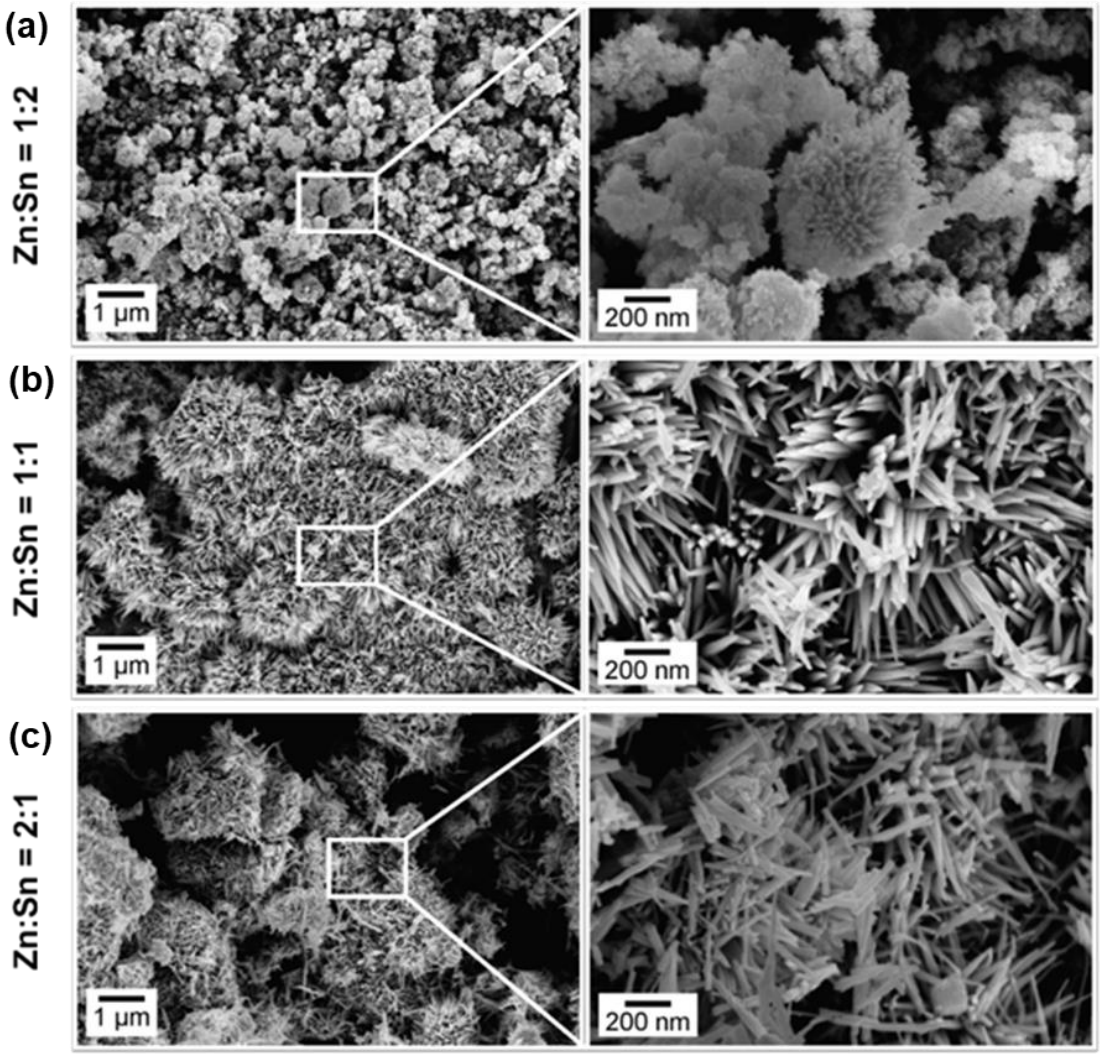

Figure 2.6. SEM micrographs of nanostructures obtained with ZnAc precursor and Zn:Sn molar ratios of: (a) 1:2, (b) 1:1 and (c) 2:1.

For synthesis with a 1:1 molar ratio of Zn:Sn, $ZnSnO_3$ nanowires are predominantly obtained, as shown by XRD and SEM analysis (**Figure 2.5**b and **Figure 2.6**b). The identification of orth-$ZnSnO_3$ is not immediately clear: not only it can be mistaken with SnO_2 (as seen before for 1:2 Zn:Sn molar ratio), but also with Zn_2SnO_4 inverse spinel-cubic phase (ICDD card 00-024-1470). EDS analysis on isolated wires shows the ratio Zn:Sn of 1:1 (**Figure 2.8**), supporting the $ZnSnO_3$ phase, which was also identified by Kovacheva *et al.*[55] on a similar XRD spectra. Raman

spectroscopy shows that the intensity of the 676 cm^{-1} peak (Zn_2SnO_4 or $ZnSnO_3$) increases while the intensity for the 538 cm^{-1} peak (Zn_2SnO_4) decreases, when compared with the sample using 1:2 Zn:Sn ratio. This confirms the predominance of the $ZnSnO_3$ phase for the ratio 1:1. (**Figure 2.7**a). While SnO_2 nanoparticles could not be confirmed by SEM analysis, deeper investigation using SEM and EDS revealed a plausible explanation for the SnO_2 peak: **Figure 2.8** shows that within the same sample some structures comprised by agglomerated nanowires could be found. Such structures were reported by Mao *et al.*[56] and have been described as ZnO-doped SnO_2. This can be explained by the higher solubility of chlorides in solvents based on ethylenediamine when compared to acetates: the prior dissolution of tin chloride would lead initially to the formation of SnO_2 nanostructures, which could then be doped by the Zn present in the solution, which falls in line to the Zn and Sn distribution measured by EDS as seen in **Figure 2.9** (see also **Figure 2.10**).

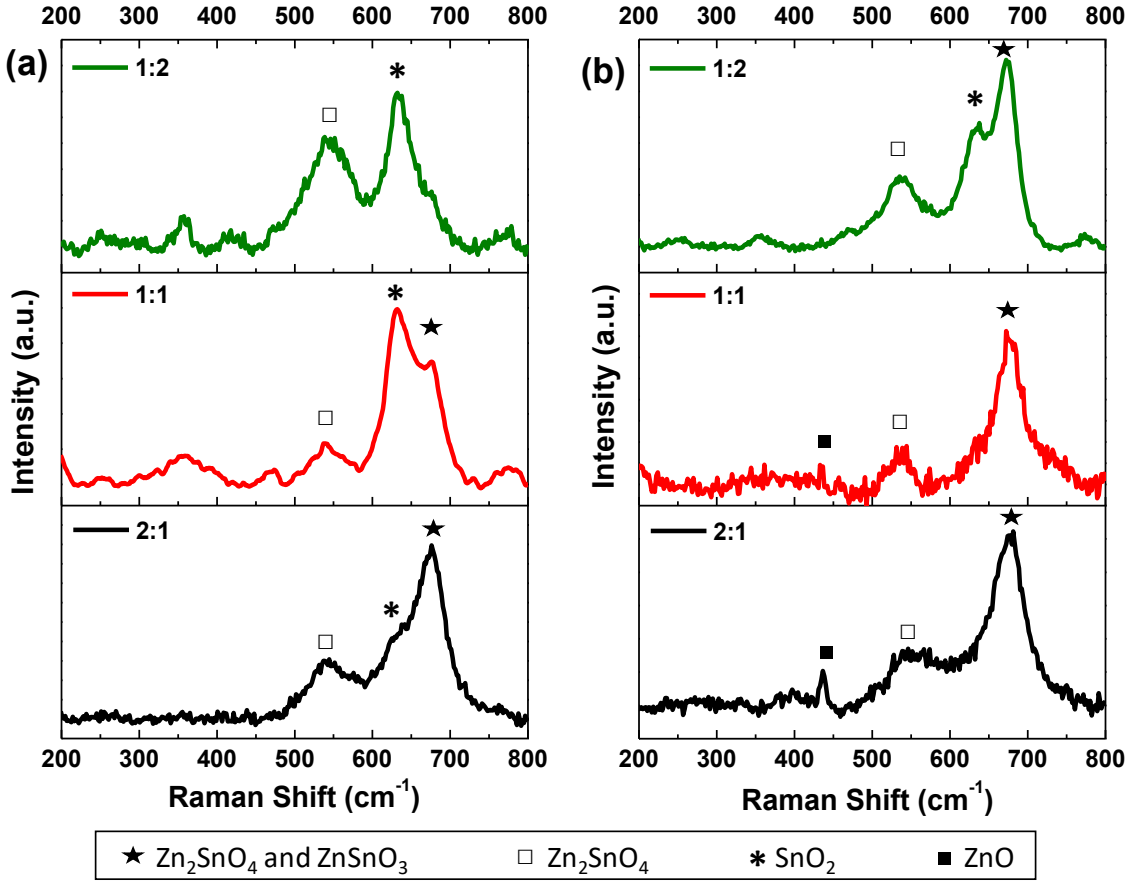

Figure 2.7. Raman shift for the three different Zn:Sn molar ratios (1:2, 1:1 and 2:1) using (a) ZnAc precursor and (b) $ZnCl_2$ precursor.

XRD data obtained for the synthesis with Zn:Sn molar ratio of 2:1 is similar to that of 1:1 condition (**Figure 2.5**b), suggesting the presence of $ZnSnO_3$ perovskite phase. However, SEM in **Figure 2.6**c readily shows that besides the $ZnSnO_3$ nanowires some other structures are present. A more detailed analysis reveals a mixture of $ZnSnO_3$ and Zn_2SnO_4 octahedrons and nanowires, microtubes comprised by agglomerates of $ZnSnO_3$ nanowires and ZnO nanoplatelets (**Figure**

2.11 and **Figure 2.12**). Raman spectroscopy data supports these results, showing the predominance of the 676 cm^{-1} peak associated with $ZnSnO_3$ and/or Zn_2SnO_4 over the 631 cm^{-1} peak from SnO_2, but also the presence of the 538 cm^{-1} peak corresponding to Zn_2SnO_4. Furthermore a small peaks at 437 and 574 cm^{-1} are detected for this synthesis condition, attributed to a vibrational mode of ZnO, concomitant with the SEM analysis.[57]

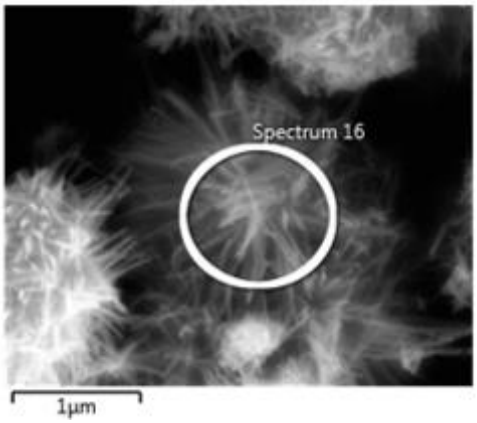

Element	Atomic concentration (%)
Zn	17
Sn	22
O	61

Figure 2.8. SEM image and EDS element quantification of isolated $ZnSnO_3$ nanowires produced by hydrothermal synthesis using ZnAc and a Zn:Sn molar ratio of 1:1.

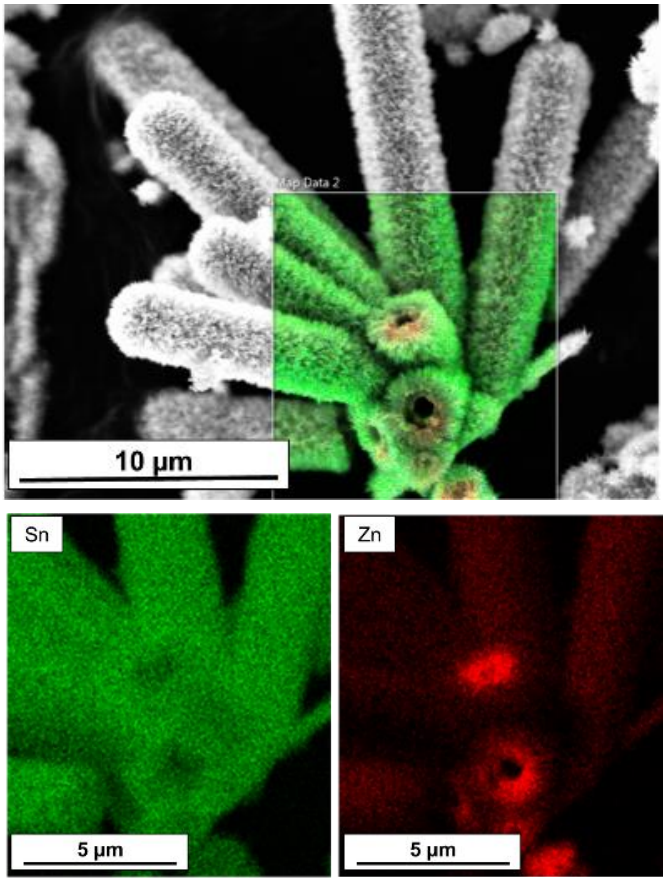

Figure 2.9. SEM micrograph and EDS maps of nanowire' agglomerates obtained with the Zn:Sn molar ratio of 1:1 using ZnAc precursor, showing the higher presence of Sn and a residual Zn content.

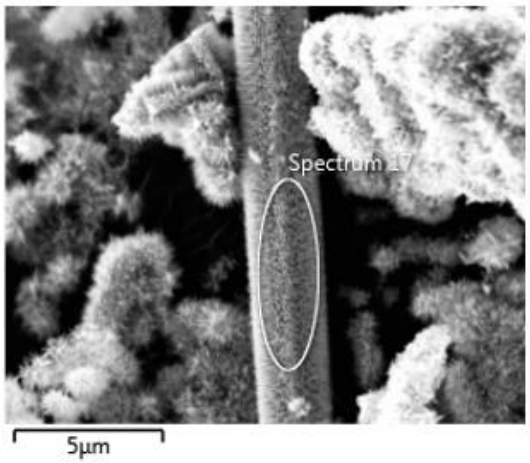

Element	Atomic concentration (%)
Zn	8
Sn	25
O	67

Figure 2.10. SEM image and EDS element quantification of SnO_2-filled $ZnSnO_3$ nanowires structures produced by hydrothermal synthesis using ZnAc and a Zn:Sn molar ratio of 1:1.

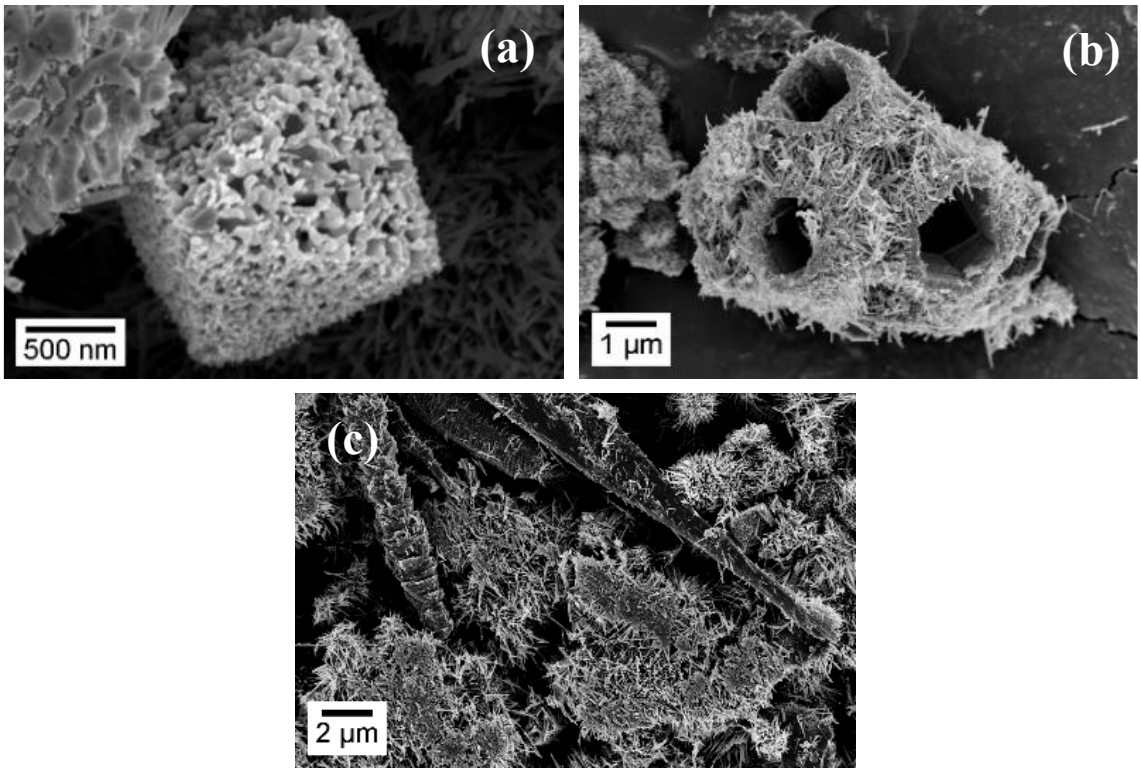

Figure 2.11. SEM micrographs of different structures obtained with a Zn:Sn molar ratio of 2:1 using ZnAc precursor: (a) $ZnSnO_3$ octahedrons, (b) microtubes comprised by $ZnSnO_3$ nanowires and (c) ZnO nanoplatelets.

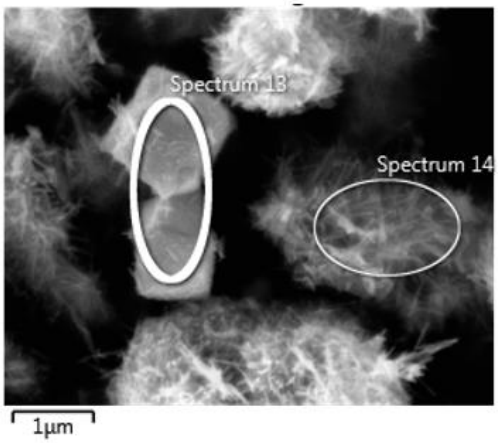

Element	Atomic concentration (%)
Zn	31
Sn	16
O	53

Figure 2.12. SEM image and EDS element quantification of Zn_2SnO_4 octahedrons produced by hydrothermal synthesis using ZnAc and a Zn:Sn molar ratio of 2:1.

It can be concluded that for the ZnAc precursor a 1:1 Zn:Sn molar ratio is the one allowing to obtain $ZnSnO_3$ nanowires without a large fraction of other Zn- and/or Sn-based nanostructures. As such, this ratio was chosen for the following studies. It should be noted that Li *et al.* reported Zn_2SnO_4 nanowires following a similar synthesis but using a stainless steel mesh as seed, favoring the growth of ZTO nanostructures similar to the cubic structure of the seed.[15]

The same study was performed using $ZnCl_2$ as zinc precursor, with the different Zn:Sn molar ratios of 1:1, 1:2, 2:1. Using a Zn:Sn molar ratio of 1:2 similar XRD data is obtained when compared to the ZnAc precursor, suggesting that a tetragonal phase of SnO_2 and/or a $ZnSnO_3$ perovskite phase exist (**Figure 2.5**b). SEM analysis reveals that both SnO_2 nanoparticles and ZTO ($ZnSnO_3$ and/or Zn_2SnO_4) nanowires are obtained, but now with more relevance to the later (**Figure 2.13**a). Raman spectroscopy data confirms this, exhibiting a more intense peak for $ZnSnO_3$ and/or Zn_2SnO_4 (676 cm^{-1}) than for SnO_2 (631 cm^{-1}), as seen in **Figure 2.7**b.

For a solution with Zn:Sn molar ratio of 1:1, the XRD spectra shows mainly the phase Zn_2SnO_4, as depicted in **Figure 2.5**b, with some small peaks attributed to $ZnSnO_3$ and SnO_2. SEM images show several types of nanostructures: while $ZnSnO_3$ nanowires are clearly observed (**Figure 2.13**b), a more detailed inspection also reveals a large amount of Zn_2SnO_4 nanocubes (**Figure 2.14**). For the Zn:Sn molar ratio of 2:1 mostly $ZnSnO_3$ nanowires are obtained (**Figure 2.13**c). Still, a few ZnO columnar nanoplatelets with hexagonal phase (ICDD card 00-036-1451) are also shown in **Figure 2.15**c. These trends are confirmed by the Raman analysis (**Figure 2.7**b), analyzing the evolution of peaks at 538 cm^{-1} (Zn_2SnO_4), 676 cm^{-1} (Zn_2SnO_4 and/or $ZnSnO_3$) and 631 cm^{-1} (SnO_2). Similar structures were already reported by Tian *et al.*[58] for the synthesis of ZnO nanostructures. **Figure 2.15**a shows an example of $ZnSnO_3$ nanowire agglomerates obtained in this condition, which is shown by EDS to have a 1:1 Zn:Sn ratio (**Figure 2.16**). Curiously, by looking at the hexagonal form in the middle, we can suggest that the ZTO nanowires are grown from an initial hexagonal ZnO microtube/wire. The initial formation of the ZnO nanowires can be attributed to the higher solubility of $ZnCl_2$ when compared to $SnCl_4{\cdot}5H_2O$,[56]

contributing to the faster formation of these structures relatively to the $ZnSnO_3$ nanowires, which is an issue when trying to obtain single phase ZTO nanostructures. However, according to Miyauchi *et al.* these ZnO nanowires can be removed with an acid solution of HNO_3,[21] allowing to achieve only $ZnSnO_3$ nanowires in the sample. As such, the Zn:Sn ratio of 2:1 was the selected condition for the following studies with the $ZnCl_2$ precursor, allowing to obtain $ZnSnO_3$ nanowires with an average length of 605 nm and a diameter around 65 nm.

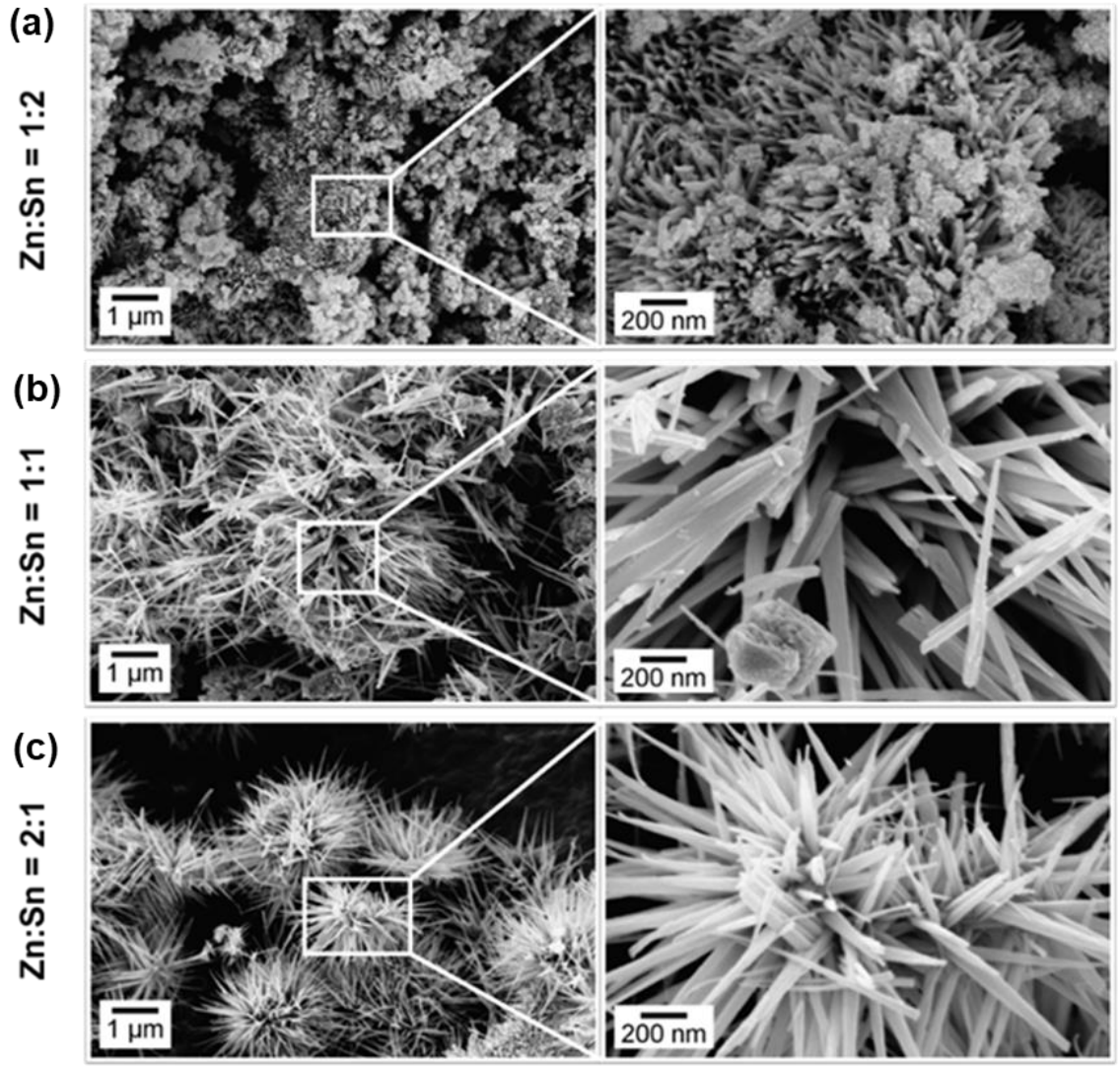

Figure 2.13. SEM micrographs of nanostructures obtained with $ZnCl_2$ precursor and Zn:Sn molar ratios of: (a) 1:2, (b) 1:1 and (c) 2:1.

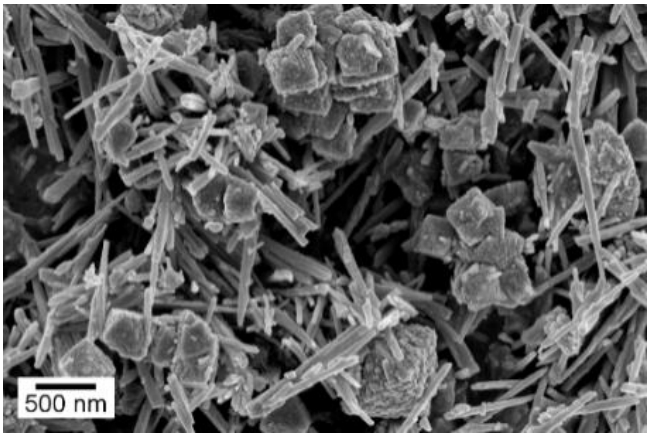

Figure 2.14. SEM micrographs of nanostructures obtained with $ZnCl_2$ precursor showing that with a 1:1 Zn:Sn molar ratio results in a mixture between $ZnSnO_3$ nanowires and Zn_2SnO_4 nanocubes.

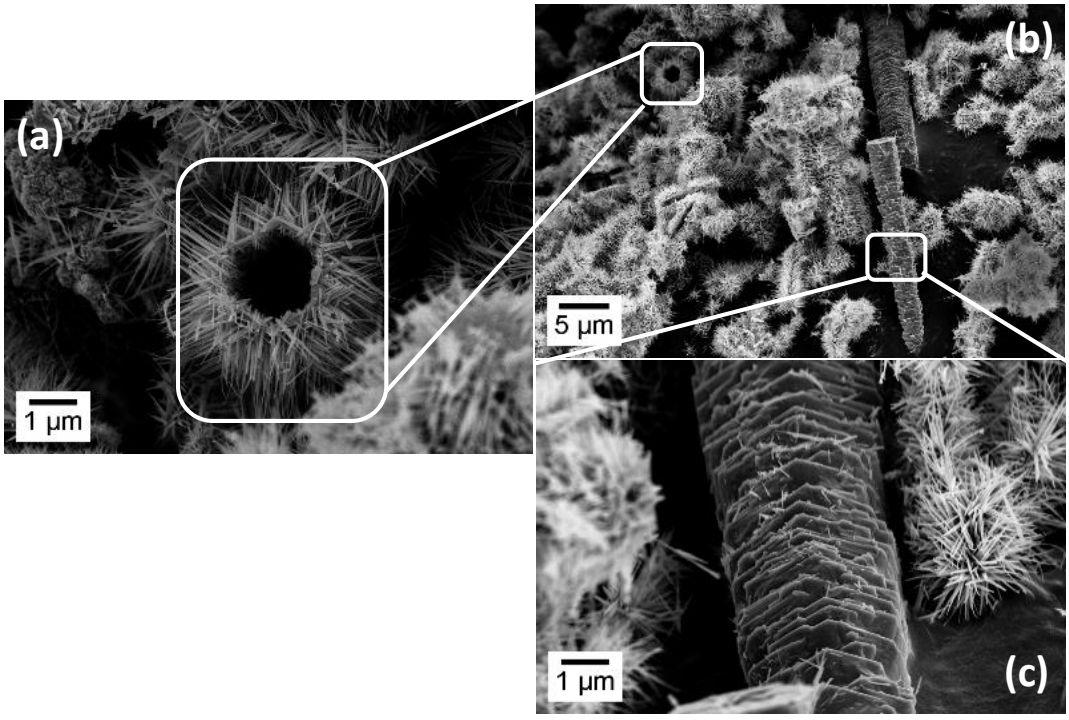

Figure 2.15. SEM micrographs of nanostructures obtained with $ZnCl_2$ precursor with a 2:1 Zn:Sn ratio. Zoom in of (b) shows: (a) $ZnSnO_3$ nanowire agglomerates and (c) ZnO nanoplatelets.

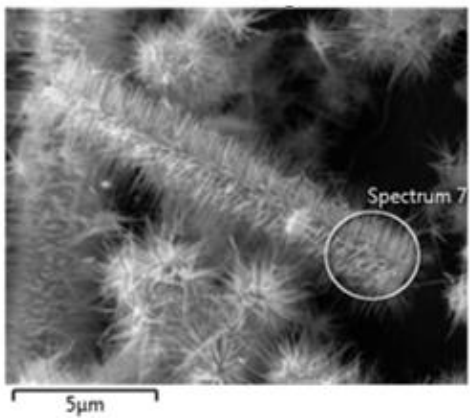

Element	Atomic concentration (%)
Zn	18
Sn	18
O	64

Figure 2.16. SEM image and EDS element quantification of $ZnSnO_3$ nanowire agglomerates produced by hydrothermal synthesis using $ZnCl_2$ and a Zn:Sn molar ratio of 2:1.

For both zinc precursors, for the Zn:Sn molar ratio of 1:2, SnO_2 nanoparticles are predominantly obtained, which can be attributed to the higher concentration of tin precursor in the solution. Even so, the initial growth of $ZnSnO_3$ nanowires is already observed. When the molar ratio is 1:1, the results differ for the two precursors. For ZnAc this was shown to be the best ratio in terms of promoting the growth of a single phase of $ZnSnO_3$ nanowires. On the other hand, for $ZnCl_2$, this ratio leads to a mixture of Zn_2SnO_4 nanocubes (predominant) and $ZnSnO_3$ nanowires. As for the 2:1 molar ratio of Zn:Sn, it is the condition that promotes better results when using $ZnCl_2$, resulting in $ZnSnO_3$ nanowires (although mixed with ZnO nanowires), while for ZnAc a higher mixture of phases, with predominance of Zn_2SnO_4 nanocubes, is achieved.

In summary, whichever the ratios, using ZnAc promotes the presence of SnO_2 while using $ZnCl_2$ results in higher amounts of ZnO. This can be explained by the different precursors' solubility: while $SnCl_4 \cdot 5H_2O$ is more soluble than ZnAc, promoting a faster growth of tin-based structures, $ZnCl_2$ is more soluble than tin chloride, promoting a preferential growth of zinc-based structures.

Table 2.1 presents the nanostructures sizes for the different conditions of both zinc precursors, obtained through the SEM images and using the software ImageJ. In general, it is possible to observe that the nanostructures produced using $ZnCl_2$ as zinc precursor have longer sizes than the nanostructures produced using ZnAc.

Table 2.1. Influence of Zn:Sn molar ratio in the type and average dimensions of the obtained nanostructures. Predominant structures, as determined by SEM-EDS, XRD and Raman data, are presented in bold.

	ZnAc			**$ZnCl_2$**		
Zn:Sn	**Phases**	**Length**	**Diameter**	**Phases**	**Length**	**Diameter**
2:1	**$ZnSnO_3$ NWs**	**185 nm**	**25 nm**	**$ZnSnO_3$ NWs**	**605 nm**	**65 nm**
	Microtubes (agglomerates of $ZnSnO_3$ NWs)	7 µm	2 µm			
	$ZnSnO_3$ Octahedrons	-	2 µm	ZnO NWs	22 µm	3 µm
	Zn_2SnO_4 octahedrons	-	1 µm			
	ZnO nanoplatelets	17 µm	2 µm			
1:1	**$ZnSnO_3$ NWs**	365 nm	64 nm	**Zn_2SnO_4 NCs**	**-**	**370 nm**
	Microtubes (agglomerates of $ZnSnO_3$ NWs)	17 µm	2 µm	$ZnSnO_3$ NWs	1 µm	77 nm
1:2	**SnO_2 NPs**	**-**	**12 nm**	**SnO_2 NPs**	**-**	**15 nm**
	ZTO NWs	40 nm	12 nm	ZTO NWs	140 nm	25 nm

Influence of the surfactant concentration

Oriented growth and morphological control of nanostructures is highly dependent on the used surfactant. The ability for interfacial adsorption of the surfactants can direct the crystals' growth. This is dependent on their nature (nonionic, anionic, cationic or zwitterionic) and thus different surfactants can be preferred according to the different materials being employed and its desired shape.[44,59] This section presents the study of the influence of the H_2O:EDA volume ratio, for the two selected conditions from the previous study: Zn:Sn = 1:1 molar ratio using the ZnAc precursor and Zn:Sn = 2:1 molar ratio using the $ZnCl_2$ precursor. The H_2O:EDA volume ratios used were 15:0, 9:6, 8:7, 7.5:7.5, 8:7, 9:6 and 15:0 mL:mL. For all conditions the mineralizer's (NaOH) concentration was kept as 0.240 M.

For the ZnAc precursor and using only H_2O as a solvent a mixture of $ZnSnO_3$ nanowires and Zn_2SnO_4 nanoplates and octahedrons comprised by nanoplates is obtained (**Figure 2.17**a and **Figure 2.18**a), with Zn_2SnO_4 being the predominant phase. These type of octahedron structures were already reported by Ji *et al.*[26]. Increasing EDA up to 7.5:7.5 there is a trend for Zn_2SnO_4 nanoparticles to disappear, while $ZnSnO_3$ nanowires dimensions get larger. SnO_2 nanoparticles initially appear as isolated structures moving to SnO_2-filled $ZnSnO_3$ nanowires as EDA volume is increased (**Figure 2.17**a, **Figure 2.18** and **Figure 2.19**a). For 7:8 volume ratio, there is an increase in the presence of ZnO nanowires and $ZnSnO_3$ nanoparticles with ordered face centered cubic structure (**Figure 2.17**a and **Figure 2.18**i and j), due to the higher amount of EDA. Note that $ZnSnO_3$ ordered face centered cubic structure and $ZnSn(OH)_6$ exhibit coincident Raman peak (603 cm^{-1})[50] and XRD peaks (**Figure 2.19** and **2.3**, respectively). Still, for this synthesis condition it is verified by FTIR analysis that no OH^- groups are present (**Figure 2.20**), confirming the $ZnSnO_3$ identification. The ratio 6:9 produces mainly ZnO nanowires and only a few $ZnSnO_3$ nanoparticles as shown by SEM and XRD (**Figure 2.18**m and **Figure 2.17**a, respectively). When no H_2O is used as solvent (0:15) it is obtained mostly SnO_2 nanoparticles and ZnO nanowires, with some $ZnSnO_3$ nanoparticles being also present (**Figure 2.17**a and **Figure 2.18**o). These results are confirmed by Raman spectroscopy (**Figure 2.19**a) and can be explained by the significantly higher solubility of $SnCl_4 \cdot 5H_2O$ in EDA compared to ZnAc, inducing a faster and preferential growth of SnO_2 nanoparticles and the later growth of ZnO nanowires. Still, probably due to the long duration of the synthesis, some $ZnSnO_3$ nanoparticles are grown, since as previously discussed ZTO nanostructures can originate from SnO_2 nanostructures.

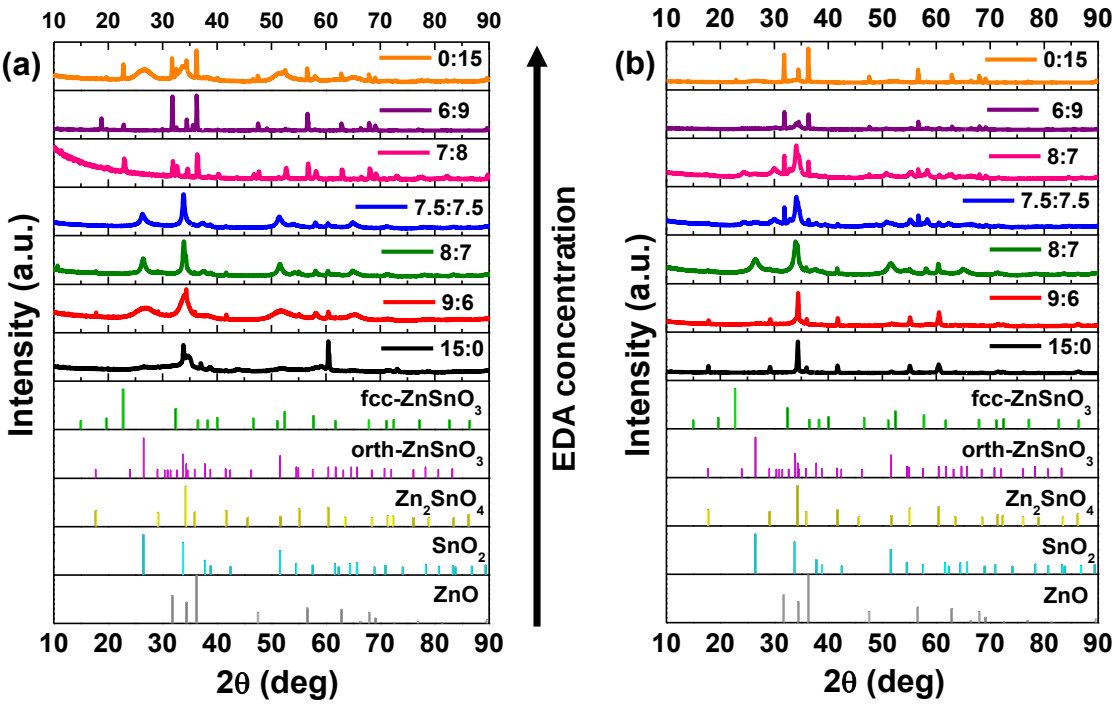

Figure 2.17. XRD patterns when using (a) ZnAc precursor (with 1:1 Zn:Sn ratio) and (b) $ZnCl_2$ precursor (with 2:1 Zn:Sn ratio), for different H_2O:EDA volume ratios. Identification following ICDD card 00-028-1486 (deleted), 00-011-0274, 00-024-1470, 01-077-0452 and #06-1451 (**Figure 2.3**).

For $ZnCl_2$ as precursor and when using only water as a solvent (15:0 H_2O:EDA), Zn_2SnO_4 nanoparticles with octahedral shape are obtained (**Figure 2.18**b). The XRD spectra (**Figure 2.17**b) shows a pure cubic spinel-type phase for these nanostructures. This is the most stable phase and shape for zinc-tin oxide in the absence of EDA, in line with the literature even for other conditions of hydrothermal synthesis.[26,60,61] With the addition of EDA, for a H_2O:EDA ratio 9:6, Zn_2SnO_4 nanostructures with a different shape than the octahedral and some $ZnSnO_3$ nanowires are obtained, as seen by SEM (**Figure 2.18**d). By XRD (**Figure 2.17**b) it can be verified the mixture of $ZnSnO_3$ and Zn_2SnO_4 phases, being Zn_2SnO_4 still predominant. Increasing EDA's concentrations (8:7, 7.5:7.5 and 7:8) the size of $ZnSnO_3$ nanowires is increased and this phase becomes predominant. As **Figure 2.18**f shows, for the 8:7 ratio, only $ZnSnO_3$ nanowires are grown, but they present a large size distribution.

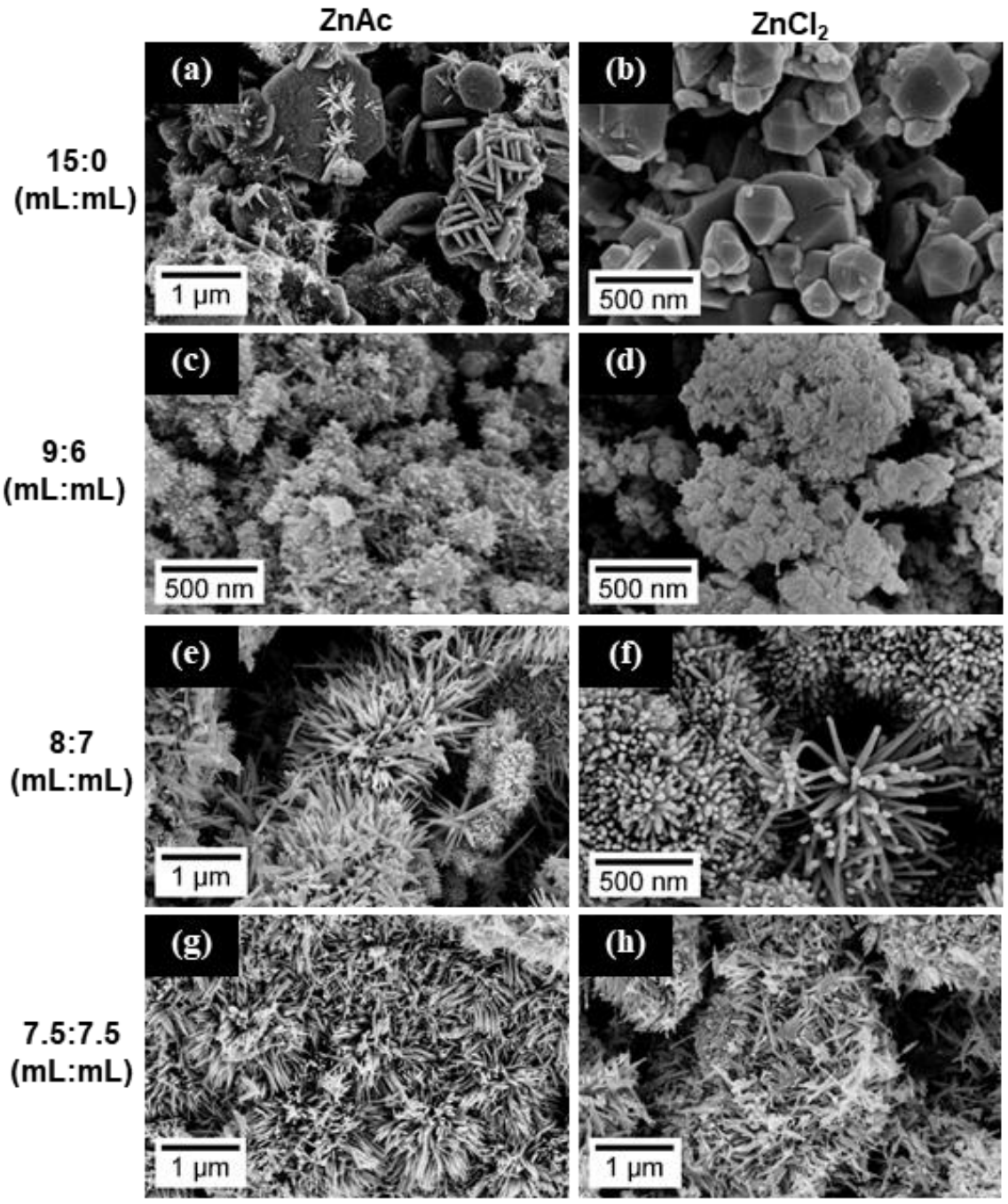
ZnAc
ZnCl2
15:0 (mL:mL)
9:6 (mL:mL)
8:7 (mL:mL)
7.5:7.5 (mL:mL)
(a)
(b)
(c)
(d)
(e)
(f)
(g)
(h)
1 µm
500 nm
500 nm
500 nm
1 µm
500 nm
1 µm
1 µm

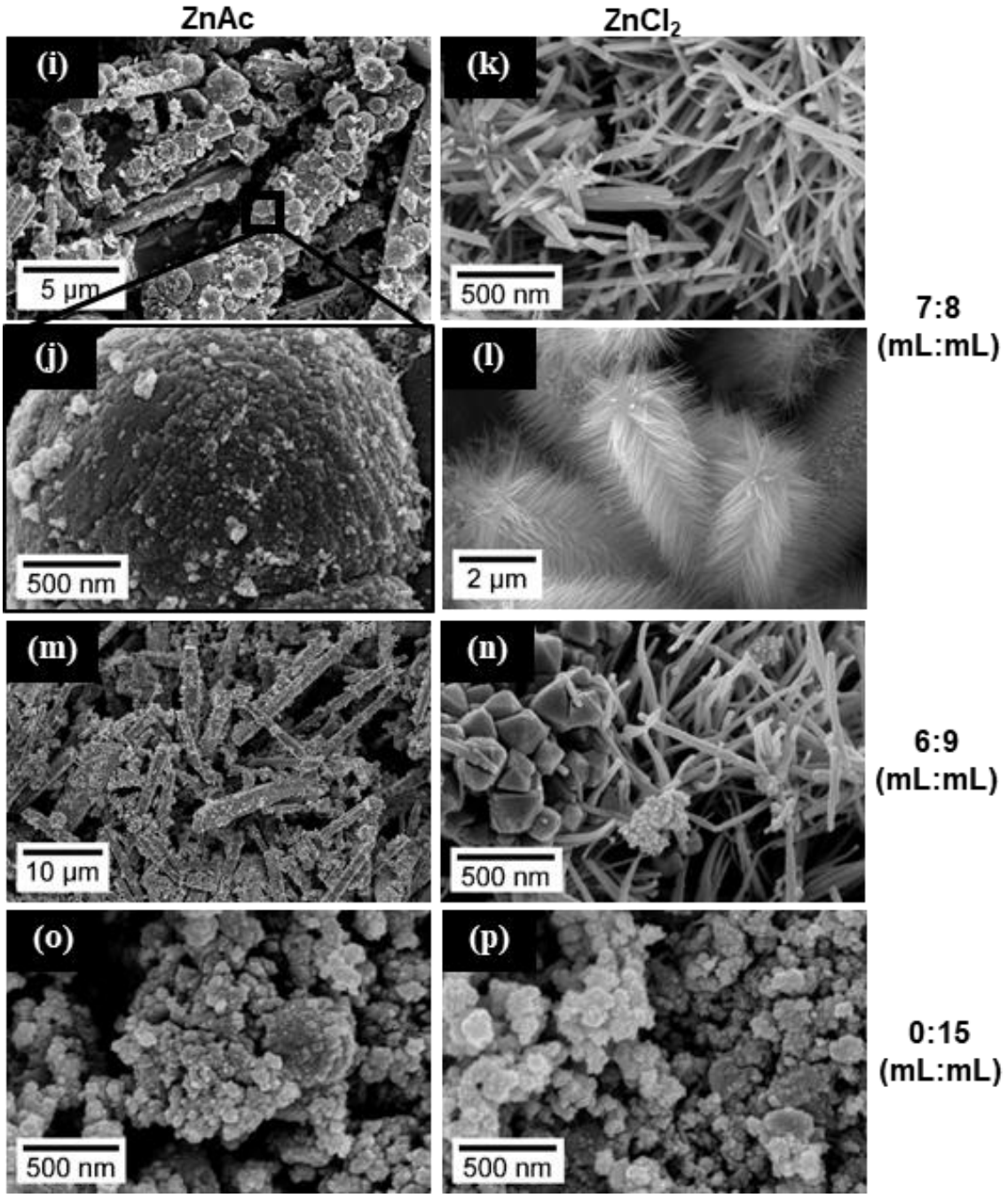

Figure 2.18. SEM micrographs of the nanostructures obtained by synthesis using ZnAc/$ZnCl_2$ as precursors, respectively, with the different H_2O:EDA volume ratios of: (a)/(b) 15:0, (c)/(d) 9:6, (e)/(f) 8:7, (g)/(h) 7.5:7.5, (i) and (j)/(k) and (l) 7:8, (m)/(n) 6:9, (o)/(p) 0:15.

For the 7.5:7.5 ratio, $ZnSnO_3$ and large wires of ZnO are obtained, as it was already discussed in section *Introduction: governing equations to obtain ZTO nanowires*. For the 7:8 ratio the $ZnSnO_3$ nanowires are highly agglomerated, as shown in **Figure 2.18**l. These structures are similar to the obtained for ZnAc (7.5:7.5, Zn:Sn = 1:1), as described by Mao *et al.*[56]. The H_2O:EDA ratio of 6:9 gives miscellaneous results, as **Figure 2.18**n and **Figure 2.21** show, with a mixture of several types of structures being obtained. It is possible to observe Zn_2SnO_4 nanocubes and

octahedrons comprised by nanoplates, $ZnSnO_3$ nanowires, SnO_2 nanoparticles and also ZnO columnar nanoplatelets agglomerates, with all of these phases being identified by XRD (**Figure 2.17**b). Using only EDA (0:15), $ZnSnO_3$ nanoparticles and ZnO nanowires are formed (**Figure 2.18**p). The strong ZnO peaks in XRD (**Figure 2.17**b) appear due to the large size of ZnO nanowires when comparing with the $ZnSnO_3$ nanoparticles. Overall, the XRD (**Figure 2.17**b) shows that for higher EDA's concentration, the formation of ZnO becomes preferential over ZTO, which is in agreement with the SEM/EDS and Raman (**Figure 2.19**b) analysis. This preferential formation of ZnO nanostructures for the higher EDA conditions can be explained by the strong coordination ability between the $ZnCl_2$ and EDA molecules.[62,63]

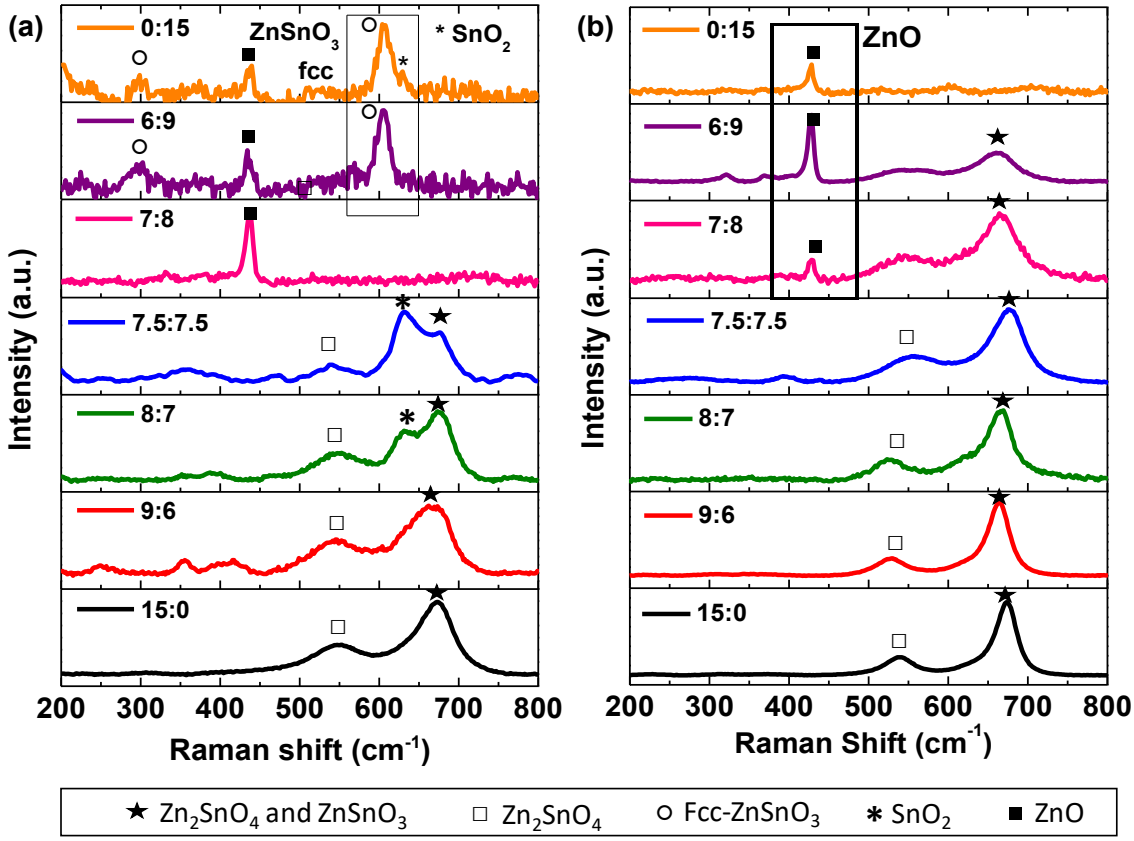

Figure 2.19. Raman shift for the different H_2O:EDA volume ratios (15:0, 9:6, 8:7, 7.5:7.5, 7:8, 6:9 and 0:15) using (a) ZnAc precursor and (b) $ZnCl_2$ precursor.

FTIR analysis helps to understand and to explain the results for the synthesis where EDA has a higher concentration than H_2O. **Figure 2.20**a shows that when using ZnAc as zinc precursor, for the conditions with H_2O:EDA ratios of 7:8, 6:9 and 0:15, precursor or solvent residuals are still present in the final product, due to the low solubility of ZnAc in EDA. In comparison, for the synthesis using $ZnCl_2$, residuals are observed when only EDA is used as a solvent (**Figure 2.20**b), which can be attributed to the higher solubility of $ZnCl_2$ in EDA, comparing to that of ZnAc. For all the other conditions no precursor peaks can be traced by FTIR analysis.

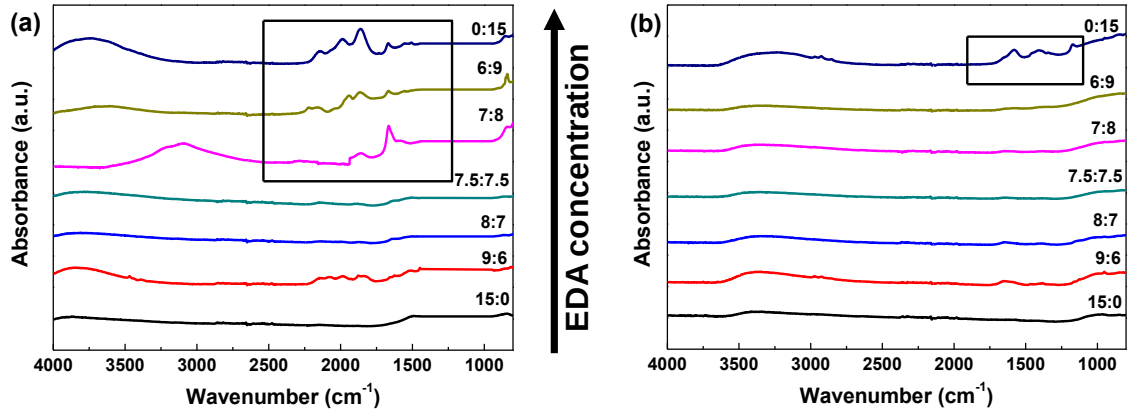

Figure 2.20. FTIR spectra of samples with different H_2O:EDA concentrations for (a) ZnAc and (b) $ZnCl_2$.

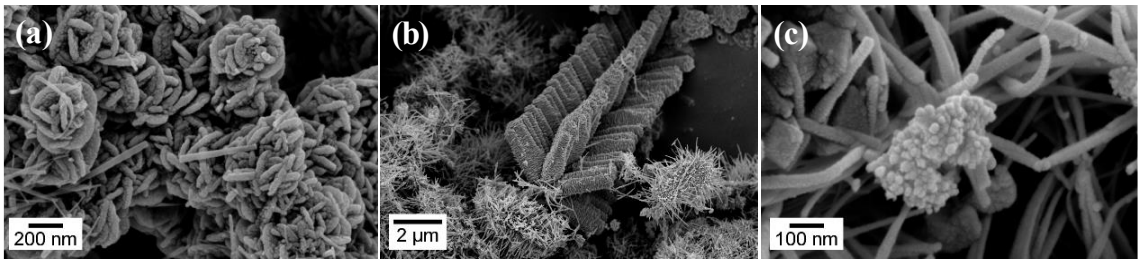

Figure 2.21. Mixture of nanostructures obtained with $ZnCl_2$ precursor with a H_2O:EDA volume ratio of 6:9: (a) Zn_2SnO_4 octahedrons comprised by nanoplates, (b) ZnO columnar nanoplatelets and (c) SnO_2 nanoparticles.

Table 2.2 summarizes the type of nanostructures obtained for the different conditions and their respective dimensions. The trend verified in the previous study regarding the longer sizes of nanostructures synthesized using $ZnCl_2$ as compared to ZnAc is again observed here. It is also reinforced the higher presence of Sn-based structures in the synthesis using ZnAc, and a predominance of Zn-based structures in the synthesis using $ZnCl_2$. The addition of EDA favors the formation of $ZnSnO_3$ nanowires over the more energetically stable Zn_2SnO_4 nanoparticles, which we attribute to the pH increase, as reported by Miyauchi *et al.*[21]. Up to a certain EDA concentration the length and diameter of these nanowires are increased. For both precursors, an optimal H_2O:EDA volume ratio of 7.5:7.5 was determined for the formation of $ZnSnO_3$ nanowires. As the EDA concentration is increased beyond this point ZnO nanostructures start to be dominant, even for the ZnAc precursor. This suggests that the predominant factor defining the type of nanostructure obtained in an environment with a high EDA concentration starts to be the pH value, as will be discussed in more detail the next section. Thus, despite the relevance of EDA to achieve the desired ZTO nanowires, the presence of the water is imperative to the formation of these nanostructures, not only to assure the complete dissolution of the precursors, but also to balance the pH in solution.

Table 2.2. Influence of H_2O:EDA volume ratio in the type and average dimensions of the obtained nanostructures. Predominant structures, as determined by SEM-EDS, XRD and Raman data, are presented in bold.

	ZnAc			$ZnCl_2$		
H_2O:EDA	**Phases**	**Length**	**Diameter**	**Phases**	**Length**	**Diameter**
15:0	**Zn_2SnO_4 nanoplates** octahedrons $ZnSnO_3$ NWs	**-** - 180 nm	**920 nm** 1 µm 30 nm	**Zn_2SnO_4 octahedrons**	**-**	**330 nm**
9:6	**$ZnSnO_3$ NWs** SnO_2 NPs	**120 nm** -	**25 nm** 30 nm	**Zn_2SnO_4 NPs**	**-**	**19 nm**
8:7	**$ZnSnO_3$ NWs**	**536 nm**	**70 nm**	**$ZnSnO_3$ NWs**	322 nm 89 nm	35 nm 28 nm
7.5:7.5	**$ZnSnO_3$ NWs** Microtubes (agglomerates of $ZnSnO_3$ NWs)	**365 nm** 17 µm	**64 nm** 2 µm	**$ZnSnO_3$ NWs** ZnO NWs	**605 nm** 22 µm	65 nm 3 µm
7:8	**ZnO NWs** $ZnSnO_3$ NPs	**9 µm** -	**2 µm** 1 µm	**$ZnSnO_3$ NWs** Agglomerates	**390 nm** 10 µm	**65 nm** 3 µm
6:9	**ZnO NWs** $ZnSnO_3$ NPs	**16 µm** -	**2 µm** 85 nm	**$ZnSnO_3$ NWs** Zn_2SnO_4 Octahedrons NCs SnO_2 NPs ZnO columnar nanoplatelets agglomerates	**440 nm** - - - 2 µm	**26 nm** 411 nm 243 nm 32 nm 545 nm
0:15	**ZnO NWs** $ZnSnO_3$ NPs SnO_2 NPs	**16 µm** - -	**2 µm** 18 nm 18 nm	**ZnO NWs** $ZnSnO_3$ NPs	**4 µm** -	**310 nm** 17 nm

Influence of NaOH concentration

NaOH plays an important role in the growth of the nanostructures, acting as a mineralizer agent, having a direct influence on the definition of the crystalline phase that is produced.

Based on the previous studies presented in this manuscript, the synthesis conditions for this study were set as: Zn:Sn = 1:1 ratio when using the ZnAc precursor, Zn:Sn = 2:1 ratio with the $ZnCl_2$ precursor, keeping a H_2O:EDA ratio of 7.5:7.5 in both conditions. Concentrations of NaOH of 0.100 M, 0.175 M, 0.240 M and 0.350 M were used to understand the influence of the mineralizer on the synthesis. The results for both zinc precursors presented the same trend, being

discussed here simultaneously. With the poorer concentration of NaOH (0.100 M) synthesis results in SnO_2 nanoparticles, whichever precursor used, as seen in **Figure 2.22** and **Figure 2.23**. Lehnen *et al.*[12] explained this behavior as an effect of the fast hydrolysis of Sn^{4+} cations, leading to the preferential formation of SnO_2. With the increasing of the NaOH concentration to 0.175 M, SnO_2 nanoparticles are still obtained, but Zn_2SnO_4 nanoparticles are now predominant. Still, SnO_2 is more evident for the ZnAc precursor, as shown in the XRD spectra (**Figure 2.22**a), which would be expected based on the higher solubility of $SnCl_4 \cdot 5H_2O$ compared to ZnAc. Increasing the NaOH concentration to 0.240 M, the Zn_2SnO_4 phase is no longer present and $ZnSnO_3$ nanowires are now produced, both in dispersed and in agglomerate shapes, as well as some ZnO nanowires as already discussed in section *Influence of the Zn:Sn molar ratio*. Finally, for the NaOH concentration of 0.350 M, only ZnO nanowires are obtained when using $ZnCl_2$, while when using ZnAc both ZnO nanowires and $ZnSnO_3$ nanoparticles (ICDD card 00-011-0274) are observed. This trend of preferentially growth of ZnO in alkaline solutions is well known, since divalent metal ions do not hydrolyze in acidic environments.[64] Even with higher concentrations of NaOH (0.500 M) the resulting structures were verified to be the same as for 0.350 M, but with a lower reaction yield. These results are in agreement with the literature, as Lehnen *et al.*[12] showed the same tendency for specific pH values: for pH ≈ 1 SnO_2 nanoparticles are obtained, pH ≈ 8.5 yields Zn_2SnO_4 nanoparticles, and higher pH values yields ZnO mixed with $ZnSn(OH)_6$.

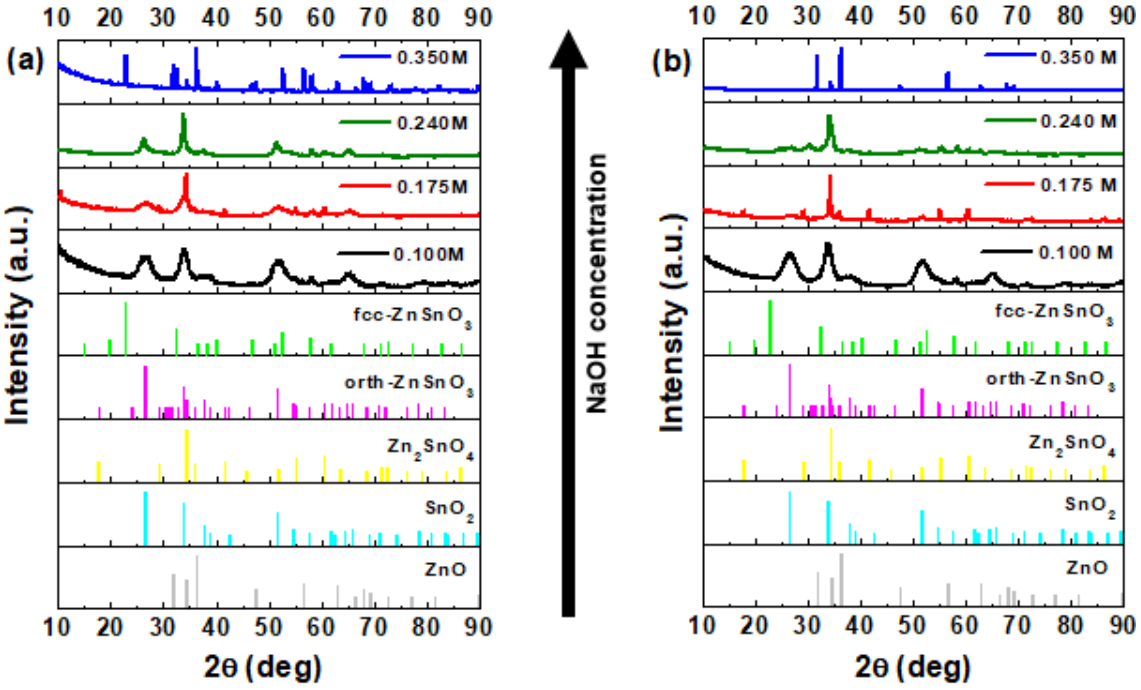

Figure 2.22. XRD pattern of the nanostructures obtained for different NaOH concentrations, using (a) ZnAc and (b) $ZnCl_2$ as zinc precursors. Identification following ICDD card 00-028-1486 (deleted), 00-011-0274, 00-024-1470, 01-077-0452 and 00-036-1451 (**Figure 2.3**).

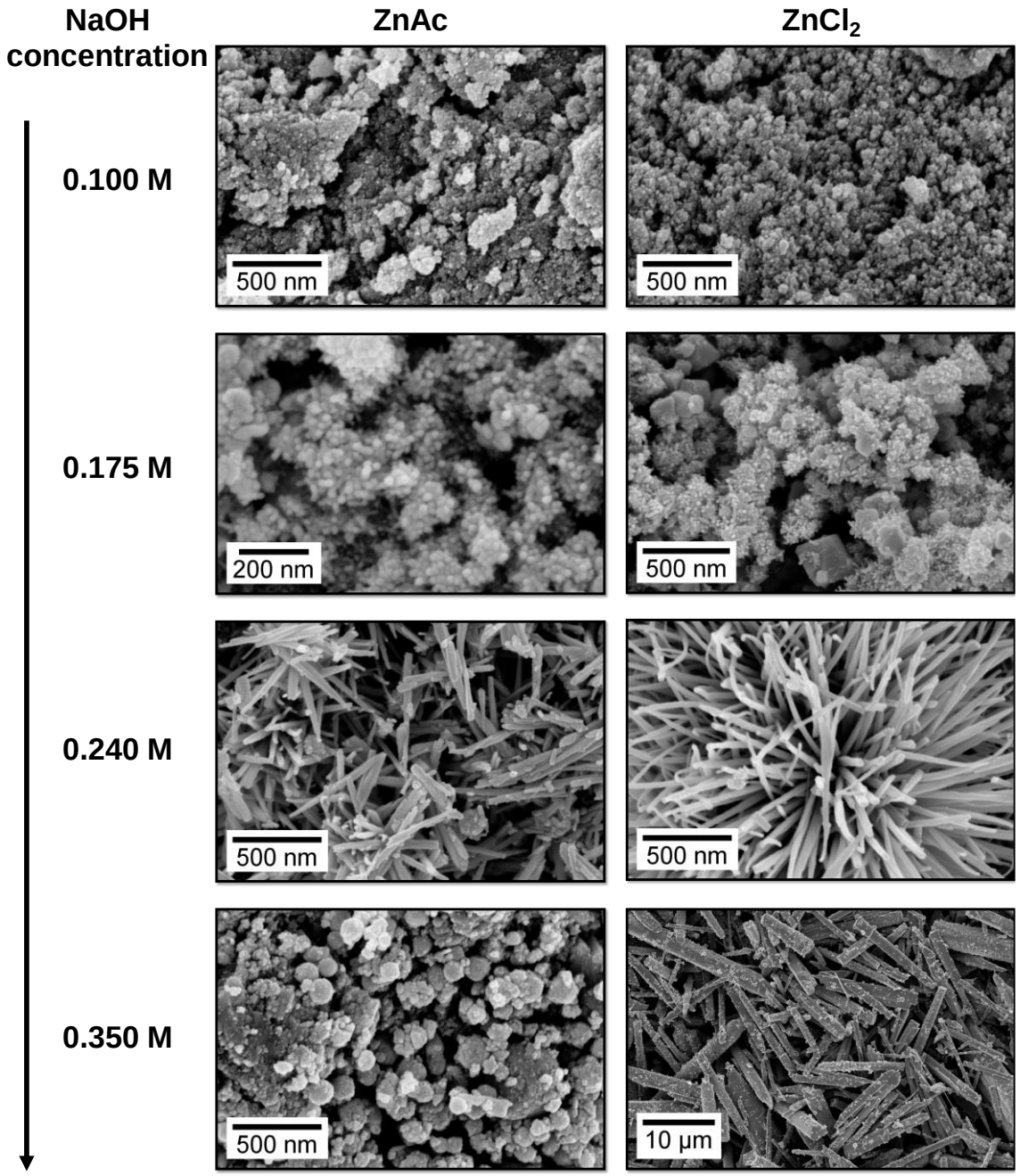

Figure 2.23. SEM micrographs of the nanostructures obtained by synthesis using different NaOH concentrations.

Our results show a similar trend, i.e., lower pH leads to SnO_2 structures and higher pH favors ZnO ones, even if the starting pH (without adding NaOH) is already 12. As such, this trend is not dependent on the pH value itself, but on the variation of the NaOH concentration for a specific synthesis.

Table 2.3 summarizes all these findings, showing that low mineralizer concentrations favor the growth of tin oxide structures over zinc oxide ones, with the trend being reversed as the NaOH concentration increases. Having in mind the specific goal of obtaining ZTO nanowires, the

optimum mineralizer concentration is around 0.240 M. As seen in the previous sections, data in **Figure 2.23** and **Table 2.3** reinforce the trend of obtaining nanostructures with larger dimensions using $ZnCl_2$ precursor instead of ZnAc, given the higher solubility of $ZnCl_2$.

Table 2.3. Influence of NaOH concentration in the type and average dimensions of the obtained nanostructures. Predominant structures, as determined by SEM-EDS, XRD and Raman data, are presented in bold.

	ZnAc			**$ZnCl_2$**		
NaOH Concentration	**Phases**	**Length**	**Diameter**	**Phases**	**Length**	**Diameter**
0.100 M	**SnO_2 NPs**	**-**	**17 nm**	**SnO_2 NPs**	**-**	**15 nm**
0.175 M	**Zn_2SnO_4 NPs**	**-**	**60 nm**	**Zn_2SnO_4 NPs**	**-**	**100 nm**
	SnO_2 NPs	-	25 nm	SnO_2 NPs	-	20 nm
0.240 M	**$ZnSnO_3$ NWs**	**365 nm**	**64 nm**	**$ZnSnO_3$ NWs**	**605 nm**	**65 nm**
	Microtubes (agglomerates of $ZnSnO_3$ NWs)	17 µm	2 µm	ZnO NWs	22 µm	3 µm
0.350 M	**$ZnSnO_3$ NPs**	**-**	**120 nm**	**ZnO NWs**	**15 µm**	**2 µm**
	ZnO NWs	12 µm	2 µm			

2.1.5. Conclusions

$ZnSnO_3$ nanowires produced by a solution process without the use of a seed-layer and with temperatures of only 200 °C were reported for the first time. To accomplish this, the work presented a detailed study on the influence of the different chemical parameters on the hydrothermal synthesis of ZTO nanostructures. More specifically the role of Zn:Sn ratio, surfactant concentration (EDA) and mineralization agent (NaOH) concentration for two zinc precursors (ZnAc and $ZnCl_2$) was studied. Adjusting these parameters, the potential to achieve ZTO structures with different phases and morphologies was shown. It was found that an intricate interdependence of the different chemical parameters would enable multiple synthesis conditions to result in the final goal of obtaining ZTO nanowires. Still, it was concluded that $ZnCl_2$ allowed for a more stable (with less mixture of phases/structures) and more reproducible reaction than ZnAc, with longer $ZnSnO_3$ nanowires being obtained. Hence, the best condition proved to be using $ZnCl_2$ as zinc precursor, with a Zn:Sn molar ration of 2:1, H_2O:EDA volume ratio of 7.5:7.5 mL:mL and a NaOH concentration of 0.240 M. These $ZnSnO_3$ nanowires presented lengths and diameters around 600 nm and 65 nm, respectively.

2.2. $ZnSnO_3$ nanowires synthesis: influence of the physical parameters

2.2.1. Abstract

$ZnSnO_3$ semiconductor nanostructures have several applications as photocatalysis, gas sensors, and energy harvesting. However, due to its multicomponent nature, the synthesis is far more complex than its binary counter parts. The complexity increases even more when aiming for low-cost and low-temperature processes as in hydrothermal methods. Knowing in detail the influence of all the parameters involved in these processes is imperative, in order to properly control the synthesis to achieve the desired final product. Thus, this paper presents a study of the influence of the physical parameters involved in the hydrothermal synthesis of $ZnSnO_3$ nanowires, namely volume, reaction time, and process temperature. Based on this study a growth mechanism for the complex Zn:Sn:O system is proposed. Two zinc precursors, zinc chloride and zinc acetate, were studied, showing that although the growth mechanism is inherent to the material itself, the chemical reactions for different conditions need to be considered.

2.2.2. Introduction

The multicomponent nature of ZTO makes the synthesis process quite challenging, given the different ionic sizes and diffusivity of the cations. Furthermore, each ZTO structure has different nucleation and growth times and requires a specific range of synthesis temperature.[65] For these reasons, a comprehensive study on the synthesis of ZTO nanostructures is needed. Studies on the influence of chemico-physical parameters on the hydrothermal synthesis of ZTO have been reported, showing the possibility to control the shape and type of the nanostructures and consequently the electrical, optical, and mechanical properties.[10,26,44] In section 2.1, we reported a thorough description of the influence of different hydrothermal synthesis' chemical parameters in the growth of ZTO nanostructures.[66] This work was conducted without employing any seed-layer; hence, the obtained structures depend exclusively on the chemico-physical parameters of the synthesis. Moreover, the obtained nanostructures are produced in form of powder, which in conjunction with a variety of transfer methods, allow for a higher degree of freedom for integration on different substrates,[45] without contamination from the seed-layer material.[46] In the last decade, the physical parameters of solution-based synthesis have also been studied showing that they have a large influence in the growth of the nanostructures. Zeng *et al.* reported the influence of temperature and time,[44] showing that in order to achieve Zn_2SnO_4 nanocrystals, a temperature of 200 °C and at least 20 h of reaction time are needed. Gou *et al.* studied the evolution of $ZnSnO_3$-orth nanoplates with the time and temperature of the synthesis, showing that producing these type of structures required 12 h at 260 °C, for that specific solution process.[8] These structures were applied to nanogenerators, in a composite with PDMS, resulting

in a piezoelectric coefficient (d_{33}) of 49 pC/N. This value is more than three times than the typically reported for ZnO nanostructures.[67]

In this section, the effect of the physical parameters on the hydrothermal synthesis of ZTO nanostructures, namely the influence of the volume of solution, temperature, and reaction time of the synthesis, is shown. In line with our previous work about the effect of the chemical conditions, this study is orientated towards the synthesis of ZTO nanowires, more specifically $ZnSnO_3$, which properties allow to envisage application on numerous next-generation nanoscale devices such as nanogenerators,[34,35,68] sensors,[31–33] photocatalysis,[30] solar cells,[37] resistive switching memories,[13,36] and transistors.[16,23] Moreover, we have previously shown that the structures synthetized using this hydrothermal method have properties that are similar to those produced by expensive and high-temperature methods,[66] thus, being promising materials for a new wave of multifunctional and low-cost devices.

2.2.3. Materials and Methods

Nanostructures' Synthesis

$ZnSnO_3$ nanowires were synthesized via hydrothermal method in a conventional oven, using the same methodologies and reagents reported previously by our group.[66] The most favorable chemical conditions to produce $ZnSnO_3$ nanowires previously obtained in [66] using tin (IV) chloride 5-hydrate ($SnCl_4 \cdot 5H_2O$) as tin precursor and both zinc chloride ($ZnCl_2$) and zinc acetate ($Zn(CH_3COO)_2$, ZnAc) as zinc precursors were maintained in this work. Briefly the ZTO hydrothermal synthesis was performed by dissolving the zinc (0.02 M/0.0657 g of ZnAc or 0.04 M/0.0818 g of $ZnCl_2$) and tin (0.02 M/0.1050 g) precursors separately in 7.5 mL of deionized water and then mixed together, 7.5 mL of the surfactant ethylenediamine (EDA) were then added and left stirring for 30 min, after which the mineralizer sodium hydroxide (NaOH, 0.24 M/0.1450 g) was added. The solution was then transferred into a 45 mL Teflon-lined stainless-steel autoclave (Parr Acid Digestion Bombs, no 4744, Moline, Ill., USA), and kept in an electric oven (Thermo Scientific, Waltham, Mass., EUA) varying the temperature and the reaction time, using a heating ramp of 200 °C/h. Aiming to study the influence of the physical parameters in the ZTO nanostructures growth, we varied the mixture volume (7.5 mL, 11 mL, and 15 mL), the synthesis temperature (150 °C, 180 °C, 200 °C, and 220 °C), and reaction time (2 h, 8 h, 12 h, 18 h, 24 h, 36 h, and 48 h). After the synthesis time, the autoclave was cooled to ambient temperature, naturally. The final product (white precipitate) comprising the nanostructures, was alternately washed with deionized water and isopropyl alcohol (at least 5 times) and centrifuged at 4000 rpm. After washed, the nanostructures were dried at 60 °C, in vacuum, for 2 h. As was previously reported,[66] the syntheses present a good reproducibility, especially when using $ZnCl_2$ due its better solubility in ethylenediamine.

Nanostructures' Characterization

The nanostructures were characterized following similar equipments/methodologies to the ones described in section 2.1.

2.2.4. Results and Discussion

Reaction Mixture Volume

A hydrothermal process is a method to produce single and polycrystalline structures, in aqueous solution at high temperature and high pressure. Both reaction mixture volume and temperature are determinant to the pressure inside the autoclave, consequently defining the growth of the nanocrystals. However, the phase transformation mechanism that occurs in polymorphs materials under high pressure is not completely controlled and understood.[69]

In order to study the influence of the pressure caused by the solution's volume in the $ZnSnO_3$ nanowires growth in this specific hydrothermal method, volumes of 7.5 mL, 11 mL, and 15 mL were tested, representing 17 %, 24 %, and 33 % of the autoclave volume, respectively. The temperature was fixed at 200 °C and the reaction time was 24 h.

In general, a mixture of ZnO nanowires, SnO_2 nanoparticles, and Zn_2SnO_4 nanostructures can be found in these syntheses, still with the increasing of the mixture volume mainly $ZnSnO_3$ nanowires are obtained. **Figure 2.24**a shows small differences in the XRD pattern for the different volumes when using the $ZnCl_2$ precursor. The most significant difference is the peak at 32 ° appearing for the volumes of 11 and 15 mL, attributed to ZnO phase. Raman analysis (**Figure 2.25**a) shows an intense peak at 437 cm^{-1}, characteristic of ZnO,[70] being this peak more intense for 11 mL, in agreement with the XRD data. The SEM images in **Figure 2.26** clearly show that less volume gives rise to smaller nanowires. As we previously identified in Reference [66], when a volume of 15 mL was used, these nanowires have the $ZnSnO_3$ orthorhombic perovskite phase, represented by the card 00-028-1486. Even if this card has been used before in several reports,[49,51–53] it was deleted from ICDD database due to matching peaks with the mixture of SnO_2 and Zn_2SnO_4. Although in 00-028-1486 card the peak with most intensity is at 26 °, this peak corresponds to the 012 plane, which is not the preferential orientation of the nanowires when measured in XRD. In order to confirm the $ZnSnO_3$ identification, we performed peak indexing in different samples, which always showed matching to an orthorhombic phase characteristic of $ZnSnO_3$ and not of Zn_2SnO_4 and SnO_2 mixture. EDS analysis confirms the 1:1 Zn:Sn ratio of the nanowires (**Figure 2.27**), reinforcing the hypothesis of the $ZnSnO_3$ phase. Nevertheless, Raman analysis suggests that both $ZnSnO_3$ and Zn_2SnO_4 should be present in the sample, given the characteristic peaks identified at 538 cm^{-1} and 676 cm^{-1}.[44]

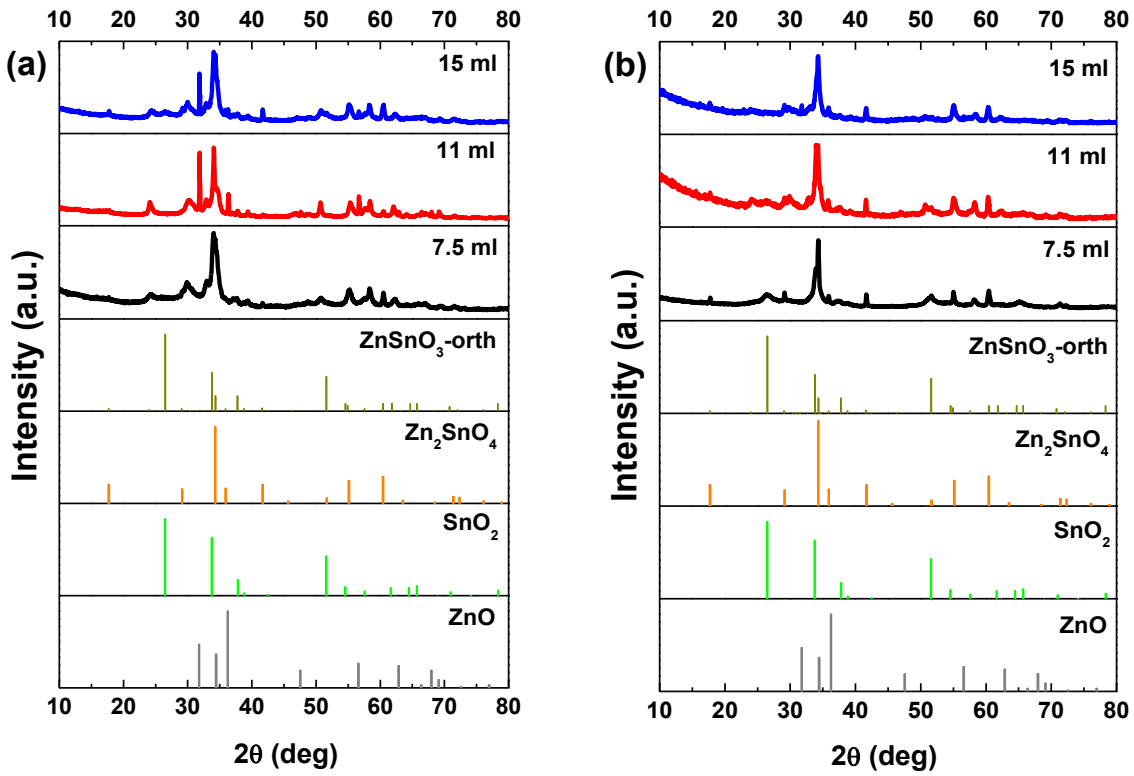

Figure 2.24. XRD patterns when using (**a**) $ZnCl_2$ precursor (with 2:1 Zn:Sn ratio) and (**b**) ZnAc precursor (with 1:1 Zn:Sn ratio), for different solution mixture volumes (7.5 mL, 11 mL, and 15 mL). Identification following ICDD card 00-028-1486 ($ZnSnO_3$-orth, deleted), 00-024-1470 (Zn_2SnO_4), 01-077-0452 (SnO_2), and 00-06-1451 (ZnO).

When ZnAc is used as the zinc source the presence of ZnO is partially or even completely suppressed. Similar to the results obtained using $ZnCl_2$, longer $ZnSnO_3$ nanowires are obtained for higher volumes of solution mixture. While for the lower volume (7.5 mL) Zn_2SnO_4 is the predominant phase, for 11 mL, $ZnSnO_3$ nanowires are predominant, although some Zn_2SnO_4 nanostructures are also observed (**Figure 2.28**) and ultimately for 15 mL, $ZnSnO_3$ nanowires are the predominant structures. SnO_2 can also be identified by XRD (**Figure 2.24**b), even if it is not clear by Raman (**Figure 2.25**b) for all the conditions. The presence of residual ZnO/SnO_2 for synthesis using the $ZnCl_2$/ZnAc precursors, is attributed to the Zn precursor's higher/lower solubility in ethylenediamine when compared to the $SnCl_4.5H_2O$, leading to an earlier availability of Zn/Sn species in the synthesis.[66]

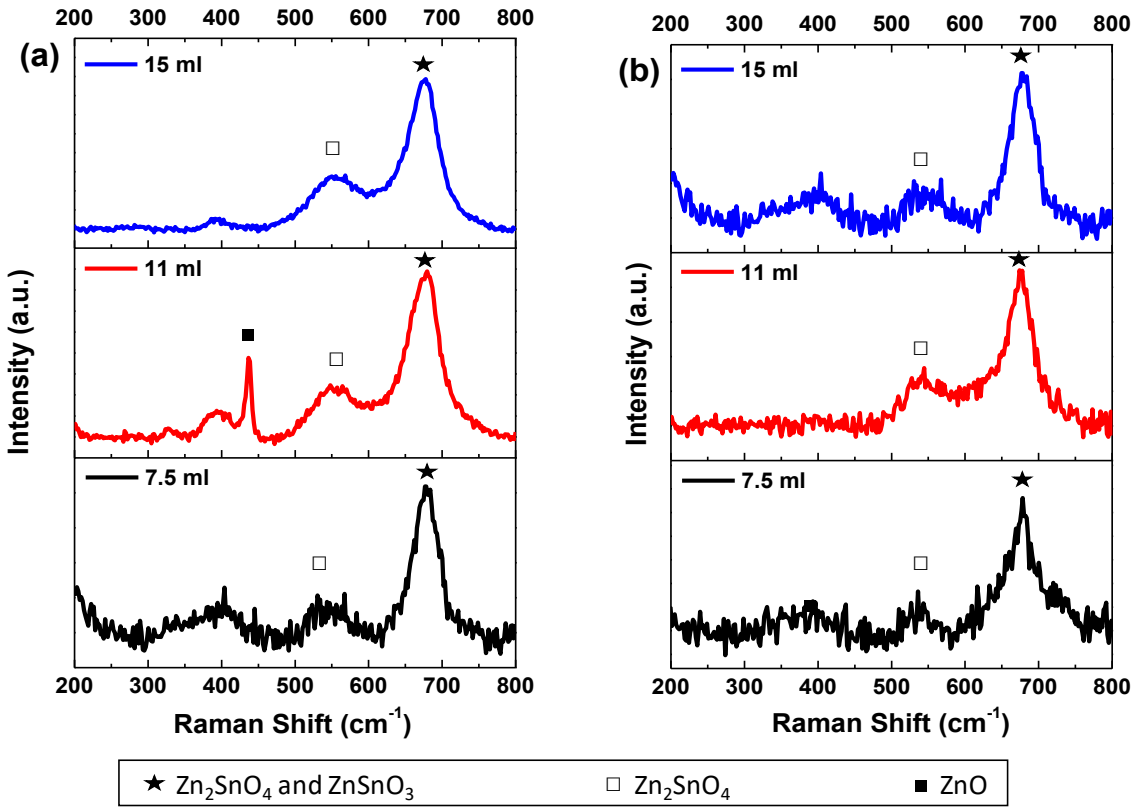

Figure 2.25. Raman shift of different reaction mixture volumes, 7.5 mL, 11 mL and 15 mL, using (a) $ZnCl_2$ (Zn:Sn molar ratio of 2:1) and (b) ZnAc (Zn:Sn molar ratio of 1:1) as zinc precursor, at 200 °C, for 24 h. Where: vibrational band at 631 cm^{-1} is associated with the expansion and contraction of the Sn−O bond peak, peaks at 538 and 676 cm^{-1} correspond to internal vibrations of the oxygen tetrahedron in Zn_2SnO_4 and to characteristic Raman M−O bonds stretching vibration mode in the MO_6 octahedron of $ZnSnO_3$ and/or Zn_2SnO_4, respectively; and peaks at 437 cm^{-1} and 574 cm^{-1} are attributed to vibrational modes of ZnO.[44,50,70]

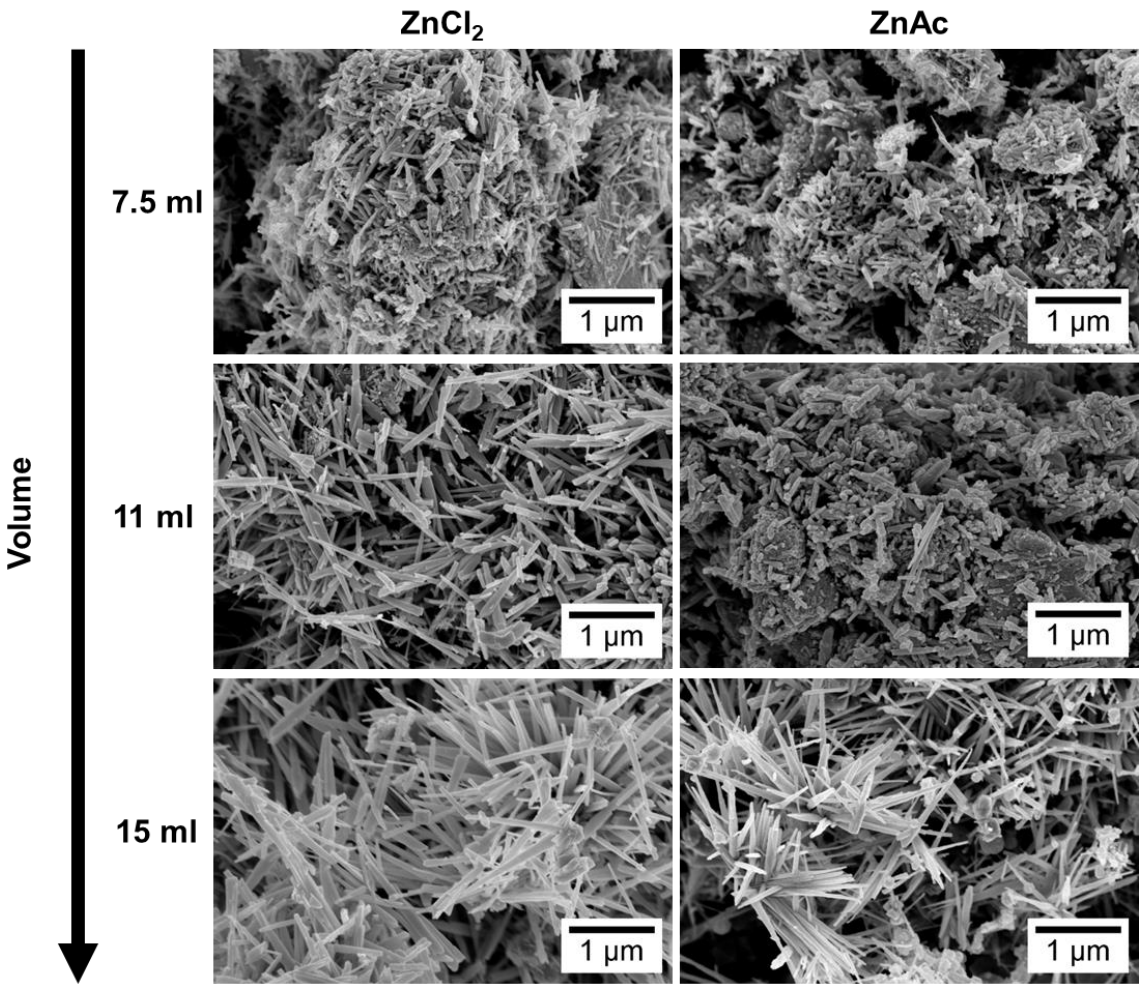

Figure 2.26. SEM images of nanostructures obtained for different reaction mixture volumes, 7.5 mL, 11 mL, and 15 mL, using $ZnCl_2$ and ZnAc as zinc precursor.

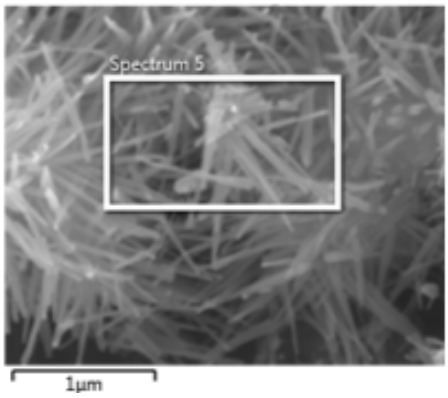

Element	Atomic concentration (%)
Zn	15
Sn	17
O	68

Figure 2.27. SEM image and EDS element quantification of $ZnSnO_3$ nanowires produced by synthesis using $ZnCl_2$, a Zn:Sn molar ratio of 2:1, a volume 15 mL at 200 °C for 24 h. This analysis shows Zn:Sn ratio of 1:1, supporting identification of the $ZnSnO_3$ phase. The higher than expected atomic concentration of oxygen can be attributed to the carbon tape.

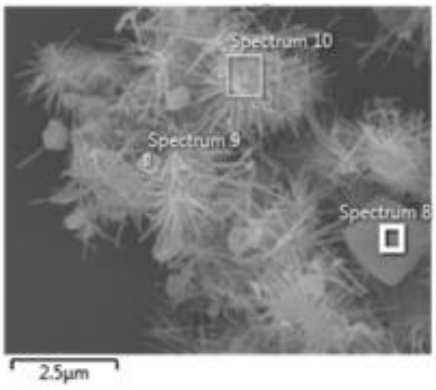

Element	Atomic concentration (%)
Zn	29
Sn	14
O	57

Figure 2.28. SEM image and EDS element quantification of isolated Zn_2SnO_4 nanostructures produced by synthesis using ZnAc, a Zn:Sn molar ratio of 1:1 using a volume of 11 m L at 200 °C for 24 h.

Nakayama *et al.* reported a theoretical study where the relation between the enthalpy and pressure for the system Zn–Sn–O was investigated.[71] They showed that the global energy minimum corresponds to the mixed phases Zn_2SnO_4 and SnO_2. Our experimental results are in agreement with this study, as for lower volume and consequently lower pressure, the formation of Zn_2SnO_4 and SnO_2 nanoparticles is favored, although mixed with $ZnSnO_3$ nanowires. Moreover, in 2010 Gou *et al.* also reported a theoretical study about the $ZnSnO_3$ phase transition under pressure.[69] According to the authors the $ZnSnO_3$ synthesis at low-temperature (<700 °C) is unfavorable, leading to a mixture of phases, mainly due to its positive formation enthalpies. This decomposition has also been reported to occur at temperature above 500 °C.[10,50] Taking into account the temperature used in this study (200 °C), our results are in fair agreement with this, since with decreasing volume, and consequently pressure, the trend is to achieve higher mixture of phases while the more homogeneous $ZnSnO_3$ nanowires are obtained when using the higher solution volume, 15 mL. The high pressure inside the autoclave, characteristic of a hydrothermal method, supplies high energy levels to the reaction, leading to an acceleration of the nucleation processes at even lower temperatures. For the reasons explained, 15 mL was the volume used for both precursors for the next studies presented here.

Synthesis Temperature

To understand the growth mechanisms of ZTO nanostructures, one needs to have in mind the chemical reaction processes. Based on different reports, the $ZnSnO_3$ nanostructures formation follows the equations (1)-(5) presented in section 2.1.[8,48,49]

$ZnSnO_3$ can have the fcc or the orthorhombic structures, and these two different structures present different heat of formation and total energies. Gou *et al.* presented these values for the different possible structures of $ZnSnO_3$.[69] On the other hand, it is already well-known that the $ZnSnO_3$ phase is metastable and according, for example, to the study reported by Bora *et al.* this

phase suffers a decomposition into the thermodynamically stable phases Zn_2SnO_4 and SnO_2 at temperatures higher than 500 °C.[10,11,50] This decomposition can be represented by the following equation:

$$2ZnSnO_3 \rightarrow Zn_2SnO_4 + SnO_2. \quad (10)$$

However, it is clear that above atmospheric pressure, as in the case of the hydrothermal method, and depending of the reaction mixture, the temperature at which the decomposition occurs can change.

In order to investigate the effect of temperature in the specific conditions of our syntheses, four different temperatures were used: 150 °C, 180 °C, 200 °C, and 220 °C, while maintaining all the other conditions and keeping the volume of the solution mixture at 15 mL.

SEM images, in **Figure 2.29**, show that at 150 °C, mainly nanoparticles are obtained. In the XRD pattern (**Figure 2.30**) a mixture of phases ($ZnSn(OH)_6$ and Zn_2SnO_4 and/or $ZnSnO_3$) can be observed using $ZnCl_2$, while when using ZnAc, only Zn_2SnO_4 is identified. Raman analysis (**Figure 2.31**) is in agreement with these results, showing the peak at 603 cm^{-1}, characteristic of $ZnSn(OH)_6$ (only for $ZnCl_2$) and the characteristics peaks of ZTO for both Zn sources (538 cm^{-1} and 676 cm^{-1}). It is important to refer that the 603 cm^{-1} vibrational band is not only a characteristic peak of $ZnSn(OH)_6$, but also of fcc-$ZnSnO_3$ that could also be present in these samples.[50] However, FTIR analysis supports the $ZnSn(OH)_6$ hypothesis by showing OH^- groups for wavenumbers above 3000 cm^{-1} (**Figure 2.32**a), corresponding to $ZnSn(OH)_6$. In EDS analysis, shown in **Figure 2.33**, it can be seen that the nanoparticles obtained using ZnAc have the Zn:Sn ratio of 2:1 corresponding to the Zn_2SnO_4 phase.

Increasing the temperature to 180 °C, some nanowires can be viewed in SEM when using the $ZnCl_2$ precursor (**Figure 2.29**), which can be $ZnSnO_3$ according to the XRD (**Figure 2.30**a). Still, at this temperature, OH^- groups are very evident from the FTIR analysis (**Figure 2.32**a) for both zinc precursors, with XRD showing predominantly the $ZnSn(OH)_6$ phase, an intermediate stage of the $ZnSnO_3$ formation. Zeng *et al.* also showed that for temperatures lower than 200 °C $ZnSn(OH)_6$ is the predominant phase.[44] Nevertheless, XRD also shows that other phases are present (**Figure 2.30**). In fact, EDS (**Figure 2.34**) and Raman (**Figure 2.31**) confirm this by showing a reasonable amount of Zn_2SnO_4 octahedrons, especially when using ZnAc as precursor. It means that, as already discussed, at these lower temperatures, and consequently lower pressures, the formation of the thermodynamically more stable Zn_2SnO_4 nanoparticles is promoted. The lower solubility of ZnAc in ethylenediamine, when compared to $ZnCl_2$, can explain why a higher mixture of phases is seen for this case.

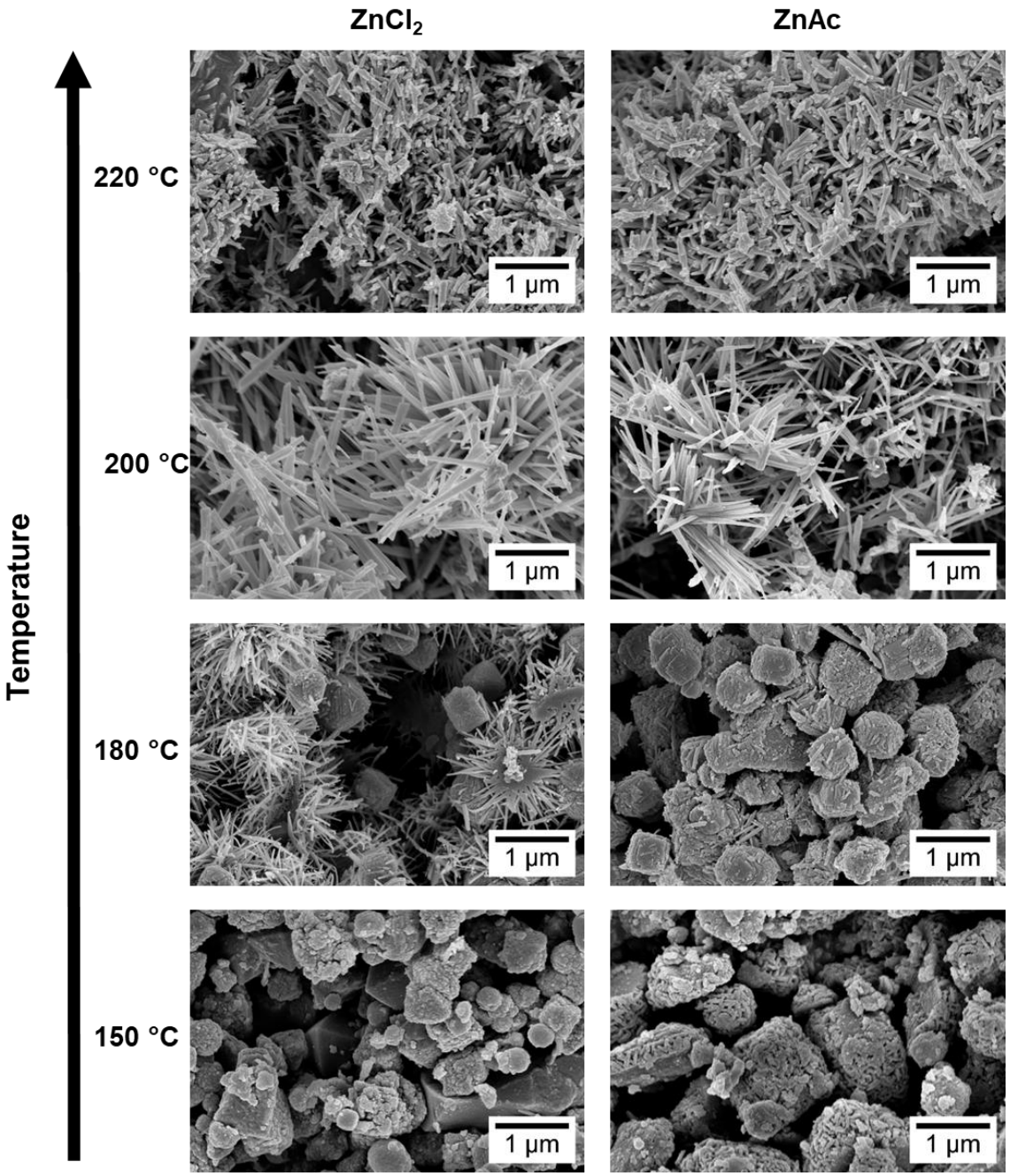

Figure 2.29. SEM images of the nanostructures obtained using the previous best conditions (15 mL) for each zinc precursor ($ZnCl_2$ and ZnAc) at different temperatures: 150 °C, 180 °C, 200 °C and 220 °C.

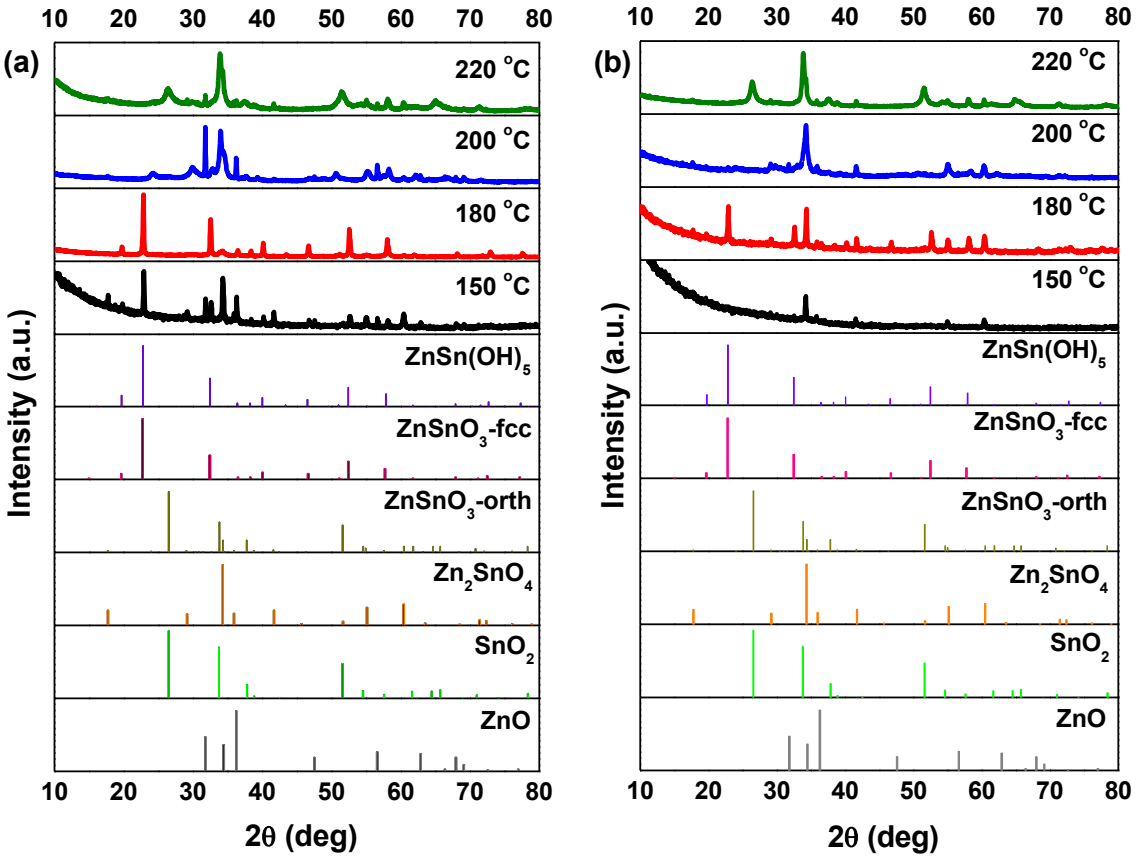

Figure 2.30. XRD patterns when using (**a**) $ZnCl_2$ precursor (with 2:1 Zn:Sn ratio) and (**b**) ZnAc precursor (with 1:1 Zn:Sn ratio), at different temperatures: 150 °C, 180 °C, 200 °C, and 220 °C. Identification following ICDD card 00-028-1486 ($ZnSnO_3$-orth—deleted), 00-011-0274 ($ZnSnO_3$-fcc), 00-024-1470 (Zn_2SnO_4), 01-077-0452 (SnO_2), and 00-06-1451 (ZnO).

The samples at 200 °C were already described in the previous section and result mainly in $ZnSnO_3$ nanowires. For this temperature, as seen in **Figure 2.32**, FTIR analysis confirms that no OH^- groups are present, meaning that the intermediate phase $ZnSn(OH)_6$ is no longer obtained at this temperature. It should be added that FTIR also shows that all the reagents were completely consumed.

Increasing the temperature to 220 °C leads to the formation of SnO_2 and Zn_2SnO_4 phases, even if the $ZnSnO_3$ nanowires are still predominant. While it is not evident in the XRD pattern, through Raman analysis (**Figure 2.31**) their presence is clear since it is possible to observe the 631 cm^{-1} and 538 cm^{-1} peaks, characteristic of Sn–O and M–O tetrahedrons bonds, respectively. This result is attributed to the decomposition of $ZnSnO_3$ into SnO_2 and Zn_2SnO_4, due to its metastability. This decomposition has been reported to occur at temperatures above 500 °C.[10,50,69] In the present study, this decomposition occurs at lower temperature due to the high energy levels inherent to the hydrothermal process (high temperature and pressure).

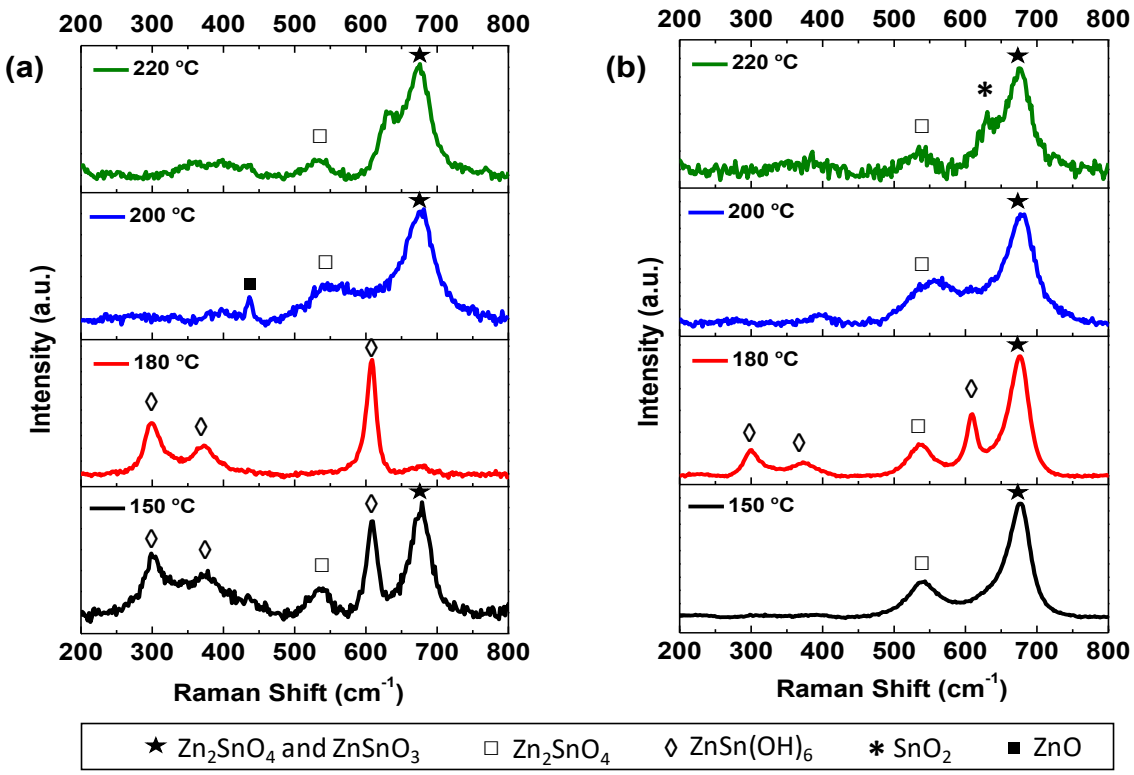

Figure 2.31. Raman shift for syntheses using (a) $ZnCl_2$ (Zn:Sn molar ratio of 2:1) and (b) ZnAc (Zn:Sn molar ratio of 1:1) as zinc precursor, with a volume of 15 mL, for 24 h at different temperatures: 150 °C, 180 °C, 200 °C and 220 °C. Where: vibrational band at 631 cm^{-1} is associated with the expansion and contraction of the Sn−O bond peak, peaks at 538 cm^{-1} and 676 cm^{-1} are corresponding to internal vibrations of the oxygen tetrahedron in Zn_2SnO_4 and to characteristic Raman M−O bonds stretching vibration mode in the MO_6 octahedron of $ZnSnO_3$ and/or Zn_2SnO_4, respectively; and the peak at 437 cm^{-1} is attributed to vibrational mode of ZnO. The peaks at 299, 372, and 603 cm^{-1} correspond to $ZnSn(OH)_6$, from the breathing vibrations of long M–OH bonds and M–OH–M (bridging OH group) bending modes.[27,44,50,70]

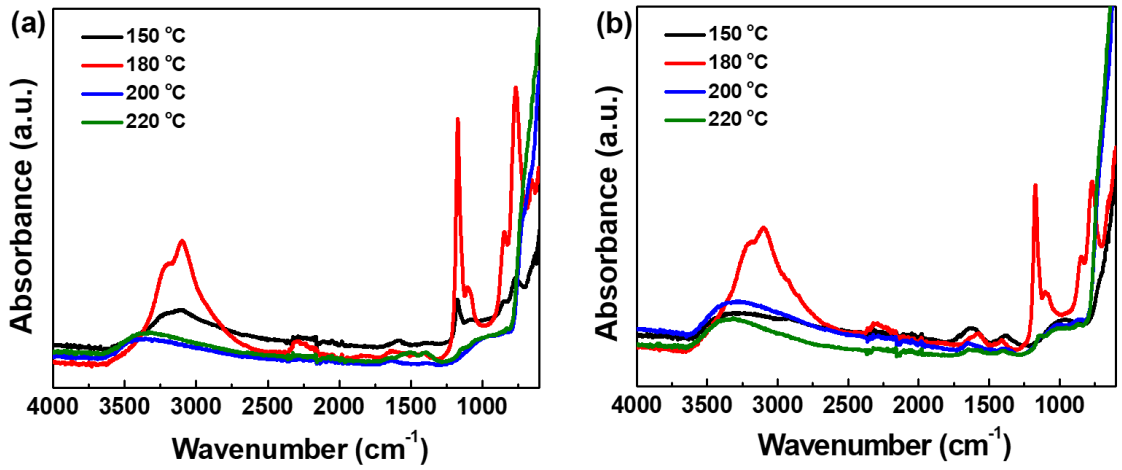

Figure 2.32. FTIR spectra of the obtained nanostructures using (a) $ZnCl_2$ and (b) ZnAc, at different temperatures (150 °C, 180 °C, 200 °C and 220 °C).

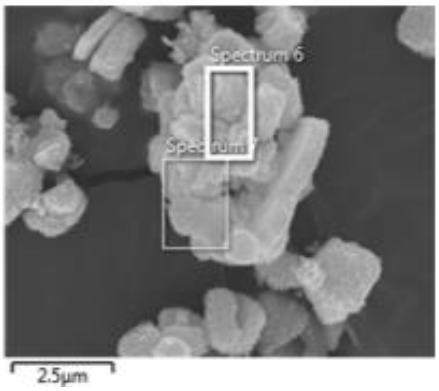

Element	Atomic concentration (%)
Zn	21
Sn	13
O	66

Figure 2.33. SEM image and EDS element quantification of isolated Zn_2SnO_4 nanostructures produced by synthesis using ZnAc, Zn:Sn molar ratio of 1:1 and a volume of 15 mL at 150 °C for 24 h.

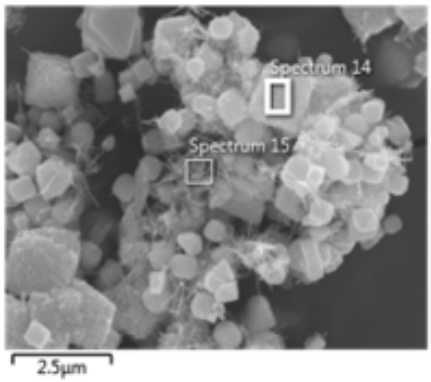

Element	Atomic concentration (%)
Zn	26
Sn	11
O	63

Figure 2.34. SEM image and EDS element quantification of isolated Zn_2SnO_4 octahedrons produced by synthesis using ZnAc and Zn:Sn molar ratio of 1:1 and a volume of 15 mL at 180 °C for 24 h.

In conclusion, it is clear that for temperatures lower than 200 °C, homogeneous nanowires are not produced as, in accordance to what was observed in the previous section, for lower available energy, the formation of $ZnSnO_3$ is not feasible, and instead the more stable phase Zn_2SnO_4 is favored (along with the intermediate phase $ZnSn(OH)_6$). Meanwhile, for temperatures around 200 °C, almost only $ZnSnO_3$ nanowires are produced. For higher temperatures (220 °C), no improvements are observed in terms of producing only nanowires, as decomposition of those into the more stable phases start to occur. This study shows that the temperature to achieve the desired structures must be carefully considered, as it should be high enough to allow the formation of the metastable phase, but not too high to promote the decomposition process.

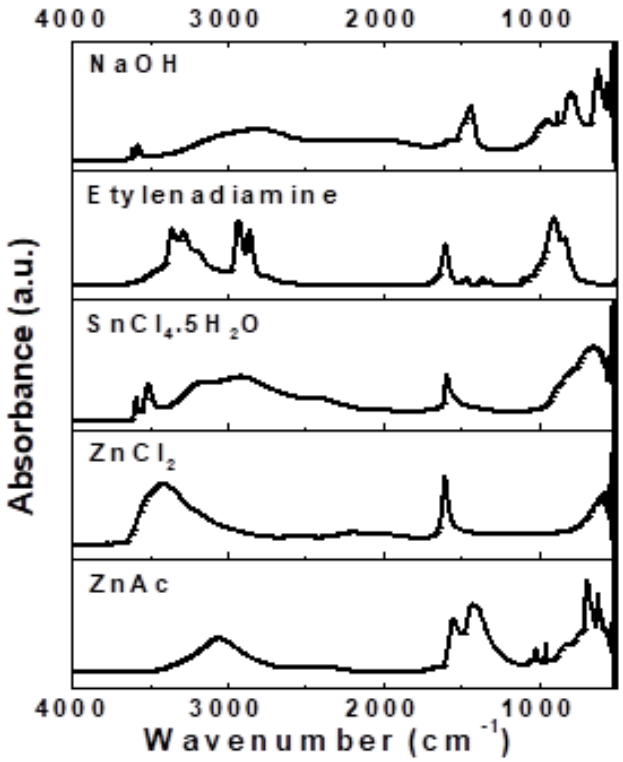

Figure 2.35. FTIR spectra of all reagents used in the syntheses: the zinc and tin precursors ($ZnCl_2$, $Zn(CH_3COO)_2$ and $SnCl_4{\cdot}5H_2O$), the mineralizer (NaOH) and the surfactant (ethylenediamine).

Reaction Time

Throughout the reaction time of the synthesis, the ZTO nanostructures undergo a complex evolution. Thus, a careful investigation on the evolution of ZTO morphology and crystallinity was performed for different reaction times (2 h, 8 h, 12 h, 18 h, 24 h, 36 h, and 48 h), for both zinc precursors ($ZnCl_2$ and ZnAc) and using the most favorable conditions as defined in the previous sections (15 mL of volume at 200 °C).

Similar to what was observed with the study of the effect of the temperature, $ZnSn(OH)_6$ appears as an intermediate phase before the formation of the $ZnSnO_3$ or the Zn_2SnO_4 phases (represented by Equations (1), (2), (3), and (4)).

In **Figure 2.36** the XRD patterns for the structures from synthesis with different reaction times are shown. For 2 h of synthesis, $ZnSn(OH)_6$ can be identified, for both zinc precursors. As already mentioned, this phase can be mistaken with fcc-$ZnSnO_3$ in XRD pattern and also in Raman analysis (**Figure 2.37**) where an intense peak at 603 cm^{-1} is evident. Nonetheless, FTIR analysis in **Figure 2.38** clarifies this by showing the presence of OH^- groups, confirming the presence of $ZnSn(OH)_6$. Although $ZnSn(OH)_6$ phase is predominant for both Zn sources, when using ZnAc, it

is also possible to identify Zn_2SnO_4 by XRD, and when using $ZnCl_2$, Raman analysis indicates $ZnSnO_3$ and/or Zn_2SnO_4 may be present.

When using $ZnCl_2$, the $ZnSn(OH)_6$ phase appears for synthesis of 2 h, while for synthesis of 8 h or longer, neither OH^- groups (from the intermediate phase $ZnSn(OH)_6$) nor leftover precursors are observed in FTIR spectra (**Figure 2.38**), unlike when using ZnAc, where these are present up to 8 h of synthesis. For 8 h of synthesis, while the nanoparticles are still predominant, some orthorhombic $ZnSnO_3$ nanowires start to be present and, from this reaction time onwards, these nanowires are the predominant structure achieved, with both precursors (**Figure 2.39**).

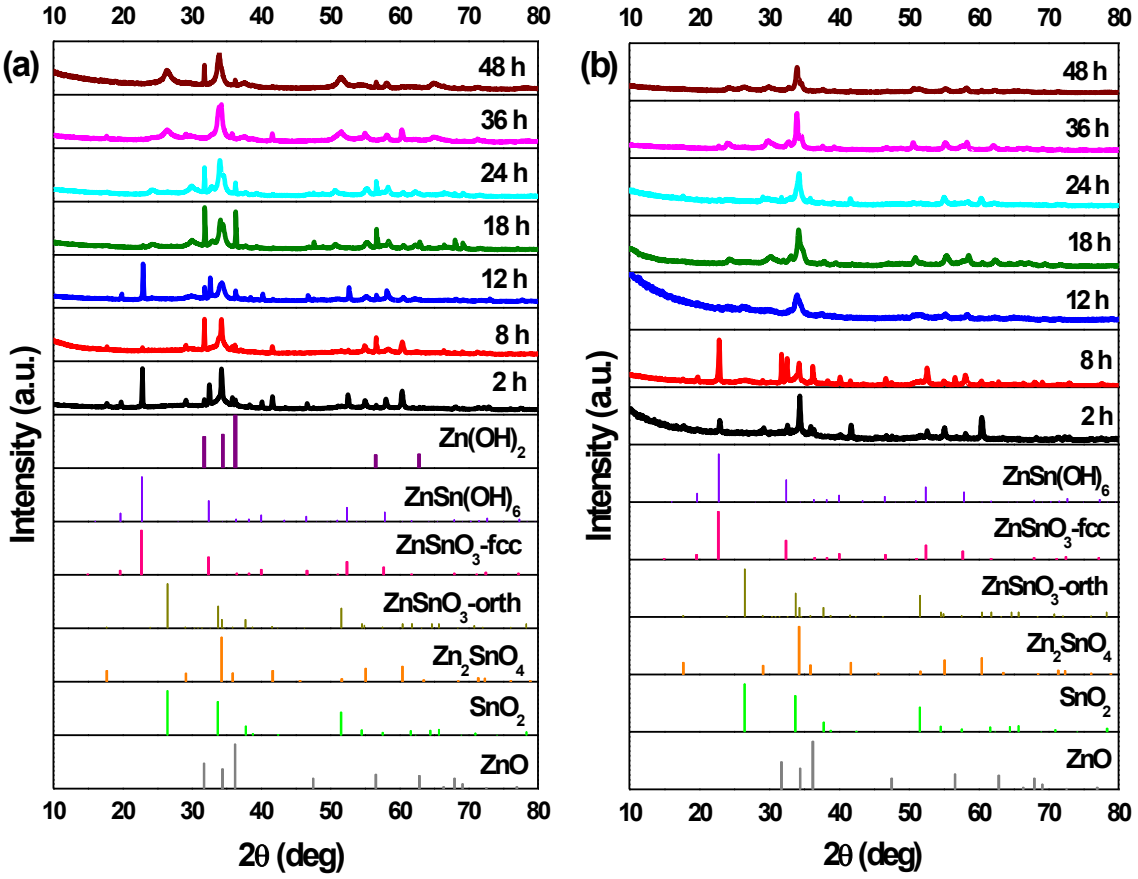

Figure 2.36. XRD patterns when using (**a**) $ZnCl_2$ precursor (with 2:1 Zn:Sn ratio) and (**b**) ZnAc precursor (with 1:1 Zn:Sn ratio), for different reaction time: 2 h, 8 h, 12 h, 18 h, 24 h, 36 h, and 48 h. Syntheses at 200 °C, using 15 mL of reaction mixture volume. Identification following ICDD cards: 00-028-1486 ($ZnSnO_3$-orth—deleted), 00-011-0274 ($ZnSnO_3$-fcc), 00-024-1470 (Zn_2SnO_4), 01-077-0452 (SnO_2), 00-06-1451 (ZnO), and 00-048-1066 ($Zn(OH)_2$).

Regarding the use of the $ZnCl_2$, a particular case is observed for the 12 h long synthesis. In this condition, $ZnSnO_3$-fcc also seems to be obtained, mixed with $ZnSnO_3$-orth. The possibility to obtain this type of structures for lower energies was already demonstrated as it is an intermediate phase between $ZnSn(OH)_6$ and $ZnSnO_3$-orth.[69] Also, it is relevant to consider the possibility of formation of $Zn(OH)_2$ due to the presence of $Zn(OH)_4^{2+}$, which is an intermediate phase of formation of both Zn_2SnO_4 and ZnO. In XRD, the phase $Zn(OH)_2$ (that is transformed in $Zn(OH)_4^{2+}$) can be mistaken with hexagonal phase ZnO. Also, in EDS mapping (shown in **Figure 2.40**), it is possible to observe some nanoparticles with a large Zn signal, that can be attributed either to

$Zn(OH)_2$ or to Zn_2SnO_4. As such, the possibility of having $Zn(OH)_2$ cannot be discarded. This emphasizes the difficulty of obtaining only one phase and one type of ZTO nanostructure using a solution-based method and the demand for a well-controlled synthesis process.

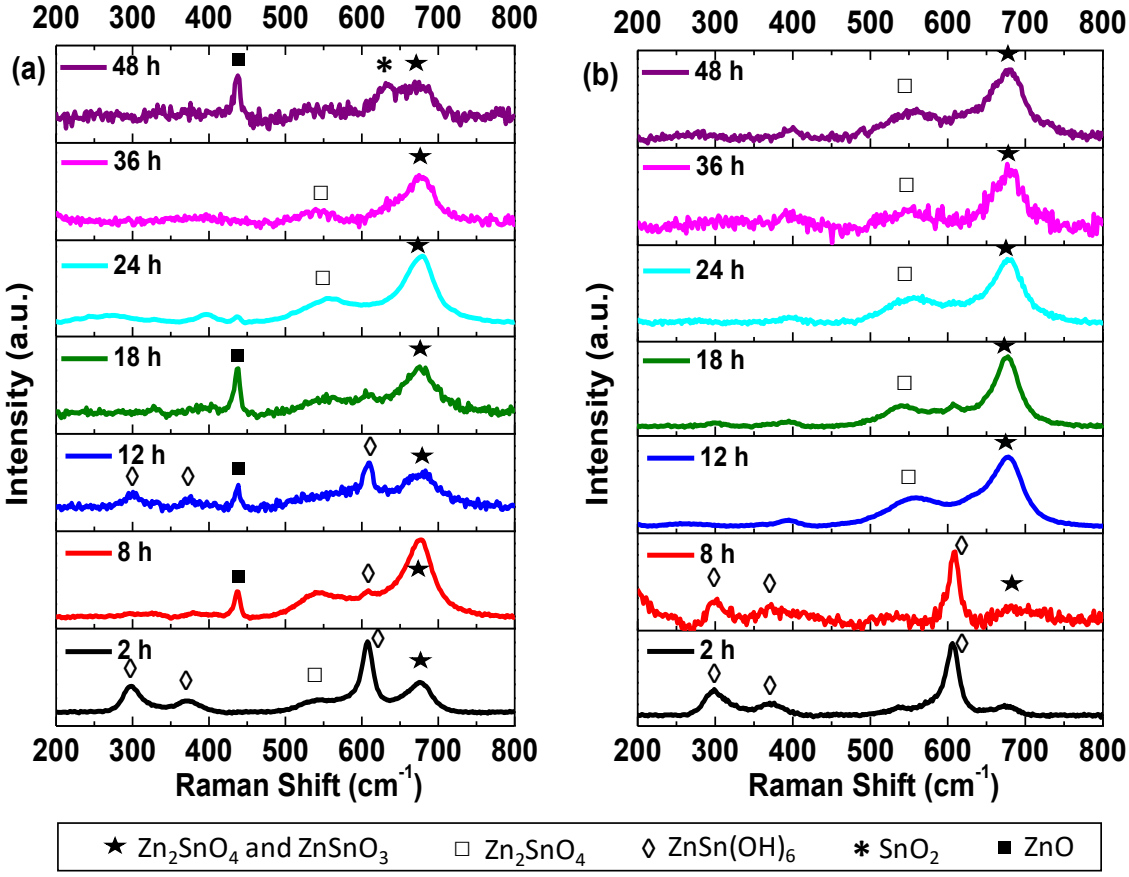

Figure 2.37. Raman shift for synthesis with different reaction times using as zinc precursor: (a) $ZnCl_2$ (Zn:Sn molar ratio of 2:1) and (b) ZnAc (Zn:Sn molar ratio of 1:1), with a volume of 15 mL, at 200 °C. Where: vibrational band at 631 cm^{-1} is associated with the expansion and contraction of the Sn−O bond, peaks at 538 cm^{-1} and 676 cm^{-1} correspond to internal vibrations of the oxygen tetrahedron in Zn_2SnO_4 and to characteristic Raman M−O bonds stretching vibration mode in the MO_6 octahedron of $ZnSnO_3$ and/or Zn_2SnO_4, respectively; and the peak at 437 cm^{-1} is attributed to vibrational mode of ZnO. The peaks at 299, 372, and 603 cm^{-1} correspond to $ZnSn(OH)_6$, from breathing vibrations of the long M–OH bonds and M–OH–M (bridging OH group) bending modes. [27,44,50,70]

In the case of using the ZnAc precursor, for synthesis of 12 h or longer, the XRD pattern (**Figure 2.36**a) seems to be similar (evidencing $ZnSnO_3$ nanowires) with a higher crystallinity for the longer synthesis when compared to 12 h. SEM images (**Figure 2.39**) show that longer nanowires are obtained for 36 h or 48 h long synthesis. **Table 2.4** shows the lengths of the nanowires for both precursors, emphasizing this observation. On the other hand, when using $ZnCl_2$, while nanowires' lengths increase up to around 18 h or 24 h, these start to significantly decrease for longer synthesis (**Figure 2.39**, **Table 2.4**). It can be observed through XRD data (**Figure 2.36**) that when synthesis is 36 h or longer, $ZnSnO_3$ phase transformation into Zn_2SnO_4

and SnO_2 starts to occur, in a similar trend to that seen in the previous section for the increase of temperature beyond 200 ºC, causing the diminishing of the nanowires' length.

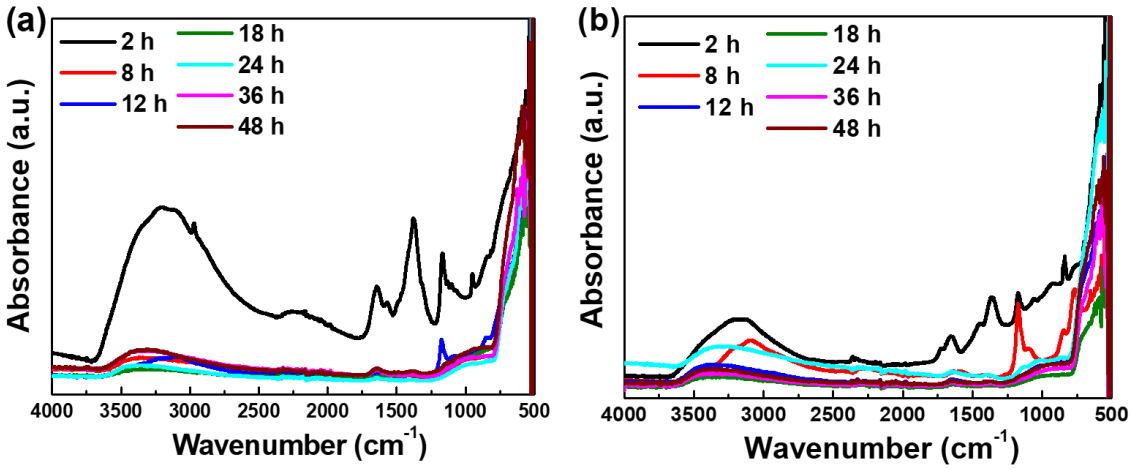

Figure 2.38. FTIR spectrum of samples with different reaction times for (a) $ZnCl_2$ and (b) ZnAc.

It can be induced that, due to the $ZnCl_2$'s higher solubility in ethylenediamine, the evolution of the phases happens faster when this precursor is used. While for $ZnCl_2$, a phase transformation of $ZnSnO_3$ to Zn_2SnO_4 and SnO_2 starts to occur at 36 h, for ZnAc, a pronounced length increase is still observed up to 36 h, supporting the assumption that a slower reaction is taking place when using ZnAc precursor. While this results in an increased synthesis time to achieve longer nanowires, these are significantly longer (more than 2x) than when using $ZnCl_2$. Nevertheless, for 48 h, there is a small deterioration in terms of nanowire length and homogeneity of the nanostructures' phases, thus 36 h is the optimal reaction time for the conditions studied.

In summary, in **Figure 2.39**, one can clearly visualize the large dependency of the nanostructures' growth with the increase of reaction time. For both precursors, it is clear that at least 12 h are necessary to start producing predominantly $ZnSnO_3$ nanowires, being that only after 24 h this production starts being homogeneous. It is also possible to observe that, similarly to what was concluded with previous studies on the influence of the chemical parameters [66], the ZTO nanostructures obtained using ZnAc are generally smaller than those obtained using $ZnCl_2$, for synthesis up to 24 h. When using ZnAc, the ZTO growth is slower so the higher dimensions are obtained for longer reaction times (36 h and 48 h), for which the nanowires reach higher dimensions than that those obtained with $ZnCl_2$. This difference in the optimal reaction time can be attributed to the lower solubility of ZnAc when compared with $ZnCl_2$ in the solvent ethylenediamine. This also leads to a constant presence of SnO_2 for the syntheses with ZnAc, while when using $ZnCl_2$, ZnO is constantly observed. This study shows that if longer nanowires are desired, ZnAc is the most suitable precursor, while if faster processing is desired, the most suitable precursor is $ZnCl_2$.

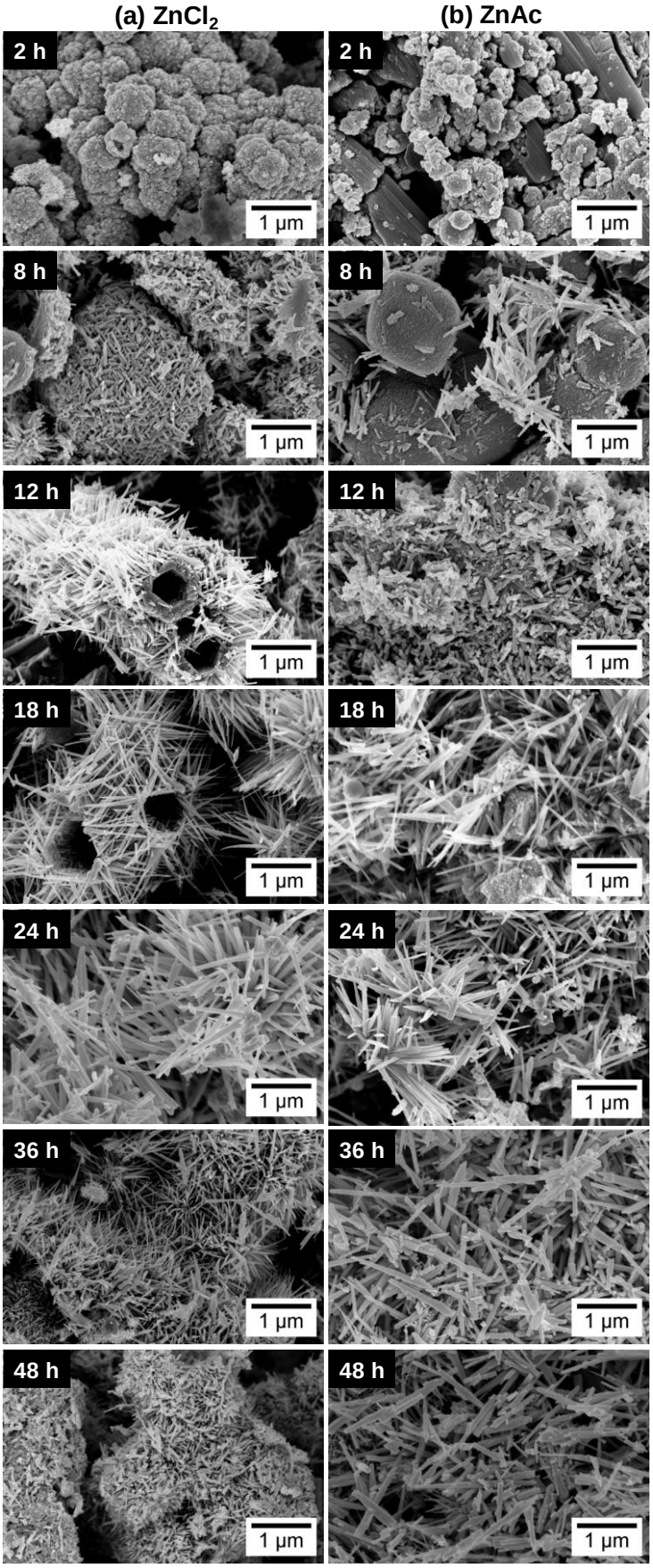

Figure 2.39. SEM images of the nanostructures obtained by synthesis using (a) $ZnCl_2$ and (b) ZnAc with different reaction time, showing the temporal evolution of the structures produced. Syntheses at 200 °C, using 15 mL of reaction mixture volume.

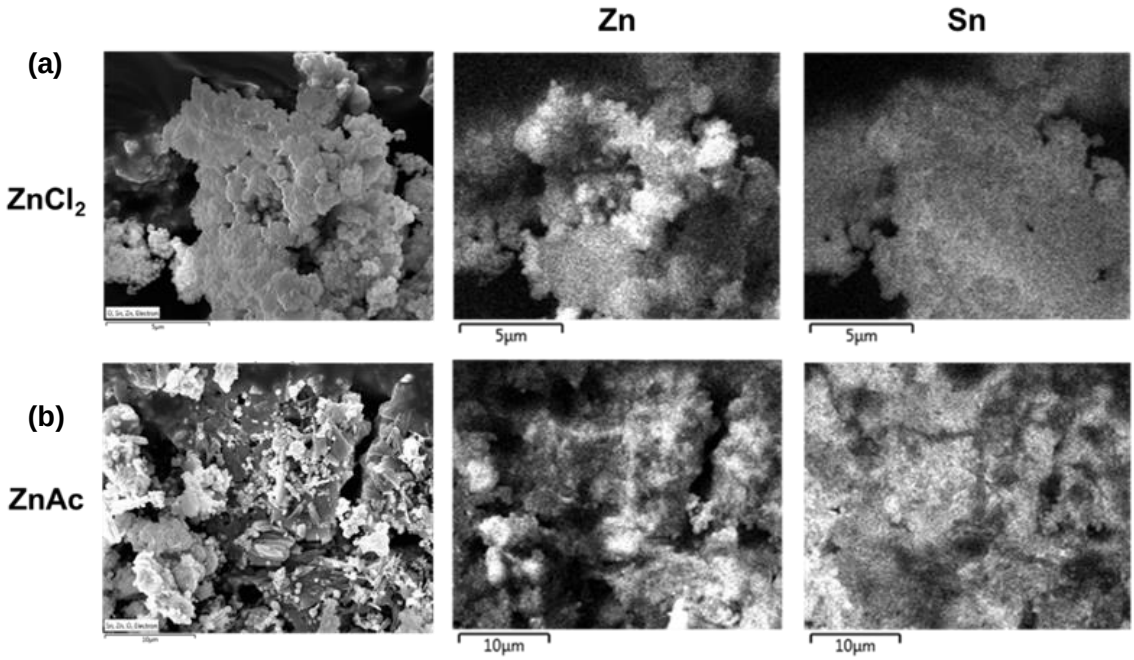

Figure 2.40. SEM image and EDS element mapping of nanostructures produced by synthesis using (a) $ZnCl_2$ (Zn:Sn molar ratio of 2:1) and (b) ZnAc (Zn:Sn molar ratio of 1:1), both at 200 °C for 2 h and a volume of 15 mL.

Table 2.4. Evolution of the average of nanowires' length with the reaction time.

Reaction time (h)	***Nanowires' length (nm)***	
	$ZnCl_2$	**ZnAc**
24	605 ± 75	540 ± 175
36	420 ± 115	1090 ± 250
48	220 ± 35	950 ± 190

Growth Mechanism of $ZnSnO_3$ Nanowires

Throughout the reaction time one of the main challenges in nanomaterials synthesis is to understand how the nanostructures grow, i.e., what are the mechanisms behind the formation of each phase and of each type of nanostructures. Obtaining only one phase and one shape is not an easy task, particularly for the Zn:Sn:O system due to its ternary composition, as evident throughout this manuscript. In the specific case of $ZnSnO_3$ nanowires formation, the metastability of this phase adds even more complexity into understanding it properly. Gou *et al.* showed the influence of pressure and temperature in the enthalpy energy of different ZTO phases, including $ZnSnO_3$ cubic perovskite, concluding that the formation of this phase is not favorable under

ambient conditions and can only be obtained under high pressure and temperature.[69] However, under those conditions, this phase tends to decompose into Zn_2SnO_4 and SnO_2.[73] Therefore, a very specific tailoring of the synthesis parameters is necessary when aiming to achieve proper structures of this metastable phase.

Owing to the careful optimization of the chemico-physical parameters performed here, it is possible to observe an evolution of the nanostructures, and its respective phase, with the increase of reaction time and increase of total energy available in the reaction. Although the aim was to achieve $ZnSnO_3$ nanowires, Zn_2SnO_4 nanostructures were also obtained, mainly for very short synthesis or for synthesis with lower temperatures or volumes, showing that this phase is achieved with lower available energy.

2.2.5. Conclusions

Due to its complexity, the synthesis of multicomponent oxide nanostructures requires an appropriate understanding of the influence of each synthesis' parameters and the growth mechanism itself. In this work, a detailed study on the influence of physical parameters on the hydrothermal synthesis of $ZnSnO_3$ nanowires is reported. Specifically, the effect of reaction mixture volume, synthesis temperature and reaction time were studied. The available energy in the reaction revealed to be one of the determinant factors on the final products. As already reported in the literature, the metastable $ZnSnO_3$ requires high pressures/energy conditions to be obtained. It was found that independently of the Zn source, ZTO nanostructures had the same time-dependence growth mechanisms, although with different time spans.

While previous reports have shown the degradation of the metastable $ZnSnO_3$ structures at temperatures above 500 °C, the present work demonstrates that owing to the high energy of the hydrothermal process, this decomposition can occur at considerably lower temperatures (24 h at 220 °C) and/or longer reaction times (36 h at 200 °C). This highlights the advantages of hydrothermal processes to obtain metastable multicomponent nanostructures such as $ZnSnO_3$ at low temperatures but also the importance of properly controlling and understanding all the synthesis parameters to achieve the desired structures. With $ZnSnO_3$ finding application as a piezoelectric material, catalyst, active material in gas sensors, resistive switching memories, batteries, and others, we expected this work to have a significant impact in the future of nanotechnology as it describes the synthesis of $ZnSnO_3$ nanowires without either direct growth in substrates or production by vapor phase methods (high temperatures). This new approach brings higher flexibility to the different applications, allowing a higher degree of freedom for integration on different substrates while avoiding contamination from the seed-layer material.

2.3. Reproducibility of the $ZnSnO_3$ nanowires synthesis

From the studies of the influence of chemical and physical parameters in the nanostructures' growth, a condition was selected for each zinc precursor in order to obtain $ZnSnO_3$ nanowires: Zn:Sn molar ratio of 1:1 for ZnAc and 2:1 for $ZnCl_2$, H_2O:EDA volume ratio of 7.5:7.5 mL and 0.240 M of NaOH. As both these syntheses result in a yield of ≈ 30 mg for the overall synthesis process, they present reagent to precursor mass ratio efficiencies of ≈ 40 % and ≈ 50 % using $ZnCl_2$ and ZnAc, respectively, when considering the effective mass of zinc and tin species only. For comparing the two precursors conditions in terms of reproducibility, syntheses in these conditions were repeated at least three times.

The results showed a better reproducibility for $ZnCl_2$ than for the ZnAc precursor as discussed next. **Figure 2.41**a shows that for three syntheses in the same conditions using $ZnCl_2$ the results are very similar, showing only some differences in the presence of some residual ZnO nanowires (confirmed by XRD spectra, in **Figure 2.42**b) and some variation in the average size of the $ZnSnO_3$ nanowires (**Figure 2.43**b). On the other hand, for the synthesis with ZnAc, three runs already show a quite significant variation on the XRD spectra (**Figure 2.42**a), even if all show the predominance of the $ZnSnO_3$ phase (see also SEM images in **Figure 2.41**b). Furthermore, the size of the obtained nanowires differs substantially for the multiple runs with ZnAc (**Figure 2.43**a). As discussed previously, ZnAc has a poor solubility in EDA when compared with $ZnCl_2$ and $SnCl_4 \cdot 5H_2O$. This can be one of the factors for the poor reproducibility when using ZnAc as zinc precursor. Moreover, when using $ZnCl_2$, since tin precursor is also a chloride, the reaction will be less complex: not only is the number of chemical species lower, but also as Cl^- reacts with Na^+, the number of possible reactions reduces. Also, in the case of ZnAc, the presence of the ionic species H^+, O^{2-} and C^+ can lead to an imbalance in the reaction precluding the formation of zinc-tin oxide nanostructures.

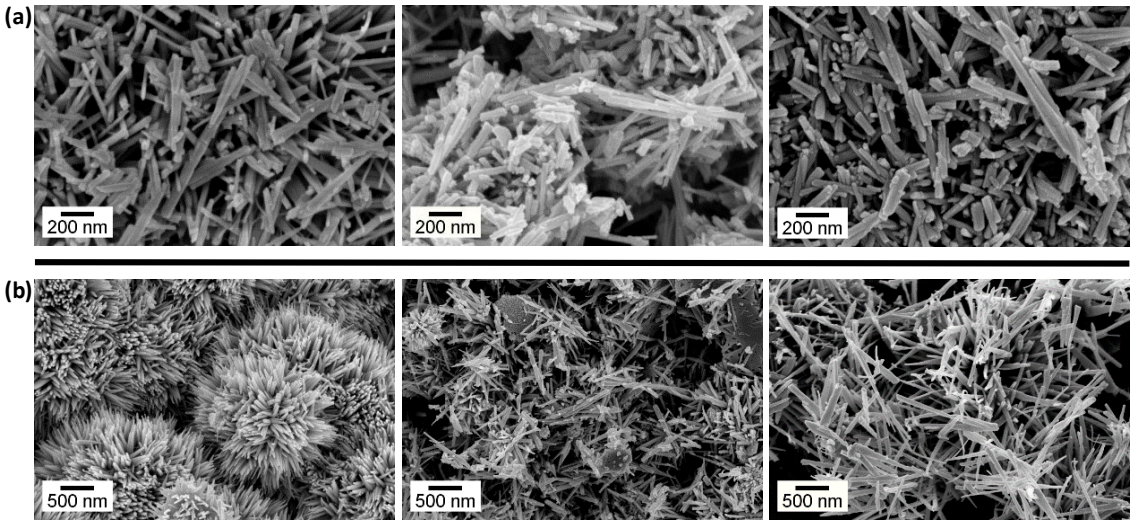

Figure 2.41. SEM micrographs of the nanostructures obtained in different repetitions of hydrothermal synthesis using (a) the $ZnCl_2$ precursor and (b) ZnAc precursor, under similar conditions.

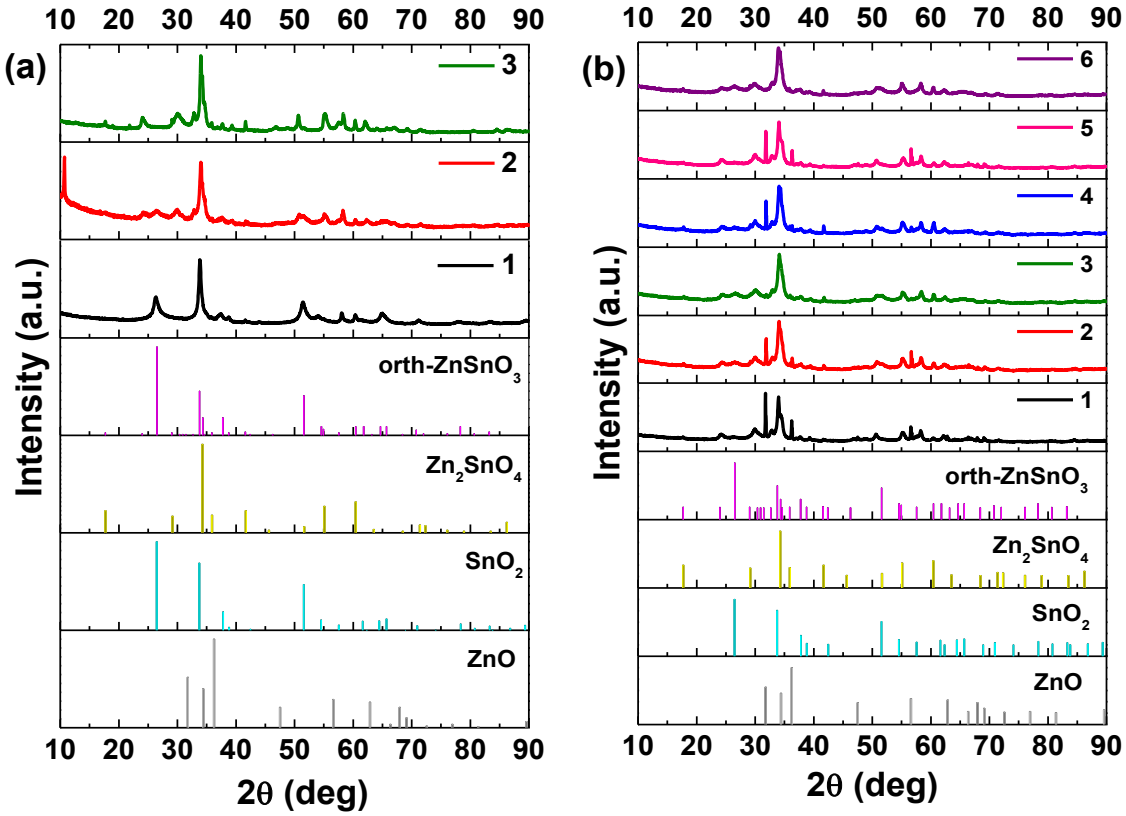

Figure 2.42. XRD patterns of the nanostructures obtained for different repetitions of hydrothermal synthesis using (a) ZnAc and (b) $ZnCl_2$ as zinc precursor, under similar conditions. Identification following ICDD cards 00-028-1486 (deleted), 00-024-1470, 01-077-0452 and 00-06-1451 (**Figure 2.3**). Numbers 1-3 and 1-6 refer to different repetitions of the same synthesis process.

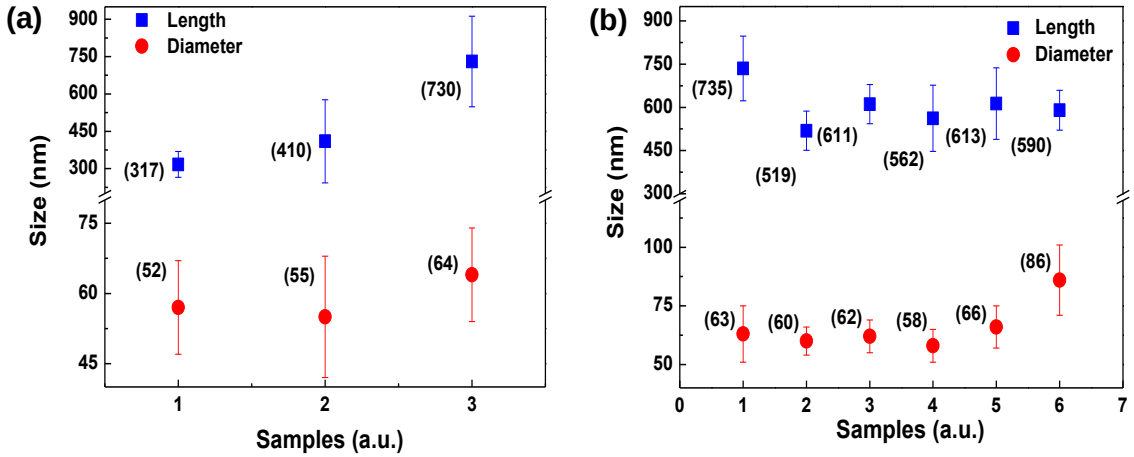

Figure 2.43. Comparison of the obtained nanostructures dimensions in different repetitions of synthesis using (a) ZnAc and (b) $ZnCl_2$ as zinc precursor, under similar conditions. Average lengths and diameters are given between brackets.

2.4. $ZnSnO_3$ Nanowires – Optical Characterization

To study the optical properties of the produced $ZnSnO_3$ nanowires, the absorption under UV and visible radiation was measured. **Figure 2.44**a shows the well-known Tauc's relation that follows the equation:

$$(\alpha hv)^x = A(hv - E_g) \quad (11)$$

Where α is the absorption coefficient, h is the Plank constant, v is the frequency, A is an energy-independent parameter, E_g is the optical band gap and x is a coefficient related to the electronic transition (x=2 for allowed direct transition).[74] The E_g values, inferred by applying the equation to the linear region of the plots, are 3.53 and 3.60 eV, for the ZnAc and $ZnCl_2$ precursors, respectively. For comparison, optical properties of pure Zn_2SnO_4 nanoparticles, produced when using only H_2O as a solvent (section: *Influence of the surfactant concentration*), were also evaluated (**Figure 2.44**a). A band gap of 3.46 eV was achieved, lower than for the $ZnSnO_3$ phase, confirming the trends verified by other authors.[15,21,22] These results also confirm the trends typically observed in multicomponent oxides, where the E_g of the resulting structure tends to be closer to the E_g of the predominant binary compound (ZnO or SnO_2).[75]

Still, the E_g values obtained in this work (both for $ZnSnO_3$ and Zn_2SnO_4) are slightly lower than the ones reported in literature (≈ 0.15-0.30 eV). This difference can be explained by an higher defect density in these nanostructures, resulting in absorption close to band edges.[76] This is a consequence of the low temperature of the reported solution-based process (200 °C) as compared to the >600 °C typically used for physical processes. These band gap values suggest a potential applicability of these nanostructures for photocatalysis and photosensors.[77,78]

Photoluminescence (PL) was also evaluated for these samples (**Figure 2.44**b). A more evident peak at around 366 nm is observed, which can be attributed to ZnO-based nanostructures.[79] By observing the PL spectra it is clear that this peak is more evident in the samples where ZnO-based structures were identified (see for instance **Table 2.2**), corroborating our previous analysis. Small peaks at 427 and 488 nm can also be identified. The presence of these UV peaks is associated with oxygen vacancies, which are major defects in this type of material,[80,81] being emissions in this region common for ZTO nanostructures.[82] Other authors also attribute a 428 nm PL peak to SnO contaminations or nanocrystals formed during ZTO synthesis,[78] which is also a plausible justification for our samples.

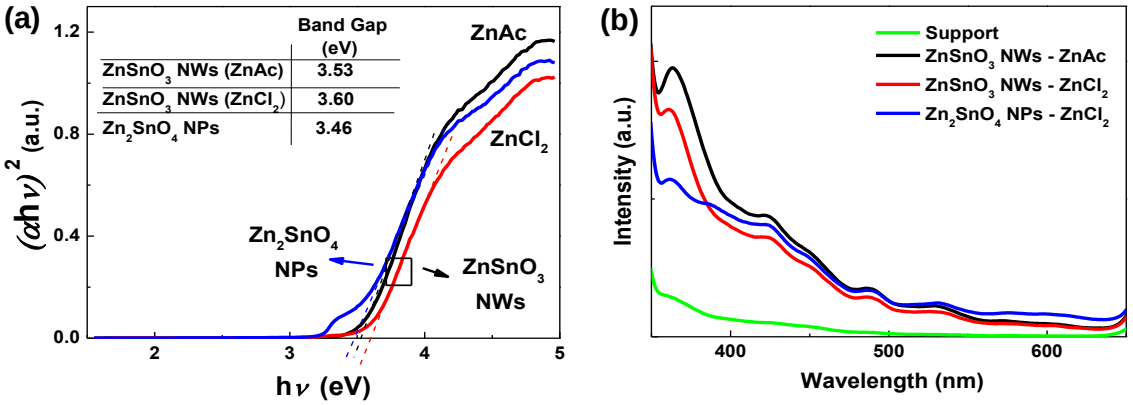

Figure 2.44. (a) Tauc's plots and (b) photoluminescence spectra for $ZnSnO_3$ nanowires using two different Zinc precursors, ZnAc and $ZnCl_2$ and for Zn_2SnO_4 octahedrons, obtained using $ZnCl_2$ precursor with only H_2O as solvent.

2.5. Final remarks

In this chapter the optimization of the chemical and physical parameters of a seed-layer free one-step hydrothermal synthesis of $ZnSnO_3$ nanowires was presented.

One of the many advantages of the hydrothermal method is the possibility to produce phases which are metastable concerning the temperature. It was shown here that the metastable phase $ZnSnO_3$ is possible to obtain under specific chemical and physical parameter conditions, although small variations from these optimal conditions will favor the growth of the more stable and more energetically favorable phases and structures such as Zn_2SnO_4, ZnO and SnO_2. This leads to having a small but non negligible amount of the other structures when aiming for the $ZnSnO_3$ nanowires (in accordance to other reports in literature). Nevertheless, in the range of parameters resulting in $ZnSnO_3$ nanowires, there is still space for a fine tuning which should lead to a further optimized synthesis.

The main conclusions from the different studies are summarized below:

- Zn:Sn precursor molar ratio

Using ZnAc as zinc precursor promotes the presence of SnO_2 while using $ZnCl_2$ results in higher amounts of ZnO. This is attributed to the precursors' solubility in the surfactant EDA: while $SnCl_4{\cdot}5H_2O$ is more soluble than ZnAc, favoring tin-based structures, $ZnCl_2$ is more soluble than $SnCl_4{\cdot}5H_2O$, favoring zinc-based structures.

- Surfactant concentration

The addition of EDA, up to certain EDA concentrations, favors the formation of $ZnSnO_3$ nanowires over the more energetically stable Zn_2SnO_4 nanoparticles. An optimal H_2O:EDA

volume ratio of 7.5:7.5 was determined for the formation of $ZnSnO_3$ nanowires. For higher concentrations, ZnO nanostructures start to be dominant, as the predominant factor starts to be the pH value, showing that the presence of the water is also imperative to the formation of the $ZnSnO_3$ nanowires by assuring the precursors dissolution and balancing the pH in solution.

- NaOH concentration

The mineralizer is required to form the intermediate phases to achieve ZnO and ZTO ($ZnSnO_3$ and Zn_2SnO_4) structures. Accordingly, it was seen that while low mineralizer concentrations favors the growth of tin-oxide structures, excessive mineralizer results in Zn-richer structures. While the Zn-richer structures are either $ZnSnO_3$ nanoparticles or ZnO nanowires depending on the zinc precursor, for intermediate mineralizer concentrations (0.240 M) ZTO nanowires are achieved, showing that there is an optimal concentration for the achievement of this kind of structure, which should result from a specific ratio between the different available (intermediate) species in the mixture.

- Reaction Mixture Volume

The mixture volume was found to be crucial in the growth of the $ZnSnO_3$ (metastable) phase, as it controls the pressure inside the autoclave. While lower volumes (corresponding to lower pressures) favors the formation of Zn_2SnO_4 and SnO_2 nanoparticles (which are the more energetically favored phases), the more homogeneous growth of $ZnSnO_3$ nanowires is obtained for the higher solution volumes (15 mL). In these conditions the elevated pressure supplies the necessary energy level to the reaction, leading to an acceleration of the nucleation processes (even at 200 °C).

- Synthesis Temperature and Reaction Time

The same time-dependence growth mechanisms for the ZTO nanostructures were seen for both Zn sources, although with different time spans. At least 12 h, and 200 ºC were necessary for the fabrication of the nanowires, with synthesis up to 24 h resulting in longer and more wires. Nevertheless, the decomposition of the $ZnSnO_3$ phase, into the more stable phases occurs when employing higher temperatures (24 h at 220 ºC) and/or longer reaction times (36 h at 200 ºC). This emphasizes that while the hydrothermal process is a viable way to achieve the metastable phase at low temperatures, a proper control and understanding of the synthesis parameters is required to achieve the desired structures.

After optimization of all the parameters, the best conditions proved to be a Zn:Sn molar ratio of 2:1 using $ZnCl_2$ as zinc precursor and 1:1 using ZnAc, H_2O:EDA volume ratio of 7.5:7.5 mL:mL and a NaOH concentration of 0.240 M. Still, testing the reproducibility for these two conditions, it was found that $ZnCl_2$ allowed for a very homogeneous (less mixture of phases/structures) and reproducible reaction, being significantly better than when employing ZnAc. Moreover, it is possible to observe that the nanostructures produced using $ZnCl_2$ have longer sizes than when

using ZnAc. These $ZnSnO_3$ nanowires presented lengths and diameters around 600 nm and 65 nm, respectively, against 485 nm and 57 nm, respectively.

As such, low-temperature hydrothermal methods proved to be a low-cost, reproducible and highly flexible route to obtain multicomponent oxide nanostructures, particularly ZTO nanowires. Due to the extensively study done by changing the conditions in $ZnSnO_3$ nanowires' synthesis it was even possible to produce Zn_2SnO_4 nanoparticles and octahedrons and SnO_2 nanoparticles.

Optical characterization of $ZnSnO_3$ nanowires (for the best condition for each zinc precursor) and of Zn_2SnO_4 octahedrons was presented, showing properties comparable with the literature. These properties show a great potential for applications such as photocatalysis and photosensors. Moreover, the achievement of the nanomaterials in powder form, is rather suitable for application in different fields, by allowing a high degree of freedom for integration on different substrates (and avoiding contamination from seed-layer materials). In line with this, $ZnSnO_3$ nanowires can be integrated as a piezoelectric material in energy harvesters, active material in sensors, resistive switching material in memories, anode in batteries, and others. These applications will be demonstrated in the next chapters of this dissertation.

2.6. References

1. Roselli, L. *et al.* Smart surfaces: Large area electronics systems for internet of things enabled by energy harvesting. *Proc. IEEE* **102**, 1723–1746 (2014).

2. Schmidt-Mende, L. & MacManus-Driscoll, J. L. ZnO - nanostructures, defects, and devices. *Mater. Today* **10**, 40–48 (2007).

3. Kołodziejczak-Radzimska, A. & Jesionowski, T. Zinc Oxide—From Synthesis to Application: A Review. *Materials (Basel).* **7**, 2833–2881 (2014).

4. Zhao, Y. *et al.* Pt/ZnO nanoarray nanogenerator as self-powered active gas sensor with linear ethanol sensing at room temperature. *Nanotechnology* **25**, 115502 (2014).

5. Zhao, Y. *et al.* Biomolecule-adsorption-dependent piezoelectric output of ZnO nanowire nanogenerator and its application as self-powered active biosensor. *Biosens. Bioelectron.* **57**, 269–275 (2014).

6. Pang, C. *et al.* Synthesis, characterization and opto-electrical properties of ternary Zn2SnO4 nanowires. *Nanotechnology* **21**, 465706 (2010).

7. Mancini, L. *et al.* Potential of life cycle assessment for supporting the management of critical raw materials. *Int. J. Life Cycle Assess.* **20**, 100–116 (2015).

8. Guo, R., Guo, Y., Duan, H., Li, H. & Liu, H. Synthesis of Orthorhombic Perovskite-Type ZnSnO3 Single-Crystal Nanoplates and Their Application in Energy Harvesting. *ACS Appl.*

Mater. Interfaces **9**, 8271–8279 (2017).

9. Wu, J. M. *et al.* Ultrahigh Sensitive Piezotronic Strain Sensors Based on a ZnSnO3 Nanowire/Microwire. *ACS Nano* **6**, 4369–4374 (2012).

10. Baruah, S. & Dutta, J. Zinc stannate nanostructures: hydrothermal synthesis. *Sci. Technol. Adv. Mater.* **12**, 013004 (2011).

11. Sun, S. & Liang, S. Morphological zinc stannate: synthesis, fundamental properties and applications. *J. Mater. Chem. A* **5**, 20534–20560 (2017).

12. Lehnen, T., Zopes, D. & Mathur, S. Phase-selective microwave synthesis and inkjet printing applications of Zn2SnO4 (ZTO) quantum dots. *J. Mater. Chem.* **22**, 17732 (2012).

13. Siddiqui, G. U., Rehman, M. M. & Choi, K. H. Resistive switching phenomena induced by the heterostructure composite of ZnSnO3 nanocubes interspersed ZnO nanowires. *J. Mater. Chem. C* **5**, 5528–5537 (2017).

14. Wu, J. M., Xu, C., Zhang, Y. & Wang, Z. L. Lead-free nanogenerator made from single ZnSnO3 microbelt. *ACS Nano* **6**, 4335–40 (2012).

15. Li, Z. *et al.* Vertically building Zn2SnO4 nanowire arrays on stainless steel mesh toward fabrication of large-area, flexible dye-sensitized solar cells. *Nanoscale* **4**, 3490–4 (2012).

16. Kim, S., Kim, H., Janes, D. B. & Ju, S. Interface studies of N2 plasma-treated ZnSnO nanowire transistors using low-frequency noise measurements. *Nanotechnology* **24**, 305201 (2013).

17. Lo, M.-K., Lee, S.-Y. & Chang, K.-S. Study of ZnSnO3-Nanowire Piezophotocatalyst Using Two-Step Hydrothermal Synthesis. *J. Phys. Chem. C* **119**, 5218–5224 (2015).

18. Inaguma, Y., Yoshida, M. & Katsumata, T. A Polar Oxide ZnSnO3 with a LiNbO3-Type Structure. *J. Am. Chem. Soc.* **130**, 6704–6705 (2008).

19. Dal Corso, A., Posternak, M., Resta, R. & Baldereschi, A. Ab initio study of piezoelectricity and spontaneous polarization in ZnO. *Phys. Rev. B* **50**, 10715–10721 (1994).

20. Mao, Y., Park, T.-J. & Wong, S. S. Synthesis of classes of ternary metal oxide nanostructures. *Chem. Commun.* 5721 (2005).

21. Miyauchi, M., Liu, Z., Zhao, Z.-G., Anandan, S. & Hara, K. Single crystalline zinc stannate nanoparticles for efficient photo-electrochemical devices. *Chem. Commun.* **46**, 1529–1531 (2010).

22. Lei, M. *et al.* A novel self-catalytic route to zinc stannate nanowires and cathodoluminescence and electrical transport properties of a single nanowire. *J. Alloys Compd.* **657**, 394–399 (2016).

23. Lim, T., Kim, H., Meyyappan, M. & Ju, S. Photostable Zn2SnO4 Nanowire Transistors for Transparent Displays. *ACS Nano* **6**, 4912–4920 (2012).

24. Annamalai, A., Carvalho, D., Wilson, K. C. & Lee, M.-J. Properties of hydrothermally synthesized Zn2SnO4 nanoparticles using Na2CO3 as a novel mineralizer. *Mater. Charact.* **61**, 873–881 (2010).

25. Shi, J.-B. *et al.* Synthesis and characterization of single-crystalline zinc tin oxide nanowires. *Nanoscale Res. Lett.* **9**, 210 (2014).

26. Ji, X. *et al.* Hydrothermal synthesis of novel Zn2SnO4 octahedron microstructures assembled with hexagon nanoplates. *J. Alloys Compd.* **503**, L21–L25 (2010).

27. Choi, K. H., Siddiqui, G. U., Yang, B. & Mustafa, M. Synthesis of ZnSnO3 nanocubes and thin film fabrication of (ZnSnO3/PMMA) composite through electrospray deposition. *J. Mater. Sci. Mater. Electron.* **26**, 5690–5696 (2015).

28. Zhou, T. *et al.* Hollow ZnSnO3 Cubes with Controllable Shells Enabling Highly Efficient Chemical Sensing Detection of Formaldehyde Vapors. *ACS Appl. Mater. Interfaces* **9**, 14525–14533 (2017).

29. Chen, Z., Cao, M. & Hu, C. Novel Zn2SnO4 hierarchical nanostructures and their gas sensing properties toward ethanol. *J. Phys. Chem. C* **115**, 5522–5529 (2011).

30. Najam Khan, M., Al-Hinai, M., Al-Hinai, A. & Dutta, J. Visible light photocatalysis of mixed phase zinc stannate/zinc oxide nanostructures precipitated at room temperature in aqueous media. *Ceram. Int.* **40**, 8743–8752 (2014).

31. Xue, X. Y., Chen, Y. J., Wang, Y. G. & Wang, T. H. Synthesis and ethanol sensing properties of ZnSnO3 nanowires. *Appl. Phys. Lett.* **86**, 1–3 (2005).

32. Wang, L. *et al.* Comparison of toluene sensing performances of zinc stannate with different morphology-based gas sensors. *Sensors Actuators, B Chem.* **227**, 448–455 (2016).

33. Zhou, T. *et al.* Highly sensitive sensing platform based on ZnSnO3 hollow cubes for detection of ethanol. *Appl. Surf. Sci.* **400**, 262–268 (2017).

34. Wu, J. M. *et al.* Flexible and transparent nanogenerators based on a composite of lead-free ZnSnO3 triangular-belts. *Adv. Mater.* **24**, 6094–6099 (2012).

35. Fu, Y. *et al.* Detecting Liquefied Petroleum Gas (LPG) at Room Temperature Using ZnSnO3/ZnO Nanowire Piezo-Nanogenerator as Self-Powered Gas Sensor. *ACS Appl. Mater. Interfaces* **7**, 10482–10490 (2015).

36. Cheng, B., Ouyang, Z., Chen, C., Xiao, Y. & Lei, S. Individual Zn2SnO4-sheathed ZnO heterostructure nanowires for efficient resistive switching memory controlled by interface states. *Sci. Rep.* **3**, 3249 (2013).

37. Mali, S. S., Su Shim, C. & Kook Hong, C. Highly porous Zinc Stannate (Zn2SnO4) nanofibers scaffold photoelectrodes for efficient methyl ammonium halide perovskite solar cells. *Sci. Rep.* **5**, 11424 (2015).

38. Wang, Y. *et al.* One Pot, Two Phases: Individual Orthorhombic and Face-Centered Cubic ZnSnO3 Obtained Synchronously in One Solution. *Inorg. Chem.* **53**, 12289–12296 (2014).

39. Fang, C., Geng, B., Liu, J. & Zhan, F. d-fructose molecule template route to ultra-thin ZnSnO3 nanowire architectures and their application as efficient photocatalyst. *Chem. Commun.* 2350 (2009).

40. Jie, J. *et al.* Growth of Ternary Oxide Nanowires by Gold-Catalyzed Vapor-Phase Evaporation. *J. Phys. Chem. B* **108**, 8249–8253 (2004).

41. Men, H. *et al.* Fast synthesis of ultra-thin ZnSnO3 nanorods with high ethanol sensing properties. *Chem. Commun.* **46**, 7581 (2010).

42. Guerfi, Y. & Larrieu, G. Vertical Silicon Nanowire Field Effect Transistors with Nanoscale Gate-All-Around. *Nanoscale Res. Lett.* **11**, 210 (2016).

43. Larrieu, G., Guerfi, Y., Han, X. L. & Clément, N. Solid-State Electronics Sub-15 nm gate-all-around field effect transistors on vertical silicon nanowires. *Solid State Electron.* **130**, 9–14 (2017).

44. Zeng, J. *et al.* Transformation process and photocatalytic activities of hydrothermally synthesized Zn2SnO4 nanocrystals. *J. Phys. Chem. C* **112**, 4159–4167 (2008).

45. Su, B., Wu, Y. & Jiang, L. The art of aligning one-dimensional (1D) nanostructures. *Chem. Soc. Rev.* **41**, 7832 (2012).

46. Tharsika, T., Haseeb, A. S. M. a., Akbar, S. a., Sabri, M. F. M. & Wong, Y. H. Gas sensing properties of zinc stannate (Zn2SnO4) nanowires prepared by carbon assisted thermal evaporation process. *J. Alloys Compd.* **618**, 455–462 (2015).

47. Ju, S. *et al.* Fabrication of fully transparent nanowire transistors for transparent and flexible electronics. *Nat. Nanotechnol.* **2**, 378–84 (2007).

48. Kumari, V., Patra, A. K. & Bhaumik, A. Self-assembled ultra-small zinc stannate nanocrystals with mesoscopic voids via a salicylate templating pathway and their photocatalytic properties. *RSC Adv.* **4**, 13626–13634 (2014).

49. Chen, Y. *et al.* An evolution from 3D face-centered-cubic ZnSnO3 nanocubes to 2D orthorhombic ZnSnO3 nanosheets with excellent gas sensing performance. *Nanotechnology* **23**, 415501 (2012).

50. Bora, T., Al-Hinai, M. H., Al-Hinai, A. T. & Dutta, J. Phase Transformation of Metastable ZnSnO3 Upon Thermal Decomposition by In-Situ Temperature-Dependent Raman

Spectroscopy. *J. Am. Ceram. Soc.* **98**, 4044–4049 (2015).

51. Song, P., Wang, Q. & Yang, Z. Biomorphic synthesis of ZnSnO3 hollow fibers for gas sensing application. *Sensors Actuators, B Chem.* **156**, 983–989 (2011).

52. Wang, Y. *et al.* One Pot, Two Phases: Individual Orthorhombic and Face-Centered Cubic ZnSnO3 Obtained Synchronously in One Solution. *Inorg. Chem.* **53**, 12289–12296 (2014).

53. Placke, A., Kumar, A. & Priya, S. Synthesis and Behavior of Cetyltrimethyl Ammonium Bromide Stabilized Zn1+xSnO3+x (0 ≤ x ≤1) Nano-Crystallites. *PLoS One* **11**, e0156246 (2016).

54. Diéguez, A., Romano-Rodríguez, A., Vilà, A. & Morante, J. R. The complete Raman spectrum of nanometric SnO2particles. *J. Appl. Phys.* **90**, 1550–1557 (2001).

55. Kovacheva, D. Preparation of crystalline ZnSnO3 from Li2SnO3 by low-temperature ion exchange. *Solid State Ionics* **109**, 327–332 (1998).

56. Mao, W. *et al.* Nanowire-based zinc-doped tin oxide microtubes for enhanced solar energy utilization efficiency. *Ceram. Int.* **43**, 6822–6830 (2017).

57. Pimentel, A. *et al.* Effect of solvents on ZnO nanostructures synthesized by solvothermal method assisted by microwave radiation: a photocatalytic study. *J. Mater. Sci.* **50**, 5777–5787 (2015).

58. Tian, Z. R. *et al.* Complex and oriented ZnO nanostructures. *Nat. Mater.* **2**, 821–826 (2003).

59. Bakshi, M. S. How Surfactants Control Crystal Growth of Nanomaterials. *Cryst. Growth Des.* **16**, 1104–1133 (2016).

60. Ivetić, T. B., Finčur, N. L., Đačanin, L. R., Abramović, B. F. & Lukić-Petrović, S. R. Ternary and coupled binary zinc tin oxide nanopowders: Synthesis, characterization, and potential application in photocatalytic processes. *Mater. Res. Bull.* **62**, 114–121 (2015).

61. Zhao, Q. *et al.* Polyhedral Zn2SnO4: Synthesis, enhanced gas sensing and photocatalytic performance. *Sensors Actuators, B Chem.* **229**, 627–634 (2016).

62. Li, J., Chen, Z., Wang, R.-J. & Proserpio, D. M. Low temperature route towards new materials: solvothermal synthesis of metal chalcogenides in ethylenediamine. *Coord. Chem. Rev.* **190**–**192**, 707–735 (1999).

63. Liu, Q. *et al.* High-yield synthesis of ultralong and ultrathin Zn2GeO4 nanoribbons toward improved photocatalytic reduction of CO2 into renewable hydrocarbon fuel. *J. Am. Chem. Soc.* **132**, 14385–14387 (2010).

64. Xu, S. & Wang, Z. L. One-dimensional ZnO nanostructures: Solution growth and functional properties. *Nano Res.* **4**, 1013–1098 (2011).

65. Shankar, K. S. & Raychaudhuri, A. K. Fabrication of nanowires of multicomponent oxides: Review of recent advances. *Mater. Sci. Eng. C* **25**, 738–751 (2005).

66. Rovisco, A. *et al.* Seed-layer free zinc tin oxide tailored nanostructures for nanoelectronic applications: effect of chemical parameters. *ACS Appl. Nano Mater.* (2018). doi:10.1021/acsanm.8b00743

67. Christian, B. *et al.* Piezo-force and Vibration Analysis of ZnO Nanowire Arrays for Sensor Application. *Procedia Eng.* **168**, 1192–1195 (2016).

68. Wu, J. M., Xu, C., Zhang, Y. & Wang, Z. L. Lead-free nanogenerator made from single ZnSnO3 microbelt. *ACS Nano* **6**, 4335–40 (2012).

69. Gou, H. *et al.* Energetic stability, structural transition, and thermodynamic properties of ZnSnO3. *Appl. Phys. Lett.* **98**, 1–4 (2011).

70. Montenegro, D. N. *et al.* Non-radiative recombination centres in catalyst-free ZnO nanorods grown by atmospheric-metal organic chemical vapour deposition. *J. Phys. D. Appl. Phys.* **46**, 235302 (2013).

71. Nakayama, M., Nogami, M., Yoshida, M., Katsumata, T. & Inaguma, Y. First-principles studies on novel polar oxide ZnSnO3; pressure-induced phase transition and electric properties. *Adv. Mater.* **22**, 2579–2582 (2010).

72. Saafi, I. *et al.* Microstructural and optical properties of SnO2-ZnSnO3ceramics. *Ceram. Int.* **42**, 6273–6281 (2016).

73. Mary Jaculine, M., Justin Raj, C. & Jerome Das, S. Hydrothermal synthesis of highly crystalline Zn2SnO4 nanoflowers and their optical properties. *J. Alloys Compd.* **577**, 131–137 (2013).

74. Pimentel, A. *et al.* Microwave Synthesized ZnO Nanorod Arrays for UV Sensors: A Seed Layer Annealing Temperature Study. *Materials (Basel).* **9**, 299 (2016).

75. Barquinha, P. & Wiley InterScience. *Transparent oxide electronics : from materials to devices*. (Wiley, 2012).

76. Barquinha, P. *et al.* Performance and Stability of Low Temperature Transparent Thin-Film Transistors Using Amorphous Multicomponent Dielectrics. *J. Electrochem. Soc.* **156**, H824 (2009).

77. An, Q., Meng, X., Xiong, K. & Qiu, Y. Self-powered ZnS Nanotubes/Ag Nanowires MSM UV Photodetector with High On/Off Ratio and Fast Response Speed. *Sci. Rep.* **7**, 1–12 (2017).

78. Karthik, K. R. G. *et al.* Physical and Electrical Properties of Single Zn2SnO4 Nanowires. *Electrochem. Solid-State Lett.* **14**, K5 (2011).

79. Zhao, J. H., Liu, C. J. & Lv, Z. H. Photoluminescence of ZnO nanoparticles and nanorods. *Optik (Stuttg).* **127**, 1421–1423 (2016).

80. Shewale, P. S. *et al.* Structural and photoluminescence characterization of SnO2: F thin films deposited by advanced spray pyrolysis technique at low substrate temperature. *J. Lumin.* **139**, 113–118 (2013).

81. Mageshwari, K., Kim, T. G. & Park, J. Effect of alkaline concentration on the structural and luminescence properties of ZnSnO3 nanoparticles obtained by facile reflux method. *J. Mater. Sci. Mater. Electron.* **27**, 4093–4097 (2016).

82. Wang, J. X. *et al.* Growth and characterization of axially periodic Zn2SnO4 (ZTO) nanostructures. *J. Cryst. Growth* **267**, 177–183 (2004).

Chapter 3 – Alternative routes to synthesize zinc-tin oxide-based nanostructures

In Chapter 2 the optimization of a seed-layer free hydrothermal synthesis of $ZnSnO_3$ nanowires was described. While the development of this method for the nanostructures synthesis was set as the primary objective of this thesis, other routes were also explored for the synthesis of zinc-tin oxide-based nanostructures and are presented in Chapter 3. Namely, microwave-assisted hydrothermal synthesis was explored as a mean to reduce the duration of the syntheses. A comparison between the nanostructures achieved with the oven method and the nanostructures achieved with the microwave method is performed, based on the optimized chemical parameters from the previous Chapter. Additionally, the use of seed-layers was also explored for achieving different ZTO structures. While this alternative route allows to influence the growth of the nanostructures, it can also be beneficial for applications where nanostructures on film are already intended, as is the case for photocatalysis and pH sensors, for which the nanostructures in discussion present excellent properties, as will be presented in latter Chapters.

The nanostructures syntheses and characterization were performed in the CENIMAT and CEMOP laboratories.

3.1. ZTO nanostructures: conventional oven vs microwave system

While conventional ovens are commonly used for hydrothermal process, in this method the temperature of the reaction vessel can be considerably higher than of the mixture itself as the heating is dependent on the thermal conductivity of the various materials and on convection currents, which can result in a slower heating of the mixture.[1]

In the last years, microwave-assisted synthesis appeared as a promising alternative for fabrication of inorganic nanostructures by allowing faster reactions and a uniform volumetric heating, due to a different heating process.[1–5] In these systems, the heating mechanism is mainly based-on two phenomena, dipolar polarization and ionic conduction (**Figure 3.1**), as dipoles and ions continuously attempt to realign themselves with the electric fields from the microwaves.[1] Molecular friction during the orientation/disorientation of dipoles with the electric field (known as dielectric loss),[1,6,7] lead to a heating of the medium, provided that the frequency of the irradiation is not so high that the dipoles cannot respond, neither so low that they can easily keep up, with frequencies of 2.54 GHz lying intermediately of these extreme cases. Regarding ions in solution, they will oscillate with the electric field colliding with neighboring molecules. This heat generation effect is much stronger than that of polarization, being particularly important for synthesis in ionic liquids.[1,8] By allowing a faster and more uniform heating for the hydrothermal synthesis, this method permits to reduce side reactions, enhancing the product purity and yield.[1]

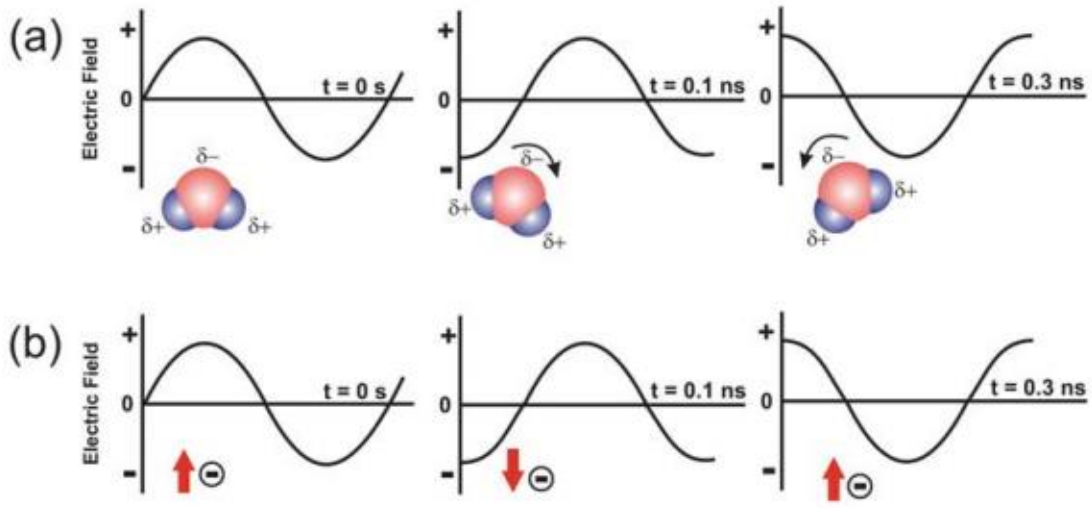

Figure 3.1. Two main heating mechanisms under microwave irradiation: (a) dipolar polarization and (b) ionic conduction mechanism.[1]

Several nanostructures by microwave-assisted synthesis have been reported, namely the ZTO binary counterparts, ZnO and SnO_2,[3,9–14] with the advantageous multicomponent oxides as ZTO being significantly more difficult to obtain. Nevertheless, ZTO nanostructures synthesized in microwave systems have been reported already. Lehnen *et al.* showed a simple method to

produce quantum dots in a conventional microwave,[4] while Nehru *et al.* combined a urea-based combustion process in a microwave system to produce Zn_2SnO_4 nanostructures.[15]

In the previous Chapter the synthesis of ZTO nanostructures by a hydrothermal method using a conventional oven was presented and discussed. Based on these results, and aiming to achieve faster processes, syntheses based on the optimized chemical conditions for the oven were explored in the microwave system.

3.1.1. Experimental details

A CEM Focused Microwave Synthesis System Discover SP was used, being the synthesis schematic shown in **Figure 3.2**. The microwave syntheses were made in a dynamic mode, in which the irradiated power is controlled by the system to maintain a defined temperature for all the synthesis duration. Aside from the different heating methods, the pressure of the reaction mixtures will differ for the two discussed systems. For the oven system, the pressure in the Teflon tubes (45 mL) inside the autoclave is not monitored during synthesis but is known to be dependent on the volume of the solution since the autoclave is sealed. On the other hand, the vessels in the microwave system (35 mL) have a small aperture: its internal pressure will try to be in equilibrium with that of the microwave chamber. This pressure is read during the process and a maximum pressure can be defined. Likewise, a maximum power can also be defined. Considering this, the adaptation of a specific synthesis from one system to another should not be direct, instead requiring optimization.

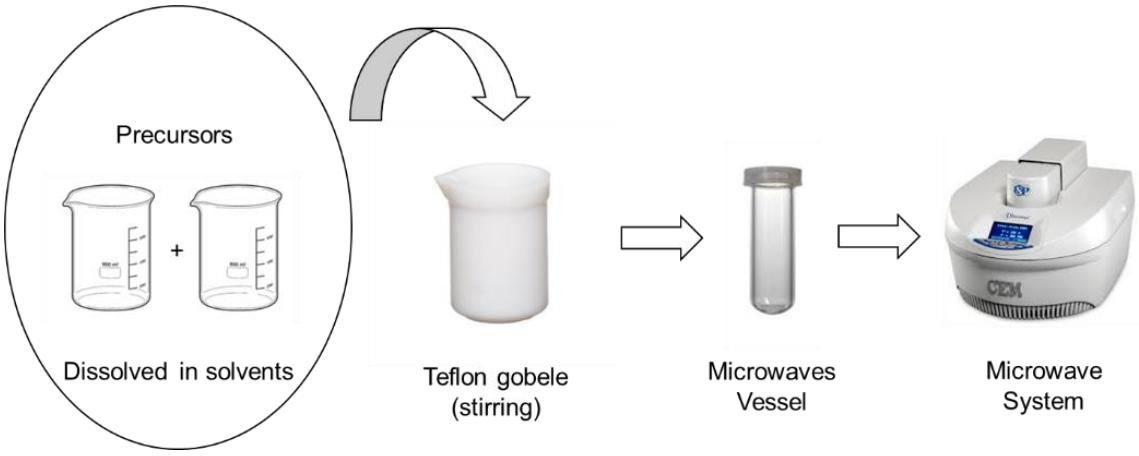

Figure 3.2. Schematic of the Schematic representation of the hydrothermal synthesis process using the microwave system.

The morphological and structural characterization for the obtained nanostructures with the microwave system was performed using the same equipment (SEM/EDS and XRD) and the same methodologies described in the previous Chapter.

3.1.2. $ZnSnO_3$ nanowires

In Chapter 2 the optimization of the seed-layer free and one-step hydrothermal synthesis of $ZnSnO_3$ nanowires, by studying the influence of both chemical and physical parameters, was presented. Based on the optimized conditions, a study of this synthesis replacing the conventional oven for a microwave system started to be explored. The syntheses were performed using a maximum pressure of 270 PSI and a constant temperature of 200 °C.

In **Figure 3.3** the SEM images and XRD patterns for different conditions to produce $ZnSnO_3$ nanowires using the microwave are presented. While the synthesis durations are much shorter than those employed in the oven, all of them resulted predominantly in $ZnSnO_3$ nanowires, even though some mixture of phases can be observed in the XRD pattern. On an early analysis, for the particular case of using the $ZnCl_2$ precursor, nanowire length seems to increase for longer synthesis, and for higher volumes (in a similar way as observed for the oven method). Regarding the ZnAc precursor, an initial test (**Figure 3.3**d), also resulted in $ZnSnO_3$ nanowires, being however noticeable that the synthesis duration of 1h is too short as indicated by the very significant mixture of phases present. Exploration of this process is still at an early stage, but these preliminary results are promising by revealing the possibility of replacing the oven by the microwave irradiation, which allows to reduce up to 20 hours of synthesis time. Nevertheless, and considering the metastable nature of the phase under study, further investigation is still required in achieving a well-controlled, reproducible and homogenous process.

Furthermore, this approach of using microwaves irradiation heating process to produce $ZnSnO_3$ nanowires is reported here for the first time, to the best of the author's knowledge.

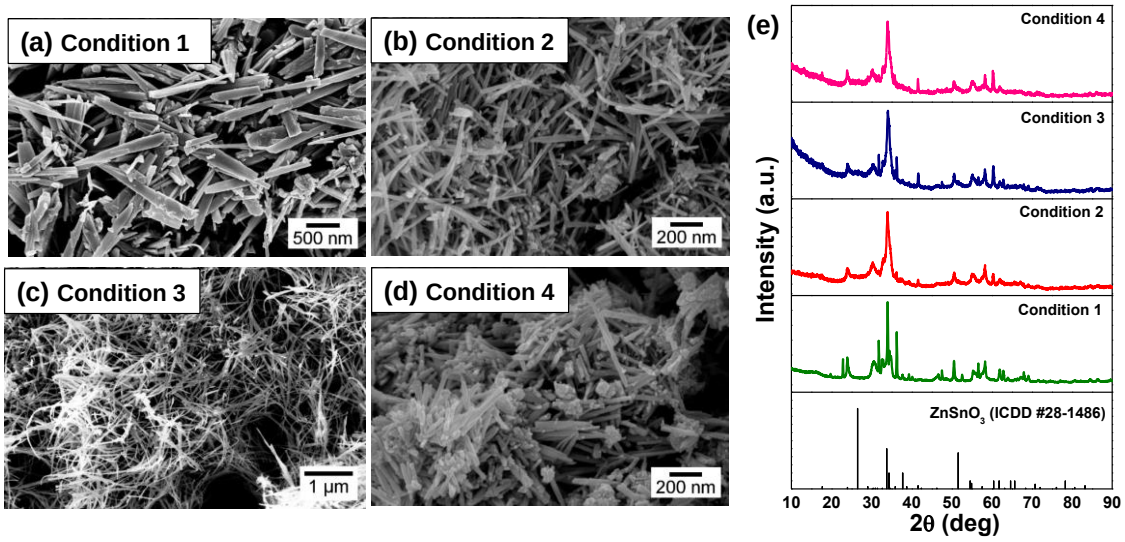

Figure 3.3. (a-d) SEM micrographs and (e) XRD pattern of microwave-assisted synthesis with different conditions. Zn precursor, mixture volume and synthesis duration are: $ZnCl_2$, 7.5 mL, 4 h (condition 1); $ZnCl_2$, 7.5 mL, 2 h (condition 2); $ZnCl_2$, 15 mL, 4 h (condition 3); and ZnAc, 7.5 mL, 1 h (condition 4).

3.1.3. Zn_2SnO_4 octahedrons

While studying the influence of H_2O:EDA volume ratio in the nanostructures growth, presented in section 2.1, conditions to obtain Zn_2SnO_4 octahedrons were achieved, in which synthesis duration was of 24 h. Following this result, an oven synthesis in similar conditions was tested with a shorter duration of 12 h. It was found that it was not enough time to produce purely the Zn_2SnO_4 phase, with some mixture of phases being seen in the XRD pattern (**Figure 3.4**). Moreover, SEM shows that Zn_2SnO_4 nanoplates are predominantly obtained (**Figure 3.5**), which are an intermediate structure on the formation of the Zn_2SnO_4 octahedrons.

Synthesis for both these structures were also explored by using a microwave system. These were performed with a maximum set power of 100 W, a maximum pressure of 270 PSI and at a constant temperature of 200 °C, with the synthesis durations being 30 and 60 minutes.

Figure 3.4 compares the XRD patterns for the nanostructures obtained with these microwave-assisted syntheses with the ones obtained via conventional oven, with SEM of the obtained structures shown in **Figure 3.5**. Even if employing significantly shorter times, the microwave synthesis presented the same trend observed for the oven syntheses: pure phases can be achieved for the longer syntheses, which result in Zn_2SnO_4 octahedrons, while shorter syntheses show some mixture of phases, yielding mainly Zn_2SnO_4 nanoplates. These syntheses proved to be an effective method to produce either Zn_2SnO_4 nanoplates or octahedrons, with the microwave heating method allowing for very short syntheses.

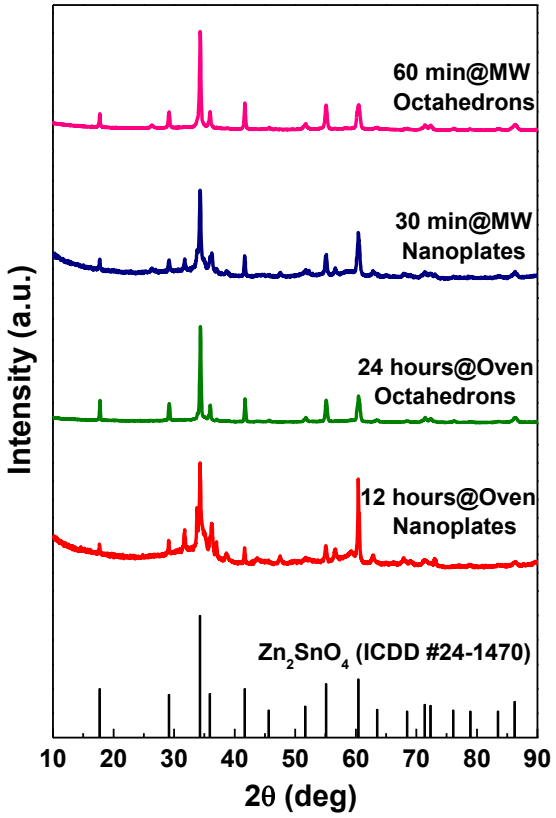

Figure 3.4. XRD pattern for the nanostructures synthesized in the oven (for 12 h and 24 h) and in the microwave system (for 30' and 60').

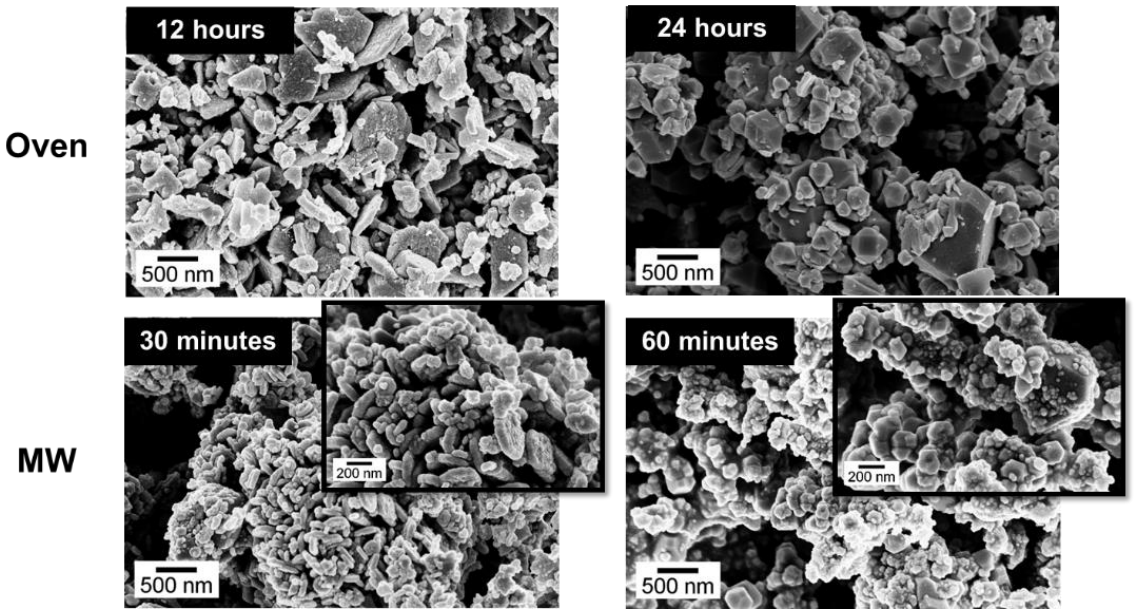

Figure 3.5. SEM images of the Zn_2SnO_4 nanoplates and octahedrons synthesized in the oven (for 12 h and 24 h) and in the microwave system (for 20' and 60').

3.1.4. Zn_2SnO_4 nanoparticles

In Chapter 2, Zn_2SnO_4 nanoparticles were achieved with some given synthesis conditions, yet, the reaction yield was significantly low. A different hydrothermal reaction, based on the method reported by Annamalai *et al.*[16], was explored to produce Zn_2SnO_4 nanoparticles. While the synthesis was not thoroughly optimized, nanostructures of this phase have interesting properties for several applications, as will be demonstrated in latter Chapters by its application in pH sensing devices and photocatalysis.

Zn_2SnO_4 nanoparticles were synthesized using as zinc and tin precursors 0.34 g of zinc chloride ($ZnCl_2$ from Merck, 98%) and 0.44 g of tin tetrachloride ($SnCl_4 \cdot 5H_2O$ from Riedel-deHean 98%), respectively, each dissolved separately in 5 mL of deionized water, and then added together. Then, sodium carbonate (Na_2CO_3 from Merck, 99.9%) solution (0.53 g in 5 mL of water) was added dropwise to the mixture, leaving then under magnetic stirring for 15 min. The mixture was kept in the electric oven (Thermo Scientific) at 200 °C for two different durations: 12 h and 24 h, with a heating ramp of 200 °C/h, and letting the autoclave cool to ambient temperature naturally at the end. The nanostructures were washed and dried using the same process presented in Chapter 2.

The chemical reaction yielding Zn_2SnO_4 can be represented by (1):

$$2ZnCl_2 + SnCl_4 + 4Na_2CO_3 + H_2O \rightarrow Zn_2SnO_4 + 8NaCl + 4CO_2 \quad (1)$$

In **Figure 3.6** the XRD patterns and the SEM images for the Zn_2SnO_4 nanoparticles are presented. It is possible to observe that for both synthesis' durations nanoparticles with pure

phases are achieved. Although the nanoparticles obtained with the shorter synthesis have larger sizes, the longer synthesis results in a higher yield of nanoparticles.

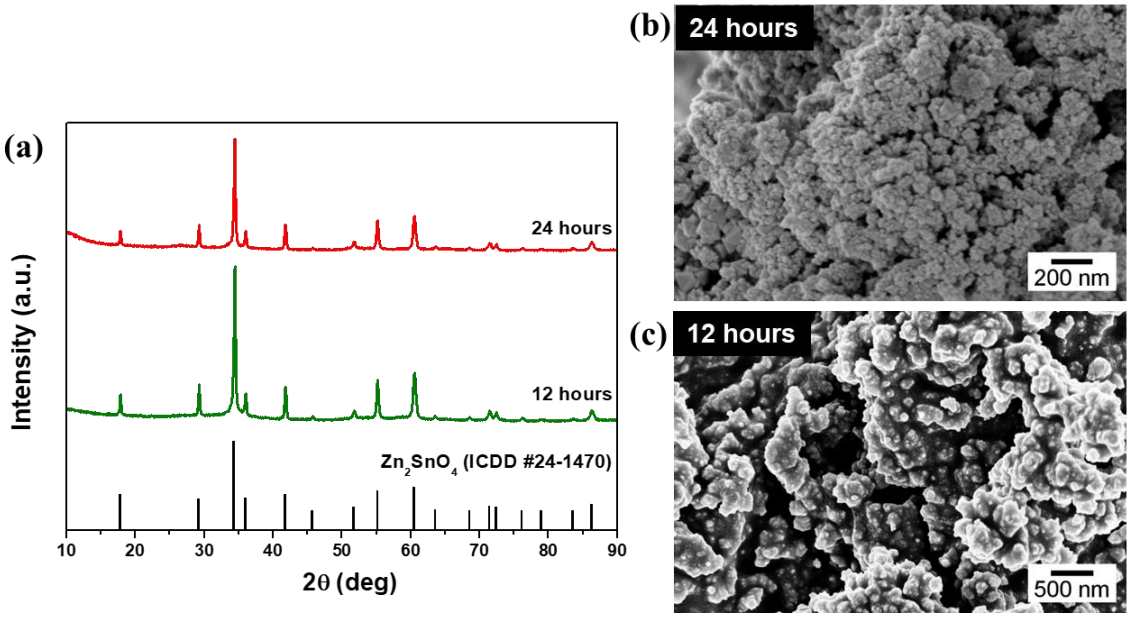

Figure 3.6. (a) XRD pattern and (b) SEM images of the Zn_2SnO_4 nanoparticles synthesized in a conventional oven at 200 °C for 12 h and 24 h.

Following from this oven synthesis' conditions, and aiming to reduce the synthesis time, the fabrication of Zn_2SnO_4 nanoparticles was explored in the microwave system. The synthesis was performed with a maximum power of 100 W, a maximum pressure of 270 PSI and a constant temperature of 200 °C. Two synthesis durations were considered, 20 minutes and 60 minutes.

In **Figure 3.7** is possible to observe that whether for 20 minutes or for 60 minutes of synthesis nanoparticles with a pure Zn_2SnO_4 phase were obtained, similarly to what was obtained using the conventional oven. This shows that it is possible to reduce at least 12 hours of synthesis to produce Zn_2SnO_4 nanoparticles with the same quality.

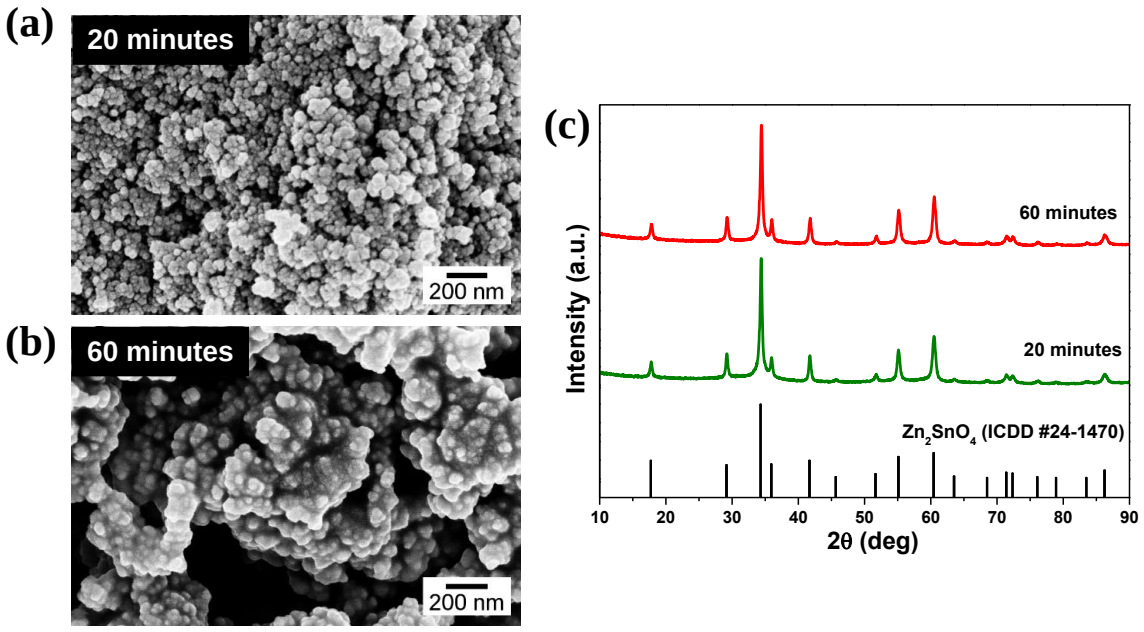

Figure 3.7. (a and b) SEM images and (c) XRD patterns of Zn_2SnO_4 nanoparticles produced by microwave-assisted synthesis for 20 min and 60 min.

3.1.5. SnO_2 nanoparticles

SnO_2 nanoparticles were also produced by using both heating methods: conventional oven and microwave system. The synthesis of these nanostructures was based on the solvothermal method reported by Men *et al.*.[17] Briefly, 0.20 g of potassium stannate (K_2SnO_3 from Sigma-Aldrich) were dissolved in 6 mL of deionized water, then 0.95 g of urea (Na_2CO_3 from Fisher Chemical, 99.9%) were added, and finally 10 mL of ethanol were added. The solution was kept in the electric oven (Thermo Scientific) at 140 °C for 4 h, with a heating ramp of 200 °C/h, letting the autoclave cool to ambient temperature naturally after the synthesis. Regarding the synthesis using the microwave system a maximum power of 80 W and a maximum pressure of 270 PSI were used while a constant temperature of 140 °C was kept for 1 h. After the syntheses, the same procedure of washing and drying the nanostructures as described before was used.

In **Figure 3.8** the structural and morphological characterization is presented. The XRD patterns are very similar for both syntheses and are well matched with the ICDD card #078-1063, corresponding to tetragonal SnO_2. A slight difference between the nanoparticles' sizes can be observed in the SEM images (**Figure 3.8**b and c), with the one produced in the microwaves being larger. Again, this suggests that the time for synthesis of these nanostructures can be significantly reduced by employing the microwave heating method.

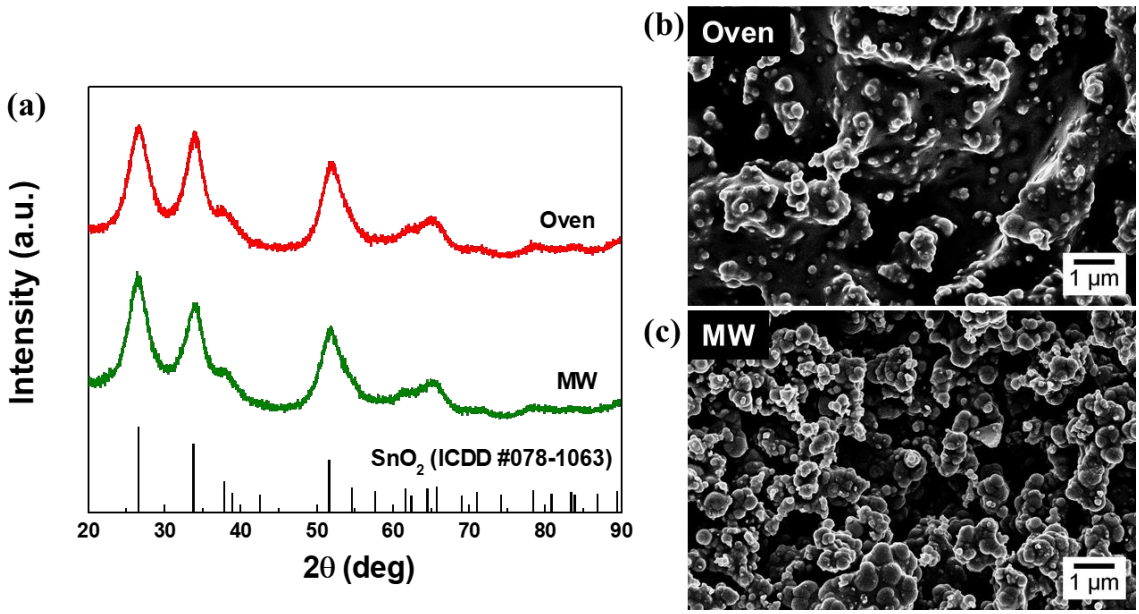

Figure 3.8. (a) XRD patterns and SEM micrographs of SnO_2 nanoparticles (b) produced using the oven and (c) the microwave system.

3.1.6. Conclusions

The studies for optimization of the hydrothermal synthesis of $ZnSnO_3$ nanowires using the conventional oven resulted also in particular conditions for fabrication of other types of structures. As such, this work enabled the establishment of processed useful to obtain structures such as Zn_2SnO_4 octahedrons, Zn_2SnO_4 nanoparticles and SnO_2 nanoparticles.

While these different types of structures present great interest for different applications, sometimes the reaction times and/or yield are not practical, especially when considering devices which require a high volume of particles. Thus, based on the synthesis implemented on the conventional oven, microwave-assisted synthesis was explored due to its faster and more uniform heating rate. The results for synthesis of different structures using both methods were compared. While employing much shorter times (a decrease of several hours) the microwave method has shown to be able to result in structures similar to those from the oven method. For the specific case of $ZnSnO_3$ nanowires synthesis, this allowed to decrease the synthesis time at least 20 hours. Additionally, the higher degree of control in the microwave system opens space for further optimization.

3.2. ZTO nanostructures on seed-layers

In the previous Chapter, the hydrothermal synthesis of $ZnSnO_3$ nanowires (in powder form) was shown, which was considered the main objective for this project. Additionally, synthesis of other ZTO-based nanostructures in the powder form was also presented. As was already mentioned, seed-layer free synthesis, resulting in powder form nanostructures, gives flexibility not only for the application of the nanostructures in devices by allowing integration on different substrates, but also by not imposing any constrains in the reagents and process parameters of the synthesis. Nevertheless, the direct growth methods also present very considerable advantages, namely by avoiding transfer methods which are often difficult to implement. Besides the possible advantage of the direct integration in the device, different designs can also be envisaged by these methods, as orientation of the nanostructures in relation to the substrate is often achieved during these growth/deposition process. While syntheses by physical processes are considered direct growth methods, chemical methods such as hydrothermal synthesis can be either substrate-free (the powder precipitates in the reaction vessel) or direct growth (if employing a substrate or a seed-layer). The seed-layers, being a support medium from which the nanostructures grow, will naturally influence the growth of the structures, being obtained different structures depending on the seed-layer material. Characteristics of these seed-layer materials such as the crystalline structure and the surface energy can play a role on the nanostructures' growth.

Several reports on seed-layer based growth of ZTO nanostructures have been published in the last years, with fluorine doped tin oxide (FTO) being the most commonly employed seed material. Lo *et al.* used a FTO film to grow rhombohedral $ZnSnO_3$ nanowires for piezophotocatalytic applications (**Figure 3.9**a).[18] In 2011 Dharmadasa *et al.* showed the growth of different types of structures (such as nanoplates and nanocolumns, shown in **Figure 3.9**b and c) from a FTO seed-layer depending on the precursors concentration.[19] Habibi *et al.* also employed FTO obtaining Zn_2SnO_4 nanoparticles which were applied for dye solar cells.[20] On the other hand, Wang *et al.* used ITO on glass and obtained $Zn_{1-x}SnO_3$ nanowires which were employed for piezophotocatalysis.[21] In 2012, Li *et al.* synthesized Zn_2SnO_4 nanowires on a stainless steel (SS) mesh for application in dye solar cells (**Figure 3.9**d-h).[22] Interestingly, the hydrothermal synthesis conditions used by Li *et al.* were the ones used as a basis for the synthesis presented in Chapter 2 of this thesis (which yielded $ZnSnO_3$ nanowires), clearly showing the influence of the seed-layers in the growth of nanostructures.

While reports show that a wide range of structures can be produced depending on substrates and synthesis' conditions, nanowires are the most commonly reported. This emphasizes the difficulty in obtaining these structures by the low-temperature solution processes, being necessary to employ the seed-layer materials to induce the growth of the less energetically favorable ZTO nanowires. Although very interesting results have been reported, correlations between the employed seed-layers and the achieved types of nanostructures are scarce.

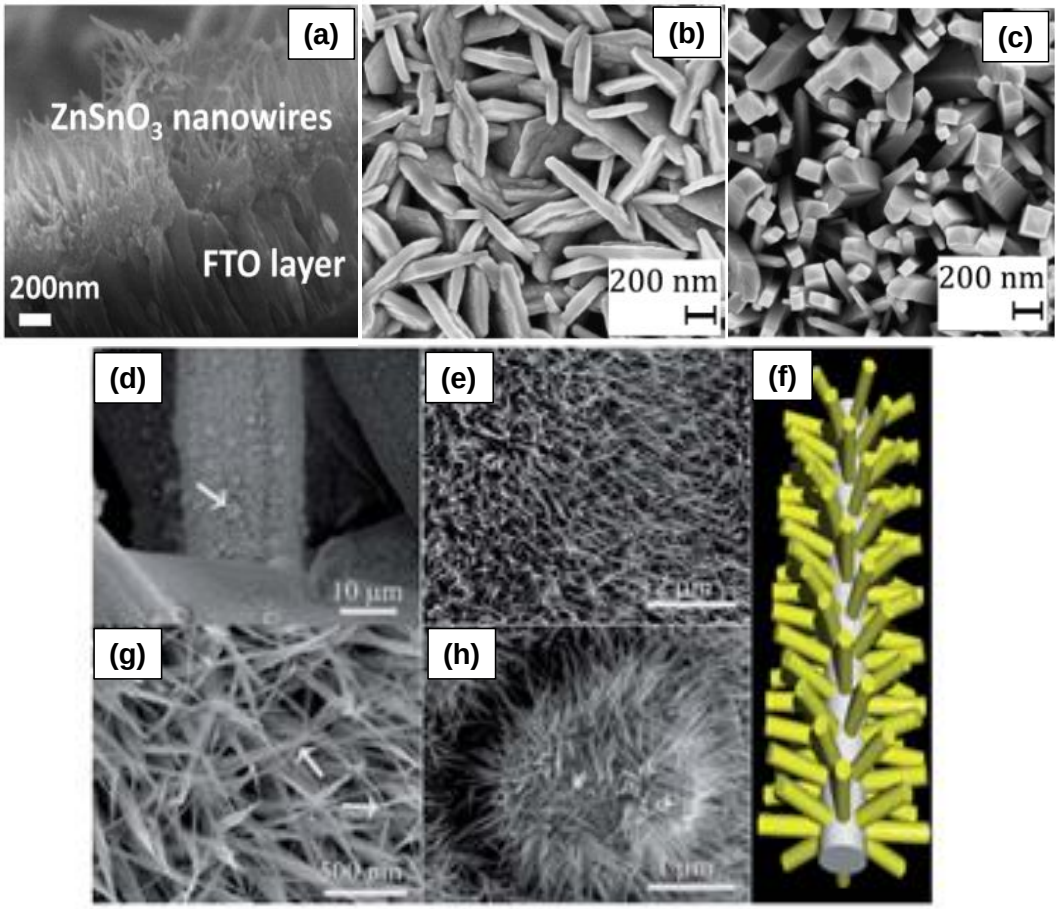

Figure 3.9. SEM images of (a) $ZnSnO_3$ nanowires on a FTO seed-layer;[18] (b,c) ZTO nanoplates and nanocolunms growth on FTO seed-layer;[19] and (d-h) schematic representation of the Zn_2SnO_4 nanowires growth on stainless steel mesh.[22]

In the next sub-sections the use of different seed-layers in the hydrothermal synthesis will be presented, attempting to correlated the type of ZTO nanostructures grown to the employed seed-layer. The use of the different seed-layers was attempted for an initial exploration of the possible types of structures to be achieved: while for some seed-layers different synthesis conditions were tested, tuning of the synthesis conditions for each layer was not performed and is left for future work. A specific aim of this study was the synthesis of Zn_2SnO_4 nanowires as these structures were not achieved for the seed-layer free hydrothermal methods previously presented in this work.

3.2.1. Experimental details

The two best synthesis conditions from Chapter 2 to produce $ZnSnO_3$ nanowires (one for each Zn precursor) were used to grow ZTO nanostructures directly on the seed-layers, and will be referenced as solutions A and B, for the $ZnCl_2$ and ZnAc precursors, respectively. Additionally, for cooper foil as seed-layer, similar conditions with the exception that 99 % pure EDA is replaced

by a 75-80 % purity one (from Sigma-Aldrich) were also employed, being referred as solutions C and D, for $ZnCl_2$ and ZnAc precursors, respectively. The 75-80 % purity EDA was employed based on past satisfactory results in the group.

Seed-layers were prepared by depositing thin films on glass substrates. ZTO and ZnO films were deposited by RF-sputtering while e-beam assisted evaporation was used to deposit Sn, Cr, Ni and Ti. Additionally, Cu nanowires in a powder form were also used as seed-layer, and were fabricated via a solution method as described in reference [23]. All the substrates were cleaned before the syntheses. Commercial substrates (FTO, copper foil, carbon fibers and stainless steel) were cleaned with IPA and deionized water. Substrates fabricated in-house were washed through ultrasonication with acetone and IPA and were then rinsed with deionized water before the thin film deposition. After drying the substrates with nitrogen, they were inserted in the Teflon tubes with the respective synthesis solutions. The syntheses were then performed just as described in Chapter 2. After the synthesis, the substrates were washed with IPA and deionized water to remove precipitate remains.

3.2.2. Influence of the seed-layer material in the nanostructures' growth

Thin films based-on zinc and tin

In the literature fluorine doped tin oxide (FTO) appears as the most common seed-layer to induce the growth of ZTO nanostructures. Thus, in this work FTO commercial glass (Sigma-Aldrich) was also explored. FTO has a tetragonal crystalline structure, meaning that $a = b \neq c$ with equal angles.

Figure 3.10 shows the SEM images for the FTO seed-layers after ZTO synthesis with the solutions A and B. While for both solutions some nanowires grew directly in the substrate, other types of structures are also present, showing a very poor uniformity/homogeneity. Nevertheless, since ZTO nanowires were produced we can assume that tuning from this syntheses' conditions could result in a homogenous growth of ZTO nanowires in the FTO films. At the present stage, the identification of these structures was not possible due to unclarity in the XRD and EDS analysis.

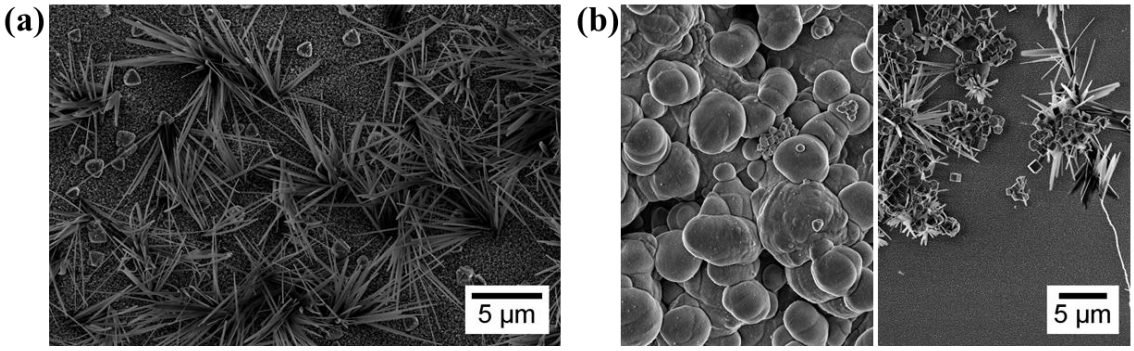

Figure 3.10. SEM images of nanostructures using FTO as seed-layer in (a) solution A and (b) solution B.

In-house deposited ZTO, ZnO and Sn films were also used with solutions A and B ($ZnCl_2$ and ZnAc). While ZTO is amorphous, ZnO presents a hexagonal wurtzite structure, whereas Sn has a body-centered tetragonal structure (bcc). Interestingly, as shown by SEM in **Figure 3.11**(a-f), all these cases resulted in the growth of nanosheets across the thin films. However, the phase identification of these structures was not clear by XRD nor EDS, with further analysis being required to draw further conclusions. Nevertheless, it should be noted that nanostructures with this shape are often reported as ZnO with a hexagonal structure.[24] Additionally, **Figure 3.11**(g and h) also shows the same type of structures, but these were achieved employing a titanium thin film (50 nm) which has an hexagonal close-packed structure. Similarly, the identification of the structural phase was not clear enough neither by XRD nor EDS, making it difficult to draw conclusions on the effect of the different kinds of seeds.

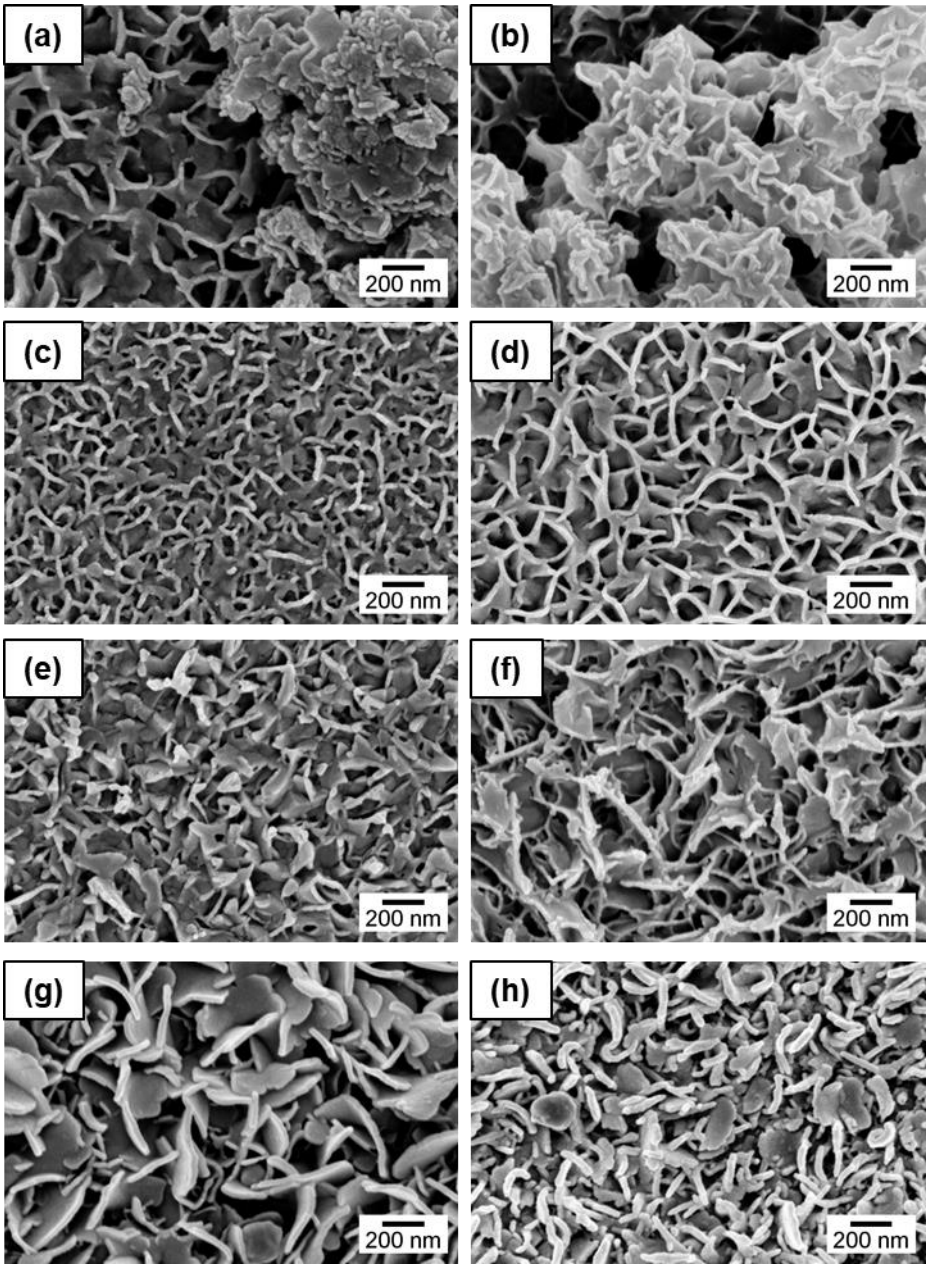

Figure 3.11. SEM images of nanostructures grown with solutions A and B, respectively, on the thin film seed-layers: ZTO (a,b), ZnO (c,d), Sn (e,f) and Ti (g,h).

Nevertheless, the obtained structures are very interesting for being used as active layer in catalytic, sensing and energy applications,[25–28] with the specific cases of Sn, FTO and Ti seed-layers having the advantage of being able to act as an electrode contacting the active layer.

Stainless steel: substrate and mesh

Based on the synthesis from Li *et al.*,[22] from which is reported the growth of Zn_2SnO_4 nanowires from a stainless steel (SS) mesh, we also employed SS as a seed-layer, both in mesh and substrate forms (Sigma-Aldrich). SS has a cubic crystalline structure, coming from both the alpha iron (ferrite, body-centered cubic, bcc) or the gamma iron (austenite, face-centered cubic fcc) configurations that SS can have.

Figure 3.12 (a and b) shows the nanoparticles grown on the surface of the SS mesh, for which the Zn_2SnO_4 phase can be identified by the XRD patterns (**Figure 3.13**a). As was observed in Chapter 2 for most of the obtained nanostructures, here it is also seen that employing the ZnAc precursor results in smaller nanoparticles than employing the $ZnCl_2$ precursor.

Interestingly, when employing the SS substrate, different nanostructures were achieved for the different zinc precursors (**Figure 3.12** (c and d)). Using the $ZnCl_2$ precursor, a sort of nanostructured thin film composed of octahedrons/pyramids was fabricated. Using ZnAc, nanowires were obtained in some areas of the sample whereas other regions are covered with octahedrons/pyramids.

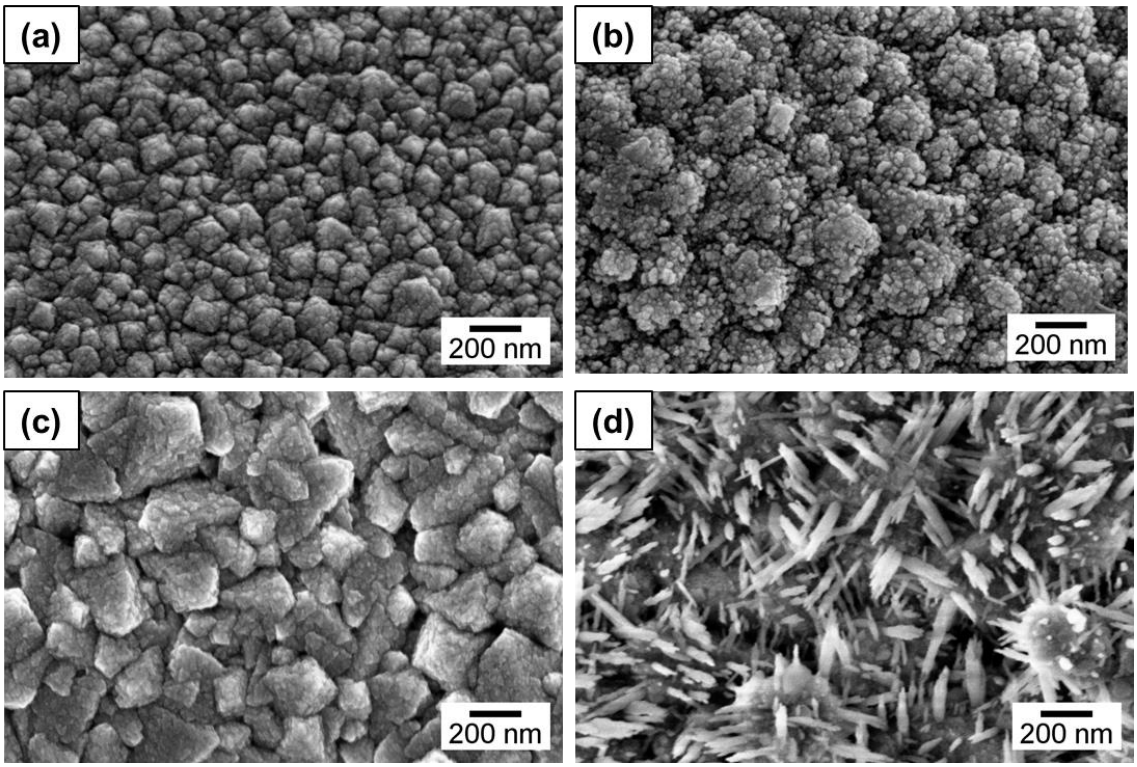

Figure 3.12. SEM images of the nanostructures in the stainless steel: (a) mesh using $ZnCl_2$; (b) mesh using ZnAc; (c) substrate using $ZnCl_2$; (d) substrate using ZnAc.

Concerning the identification of these structures, the Zn_2SnO_4 phase was identified (**Figure 3.13**) by the XRD patterns. Moreover, EDS element analysis presented a Zn:Sn atomic ratio of 2:1, supporting the identification of the Zn_2SnO_4 phase by XRD. The XRD patterns in **Figure 3.13** show that the alloys from the mesh and the substrate differ in structure: the SS mesh shows both austenite and ferrite structures while the SS substrate presents only the austenite. While this can be related to why different types of structures were achieved in these layers, it should be noted that both have a cubic crystalline structure, which can be related to the induction of the Zn_2SnO_4 phase, that has a spinel inverse cubic structure.

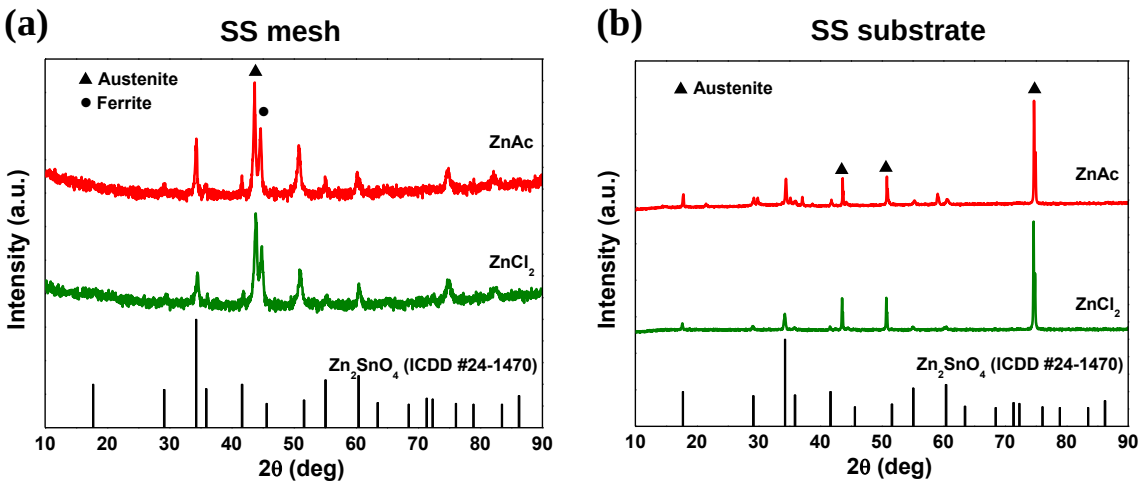

Figure 3.13. XRD patterns for (a) SS mesh and (b) SS substrate using $ZnCl_2$ and ZnAc.

Copper (Cu): foil and nanowires

Commercial copper (Cu) foils (Coppertex, Illinois) were also explored as seed-layer, as its cubic face-centered structure is thought to be effective in inducing the Zn_2SnO_4 structure for the nanowires. For this, seed-layers solutions A to D were used, with synthesis durations of 12 h and 24 h for each.

Figure 3.14 presents the SEM images of several nanostructures obtained in these conditions. It is interesting to note that the employment of a lower purity EDA (75-80 % purity, for solutions C and D) results in different structures than for the case of the purer EDA (99 % purity, for solutions A and B).

Regarding the morphology of the obtained structures, while using $ZnCl_2$ and 75-80 % pure EDA (solution C) yielded a nanostructured film of octahedrons, using purer EDA (solution A) resulted in the Zn_2SnO_4 nanowires (all phases are identified by the XRD analysis, as shown next). This highlights the role of EDA in directing the structures growth. Using ZnAc precursor, for 75-80 % pure EDA (solution D) a nanostructured film of Zn_2SnO_4 nanoplates was produced, while 99 % pure EDA (solution B) yielded Zn_2SnO_4 octahedrons. In general, it was observed that for 24 h long synthesis the nanostructures start to aggregate in a thin film like morphology (insets of **Figure 3.14**).

Figure 3.15 shows the XRD patterns for the nanostructures grown on Cu foil using the different solutions. It can be observed that Zn_2SnO_4 is the identified phase for all samples (using the ICDD card #24-1470). It is important to notice that, similarly to the SS substrate, Cu also has a face-centered cubic (fcc) crystal structure, and the achievement of the Zn_2SnO_4 phase was similarly observed.

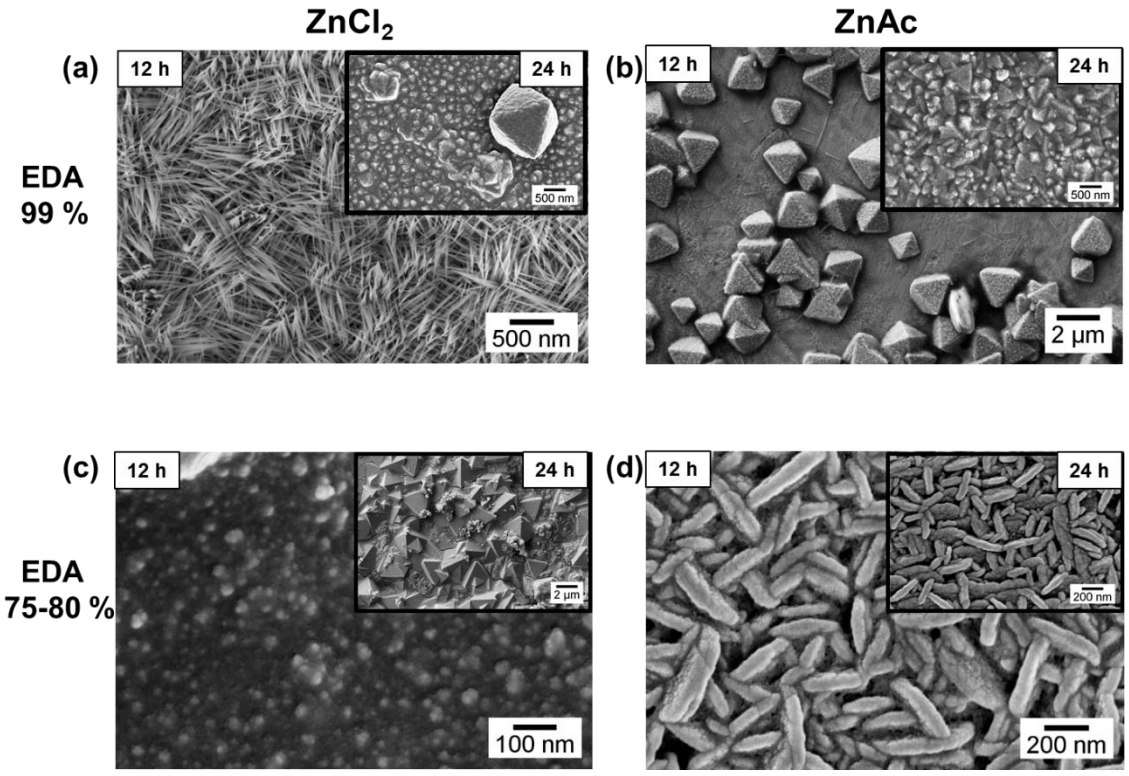

Figure 3.14. SEM images of ZTO nanostructures growth on Cu foil by the 12 h hydrothermal syntheses with solutions A-D. The Zn precursors are: (a, c) $ZnCl_2$ and (b, d) ZnAc and the EDA purities are (a, b) 99 % and (c, d) 75 %. Insets correspond to syntheses with 24 h.

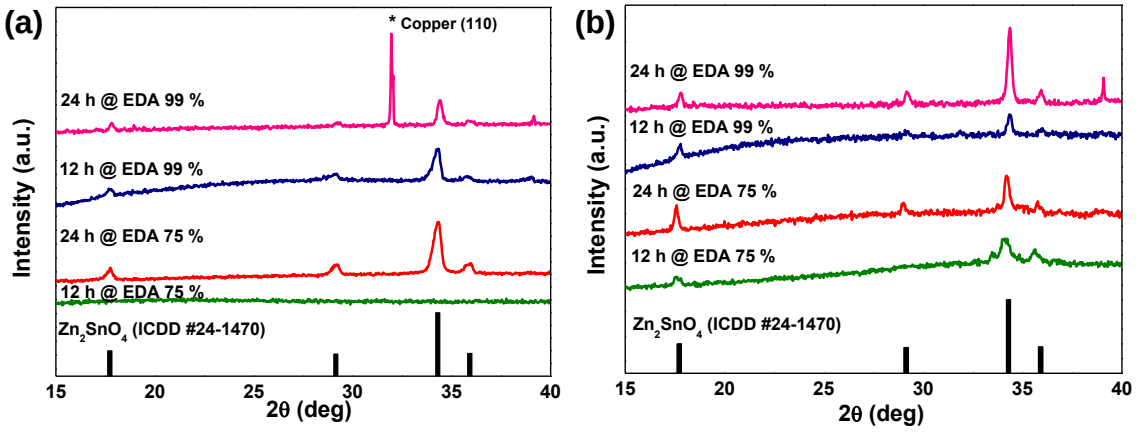

Figure 3.15. XRD patterns for the ZTO nanostructures grown on Cu foil using (a) $ZnCl_2$ (solutions A and C) and (b) ZnAc (solutions B and D) as zinc precursor, for different EDA purities and different synthesis times.

Following from the satisfactory results achieved by employing solution A with the Cu foil, Cu nanowires were also tested as seed-layers for these conditions. Several reports show that decorating nanowires with nanostructures results in enhanced properties for applications such as sensing and catalysis.[29] The Cu nanowires fabrication was reported in reference [23], and revealed a dominance of cubic Cu (ICDD #04-0836) phase, with the CuO (monoclinic) and Cu_2O (cubic) phases being also identified.

Figure 3.16 shows the SEM images and EDS mapping of ZTO nanowires grown directly on the Cu nanowires. The EDS element analysis showed an atomic concentration ratio of: 21.22 % of Zn, 22.83 % of Sn, 55.00 % of O and 0.95 % of Cu, consistent with the $ZnSnO_3$ phase which is also the mainly identified in the XRD pattern (**Figure 3.16**c).

It is interesting to notice that different phases are achieved when using Cu foil or Cu nanowires as seed-layers. It is important to add that even if the nanostructures grown on the Cu foil are Zn_2SnO_4 nanowires, the nanostructures achieved in a precipitate form during that synthesis are $ZnSnO_3$ nanowires, which are consistent with those obtained without seed-layers as described in Chapter 2. This shows that under these chemical conditions and without the influence of a seed-layer this is the preferentially grown structure. Since the Cu nanowires do not have a Cu pure phase, with CuO being also identified, it is probable that the surface of the Cu nanowires consists on CuO (due to Cu easily oxidizing). CuO has a monoclinic structure which, similarly to the orthorhombic structure, has unequal lengths ($a \neq b \neq c$). As such, CuO might either be inducing the formation of the orthorhombic phase ($ZnSnO_3$) or even if not playing a significant role in influencing the growth of the nanostructures, the $ZnSnO_3$ phase is still the preferential under this synthesis chemical conditions.

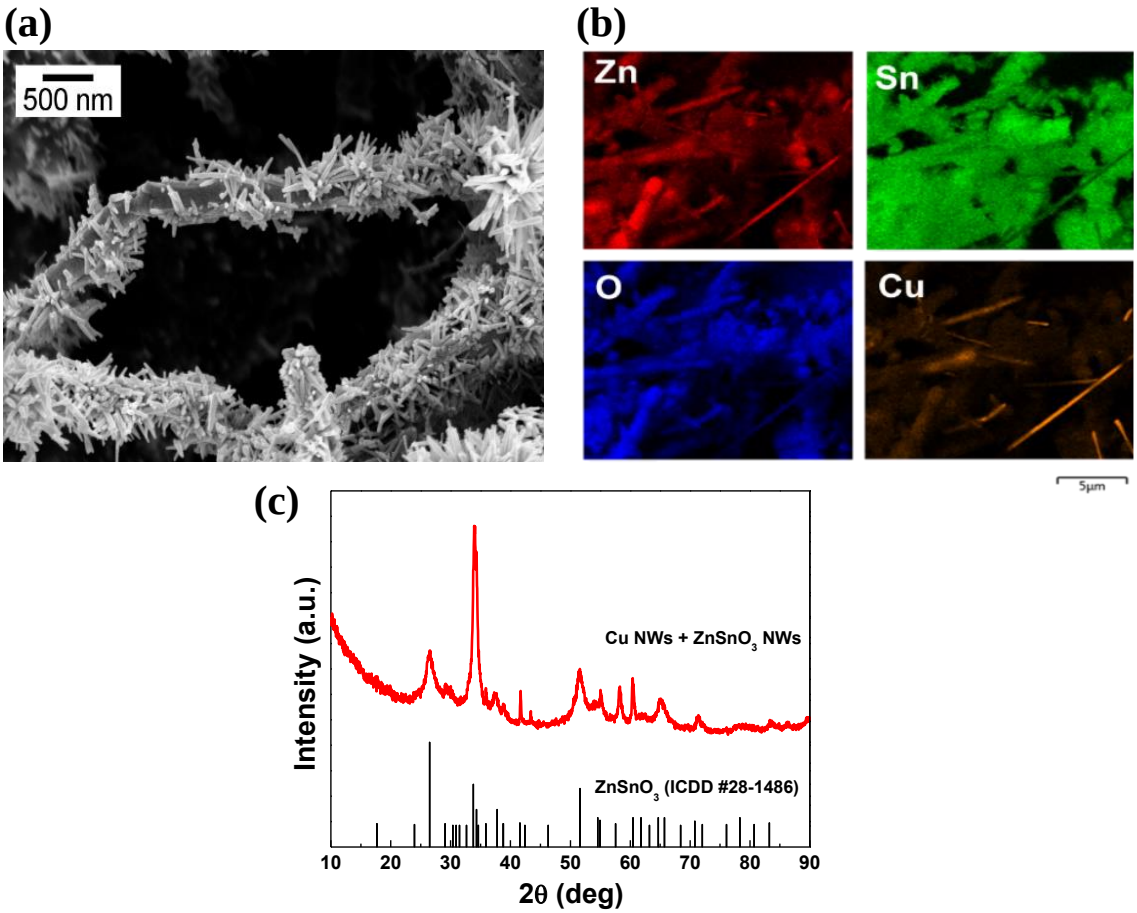

Figure 3.16. (a) SEM image, (b) EDS analysis and (c) XRD pattern for the $ZnSnO_3$ nanowires grown on Cu nanowires by the hydrothermal synthesis using solution A.

Seed-layers of other materials

Other materials were used as seed-layer, giving rise to interesting nanostructures.

A thin film (50 nm) of Cr was used in the syntheses with solutions A and B. Like Cu and SS, Cr has a cubic crystal structure, being however a body-centered cubic structure (bcc). **Figure 3.17** (a and b) shows the SEM images of the nanostructures resultant from these syntheses were flattened nanowires, here called as nanograss.

A thin film (50 nm) of Ni was also used as seed-layer with solutions A and B, since it has a face-centered cubic (fcc) crystal structure, like Cu and SS. SEM images, in **Figure 3.17** (c and d), show the resultant structures for these syntheses, which are wider than the nanograss like structures, almost nanosheet like.

While both Cr and Ni seed-layers have a cubic structure, similarly to other seed-layers tested before, it was not possible to clearly identify the phase of the resultant nanostructures as both the XRD patterns and EDS analysis present several unidentified peaks.

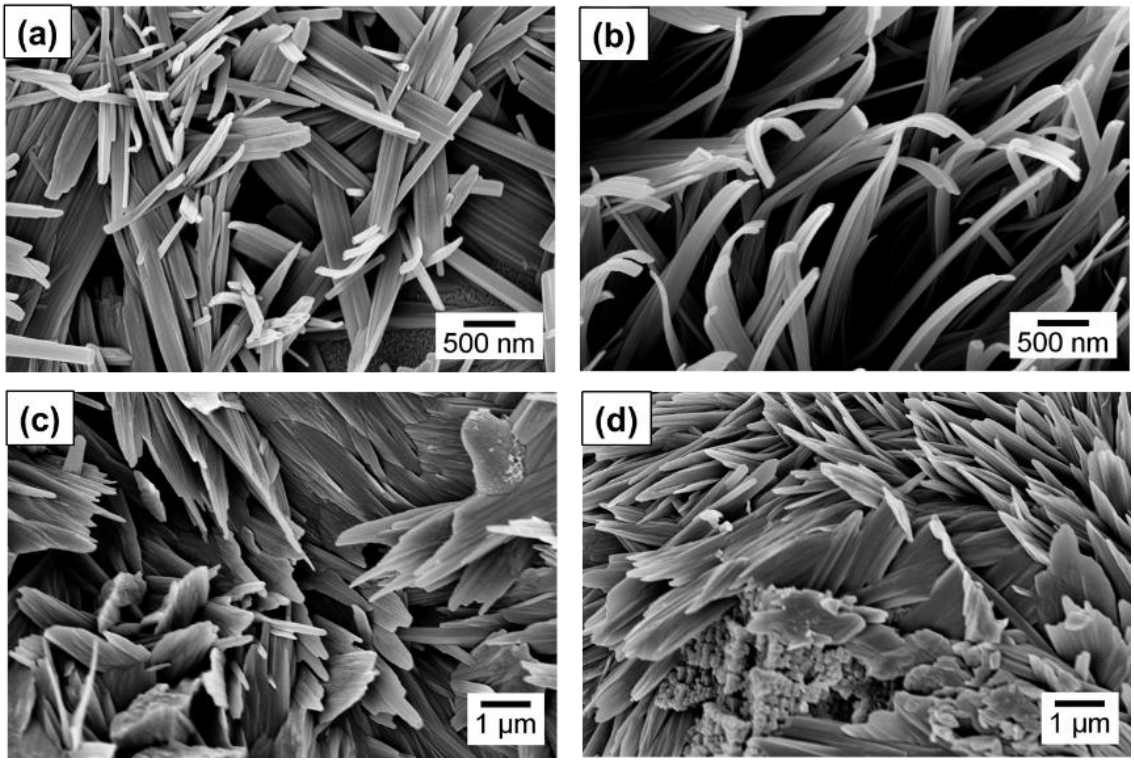

Figure 3.17. SEM images of nanostructures obtained using: (a and b, respectively) Cr thin films as the seed-layer in the solutions A and B, and (c and d, respectively) Ni thin films as the seed-layer in the solutions A and B.

Carbon fibers were also used as seed-layer in synthesis with the solution A, as these materials are interesting for application in energy storage, such as supercapacitors and Li-batteries.[30] Flower-like nanostructures grew in the fibers as shown in **Figure 3.18**. However, the XRD pattern does not present any peaks, either due to the low amount of nanostructures in the

surface of the carbon fibers or due to a poor crystallinity of these nanostructures, with further analysis being needed for the identification of these nanostructures.

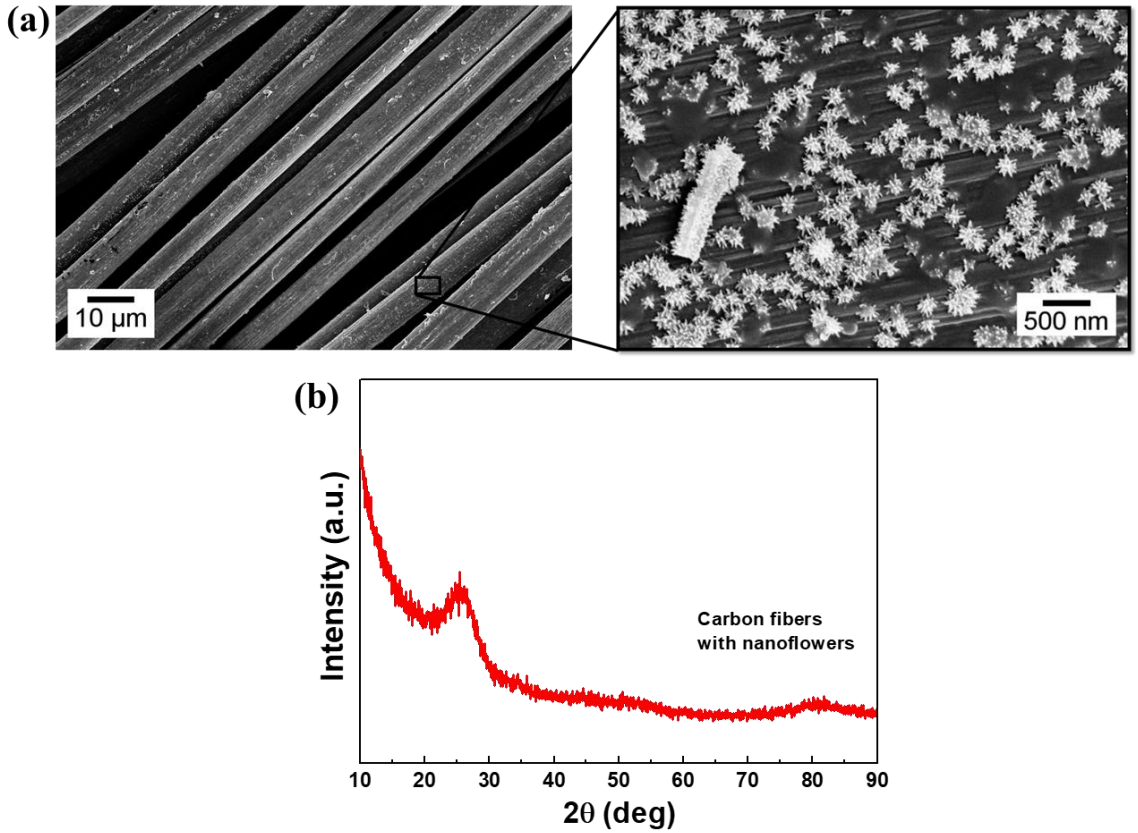

Figure 3.18. (a) SEM images and (b) XRD pattern of nanoflowers grown on carbon fibers by the hydrothermal synthesis with solution A for 24 hours.

3.2.3. Conclusions

In summary, several seed-layers were tested for the synthesis of the ZTO nanostructures. It was seen, in general, that the structures grown on the seed-layers were different than those obtained with the seed-layer free hydrothermal method (under similar synthesis conditions) showing the effectiveness of the seed-layers in influencing its growth. Several types of structures were obtained such as $ZnSnO_3$ nanowires and Zn_2SnO_4 nanoparticles, octahedrons and nanowires.

Seed-layers with hexagonal structures (ZnO and Ti) and tetragonal structures (FTO and Sn) resulted in the growth of nanosheets of unidentified phase. Additionally, amorphous ZTO seed-layers also resulted in these nanosheets.

The seed-layers of stainless steel (both mesh and substrate) and Cu foil, which have a cubic phase, induced the growth of Zn_2SnO_4 phase (inverse spinel cubic structure). Different synthesis conditions resulted in nanostructures with different morphologies being that Zn_2SnO_4 nanowires were also successfully obtained. Nonetheless, for Cr and Ni seed-layers (both also having a cubic

structure) nanograss structures of an unidentified phase were achieved. Using Cu nanowires as seed-layers resulted in $ZnSnO_3$ nanowires, similarly to the seed-layer free synthesis, which can be related to the CuO monoclinic phase present in the Cu nanowires.

Additionally, carbon fibers as seed-layer promoted the growth of small flower-like nanostructures whose phase was not identified.

While there seems to be a correlation between the phase of the employed seed-layer and the resultant phase of the nanostructures, this can be further clarified by a proper identification of the so-far unidentified structures. Furthermore, when employing the seed-layers, it was generally seen that while shorter times favored the producing of nanostructures, longer times resulted in thin films with a nanostructured surface. This emphasizes the influence of the seed-layers in nanostructures' growth, not only by inducing the phase but also by accelerating the growth process.

3.3. Final remarks

This chapter focused on alternative synthesis' routes for achieving different types of nanostructures.

While the optimized conditions for the seed layer free synthesis in the conventional oven was shown as a viable method to achieve $ZnSnO_3$ nanowires, the employment of microwave irradiation as heating method allowed to significantly reduce the time of synthesis. Additionally, and aiming to achieve other types of nanostructures (and with a reasonable yield), alternative processing conditions, very distinct from those of the previous chapter, were tested. From these, Zn_2SnO_4 nanoparticles, Zn_2SnO_4 octahedrons and SnO_2 nanoparticles were synthesized. Moreover, synthesis of these nanostructures using the microwave system was also explored, with the similarity between the resultant structures showing the viability of this approach. A very significant reduction in the synthesis duration was seen for all cases, with decreases up to 20 h.

As another approach to achieve different types of nanostructures, the employment of seed-layers during the hydrothermal process was tested. Several seed-layers were explored which allowed to achieve ZTO nanostructures with different morphologies and phases, namely Zn_2SnO_4 nanowires which had not been achieved by the seed-layer free syntheses, emphasizing the influence of the seed-layers in the nanostructures' growth. While some nanostructures' phases were not identified, there seemed to be, in general, a correlation between the phase of the employed seed-layer and the achieved nanostructures. Therefore, the direct growth of ZTO nanostructures in the seed-layers presented as an interesting method for inducing the desired type of nanostructures, being suitable for direct integration in devices by proper patterning of the seed-layer materials.

3.4. References

1. Bilecka, I. & Niederberger, M. Microwave chemistry for inorganic nanomaterials synthesis. *Nanoscale* **2**, 1358–1374 (2010).

2. Chen, D., Wang, Q., Shen, G., Wang, R. & Shen, G. Ternary oxide nanostructured materials for supercapacitors : a review. *J. Mater. Chem. A Mater. energy Sustain.* **3**, 10158–10173 (2015).

3. Wojnarowicz, J., Chudoba, T., Gierlotka, S. & Lojkowski, W. Effect of Microwave Radiation Power on the Size of Aggregates of ZnO NPs Prepared Using Microwave Solvothermal Synthesis. *Nanomaterials* **8**, 343 (2018).

4. Lehnen, T., Zopes, D. & Mathur, S. Phase-selective microwave synthesis and inkjet printing applications of Zn2SnO4 (ZTO) quantum dots. *J. Mater. Chem.* **22**, 17732 (2012).

5. Chen, D., Wang, Q. & Shen, G. Ternary oxide nanostructured materials for supercapacitors : a review. *J. Mater. Chem. A Mater. energy Sustain.* **3**, 10158–10173 (2015).

6. Mingos, D. M. P. & Baghurst, D. R. Applications of microwave dielectric heating effects to synthetic problems in chemistry. *Chem. Soc. Rev.* **20**, 1 (1991).

7. Kappe, C. O. Controlled microwave heating in modern organic synthesis. *Angew. Chemie - Int. Ed.* **43**, 6250–6284 (2004).

8. Kappe, C. O., Dallinger, D. & Murphree, S. S. Microwave Synthesis - An Introduction. in *Practical Microwave Synthesis for Organic Chemists* 1–9 (Wiley-VCH Verlag GmbH & Co. KGaA, 2009).

9. Pimentel, A. *et al.* Microwave Synthesized ZnO Nanorod Arrays for UV Sensors: A Seed Layer Annealing Temperature Study. *Materials (Basel).* **9**, 299 (2016).

10. Pimentel, A. *et al.* Synthesis of Long ZnO Nanorods under Microwave Irradiation or Conventional Heating. *J. Phys. Chem. C* **118**, 14629–14639 (2014).

11. Pimentel, A. *et al.* Effect of solvents on ZnO nanostructures synthesized by solvothermal method assisted by microwave radiation: a photocatalytic study. *J. Mater. Sci.* **50**, 5777–5787 (2015).

12. Nunes, D. *et al.* Photocatalytic behavior of TiO2 films synthesized by microwave irradiation. *Catal. Today* **278**, 262–270 (2016).

13. Nunes, D. *et al.* Cu 2 O polyhedral nanowires produced by microwave irradiation. *J. Mater. Chem. C* **2**, 6097 (2014).

14. Xiao, L. *et al.* Microwave assisted fast and facile synthesis of SnO2 quantum dots and

their printing applications. *Chem. Commun.* **46**, 6509–6511 (2010).

15. Nehru, L. C. & Sanjeeviraja, C. Processing Research Controllable growth of Zn2SnO4 nanostructures by urea assisted microwave-assisted solution combustion process. **14**, 606–609 (2013).

16. Annamalai, A., Carvalho, D., Wilson, K. C. & Lee, M.-J. Properties of hydrothermally synthesized Zn2SnO4 nanoparticles using Na2CO3 as a novel mineralizer. *Mater. Charact.* **61**, 873–881 (2010).

17. Men, H. *et al.* Fast synthesis of ultra-thin ZnSnO3 nanorods with high ethanol sensing properties. *Chem. Commun.* **46**, 7581 (2010).

18. Lo, M.-K., Lee, S.-Y. & Chang, K.-S. Study of ZnSnO3-Nanowire Piezophotocatalyst Using Two-Step Hydrothermal Synthesis. *J. Phys. Chem. C* **119**, 5218–5224 (2015).

19. Dharmadasa, R., Tahir, A. A. & Wijayantha, K. G. U. Single Step Growth and Characterization of Zinc Oxide, Tin Oxide, and Composite (ZnxSn1−xOy) Nanoplate and Nanocolumn Electrodes. *J. Am. Ceram. Soc.* **94**, 3540–3546 (2011).

20. Habibi, M. H., Mardani, M., Habibi, M. & Zendehdel, M. Enhanced photovoltage (Voc) of nano-structured zinc tin oxide (ZTO) working electrode prepared by a green hydrothermal route for dye-sensitized solar cell (DSSC). *J. Mater. Sci. Mater. Electron.* **28**, 3789–3795 (2017).

21. Wang, Y.-T. & Chang, K.-S. Piezopotential-Induced Schottky Behavior of Zn1−xSnO3 Nanowire Arrays and Piezophotocatalytic Applications. *J. Am. Ceram. Soc.* **99**, 2593–2600 (2016).

22. Li, Z. *et al.* Vertically building Zn2SnO4 nanowire arrays on stainless steel mesh toward fabrication of large-area, flexible dye-sensitized solar cells. *Nanoscale* **4**, 3490–4 (2012).

23. Santos, R. Copper nanowires for next generation transparent conductors (Master Thesis). (Faculdade de Ciências e Tecnologia, 2016).

24. Zhang, B. *et al.* A Facile Self-assembly Synthesis of Hexagonal ZnO Nanosheet Films and Their Photoelectrochemical Properties. *Nano-Micro Lett.* **8**, 137–142 (2016).

25. Liu, Y. *et al.* Hierarchical SnO2 nanostructures made of intermingled ultrathin nanosheets for environmental remediation, smart gas sensor, and supercapacitor applications. *ACS Appl. Mater. Interfaces* **6**, 2174–2184 (2014).

26. Cai, D. *et al.* Enhanced performance of supercapacitors with ultrathin mesoporous NiMoO4 nanosheets. *Electrochim. Acta* **125**, 294–301 (2014).

27. Wang, W.-W., Zhu, Y.-J. & Yang, L.-X. ZnO–SnO2 Hollow Spheres and Hierarchical Nanosheets: Hydrothermal Preparation, Formation Mechanism, and Photocatalytic

Properties. *Adv. Funct. Mater.* **17**, 59–64 (2007).

28. Chen, Y. *et al.* An evolution from 3D face-centered-cubic ZnSnO3 nanocubes to 2D orthorhombic ZnSnO3 nanosheets with excellent gas sensing performance. *Nanotechnology* **23**, 415501 (2012).

29. Ghosh, R. *et al.* Multifunctional Ag nanoparticle decorated Si nanowires for sensing, photocatalysis and light emission applications. *J. Colloid Interface Sci.* **532**, 464–473 (2018).

30. Ke, Q. *et al.* 3D TiO2@Ni(OH)2 Core-shell Arrays with Tunable Nanostructure for Hybrid Supercapacitor Application. *Sci. Rep.* **5**, 13940 (2015).

Chapter 4 – $ZnSnO_3$ Nanowires for Energy Harvesting and Electronic Applications

In this Chapter it is described the application in energy and electronic devices of the synthetized $ZnSnO_3$ nanowires, from the optimized hydrothermal method as presented in Chapter 2. Due to its interesting properties as a semiconductor, several applications can be explored for this material, nonetheless, the $ZnSnO_3$ phase is well-known as a piezoelectric material. In this regard, the first part of this Chapter presents energy harvester devices fabricated with a composite of $ZnSnO_3$ nanowires with a micro-structured film of PDMS. An electrical characterization of the nanowires is then presented on the Chapter. Next on the chapter, and even if piezoelectric devices can be considered as the most promising application for this material, its multifunctionality is shown by its application on resistive switching memory devices. The fabrication and characterization of the devices were performed in the clean room facilities and laboratory resources of CEMOP and CENIMAT.

The following sub-sections 4.1 (energy harvesting), 4.2 (electrical characterization) and 4.3 (resistive switching devices) are based on the following papers, in respective order:

- **A. Rovisco**, A. dos Santos, T. Cramer, J. Martins, R. Branquinho, H. Águas, B. Fraboni, E. Fortunato, R. Martins, R. Igreja and P. Barquinha, Piezoelectricity Enhancement of Nanogenerators based on PDMS and $ZnSnO_3$ Nanowires through Micro-structuration, under revision ACS Applied Materials and Interfaces 2019
- **A. Rovisco**, R. Branquinho, J. Martins, M. João Oliveira, D. Nunes, E. Fortunato, R. Martins and P. Barquinha, Seed-Layer Free Zinc Tin Oxide Tailored Nanostructures for Nanoelectronic Applications: Effect of Chemical Parameters. *ACS Appl. Nano Mater.* **1**, 3986–3997 (2018), DOI: 10.1021/acsanm.8b00743
- **A. Rovisco**, J. Martins, A Kiazadeh, R. Branquinho, E. Fortunato, R. Martins and P. Barquinha, $ZnSnO_3$ nanowires resistive switching memories, under preparation 2019

4.1. Piezoelectric energy harvesters based on a micro-structured film of PDMS and $ZnSnO_3$ nanowires

4.1.1. Abstract

The current trend for smart, self-sustainable and multifunctional technology demands for the development of energy harvesters based on widely available and environmentally friendly materials. In this context, $ZnSnO_3$ nanostructures show a promising potential due to their high polarization, which can be explored in hybrid piezoelectric and triboelectric devices. Nevertheless, a pure phase of $ZnSnO_3$ is hard to achieve due to its metastability and obtaining it in the form of nanowires is even more challenging. Although some groups have already reported the mixing of $ZnSnO_3$ nanostructures with polydimethylsiloxane (PDMS) to produce a nanogenerator, the resultant polymeric film is usually flat and does not take advantage of an enhanced triboelectric contribution achieved through its micro-structuration. Herein, a micro-structured composite of nanowires synthesized by a seed-layer free hydrothermal route mixed with PDMS ($ZnSnO_3$@PDMS) is proposed to produce energy harvesters. The performance of the harvester with the optimized micro-structuration reaches an output voltage, current, and instantaneous power density of 120 V, 13 μA, and 230 $\mu W \cdot cm^{-2}$, respectively. The micro-structuration introduced herein has a double effect of enhancing the piezoelectric effect of the $ZnSnO_3$ nanowires and increasing the triboelectric effect of PDMS. The performance of this harvester enables lighting up multiple LEDs, thus proving great potential for wearables and portable electronics.

4.1.2. Introduction

Nowadays, there is an increasing demand for smart, self-sustainable and multifunctional technology to meet near-future concepts such as internet-of-things (IoT), while still desiring low-cost and compact devices. For this, an increasing number of objects with embedded electronics, sensors and connectivity is required. Developing self-powered sensors that can use the ambient environmental energy may be the key for these systems, allowing also the preservation of global environment and sustainable economic growth.[1]

One great renewable electricity source is the vibration energy harvesting, which has been explored essentially from electromagnetic, electrostatic and piezoelectric transduction.[2] Electromagnetic energy harvesters are the least reported ones, with an output voltage that is poorer when compared with the other two types, despite being the most indicated for stimuli with lower frequencies.[3] Piezoelectric nanogenerators (PENG) are the most used transducers for mechanical vibrations, human motion, stream flow and acoustic noise.[4] This type of energy harvester provides higher output voltages, being however more efficient for high frequencies.[1,3,5] Triboelectric effect consists in the electric potential difference established when a periodic gap or

mismatch is induced by friction between two contacted surfaces with opposite triboelectric polarities. In a triboelectric nanogenerator (TENG), this physical contact creates electrostatic charges, driving the electrons to flow back and forth between back-coated electrodes, and this phenomenon is more efficient for a low frequency range.[1,2] Therefore, PENGs and TENGs have a high potential for different applications such as sustainable energy sources, biomedical systems and smart sensors.[6]

Several materials have been used for piezoelectric energy harvesters, being the most common $Pb(Zr,Ti)O_3$ (PZT), ZnO, $ZnSnO_3$, $BaTiO_3$ and GaN. Although PZT is the one with the highest piezoelectric constant, its conductivity is low and it is environmentally harmful.[4] When looking for sustainable options it is important to have in mind the critical raw materials, avoiding not only the ones which are toxic and non-recyclable but also those which are scarce. Within these premises, Zn-based metal oxides such as ZnO and $ZnSnO_3$ are some of the most promising materials. ZnO has been widely used due to its easy synthesis and because of the coupling of piezoelectric and semiconductor properties.[1,7–9] $ZnSnO_3$ appears to be an even better candidate for energy harvesting applications, having a higher polarization (≈59 μC/cm^2) along the c-axis.[10] Moreover, the advantages of zinc tin oxide (ZTO) are numerous. Not only both zinc and tin are abundant and recyclable, but also being ZTO a ternary oxide, its properties can be tuned by adjusting the cationic ratio, boosting its multifunctionality. Depending on the synthesis method, different morphologies can be produced.[11,12] $ZnSnO_3$ can even crystallize in two different structures, rhombohedral and orthorhombic.[11,13,14] However, when subjected to high temperatures (> 700 °C) $ZnSnO_3$ can suffer a phase transformation into Zn_2SnO_4.[15] Moreover, the presence of two cations in ZTO makes the synthesis of a pure single phase very hard to achieve. Several reports about the application of $ZnSnO_3$ micro and nanostructures in piezo and triboelectric nanogenerators were published in the last years. $ZnSnO_3$ nanocubes have been the most reported structure with piezoelectric and piezoresistive effects for applications in energy harvesting and sensitive human motion sensors.[1,4,16–23] More recently, in 2017 Guo *et al.* reported piezo-nanogenerators using flat films of polydimethylsiloxane (PDMS) mixed with $ZnSnO_3$ nanoplates, produced by hydrothermal method, showing the difficulty to obtain a single and pure phase of this material by solution process [4]. Concerning $ZnSnO_3$ micro/nanowires, due to the difficulty to produce this type of structures by solution processes, there are only a few reports of generators making use of vapor phase-based materials. In 2012 and 2013 Wu *et al.* reported nanogenerators of $ZnSnO_3$ microbelts, produced by thermal evaporation at 900 °C, generating a power output around 11 μW·cm^{-3}.[16,18,24] Furthermore, these $ZnSnO_3$-based nanogenerators are generally based in flat films of a mixture of PDMS or other polymer and the oxide nano or micro-structures,[4,18,21–23,25–27] or simply use PDMS to encapsulate such structures,[16,24] therefore not taking advantage of the micro-structuration of the polymeric film to increase the efficiency in the transduction of a force into an electrical output.[28–34]

As presented in chapter 2, a seed-layer free hydrothermal route at 200 °C was optimized to produce well-controlled $ZnSnO_3$ nanowires.[14,35] Also in a previous work of our group, the micro-

structuration of PDMS film by laser engraving technique was studied and optimized to produce piezoresistive sensors, where several architectures were developed.[36–38] To the best of the authors' knowledge, this is the first report on the use of $ZnSnO_3$ nanowires synthesized by a seed-layer free hydrothermal route for energy harvesters. Furthermore, a new approach is explored herein, based in the micro-structuration of a robust composite of nanowires mixed with PDMS ($ZnSnO_3$@PDMS) to improve the efficiency of the force delivery to the nanowires, thus increasing their piezoelectric signal, and to enhance the triboelectric effect. By taking advantage of both effects, the device is able to work under a wider range of frequencies. The composite shows a great performance for piezo/triboelectric harvesters, especially when it is micro-structured, highlighting its potential for energy harvesting applications. Moreover, it presents a significant boost on the energy harvesting capability compared to a ZnO@PDMS composite, which is a clear demonstration of the advantages of $ZnSnO_3$ over ZnO for these applications.

4.1.3. Experimental Section

$ZnSnO_3$ nanowires' synthesis

The $ZnSnO_3$ nanowires were produced by hydrothermal synthesis in a conventional oven, using $SnCl_4.5H_2O$ from Riedel-de Haën (0.01 M), $ZnCl_2$ from Merck (0.02 M) and NaOH from Sigma-Aldrich (0.24 M) as precursors, and H_2O and ethylenediamine from Sigma-Aldrich in a volume proportion of 7.5:7.5 mL as solvents, at 200 °C for 24 hours, based on the optimized process presented in Chapter 2.[14,35] The resultant precipitate of nanowires' syntheses was centrifuged at 6000 rpm and washed several times with deionized water and isopropyl alcohol, alternately. The nanostructures were finally dried at 60 °C, in vacuum, for 2 hours.

ZnO nanowires synthesis

For ZnO nanostructures synthesis zinc acetate dihydrate ($Zn(CH_3COO)_2{\cdot}2H_2O$; 0.45 M) from Sigma-Aldrich was dissolved in deionized water and sodium hydroxide (NaOH; 8 M) from Eka was added (solution A). In order to stabilize the nanostructures, to prevent the formation of agglomerates and to help with the nanorods length growth, a surfactant, sodium lauryl sulfate ($NaC_{12}H_{25}SO_4$) from Scharlau was used, being also dissolved in deionized water with a molar concentration of 1.04 mM (solution B). The final solution was achieved mixing 2 mL of solution A, 5 mL of solution B and 10 mL of deionized water. The mixture was then transferred into a Teflon vessel (with a capacity of 50 mL). Three vessels were loaded at the same time into a CEM Mars One microwave, with a capacity for 12 vessels, being the microwave parameters set as 110 °C of temperature, 600 W of power, 7 min until reaching the set temperature and then 40 min of synthesis. The resultant precipitate of nanowires' syntheses was centrifuged at 4000 rpm and washed several times with deionized water and isopropyl alcohol, alternately. The nanostructures were finally left drying at room temperature for at least 72 h.[39]

Nanogenerators fabrication

The $ZnSnO_3$ nanowires were mixed with PDMS with a weight ratio of 20 wt.%. Then, the curing agent was added to the previous mixture in a 1:10 w/w ratio of curing agent to elastomer. The mixture was then spin-coated onto each engraved acrylic mold at 250 rpm for 90 s, and degassed before curing the $ZnSnO_3$@PDMS composite in an oven at 85 °C. After 30 minutes of curing, a commercial PET/ITO substrate was placed on top of composite films, which were left in the oven until completing the curing. Four acrylic molds were used, combining aligned or misaligned micro-cones cavities with pitches of 150 µm or 300 µm. These acrylic molds were produced on a previous work.[36] The functional area of the fabricated devices is 4 cm^2. A composite of ZnO@PDMS was also explored to produce devices, aiming the comparison of ZnO and ZTO nanowires performance. A representative schematic of the devices' fabrication is illustrated in **Figure 4.1**.

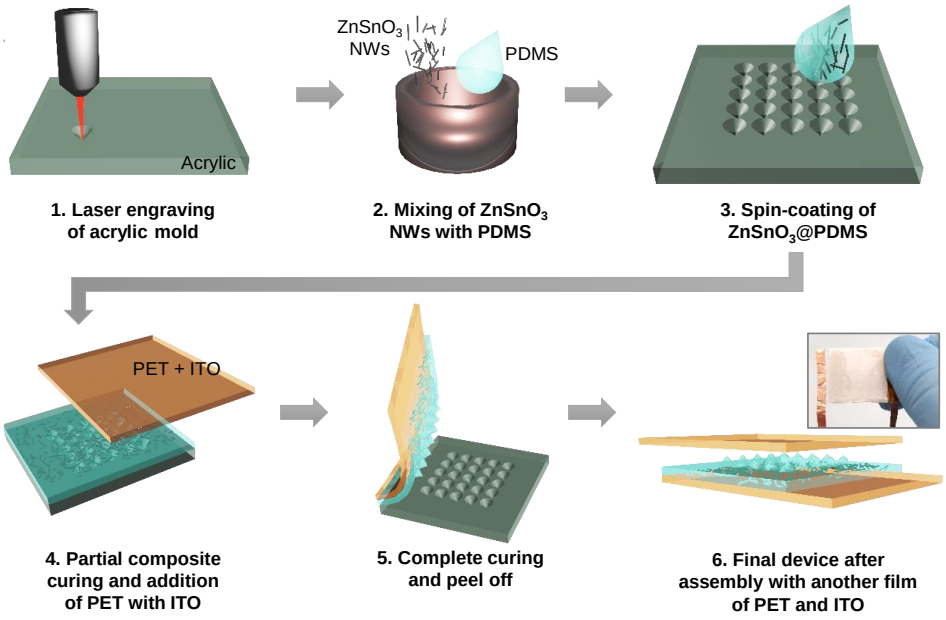

Figure 4.1. Fabrication steps of a micro-structured nanogenerator. The inset is a photograph of one nanogenerator.

Materials characterization

The structural characterization of the produced $ZnSnO_3$@PDMS composite was done using a PANalytical's X'Pert PRO MRD diffractometer with Cu Ka radiation. The XRD data was acquired in the 10 ° – 90 ° 2θ range with a step size of 0.033 °. The morphology and element analysis (SEM/EDS) were performed with a Carl Zeiss AURIGA CrossBeam (FIB-SEM) workstation.

Nanogenerators characterization

A constant force of approximately 10 N was applied by a home-made pushing machine (**Figure 4.2**) with a linear motor (and a pushing area of 0.3 cm^2) at a frequency ranging from 0.5 Hz to 2 Hz to all devices. Besides the pushing machine, in order to test the devices with

different forces, a pen was used to apply human force between 12 N and > 100 N in an area of 0.7 cm^2. The output voltage was collected by a digital oscilloscope (Tektronix TDS 2001C), while the current output signals were acquired using a Keysight B1500A system. The force applied in the produced devices was estimated using a commercial force sensing resistor from Interlink Electronics (Ref. SEN05003).

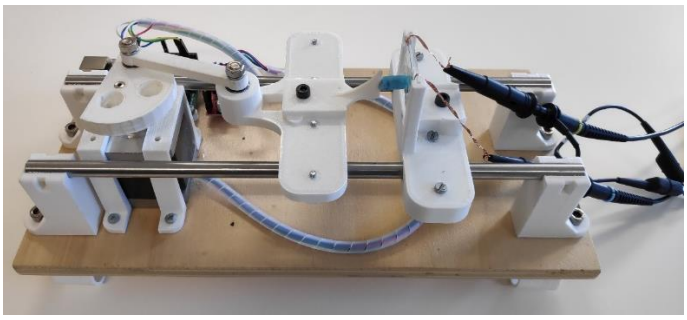

Figure 4.2. Photograph of the pushing machine used for the measurements.

4.1.4. Results and analysis

Characterization of the nanowires and the composite films

Figure 4.3 shows the XRD patterns and morphology of $ZnSnO_3$ nanowires. These structures have an average length of 600 nm and diameter of 65 nm. Concerning the crystalline identification, although the #28-1486 card was deleted from ICDD database, this card fits well with $ZnSnO_3$ orthorhombic phase. In ref [14] this identification was proven. Moreover, this card has been also widely reported as $ZnSnO_3$ orthorhombic phase, emphasizing the identification.[17,20,40–42]

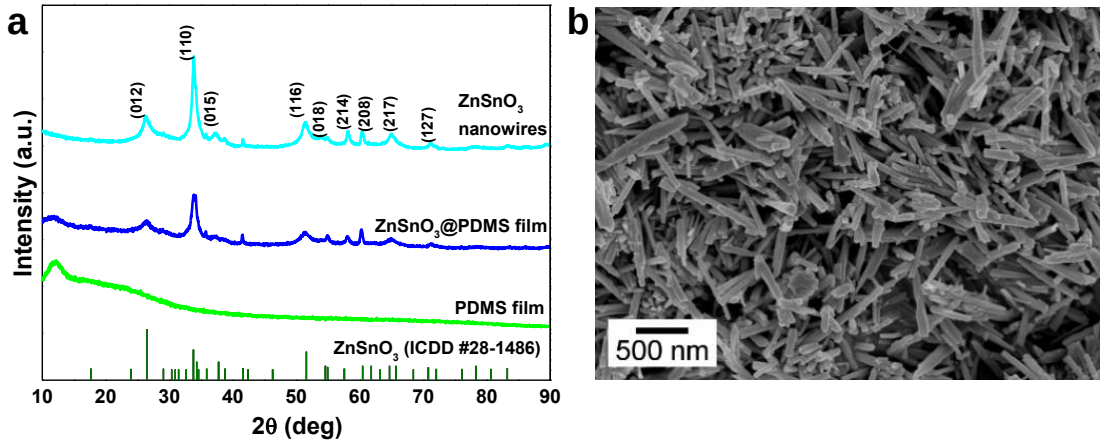

Figure 4.3. (a) XRD patterns of PDMS, $ZnSnO_3$ nanowires@PDMS film and $ZnSnO_3$ nanowires before mixed with PDMS. The identification was following ICDD card #28-1486 as explained in ref [14]. (b) SEM image of $ZnSnO_3$ nanowires.

Figure 4.4a shows the SEM image of the ZnO nanowires before being mixed with PDMS, while in **Figure 4.4**b the surface of ZnO nanowires@PDMS film is shown, being possible to observe the nanowires, which seem to be aligned horizontally. In **Figure 4.4**c the XRD patterns of ZnO nanowires, ZnO@PDMS film, and just PDMS film are presented. A pure hexagonal ZnO phase is identified by the ICDD card #36-1451.

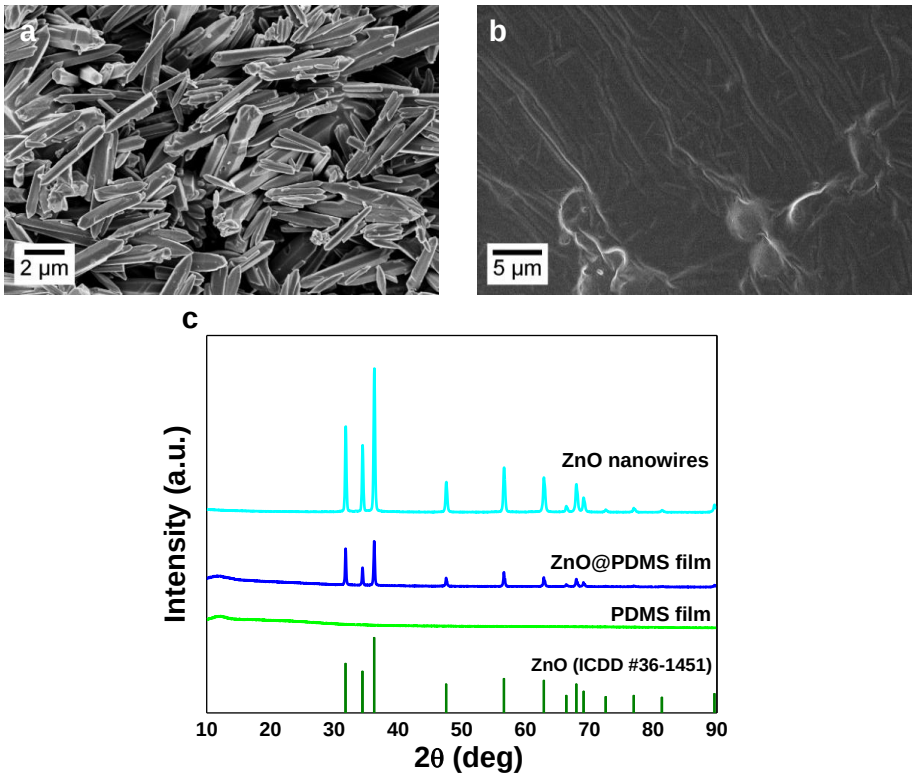

Figure 4.4. Characterization of ZnO nanowires and ZnO nanowires@PDMS film: (a and b, respectively) SEM images and (c) XRD pattern. The identification was following ICDD card #36-1451.

Piezoelectricity of $ZnSnO_3$ nanowires

The piezoelectric constant (d_{33}) of the $ZnSnO_3$ nanowires was determined by piezoresponse force microscopy (PFM) measurements, performed in the University of Bologna, with a value of 23 ± 4 pm/V having been achieved. This value compares fairly well with what has been reported in the literature for 1D nanostructures produced by hydrothermal synthesis, as resumed by Ghasemian *et al.* and presented in Table 4.1.[43] In fact, the obtained d_{33} (23 ± 4 pm/V) is surpassed only by the well-known $BaTiO_3$ (31.1 pm/V) and $LiNbO_3$ (25 pm/V) which contain critical raw materials, highlighting the interest in this material for piezoelectric applications.

Table 4.1. Piezoelectric coefficient of some of 1D piezoelectric nanostructures produced by hydrothermal synthesis.[43]

Material	d_{33} (pm/V)	Ref.
$ZnSnO_3$	23 ± 4	This work
BNT	15	[43]
$KNbO_3$	10.8	[44]
SbSI	12	[45]
$Na_6(W_6O_{19})(SeO_3)_2$	12	[46]
$NaNbO_3$	4	[47]
$BaTiO_3$	31.1	[48]
$LiNbO_3$	25	[49]
$KNbO_3$	11.6	[50]

Devices characterization

Optimization of the devices' architecture

Herein, two different nanogenerator architectures (an unstructured and a micro-structured one) were explored to study the influence of the micro-structuration of the $ZnSnO_3$@PDMS composite in the devices' performance. For the unstructured $ZnSnO_3$@PDMS device the piezoelectric effect of the nanowires is emphasized, while for the micro-structured composite the triboelectric effect is potentiated. For the latter case, four different designs were explored, with aligned or misaligned micro-cones with different pitches (150 µm or 300 µm).

For a better comparison between the devices and to get more reproducible results, a pushing machine was used with a pushing force of 10 N applied at a frequency of 2 Hz, with a pushing area of 0.3 cm^2. **Figure 4.5**a and b show the output voltage and current of devices with the different configurations previously described. In general, all the configurations present a reproducible output, both voltage and current. The insets in **Figure 4.5** present the voltage and current output of the device that presented the best performance (aligned cones with a pitch of 300 µm), which shows a typical signal of a piezoelectric or triboelectric device, with a positive peak originated from the pushing force and a negative peak resultant from the force releasing.

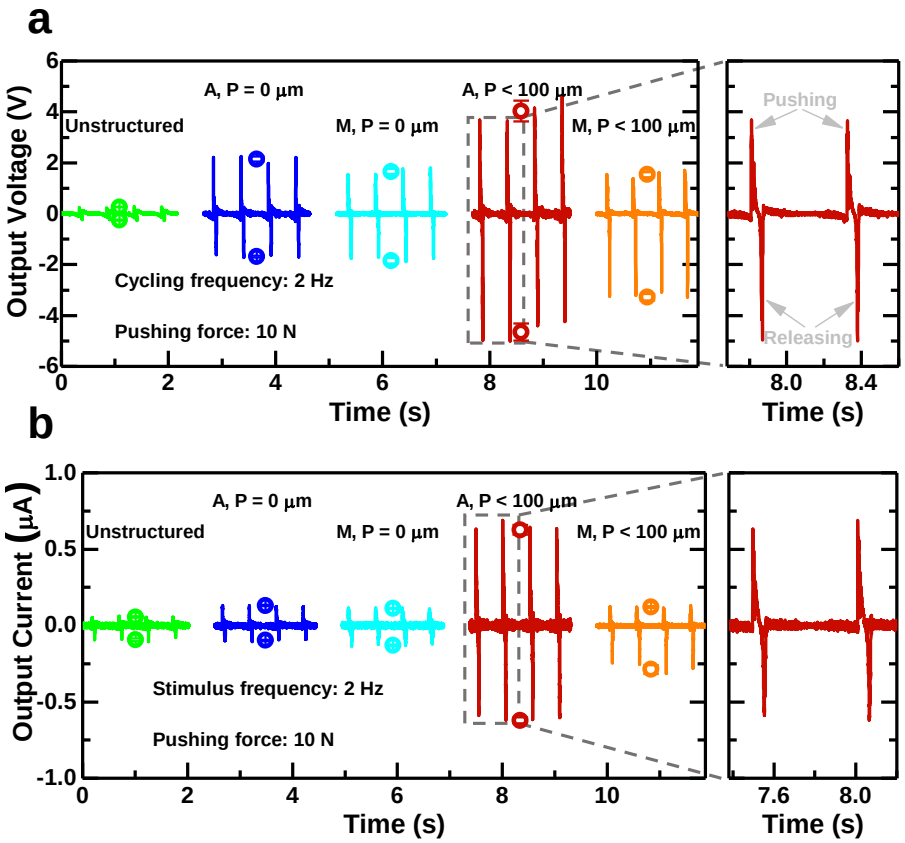

Figure 4.5. Output (a) voltage and (b) current generated from the $ZnSnO_3$@PDMS device with different configurations: unstructured films, micro-structured films with aligned or misaligned micro-cones with a pitch of 300 μm. The insets show a magnified view of output voltage and current from the $ZnSnO_3$@PDMS micro-structured films device with aligned micro-cones with a pitch of 300 μm. The circles represent average values with standard deviations (of 4 to 6 measurements) for positive and negative peaks. Abbreviations: A – Aligned, M – Misaligned, P – Pitch.

The unstructured device has an evident piezoelectric output that comes from the $ZnSnO_3$ nanowires, showing a voltage and current output that is twice as high as that of a device without nanowires (**Figure 4.6** and **Table 4.2**). Still, the results highlight that the presence of a micro-structuration in the devices gives rise to a higher output when compared to the unstructured devices, suggesting two possible effects. Firstly, it is thought that the micro-structuration of the films concentrates the compressive forces into the cones, and so upon their compression and deformation, the nanowires dispersed in the micro-structures undergo a greater compression/bending, thus increasing their piezoelectric signal. The compressive forces do not actuate so effectively upon the nanowires in unstructured devices, which is illustrated in **Figure 4.7**. Secondly, the micro-structures contribute for the enhancement of the triboelectric effect due to the air gaps created between the cones and the PET/ITO electrode. Furthermore, devices with aligned cones present a slightly higher voltage than devices with misaligned cones, while for current output the alignment does not seem to produce a significant influence.

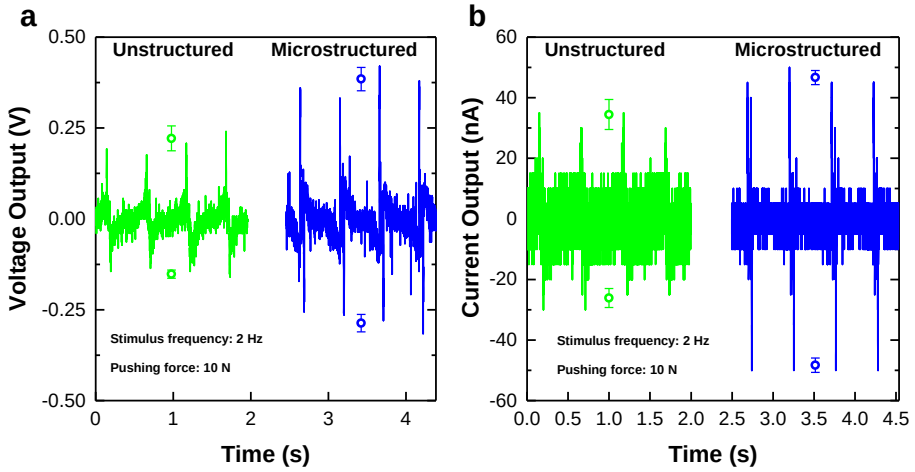

Figure 4.6. Output (a) voltage and (b) current signals of unstructured (green) and micro-structured (with aligned micro-cones with a pitch of 300 µm, blue) PDMS films.

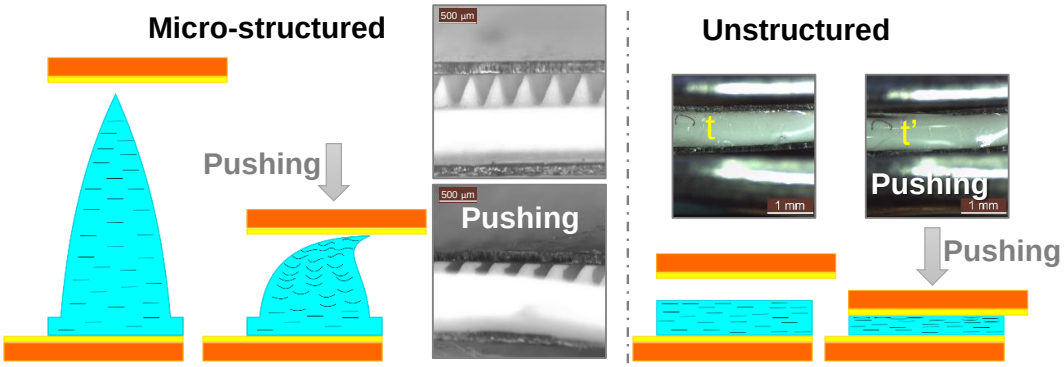

Figure 4.7. Proposed schematic of force deformation for a micro-structured and unstructured device and photographs showing the cross-section of the devices before and after pushing force. Note that the images are not at scale. t (782 µm) and t' (724 µm) are the thickness of the unstructured $ZnSnO_3$@PDMS film before and after pushing, respectively.

Table 4.2 presents the peak-to-peak output voltage and current values of all the devices shown in **Figure 4.5** and **Figure 4.6**. The configuration with aligned micro-cones with a pitch of 300 µm has the best performance with a peak-to-peak voltage of 8.7 V and a peak-to-peak current of 1.25 µA (an instantaneous power density of 3.24 $\mu W \cdot cm^{-2}$), possibly due to a higher air-gap between the base of the micro-cones and the PET/ITO electrode. This air-gap is smaller for the pitch of 150 µm due to a fusion effect that results from the fabrication process of these films (**Figure 4.8**).[36] Additionally, the micro-cones for a pitch of 300 µm are higher, and so there is a greater volume to be compressed. Consequently, a greater number of nanowires may be bent, thus increasing their piezoelectric signal.

Table 4.2. Piezoelectric/triboelectric peak-to-peak voltage and current from the devices shown in **Figure 4.5** and **Figure 4.6**.

Design	Peak-to-Peak Voltage (V)	Peak-to-Peak Current (μA)
Unstructured PDMS	0.40 ± 0.05	0.06 ± 0.01
Unstructured $ZnSnO_3$@PDMS	0.50 ± 0.02	0.15 ± 0.01
Micro-structured $ZnSnO_3$@PDMS (Aligned cones, Pitch = 150 μm)	3.80 ± 0.11	0.23 ± 0.01
Micro-structured $ZnSnO_3$@PDMS (Misaligned cones, Pitch = 150 μm)	3.50 ± 0.16	0.24 ± 0.01
Micro-structured $ZnSnO_3$@PDMS (Aligned cones, Pitch = 300 μm)	8.70 ± 0.12	1.25 ± 0.03
Micro-structured PDMS (Aligned cones, Pitch = 300 μm)	0.70 ± 0.05	0.10 ± 0.01
Micro-structured $ZnSnO_3$@PDMS (Misaligned cones, Pitch = 300 μm)	4.80 ± 0.15	0.41 ± 0.03

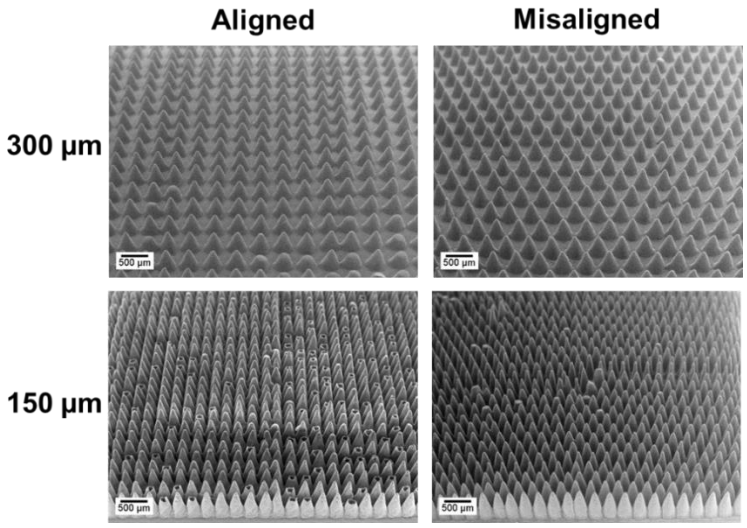

Figure 4.8. SEM images of micro-structured PDMS films.

The voltage and current outputs for the device with the optimized configuration (micro-structured film with aligned cones with a pitch of 300 μm) but with different composites ($ZnSnO_3$@PDMS, ZnO@PDMS or only PDMS) are shown in **Figure 4.9** to further investigate the origin of the output. ZnO was also used in the comparison due to its well-known piezoelectric effect and wide application.[1] A much higher output is observed for the $ZnSnO_3$@PDMS device when compared with the other two. Additionally, given the enhanced piezoelectric effect in the $ZnSnO_3$@PDMS device, it has a better performance than the one without nanowires, for which only triboelectricity is generating a signal, highlighting the role of the $ZnSnO_3$ nanowires piezoelectricity in the devices' performance.

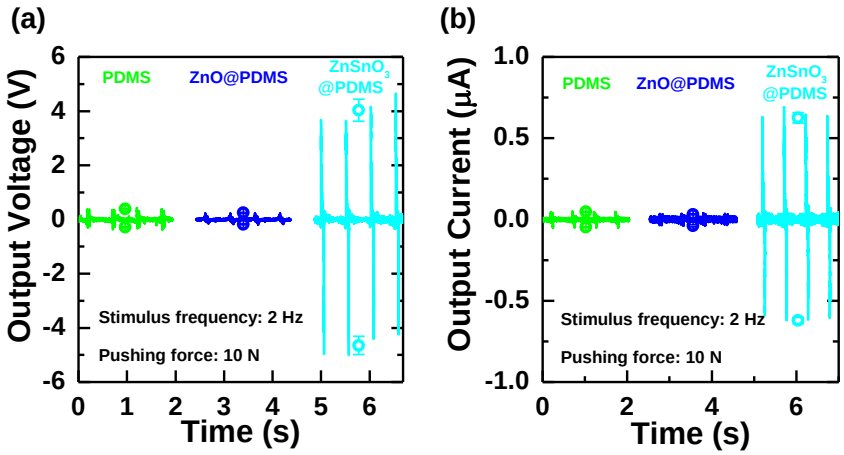

Figure 4.9. Output (a) voltage and (b) current generated from the PDMS, ZnO@PDMS and $ZnSnO_3$@PDMS micro-structured films devices with aligned micro-cones with a pitch of 300 µm. The circles represent average values with standard deviations (of 4 to 6 measurements) for positive and negative peaks.

Frequency and pushing force dependence

The voltage and current output variation with frequency is a well-known phenomenon for piezoelectric and/or triboelectric energy harvesters, and so it was investigated for the $ZnSnO_3$@PDMS device with the optimized configuration. These tests were done with the pushing machine applying a fixed force stimulus at a variable frequency, from 0.5 to 2 Hz. As shown in **Figure 4.10**a and b, both voltage and current output show a general trend to increase with increasing force stimulus frequency, reaching a maximum of 8.7 V and 1.25 µA with a pushing force of 10 N. This trend is in agreement with what has been reported for piezoelectric and triboelectric devices, which present higher output values with stimuli of greater frequencies, possibly due to charges accumulation in the electrode.[34,51,52] As it was previously verified, the optimized device has a constant and reproducible performance even for different pushing frequencies.

To stimulate the device with larger forces, different levels of tapping force using a pen (with an area of 0.7 cm^2) were tested. **Figure 4.10**c to f show the peak-to-peak voltage and current outputs obtained in these experiments. The results highlight that the nature of these manual stimuli is different from those applied by the pushing machine: while the first are more impulse like, the latter resemble continuous-like stimulus. Therefore, for similar forces applied manually (between 12 N and 15 N), the device has a higher voltage and current output with values of 31.2 V and 1.8 µA, corresponding to an instantaneous power density of 8.2 $\mu W \cdot cm^{-2}$. The maximum output of the device with this type of stimuli was ≈ 120 V and ≈ 13 µA, corresponding to an instantaneous power density of ≈ 230 $\mu W \cdot cm^{-2}$.

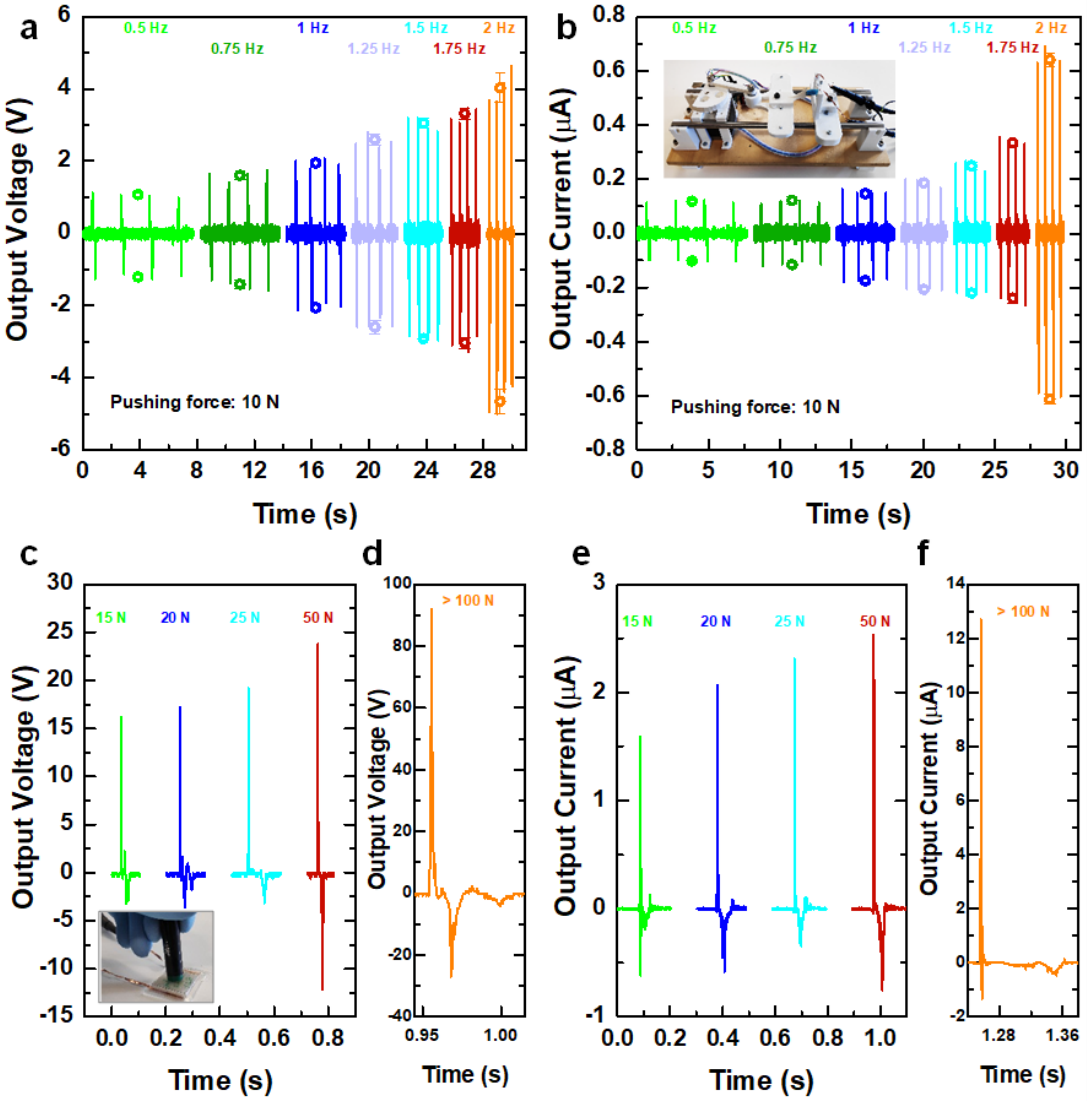

Figure 4.10. Output (a) voltage and (b) current generated from the $ZnSnO_3$@PDMS micro-structured films with aligned micro-cones with a pitch of 300 μm. The device was tested with a pushing force of 10 N applied at a frequency ranging from 0.5 to 2 Hz, with a step of 0.25 Hz using a pushing machine (inset). The circles represent average values with standard deviations (of 4 to 6 measurements) for positive and negative peaks. Output voltage generated applying a human force (c) from 15-50 N and (d) over 100 N using a pen (inset) to deliver the stimulus. Output current generated applying a human force (e) from 15-50 N and (f) over 100 N using a pen to deliver the stimulus.

Device stability

In order to study device stability over time 12000 cycles were applied for 100 minutes without interruption with the pushing machine, on a nanogenerator with the optimized $ZnSnO_3$@PDMS micro-structured films. As shown in **Figure 4.11**a and b, despite a slight variation in the output, the device presents a stable performance even after being pushed over 12000 cycles. A similar performance is observed for this device when repeating the same proceeding one month later, as illustrated by **Figure 4.11**c and d (comparing to **Figure 4.5**).

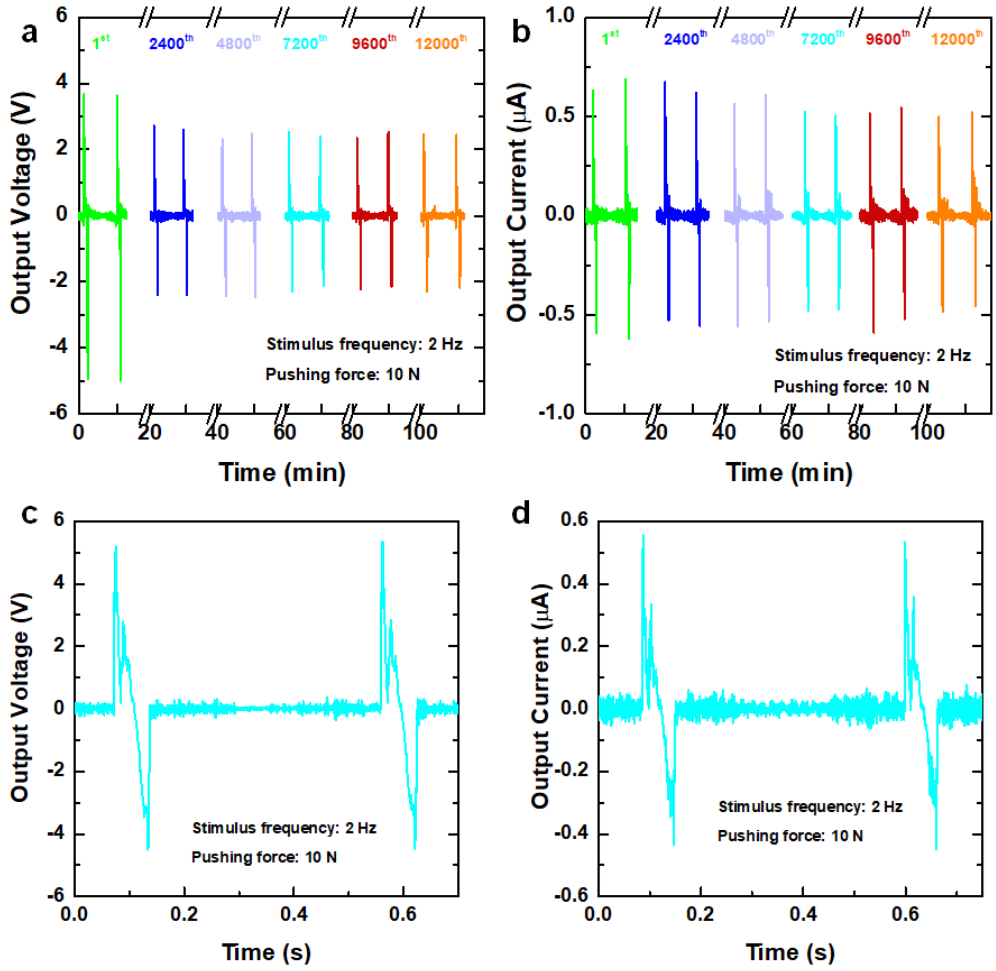

Figure 4.11. Output (a) voltage and (b) current generated from the $ZnSnO_3$@PDMS micro-structured films with aligned micro-cones with a pitch of 300 µm. The device was tested with a pushing force of 10 N applied at a frequency of 2 Hz for 12000 cycles (100 min) using a pushing machine. Output (c) voltage and (d) current generated from the $ZnSnO_3$@PDMS micro-structured films with aligned micro-cones with a pitch of 300 µm, one month after the measurements shown in **Figure 4.5**. The device was tested with a pushing force of 10 N applied at a frequency of 2 Hz using a pushing machine.

Proof of Concept

To test the device for a practical application it is relevant to investigate the electric power that the device can provide. Therefore, the output voltage, current, and instantaneous power of the device with the optimized configuration were evaluated under several load resistances, as shown in **Figure 4.12**a and b. The output current decreases with an increasing load resistance while the output voltage increases. The instantaneous power increases with the load resistance, reaching a maximum peak of 1 µW with 15 MΩ, then decreasing for higher load resistances.

The device with the optimized configuration was then directly connect to one white LED or five blue LEDs in series. The I-V curves of the single and five LEDs are shown in **Figure 4.13** and highlight that the single white LED needs at least 2.3 V and 1.56 µA to light up, while the five blue LEDs in series need 11.4 V and 0.13 µA. **Figure 4.12.**c and d show that after manually pushing the device either the single or the multiple LEDs in series could be light up, thus proving the applicability of the device as a power energy harvester and supplier.

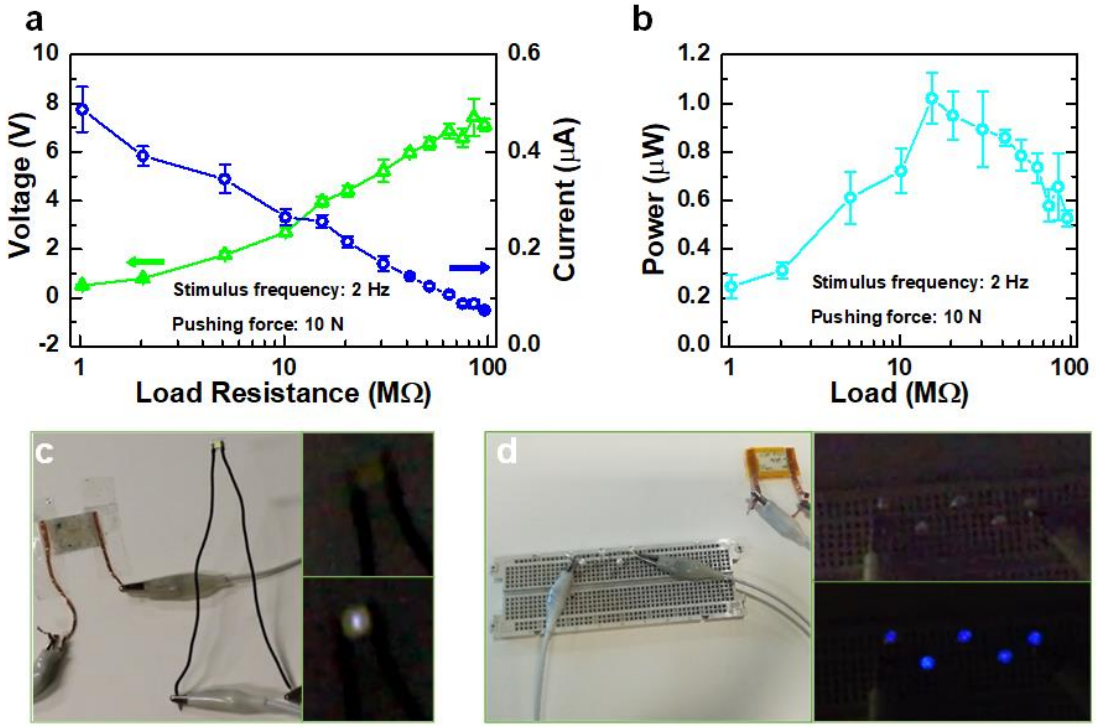

Figure 4.12. Output (a) voltage and current and (b) instantaneous power generated from the $ZnSnO_3$@PDMS micro-structured films with aligned micro-cones with a pitch of 300 μm under several load resistances. The device was tested with a pushing force of 10 N applied at a frequency of 2 Hz using a pushing machine. Photograph of a device directly connected to (c) a single LED and (d) five LEDs in series, with the respective insets showing the LED/LEDs off and on (driven by the energy of the device).

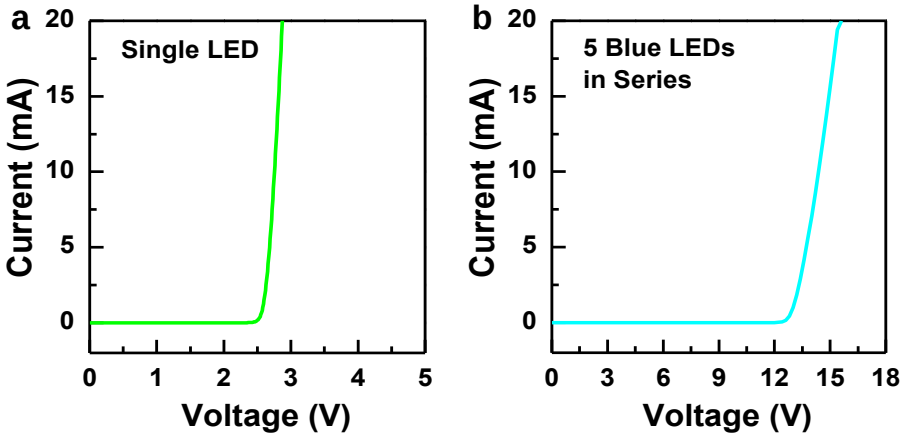

c

LEDs	Voltage (V)	Current (μA)
Single	2.3	1.56
5 in series	11.4	0.13

Figure 4.13. I-V curve of (a) a single (white) LED, and (b) five (blue) LEDs in series. (c) Table showing the necessary voltage and current outputs to turn on the LEDs. The I-V curves of commercial LEDs, used as practical applications of the fabricated $ZnSnO_3$ nanowires@PDMS devices, were obtained by applying voltage sweep, using a Keysight B1500A system.

Table 4.3 shows a comparison between the device with the best performance produced in this work with the literature. Although a direct comparison is not possible due to the lack of some information from other works, the device produced herein shows a high performance for energy harvesting from stimuli with a moderate force, compatible with everyday activities. For example, the harvester could be attached to the bottom of shoes to get energy from walking or running. The instantaneous power density reached herein is also one of the highest reported so far, and only the $ZnSnO_3$ nanocubes@PDMS composite reported by Wang *et al.* [25] has a higher response, but due to the lack of information and quantification about the applied force, a direct comparison is not feasible. Nevertheless, these results highlight the potential for powering portable electronics. Furthermore, given the higher flexibility of the wires morphology when compared with cubes or other structures, the optimization of the weight ratio between $ZnSnO_3$ nanowires and PDMS is expected to result in devices with a greater output for the same stimulus, when compared to those presented in **Table 4.3**. Another strategy to further maximize the performance of the devices is to align the $ZnSnO_3$ nanowires poles inside the PDMS matrix with an external electric field.

Table 4.3. Performance comparison of $ZnSnO_3$ nanostructures-based piezo/triboelectric harvesters.

Material	Stimulus/ Applied Force	Output Voltage	Output Current	Instantaneous Power Density	Year/Ref
Single-$ZnSnO_3$ microbelt@high temperature process	Compressive strain N/A	110 mV	80 nA	N/A	2012/[16]
Single-$ZnSnO_3$ microbelt@high temperature process	Compressive strain N/A	5.3 V	0.13 µA	11 $\mu W \cdot cm^{-3}$	2012/[18]
$ZnSnO_3$ nanocubes@PDMS	Motion of vehicle tires N/A	20 V	1 $\mu A \cdot cm^{-2}$	-	2014/[23]
$ZnSnO_3$/MWCNTs	Strain N/A	40 V	0.4 µA	10.8 $\mu W \cdot cm^{-3}$	2015/[22]
$ZnSnO_3$ nanocubes@PDMS	Linear motor / Bending N/A	400 V	28 µA	280 $\mu W \cdot cm^{-2}$	2015/[25]
$ZnSnO_3$ nanocubes@PVDF	Fatigue testing system 489 N	520 V	2.7 $\mu A \cdot m^{-2}$	-	2016/[26]
$ZnSnO_3$ nanocubes@PVC	Human finger N/A	40 V	1.4 µA	≈ 3.7 $\mu W \cdot cm^{-2}$	2016/[27]
$ZnSnO_3$ nanoplates@PDMS	Bending N/A	20 V	0.6 µA	-	2017/[4]
$ZnSnO_3$ Nanowires@PDMS	**Pen > 100 N**	**≈ 120 V**	**≈ 13 µA**	**≈ 230 $\mu W \cdot cm^{-2}$**	**This work**

4.1.5. Conclusions

Piezo/triboelectric nanogenerators were fabricated using a composite film of PDMS and $ZnSnO_3$ nanowires produced by hydrothermal synthesis at only 200 °C. The $ZnSnO_3$ nanowires piezoelectric properties were assessed through PFM measurements, with a d_{33} between 20 and 25 pm/V being determined. Several micro-structuration designs for the composite films were also studied to enhance the performance of the sensors. Due to the natural orientation of the nanowires in the PDMS film, the micro-cones helped to improve the piezoelectric signal coming from the extremities of the nanowires (c-axis) through an increased efficiency in the force transmission to the nanowires. Furthermore, the higher air-gap between the base of the micro-cones and the PET/ITO electrode enhances the triboelectric effect when compared to unstructured films. The combination of both effects results in a better performance achieved for the configuration with aligned micro-cones with a pitch of 300 µm, showing a peak-to-peak voltage around 9 V and a peak-to-peak current of 1.25 µA for a 10 N stimulus applied by a pushing machine at a frequency of 2 Hz. When stimulated manually with a pen (a force over 100 N), a maximum output of 120 V and 13 µA was achieved, with an estimated instantaneous power density of 230 $\mu W \cdot cm^{-2}$. This instantaneous power density is enough for practical applications, such as lighting up LEDs, showing a great potential for energy harvesting in wearables.

4.2. Electrical properties

As shown in Chapter 1, semiconductor nanowires have been increasingly used for electronic applications.[53] Nanowires, by confining 2 dimensions, limit the carrier's movement to a single dimension and the quantum-confinement effect increases the density of states. This allows for an elevated carrier mobility and reduces low-angle scattering resulting in an efficient electrical transport, especially desired for electronic applications.[54] Regarding these applications, one of the defining characteristics of a semiconductor material is its electrical resistivity. Thus, herein this property was analyzed in single nanowires and will be presented next.

4.2.1. Electrical characterization of $ZnSnO_3$ nanowires

Electrical measurements on single nanowires, although highly desirable for determining its electrical properties, presents itself as a real challenge. In literature the reported characterizations are mainly related to nanowires with lengths > 10 µm. In this work, we present electrical characterization of single nanowires with lengths below 1 µm. For this reason, the electrical characterization was performed inside an Auriga system (SEM) using 2-point probe structure with nanomanipulators, meaning that it was performed in vacuum. For these measurements the nanowires were drop-casted on a Si/SiO_2 substrate, after being dispersed in isopropyl alcohol, yielding a low concentration solution which was sonicated during 5 min. After drying, using a pick-and-place approach isolated nanowires were contacted by Pt electrodes, deposited using localized e-beam assisted decomposition of a $C_5H_4CH_3Pt(CH_3)_3$ precursor introduced close to the sample surface using a gas injector system. Kleindiek nanomanipulators with W tips were then used to access the current-voltage characteristics, together with a semiconductor parameter analyzer (Agilent 4155 C). **Figure 4.14** shows images of the SEM nanomanipulators and the W tips of the nanomanipulators contacting the Pt electrodes during electrical characterization of a single nanowire.

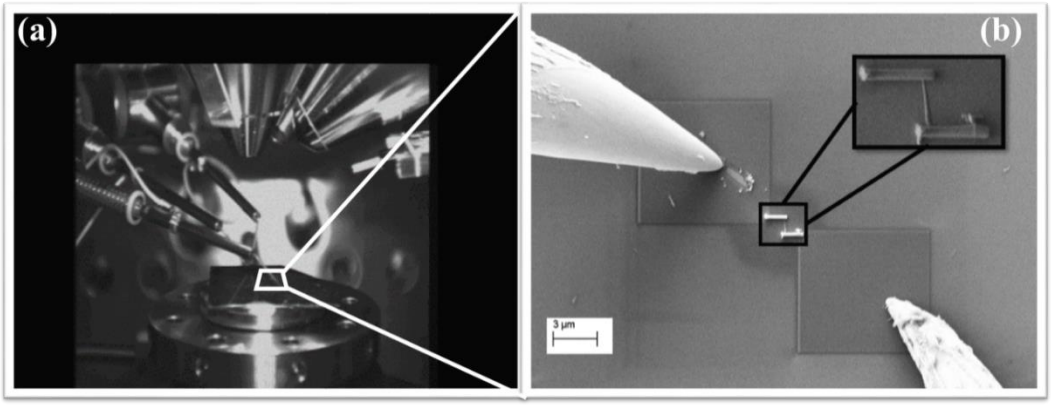

Figure 4.14. Images of (a) SEM nanomanipulators and (b) the W tips of the nanomanipulators contacting the Pt electrodes during electrical characterization of a single ZTO NW.

The employed nanowires were synthetized by using the $ZnCl_2$ precursor, with a Zn:Sn molar ratio of 2:1, H_2O:EDA volume ratio of 7.5:7.5 ml and 0.240 M of NaOH, as these are the optimal conditions in terms of reproducibility and homogeneity. **Figure 4.15**a shows the obtained I-V curve by applying a voltage range of -5 V to 5 V between the contacts, for a single nanowire with length and diameter of 769 nm and 63 nm, respectively. The background current between two electrodes deposited in the same configuration and distance (but without a nanowire connecting them) was also measured, as shown in the inset of **Figure 4.15**b. This background current, resultant from a residual deposition of the electrodes' material over the sample, was taken into account on the calculation of the nanowire resistivity. The significantly lower background current level compared to the actual measurement performed in the nanowire reinforces the validity of the nanostructure measurement.

Since an ohmic behavior is observed, it is possible to determine the electrical resistance (R) of the nanowire, by fitting the I-V curve, with the Ohm's law. With the determined electrical resistance the resistivity, ρ, was calculated, which is defined as:

$$\rho = R\frac{A}{l} = \frac{V}{I} \times \frac{\pi r^2}{l}$$

Where R is the electrical resistance of the nanowire as already mentioned, l is the nanowire length, A is the cross-sectional area of the nanowire and $r = d/2$, where d is the nanowire's diameter.

Considering then Ohm's law and the physical dimensions of the nanowire, a resistivity of 1.42 kΩ·cm was obtained, which is significantly higher than the reported by Xue *et al.* (≈73 Ω·cm)[55] for $ZnSnO_3$ nanowires, and by Karthik *et al.* (6 Ω·cm in vacuum) for Zn_2SnO_4 nanowires.[56]

In **Figure 4.15**c the resistivity for $ZnSnO_3$ nanowires from different synthesis runs is shown. The resistivity values are shown to be relatively close, with an average resistivity of 7.80 ± 8.63 kΩ·cm. The error bar presented in **Figure 4.15**c represents the uncertainty of the resistivity, calculated from the propagation of uncertainty, given by:

$$\Delta\rho = \sqrt{\left(\frac{A}{l}\Delta R\right)^2 + \left(\frac{R}{l}\Delta A\right)^2 + \left(-\frac{RA}{l^2}\Delta l\right)^2}$$

Where ΔR, ΔA and Δl are the uncertainty from the resistance, the area and the length, respectively.

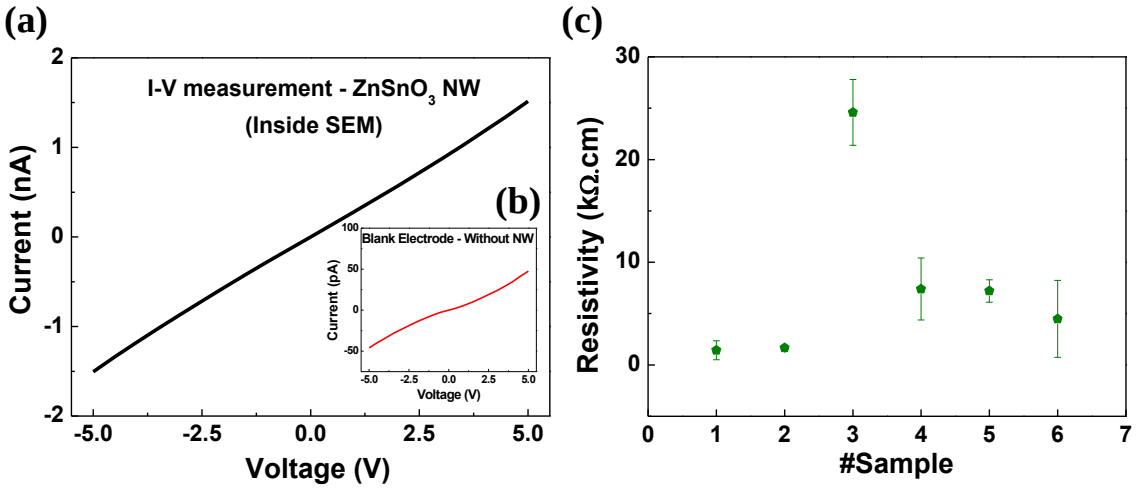

Figure 4.15. (a) I-V curve for a single $ZnSnO_3$ NW contacted by 2 Pt electrodes, measured inside SEM using nanomanipulators. (b) The inset shows an I-V curve used for background current extraction, taken from a similar sized Pt electrode structure, but without any NW connecting. (c) Resistivity values calculated for $ZnSnO_3$ nanowires from different syntheses with respective uncertainties represented by the error bar. The measurements were performed in vacuum inside SEM tool.

Samples 5 and 6 are from hydrothermal synthesis in a microwave setting the power at 80 W, maximum pressure at 270 PSI, at 200 °C for 4 h and 3 h, respectively. It can be observed that the values fall in line with those obtained from synthesis using the oven, which seems to indicate that the microwave approach can be a good alternative for this type of synthesis.

As explained for the optical properties analysis, the higher defect density associated with the low-temperature solution-based process is the most plausible explanation for the higher electrical resistivity reported here (Xue *et al.*[55] synthesized nanowires by thermal evaporation at 990 °C and Karthik *et al*. [56] synthesized by vapor phase methods at 900 °C).

We consider that to conclude whether the resistivity obtained here is too high for our targeted electronic applications would require device fabrication, e.g. field-effect transistors, where many other challenges need to be addressed, such as contact properties or electrostatic coupling between dielectric and semiconductor nanowire. Even if the synthesized ZTO nanowires reveal to be too resistive for a certain application, there is still room for improvement, for instance by passivation of surface-related defects by post-annealing in different environments and/or by coating with encapsulation films.[57,58] Nevertheless, even with the as-prepared nanowires other electronic applications can be explored, as the resistive switching memories shown in the next section.

4.3. Memristive and Light sensing Properties of Solution Based $ZnSnO_3$ Nanowires

4.3.1. Abstract

Among oxide semiconductors zinc-tin oxide is an excellent option for this class of materials: while critical-element free, its different nanostructures' phases/morphologies culminate in a wide array of applications due to their different and excellent properties. In this work, memristors employing drop-casted $ZnSnO_3$ nanowires, produced by a seed-layer free hydrothermal synthesis at only 200 °C, are reported. The devices showed a very good performance with on/off ratios $> 10^7$, and retention time higher than 5×10^4 s, bipolar operation and set/reset polarity points towards modulation of a Schottky-like barrier for the resistance change mechanism. Moreover, these devices possess a remarkable sensibility to visible light showing an increase of 35 μA/s under illumination. The low-cost fabrication and room-temperature processing turn these results as promising for combined memristor sensing integration in ZTO-based multifunctional smart surfaces.

4.3.2. Introduction

Metal oxide materials have been widely used in thin-film technology, either as dielectric, conductor or semiconductor. Nanostructures of these metal oxides are very promising as next generation materials, with nanoscale devices based on them being in line with the demand for smart and multifunctional surfaces where transparency and flexibility are a requirement.[59] Different applications have been explored using these materials, such as sensors, nanogenerators, transistors and memories.[59–62] In respect of the latter, resistive switching memories (memristors) have been proposed as a superior alternative for memories by possessing both very high integration capability and non-volatility (higher than flash), while enabling access speeds close to that of dynamic random-access memory (DRAM). Memristors also allow to overcome the low efficiency in data processing between memory and central process unit (CPU) by permitting in-memory computing. Additionally, high-speed data transmission can be achieved by photons when employing optoelectronic resistive switching devices, allowing for parallel data processing/communication or other concepts such as image processing.[63] Memristors are typically composed by a metal-oxide-metal structure,[64] where the modification of the resistance state is due to the change of an internal state variable in the oxide layer and the resistance change is non-volatile. Wide band gap semiconductors are good candidates for this application due to its highly mobile Fermi level, allowing for a strong modulation of the resistance state.[65] Furthermore, oxide semiconductors are also known as persistent photoconductors [66,67] which can be further studied for light sensor applications. Additionally, these properties can be applied for memsensing

devices, which combine the features of resistive switching and sensing behavior in a simple MIM structure,[68,69] meaning that the resistive switching can be also controlled by an external stimuli (photo illumination in this case).[70]

Lately, semiconductor nanostructures have been used as the resistive switch layer [61], with zinc-tin oxide (ZTO) being one of the employed materials. While avoiding critical elements, such as In and Ga present in the well-established indium-gallium zinc oxide (IGZO), ZTO still allows to achieve good optical, electrical and mechanical properties. As with IGZO, the multicomponent nature of ZTO allows for a large flexibility in tailoring material properties by tuning the cationic ratio.[71] ZTO can crystalline in two phases: Zn_2SnO_4 and $ZnSnO_3$. Zn_2SnO_4 is an n-type semiconductor material which has a high thermal stability and a high electron mobility (>100 $cm^2V^{-1}s^{-1}$).[72] The $ZnSnO_3$ phase is a perovskite material with excellent piezo and ferroelectric properties.[73] These remarkable properties culminate in a wide range of applications, the most common being photocatalysis, gas sensors, energy harvesting and electronics [11,12]. ZTO was already reported as the active material in resistive switching memories in different forms, such as thin film,[74–77] $ZnSnO_3$ nanocubes incorporated in polymers,[78,79] $ZnSnO_3$ nanocubes interspersed ZnO nanowires,[80] and Zn_2SnO_4 nanowires.[81,82] Additionally, $ZnSnO_3$ nanowires were already reported for light sensing applications.[66,83]

Nanowire structures are the most attractive for memristive applications, with the tailoring of its dimensions in line with the scaling pathway of semiconductor devices.[84] The fabrication method of these nanowires typically consists in high-temperature, expensive physical techniques such as chemical vapor deposition (CVD) and thermal evaporation.[55,81,82] In the current work we present devices fabricated using $ZnSnO_3$ nanowires produced by a one-step seed-layer free hydrothermal synthesis at 200 °C and subsequently integrated in the memristor structure by drop casting.[14] We note that the intuitive stochastic electrical properties of memristors based on a network of nanowires/particles is a critical challenge stemmed from fabrication steps, being extremely difficult to maintain uniform electrical properties. However, thanks to compressive sensing applications, the randomness is not an issue and can even benefit low circuit complexity.[85] Herein, the resistive switching properties of $ZnSnO_3$ nanowires are shown. The resistance states were found to be strongly modulated by the current compliance with on/off resistance ratios up to $\approx 10^7$ being achievable. The resistive switching properties are demonstrated for the first time for $ZnSnO_3$ nanowires, to the authors' best knowledge, furthermore, simultaneous light sensitivity was demonstrated, highly interesting for future concepts involving optoelectronic memristors.[63]

4.3.3. Materials and Methods

Device fabrication and characterization

Random $ZnSnO_3$ nanowires were deposited by drop casting on a glass substrate with a Pt thin-film (50 nm thick) deposited by e-beam evaporation (home-made system). Ti/Au top

electrodes (6/60 nm thick and 500 µm diameter) were also evaporated in the same system, employing a shadow mask for patterning. The electrical characterization of the ZTO nanowires memristors was performed using a semiconductor parameter analyzer (Keysight B1500A, Santa Rosa, CA, USA) and a manual probe station (Cascade EPS150 Triax, San Jose, CA, USA) under room temperature and in the dark. The common bottom electrode (Pt) was grounded and biasing was applied to the top electrode (Ti/Au).

4.3.4. Results and Discussion

Resistive Switching Memory Devices

Memristors were fabricated with random orth-$ZnSnO_3$ nanowires deposited on a continuous Pt film, and Ti/Au electrodes were deposited on the top. The inset of **Figure 4.16**a illustrates the device schematic.

I-V curves were acquired by applying a voltage sweep to the top Ti/Au electrode while the bottom Pt electrode was grounded. The pristine state, shown in **Figure 4.16**a, resembles a diode-like characteristic where a higher current flow is seen for negative voltages, corresponding to a forward bias of a ZTO-Pt Schottky-like barrier. In **Figure 4.16**b a typically obtained I-V curve for these devices is presented, illustrating set and reset states. The devices showed a bipolar behavior with set (change from a high-resistance state (HRS) to a low resistance state (LRS)) occurring abruptly for negative voltages applied to the top electrode. The reset (change from LRS to HRS) is operated without current compliance and is typically an abrupt change too. The set and reset voltages presented some variation, with set voltages comprised typically between – 1.6 V and – 7 V, while reset occurred typically between 0.6 V and 4 V. Even if the voltage required for the first set is not consistently higher than for subsequent sets, suggesting a forming-free operation, the HRS after resets is considerably more conductive than the pristine state showing an irreversible resistance change. The variation within set and reset voltages can be attributed to the sample preparation method, which should result in a random nanowire distribution, hence the conductive paths can be formed in different ways and in films with low compactness. It is interesting to note that the HRS still presents higher current for negative bias (forward polarization of the ZTO-Pt barrier) than for positive bias, as in the pristine state. In fact, for positive bias, and specially for low voltages (0.1 V) very good on/off ratios can be obtained, with around 7 orders of magnitude between resistance states for devices set with 10 mA of current compliance.

Device set regarding different current compliances (CC) was evaluated and **Figure 4.16**c shows the different LRS and HRS (read at + 0.1 V) obtained as a function of CC. Higher currents during the set process result in LRS with higher conductivities. Interestingly, the HRS is not significantly changed for CCs up to 10 mA, with resistances close to the pristine resistance being observed, suggesting an efficient reset process. A significant decrease of the HRSs as CC is

increased above 10 mA is observed, suggesting that the set process is now changing the device permanently from its initial HRS. Retention tests were carried out using a reading voltage of - 0.1 V on devices SET with 10 mA of CC. As presented in **Figure 4.16**d, devices showed a retention time of at least 3×10^4 s with the current in the both states being fairly constant along the reading time.

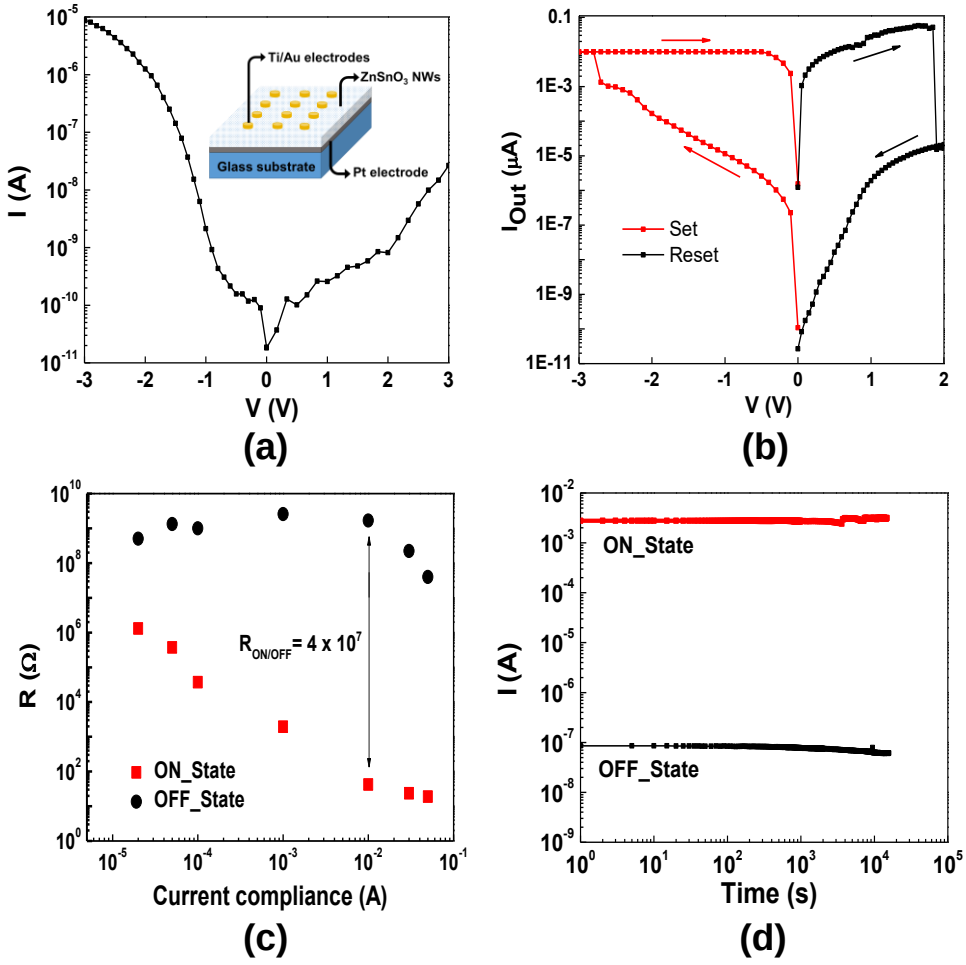

Figure 4.16. Electrical characteristics of the $ZnSnO_3$ nanowire memristors. (a) Pristine diode-like I-V characteristics and device schematic in the inset, (b) typical set and reset process, (c) LRS and HRS for devices set with different CC showing different possible resistance states and (d) retention characteristics for HRS and LRS (read at -0.1 V).

As the metals employed for electrodes in these devices are not known to easily migrate under electric bias (unlike Cu or Ag), we exclude the hypotheses of the formation of a metallic filament. Nonetheless, memristors of metal oxides employing a Ti electrode typically present the valence change mechanism, in which a filament comprised of oxygen vacancies (abundant in the reduced oxide region at the oxide-Ti interface)[61] can be formed between both electrodes resulting in the resistance change. However, the polarity of the operation of our devices is not consistent with this mechanism. In fact, the contribution of the top interface can be excluded, as oxygen vacancies (positively charged) will not migrate through the bulk for negative voltages applied in the Ti electrode. On the contrary, the active interface should be the ZTO-Pt where a Schottky-like barrier plays an important role in the resistive switching. For this type of devices, HRS to LRS

change is seen for forward biasing of the rectifying junction, possibly by modulation of the potential profile of the barrier. Possible mechanisms for this modulation include depletion width modulation by electrochemical migration of oxygen vacancies in the vicinity of the interface,[86] charge trapping at the interface,[87] and reversal of the ferroelectric polarization (by exceeding the coercive field)[88,89] in ferroelectric materials such as $ZnSnO_3$.[90,91] Additionally, a local reduction of the oxide species could also result in a high carrier flow through the interface by forming a metal-metal junction. Regarding the absence of the filament mechanism by driving of the oxygen vacancies, we suggest that it can be explained by the random nanowire dispersion, which would difficult the formation of a continuous filament through all ZTO thickness. It should be noted that although crystalline, these nanowires have a considerable amount of oxygen vacancies.[14] Employing an inert top-electrode, that does not induce an oxygen vacancy pool in the ZTO, can be used to further clarify whether those vacancies are contributing to the resistance change. Temperature dependency of the current can also elucidate on the type of conduction, as does the scaling of devices to investigate the area dependency. The improvement of the integration of the nanowires in the device, either by controlled transfer methods for individualized devices or even pick-up approaches for single device structures are envisaged for future work to enable these experiments.[14] Nevertheless, the performance of these devices already fares well compared to other previously reported employing $ZnSnO_3$ nanostructures as shown in **Table 4.4**. This comparison emphasizes the potential of the devices fabricated in this work, showing the higher on/off ratio reported for $ZnSnO_3$ nanostructures.

Table 4.4. Performance comparison of $ZnSnO_3$ nanostructures-based ReRAM.

Active Layer	V_{SET} / V_{RESET} (V)	On/off ratio	Retention	Current compliance	Year/Ref
$ZnSnO_3$ nanowires (Solution process at 200 °C)	-7 / 4	4×10^7	14 h	10 mA	This work
Zn_2SnO_4 nanowires (Thermal evaporation at 800 °C)	1.6 / - 1	10^5	5 months	N/A	2012/[82]
$ZnSnO_3$ (powder) printed film	8 / -8	300	3.33 h	1 µA	2016/[75]
$ZnSnO_3$ nanocubes@PVOH	1.5 / -1.5	1.65×10^2	36 h	100 mA	2016/[78]
$ZnSnO_3$ Nanocubes	-2 / 2	10	24 h	100 nA	2016/[92]

Light sensing properties

Due to the optical band gap of the ZTO,[14] allied with the nanostructured nature here employed, this material is expected to be a photosensitive semiconductor. Reports have already shown ZnO [93–95] and ZTO [66,96] nanostructures with light sensing properties. In fact, the devices in this work showed to be significantly photo sensible, even if employing an opaque top electrode material. The devices were illuminated with visible light and biased with 0.1 V during and after illumination to read the device current. The light sensing properties are demonstrated in **Figure 4.17**, where the response of the device under and after illumination is shown.

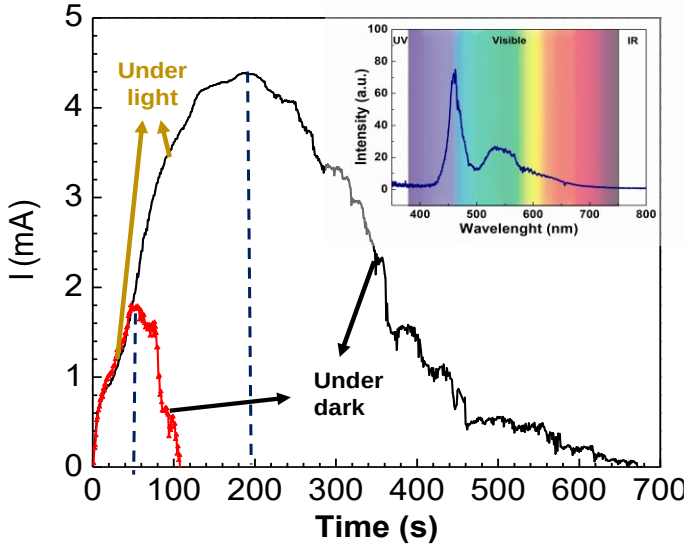

Figure 4.17. Photoresponse of the $ZnSnO_3$ nanowire memristive device, under a visible light, with its spectrum shown in the inset. The dashed line represents the moment at which the light is turned off.

Two superimposed curves are shown in **Figure 4.17**. The red curve depicts an initial faster increase/decrease of the current level with/without illumination. The black curve shows that, given enough time of illumination, the current level can saturate in current values similar to those of the LRSs (for higher current compliances). A remarkable increase/decrease of approximately 35 µA/s under illumination/dark is seen in this device, for currents far from the saturation current. While the nanowires' conductivity is expected to increase under photo illumination,[66] a narrowing of the Schottky barrier will also contribute to the increase of the device current: photo-generated holes can recombine with electrons in the space charge region and, additionally, oxygen vacancies ionized by the UV can move towards the interface.[95,97] After removing illumination, the conductivity of the device will decrease slowly to its initial state, as both ionized oxygen vacancies and the captured holes are slow to drift back to their original states due to their large effective mass and low mobility.[97]

4.3.5. Conclusions

In summary, resistive switching memories using $ZnSnO_3$ nanowires produced by solution-based synthesis were successfully fabricated and reported for the first time. Although a preliminary integration method (drop-casting) was employed for device fabrication, very good performance was obtained revealing these structures as very promising for memristive applications. On/off ratios in the order of 10^7 were obtained and the retention time is higher than 14 h. Interestingly, the resistance change mechanism seemed to be due to the modulation of a ZTO-Pt barrier, while filament formation by oxygen vacancy diffusion doesn't seem to happen. This gives more flexibility in the employment of electrodes and allows to avoid the typically more unreliable filamentary mechanisms. Additionally, the devices have shown an average increase of 35 µA/s under illumination, showing potential for implementation as optoelectronic memristors or light sensing devices. It is expected that these results have a significant impact in advancing nanoelectronics as they demonstrate the feasibility of employing ZTO nanowires by inexpensive low-temperature method to achieve high performing memristors, an important feature to be integrated with other ZTO based devices such as gas sensors, memories, batteries and energy harvesters, for achieving truly multifunctional smart surfaces.

4.4. Final remarks

In this chapter energy and electronic applications were explored by implementation of the $ZnSnO_3$ nanowires achieved with the optimized synthesis conditions. Piezoelectric nanogenerators were fabricated using a composite film of PDMS and the $ZnSnO_3$ nanowires. The $ZnSnO_3$ nanowires piezoelectric properties were assessed through PFM measurements, with a d_{33} of 23 ± 4 pm/V being determined. While a micro-structured design of the film slightly improves the device response when not using the nanowires (due to enhancement of the triboelectric effect), a much more significant increase is seen when employing the $ZnSnO_3$ nanowires, which is attributed to their piezoelectric effect. Assuming a horizontal natural orientation of the nanowires in the PDMS film, the micro-cones improve the force transmission to the extremities of the nanowires (c-axis), otherwise perpendicular to this axis. The practical implementation of the devices was shown by lighting up LEDs, revealing great potential for energy harvesting in wearables.

Electrical characterization of several single nanowires was successfully performed inside a SEM tool. An average resistivity of 7.80 ± 8.63 kΩ·cm was calculated, which is significantly higher than the reported in the literature (≈73 Ω·cm) for $ZnSnO_3$ nanowires. This can be attributed to the higher defect density resulting from the low-temperature solution-based process. While post-processing steps such as annealing and/or passivation can still be explored for decreasing the defect density of the nanowires, these properties have shown to be suitable for applications such as memristors and photosensors.

Resistive switching memories employing the $ZnSnO_3$ nanowires were fabricated by drop-casting the nanowires onto a platinum-covered substrate. While drop-casting was used as a preliminary integration method, a very good performance was obtained with on/off ratios in the order of 10^7 and retention times higher than 14 h. While still under investigation, the resistance change mechanism seems to be due to the modulation of a ZTO-Pt Schottky like barrier, whereas filament formation by oxygen vacancy diffusion is apparently excluded. Additionally, the devices have shown a significant response under visible illumination, with an increase of 35 µA/s. This can be applied for the implementation of optoelectronic memristors or for light sensing devices.

In summary, great results were shown with the application of the $ZnSnO_3$ nanowires produced by solution-based processes as energy harvesters and resistive switching memories. The implementation of the nanowires in these devices was facilitated by its powder form arising from the seed-layer free nature of the optimized synthesis. These two applications show already the great potential of $ZnSnO_3$ nanowires as multifunctional material, and that it should be considered for the future of smart and self-sustainable surfaces.

4.5. References

1. Lee, K. Y., Gupta, M. K. & Kim, S. W. Transparent flexible stretchable piezoelectric and triboelectric nanogenerators for powering portable electronics. *Nano Energy* **14**, 139–160 (2015).
2. Chen, J. & Wang, Z. L. Reviving Vibration Energy Harvesting and Self-Powered Sensing by a Triboelectric Nanogenerator. *Joule* **1**, 480–521 (2017).
3. Rahimi, A., Zorlu, Ö., Muhtaroğlu, A. & Külah, H. A Compact Electromagnetic Vibration Harvesting System with High Performance Interface Electronics. *Procedia Eng.* **25**, 215–218 (2011).
4. Guo, R., Guo, Y., Duan, H., Li, H. & Liu, H. Synthesis of Orthorhombic Perovskite-Type ZnSnO3 Single-Crystal Nanoplates and Their Application in Energy Harvesting. *ACS Appl. Mater. Interfaces* **9**, 8271–8279 (2017).
5. Li, W. *et al.* Nanogenerator-based dual-functional and self-powered thin patch loudspeaker or microphone for flexible electronics. *Nat. Commun.* **8**, 15310 (2017).
6. Askari, H., Khajepour, A., Khamesee, M. B., Saadatnia, Z. & Wang, Z. L. Piezoelectric and triboelectric nanogenerators: Trends and impacts. *Nano Today* **22**, 10–13 (2018).
7. Wang, Z. L. Piezoelectric Nanogenerators Based on Zinc Oxide Nanowire Arrays. *Science (80-.).* **312**, 242–246 (2006).
8. Zhao, Y. *et al.* Pt/ZnO nanoarray nanogenerator as self-powered active gas sensor with linear ethanol sensing at room temperature. *Nanotechnology* **25**, 115502 (2014).
9. Zhao, Y. *et al.* Biomolecule-adsorption-dependent piezoelectric output of ZnO nanowire nanogenerator and its application as self-powered active biosensor. *Biosens. Bioelectron.* **57**, 269–275 (2014).
10. Inaguma, Y., Yoshida, M. & Katsumata, T. A Polar Oxide ZnSnO3 with a LiNbO3-Type Structure. *J. Am. Chem. Soc.* **130**, 6704–6705 (2008).
11. Sun, S. & Liang, S. Morphological zinc stannate: synthesis, fundamental properties and applications. *J. Mater. Chem. A* **5**, 20534–20560 (2017).

12. Baruah, S. & Dutta, J. Zinc stannate nanostructures: hydrothermal synthesis. *Sci. Technol. Adv. Mater.* **12**, 013004 (2011).

13. Gou, H. *et al.* Energetic stability, structural transition, and thermodynamic properties of ZnSnO3. *Appl. Phys. Lett.* **98**, 1–4 (2011).

14. Rovisco, A. *et al.* Seed-Layer Free Zinc Tin Oxide Tailored Nanostructures for Nanoelectronic Applications: Effect of Chemical Parameters. *ACS Appl. Nano Mater.* **1**, 3986–3997 (2018).

15. Bora, T., Al-Hinai, M. H., Al-Hinai, A. T. & Dutta, J. Phase Transformation of Metastable ZnSnO3 Upon Thermal Decomposition by In-Situ Temperature-Dependent Raman Spectroscopy. *J. Am. Ceram. Soc.* **98**, 4044–4049 (2015).

16. Wu, J. M., Xu, C., Zhang, Y. & Wang, Z. L. Lead-free nanogenerator made from single ZnSnO3 microbelt. *ACS Nano* **6**, 4335–40 (2012).

17. Fu, Y. *et al.* Detecting Liquefied Petroleum Gas (LPG) at Room Temperature Using ZnSnO3/ZnO Nanowire Piezo-Nanogenerator as Self-Powered Gas Sensor. *ACS Appl. Mater. Interfaces* **7**, 10482–10490 (2015).

18. Wu, J. M. *et al.* Flexible and transparent nanogenerators based on a composite of lead-free ZnSnO3 triangular-belts. *Adv. Mater.* **24**, 6094–6099 (2012).

19. Wu, J. M. *et al.* Ultrahigh Sensitive Piezotronic Strain Sensors Based on a ZnSnO3 Nanowire/Microwire. *ACS Nano* **6**, 4369–4374 (2012).

20. Choi, K. H., Siddiqui, G. U., Yang, B. & Mustafa, M. Synthesis of ZnSnO3 nanocubes and thin film fabrication of (ZnSnO3/PMMA) composite through electrospray deposition. *J. Mater. Sci. Mater. Electron.* **26**, 5690–5696 (2015).

21. Yang, Y. J. *et al.* Highly Sensitive Flexible Human Motion Sensor Based on ZnSnO3/PVDF Composite. *J. Electron. Mater.* **46**, 4172–4179 (2017).

22. Alam, M. M., Ghosh, S. K., Sultana, A. & Mandal, D. Lead-free ZnSnO3/MWCNTs-based self-poled flexible hybrid nanogenerator for piezoelectric power generation. *Nanotechnology* **26**, 165403 (2015).

23. Lee, K. Y. *et al.* Unidirectional high-power generation via stress-induced dipole alignment from ZnSnO3 nanocubes/polymer hybrid piezoelectric nanogenerator. *Adv. Funct. Mater.* **24**, 37–43 (2014).

24. Wu, J. M., Chen, K.-H., Zhang, Y. & Wang, Z. L. A self-powered piezotronic strain sensor based on single ZnSnO3 microbelts. *RSC Adv.* **3**, 25184 (2013).

25. Wang, G. *et al.* Hybrid nanogenerators based on triboelectrification of a dielectric composite made of lead-free ZnSnO3 nanocubes. *Nano Energy* **18**, 28–36 (2015).

26. Soin, N. *et al.* High performance triboelectric nanogenerators based on phase-inversion piezoelectric membranes of poly(vinylidene fluoride)-zinc stannate (PVDF-ZnSnO3) and polyamide-6 (PA6). *Nano Energy* **30**, 470–480 (2016).

27. Paria, S. *et al.* A Facile Approach to Develop a Highly Stretchable PVC/ZnSnO3 Piezoelectric Nanogenerator with High Output Power Generation for Powering Portable Electronic Devices. *Ind. Eng. Chem. Res.* **55**, 10671–10680 (2016).

28. Zhang, H. *et al.* Human Skin Based Triboelectric Nanogenerators for Harvesting Biomechanical Energy and as Self-Powered Active Tactile Sensor System. *ACS Nano* **7**, 9213–9222 (2013).

29. Seol, M. L. *et al.* Nature-replicated nano-in-micro structures for triboelectric energy harvesting. *Small* **10**, 3887–3894 (2014).

30. Han, X. *et al.* Self-Powered High-Resolution and Pressure-Sensitive Triboelectric Sensor Matrix for Real-Time Tactile Mapping. *Adv. Mater.* **28**, 2896–2903 (2016).

31. Xie, Y. *et al.* Triboelectric Active Sensor Array for Self-Powered Static and Dynamic Pressure Detection and Tactile Imaging. *ACS Nano* **7**, 8266–8274 (2013).

32. Fan, F. R. *et al.* Transparent triboelectric nanogenerators and self-powered pressure sensors based on micropatterned plastic films. *Nano Lett.* **12**, 3109–3114 (2012).

33. Zhu, Y. *et al.* A flexible and biocompatible triboelectric nanogenerator with tunable internal resistance for powering wearable devices. *Sci. Rep.* **6**, 22233 (2016).

34. Wang, X. *et al.* A flexible triboelectric-piezoelectric hybrid nanogenerator based on P(VDF-TrFE) nanofibers and PDMS/MWCNT for wearable devices. *Sci. Rep.* **6**, 36409 (2016).

35. Rovisco, A. *et al.* Growth Mechanism of Seed-Layer Free ZnSnO3 Nanowires: Effect of Physical Parameters. *Nanomaterials* **9**, 1002 (2019).

36. dos Santos, A. *et al.* Piezoresistive E-Skin Sensors Produced with Laser Engraved Molds. *Adv. Electron. Mater.* **4**, 1–10 (2018).

37. Santos, A. dos *et al.* E-Skin Pressure Sensors Made by Laser Engraved PDMS Molds. *Proceedings* **2**, 1039 (2018).

38. dos Santos, A. *et al.* E-Skin Bimodal Sensors for Robotics and Prosthesis Using PDMS Molds Engraved by Laser. *Sensors* **19**, 899 (2019).

39. Coelho, D. Solution Based Synthesis of ZnO Nanorods for Optoelectronic Applications. (FCT-UNL, 2019).

40. Biswas, A., Saha, S. & Jana, N. R. ZnSnO3 Nanoparticle-Based Piezocatalysts for Ultrasound-Assisted Degradation of Organic Pollutants. *ACS Appl. Nano Mater.* **2**, 1120–1128 (2019).

41. Xue, X. Y., Chen, Y. J., Wang, Y. G. & Wang, T. H. Synthesis and ethanol sensing properties of ZnSnO3 nanowires. *Appl. Phys. Lett.* **86**, 1–3 (2005).

42. Placke, A., Kumar, A. & Priya, S. Synthesis and Behavior of Cetyltrimethyl Ammonium Bromide Stabilized Zn1+xSnO3+x (0 ≤ x ≤1) Nano-Crystallites. *PLoS One* **11**, e0156246 (2016).

43. Ghasemian, M. B. *et al.* Morphology control and large piezoresponse of hydrothermally synthesized lead-free piezoelectric (Bi0.5Na0.5)TiO3 nanofibres. *RSC Adv.* **7**, 15020–15026 (2017).

44. Shoji, I., Kondo, T., Kitamoto, A., Shirane, M. & Ito, R. Absolute scale of second-order nonlinear-optical coefficients. *J. Opt. Soc. Am. B* **14**, 2268 (1997).

45. Liang, L., Kang, X., Sang, Y. & Liu, H. One-Dimensional Ferroelectric Nanostructures: Synthesis, Properties, and Applications. *Adv. Sci.* **3**, 1500358 (2016).

46. Nguyen, S. D. & Halasyamani, P. S. Synthesis, Structure, and Characterization of Two New Polar Sodium Tungsten Selenites: Na2(WO3)3(SeO3)·2H2O and Na6(W6O19)(SeO3)2. *Inorg. Chem.* **52**, 2637–2647 (2013).

47. Ke, T.-Y. *et al.* Sodium Niobate Nanowire and Its Piezoelectricity. *J. Phys. Chem. C* **112**, 8827–8831 (2008).

48. Tang, H., Zhou, Z. & Sodano, H. A. Large-scale synthesis of BaxSr1−xTiO3 nanowires with controlled stoichiometry. *Appl. Phys. Lett.* **104**, 142905 (2014).

49. Yun, B. *et al.* Lead-free LiNbO3 nanowire-based nanocomposite for piezoelectric power generation. *Nanoscale Res. Lett.* **9**, 4 (2014).

50. Joung, M.-R. *et al.* Structural dependence of the piezoelectric properties of KNbO3 nanowires synthesized by the hydrothermal method. *Acta Mater.* **61**, 3703–3708 (2013).

51. Fan, F.-R., Tian, Z.-Q. & Wang, Z. L. Flexible triboelectric generator. *Nano Energy* **1**, 328–334 (2012).

52. Ko, Y. H., Nagaraju, G., Lee, S. H. & Yu, J. S. PDMS-based Triboelectric and Transparent Nanogenerators with ZnO Nanorod Arrays. *ACS Appl. Mater. Interfaces* **6**, 6631–6637 (2014).

53. Wan, Sun, J. & Liu, H. Semiconducting Oxide Nanowires: Growth, Doping and Device applications. in *Nanowires - Implementations and Applications* 59–98 (InTech, 2011).

54. Chen, D., Liu, Z., Liang, B., Wang, X. & Shen, G. Transparent metal oxide nanowire transistors. *Nanoscale* **4**, 3001 (2012).

55. Xue, X. Y. *et al.* Electronic transport characteristics through individual ZnSnO3 nanowires. *Appl. Phys. Lett.* **88**, 182102 (2006).

56. Karthik, K. R. G. *et al.* Physical and Electrical Properties of Single Zn2SnO4 Nanowires. *Electrochem. Solid-State Lett.* **14**, K5 (2011).

57. Chang, P.-C. & Lu, J. G. ZnO Nanowire Field-Effect Transistors. *IEEE Trans. Electron Devices* **55**, 2977–2987 (2008).

58. Park, W. Il, Kim, J. S., Yi, G. C., Bae, M. H. & Lee, H. J. Fabrication and electrical characteristics of high-performance ZnO nanorod field-effect transistors. *Appl. Phys. Lett.* **85**, 5052–5054 (2004).

59. Huang, H. *et al.* Metal oxide nanowire transistors. *J. Mater. Chem.* **22**, 13428 (2012).

60. Wang, Z. L. & Wu, W. Piezotronics and piezo-phototronics: Fundamentals and applications. *Natl. Sci. Rev.* **1**, 62–90 (2014).

61. Rosa, J. *et al.* Memristors Using Solution-Based IGZO Nanoparticles. *ACS Omega* **2**, 8366–8372 (2017).

62. Nunes, D. *et al.* Metal oxide nanostructures for sensor applications. *Semicond. Sci. Technol.* **34**, 043001 (2019).

63. Tan, H., Liu, G. & Li, R.-W. Multifunctional Optoelectronic Device Based on Resistive Switching Effects. in *Recent Development in Optoelectronic Devices* **i**, 13 (InTech, 2018).

64. Nagashima, K. *et al.* Intrinsic mechanisms of memristive switching. *Nano Lett.* **11**, 2114–2118 (2011).

65. Fortunato, E., Barquinha, P. & Martins, R. Oxide semiconductor thin-film transistors: a review of recent advances. *Adv. Mater.* **24**, 2945–86 (2012).

66. Xue, X. Y., Guo, T. L., Lin, Z. X. & Wang, T. H. Individual core-shell structured ZnSnO3 nanowires as photoconductors. *Mater. Lett.* **62**, 1356–1358 (2008).

67. Lin, D., Wu, H. & Pan, W. Photoswitches and memories assembled by electrospinning aluminum-doped zinc oxide single nanowires. *Adv. Mater.* **19**, 3968–3972 (2007).

68. Carrara, S. *et al.* Memristive-biosensors: A new detection method by using nanofabricated memristors. *Sensors Actuators B Chem.* **171–172**, 449–457 (2012).

69. Zheng Fan, Xudong Fan, Li, A. & Lixin Dong. Nanorobotic in situ characterization of nanowire memristors and 'memsensing'. in *2013 IEEE/RSJ International Conference on Intelligent Robots and Systems* 1028–1033 (IEEE, 2013).

70. Ungureanu, M. *et al.* A light-controlled resistive switching memory. *Adv. Mater.* **24**, 2496–2500 (2012).

71. Pang, C. *et al.* Synthesis, characterization and opto-electrical properties of ternary Zn2SnO4 nanowires. *Nanotechnology* **21**, 465706 (2010).

72. Kim, S., Kim, H., Janes, D. B. & Ju, S. Interface studies of N2 plasma-treated ZnSnO nanowire transistors using low-frequency noise measurements. *Nanotechnology* **24**, 305201 (2013).

73. Nakayama, M., Nogami, M., Yoshida, M., Katsumata, T. & Inaguma, Y. First-principles

studies on novel polar oxide ZnSnO3; pressure-induced phase transition and electric properties. *Adv. Mater.* **22**, 2579–2582 (2010).

74. Murali, S. *et al.* Resistive switching in zinc-tin-oxide. *Solid. State. Electron.* **79**, 248–252 (2013).

75. Ali, S., Bae, J. & Lee, C. H. Printed non-volatile resistive switches based on zinc stannate (ZnSnO3). *Curr. Appl. Phys.* **16**, 757–762 (2016).

76. Hsu, C. C., Chen, Y. T., Chuang, P. Y. & Lin, Y. S. Abnormal Volatile Memory Characteristic in Normal Nonvolatile ZnSnO Resistive Switching Memory. *IEEE Trans. Electron Devices* **65**, 2812–2819 (2018).

77. CasaBranca, N. *et al.* 2D Resistive Switching Based on Amorphous Zinc–Tin Oxide Schottky Diodes. *Adv. Electron. Mater.* **1900958**, 1–8 (2019).

78. Siddiqui, G. U., Rehman, M. M. & Choi, K. H. Enhanced resistive switching in all-printed, hybrid and flexible memory device based on perovskite ZnSnO3 via PVOH polymer. *Polymer (Guildf).* **100**, 102–110 (2016).

79. Yang, Y. J., Rehman, M. M., Siddiqui, G. U., Na, K. H. & Choi, K. H. Effect of adding a polymer and varying device size on the resistive switching characteristics of perovskite nanocubes heterojunction. *Curr. Appl. Phys.* **17**, 1733–1741 (2017).

80. Siddiqui, G. U., Rehman, M. M. & Choi, K. H. Resistive switching phenomena induced by the heterostructure composite of ZnSnO3 nanocubes interspersed ZnO nanowires. *J. Mater. Chem. C* **5**, 5528–5537 (2017).

81. Cheng, B., Ouyang, Z., Chen, C., Xiao, Y. & Lei, S. Individual Zn2SnO4-sheathed ZnO heterostructure nanowires for efficient resistive switching memory controlled by interface states. *Sci. Rep.* **3**, 3249 (2013).

82. Dong, H. *et al.* High performance bipolar resistive switching memory devices based on Zn2SnO4 nanowires. *Nanoscale* **4**, 2571 (2012).

83. Wu, J. M., Hsu, G. K., Yeh, H.-H. & Lin, H.-C. Metallic Zinc Nanowires Effect in High-Performance Photoresponsive and Photocatalytic Properties of Composite Zinc Stannate Nanowires. *J. Electrochem. Soc.* **159**, H497–H501 (2012).

84. Ielmini, D., Cagli, C., Nardi, F. & Zhang, Y. Nanowire-based resistive switching memories: Devices, operation and scaling. *J. Phys. D. Appl. Phys.* **46**, (2013).

85. Qian, F., Gong, Y., Huang, G., Anwar, M. & Wang, L. Exploiting Memristors for Compressive Sampling of Sensory Signals. *IEEE Trans. Very Large Scale Integr. Syst.* **26**, 2737–2748 (2018).

86. Sawa, A. Resistive switching in transition metal oxides. *Mater. Today* **11**, 28–36 (2008).

87. Sawa, A., Fujii, T., Kawasaki, M. & Tokura, Y. Colossal Electro-Resistance Memory Effect at Metal/La2CuO4 Interfaces. *Jpn. J. Appl. Phys.* **44**, L1241–L1243 (2005).

88. Lü, W. *et al.* Multi-Nonvolatile State Resistive Switching Arising from Ferroelectricity and Oxygen Vacancy Migration. *Adv. Mater.* **29**, 1–8 (2017).

89. Blom, P. W. M., Wolf, R. M., Cillessen, J. F. M. & Krijn, M. P. C. M. Ferroelectric Schottky Diode. *Phys. Rev. Lett.* **73**, 2107–2110 (1994).

90. Son, J. Y. *et al.* Heteroepitaxial Ferroelectric ZnSnO3 Thin Film. *J. Am. Chem. Soc.* **131**, 8386–8387 (2009).

91. Datta, A., Mukherjee, D., Kons, C., Witanachchi, S. & Mukherjee, P. Evidence of Superior Ferroelectricity in Structurally Welded ZnSnO3 Nanowire Arrays. *Small* **10**, n/a-n/a (2014).

92. Siddiqui, G. U. D., Ali, J., Doh, Y. H. & Choi, K. H. Fabrication of zinc stannate based all-printed resistive switching device. *Mater. Lett.* **166**, 311–316 (2016).

93. Vahl, A. *et al.* Concept and modelling of memsensors as two terminal devices with enhanced capabilities in neuromorphic engineering. *Sci. Rep.* **9**, 1–9 (2019).

94. Chiolerio, A. *et al.* Ultraviolet mem-sensors: flexible anisotropic composites featuring giant photocurrent enhancement. *Nano Res.* **8**, 1956–1963 (2015).

95. Bera, A. *et al.* A versatile light-switchable nanorod memory: Wurtzite ZnO on perovskite SrTiO3. *Adv. Funct. Mater.* **23**, 4977–4984 (2013).

96. Dong, Y. *et al.* Zinc Stannate Nanocrystal–Based Ultrarapid-Response UV Photodetectors. *Adv. Mater. Technol.* **3**, 1–8 (2018).

97. Tan, H. *et al.* Light-Gated Memristor with Integrated Logic and Memory Functions. *ACS Nano* **11**, 11298–11305 (2017).

Chapter 5 – Photocatalytic activity of ZTO nanostructures

While the electronic and energy harvesting applications of $ZnSnO_3$ nanowires presented in the previous charter were the most explored during the work of this dissertation, electrochemical applications were also evaluated. In this Chapter, the photocatalytic behavior of three different ZTO nanostructures (nanowires, nanoparticles and octahedrons) in the degradation of two different dyes is presented, under UV and visible light. The fabrication and characterization of the devices were performed in the clean room facilities and laboratory resources of CEMOP and CENIMAT. The contents of this chapter are adapted from the following article:

- **A. Rovisco**, R. Branquinho, J. Deuermeier, J. Martins, T. Freire, E. Fortunato, R. Martins and P. Barquinha, Photocatalytic behavior of solution-based Zn:Sn:O nanostructures, under submission 2019

5.1. Abstract

Water pollutants are currently a major concern, and so there is a demand for simple processes for water treatment, with photocatalysis being one of the most efficient and promising. Metal oxide materials are being widely studied for this application, due to their wide band gaps, with nanostructures being very interesting in particular because of their high surface to volume ratios. In this context ZTO nanostructures are very interesting, avoiding critical elements in favor of abundant and non-toxic materials. In this section three different ZTO nanostructures, namely $ZnSnO_3$ nanowires, Zn_2SnO_4 nanoparticles and Zn_2SnO_4 octahedrons, were studied for the photodegradation of methylene blue and rhodamine B under both UV and visible light irradiation. The nanostructures were synthesized by a low-cost seed-layer free hydrothermal method at only 200 °C, which increases application flexibility by avoiding the use of rigid substrates. In particular, $ZnSnO_3$ nanowires showed an enhanced photocatalytic activity, especially under UV light, degrading both dyes in only 90 min. Moreover, these nanostructures clearly outperform Zn_2SnO_4 nanoparticles and octahedrons in photocatalytic activity. This work shows the feasibility of a simple, low-cost fabrication method in achieving structures with a good photocatalytic activity.

5.2. Introduction

Nowadays, environmental issues are a major concern around the world. Looking for sustainable approaches to decrease the problems caused by human activities and industrial actions, some metal oxides are being used as photocatalysts to breakdown different water pollutants.[1–3] Briefly, the photocatalysis is characterized by the degradation of toxic contaminants into environmentally friendly remains, being textile dyes the most common contaminants, which are not only toxic but also potentially carcinogenic.[4,5] The photocatalysis is defined by the rate of a chemical reaction under UV, visible or infrared radiation, in the presence of a substance/material, named catalyst, which suffers electronic excitation by light absorption, occurring a photoredox reaction and, consequently, the generation of an electron-hole pair.[6,7] The light energy for this electron-hole pair generation should be equal or higher than the band gap of the material.

Although visible light represents close to 50 % of solar light, UV light, representing only ≈ 5 %, is the most common source for photocatalysts studies, since there are many materials that only have catalyst activity under UV light due to their optical band gaps. Metal oxide semiconductor nanostructures are particularly interesting for this application, with band gaps close to the visible light energy, and high surface to volume ratios.[8] Besides, semiconductors are advantageous when compared to insulators, since the band gap is much lower, meaning that a lower light energy is necessary to generate the electron-hole pairs.[1] Furthermore, oxygen vacancies and the presence of defects play an important role in the photocatalytic activity,

increasing the importance of the metal oxide semiconductor nanostructures, especially when produced by solution processes which typically results in a higher defect density, due to the lower temperatures employed.[7]

Thus, several metal oxide materials have been studied as photocatalysts, such as titanium oxide, zinc-based oxides and manganites.[3,5,9–14] Although binary metal oxides have already demonstrated great catalyst properties, ternary oxides show higher stability in aqueous environments.[12] Moreover, in ternary oxides by adjusting the cationic ratio it is possible to tune the material properties. Regarding zinc-based oxides, zinc-tin oxide (ZTO) has been greatly explored as photocatalyst.[12,13,15–22] Furthermore, ZTO is a low-cost and environmentally friendly material, and its nanostructures have been applied in several fields, such as gas sensors,[23–25] energy harvesting [26–29] and electronics.[30–34]

The mechanism behind the photocatalytic activity of semiconductors such as ZTO, can be represented by the following equations and by the schematic representation in **Figure 5.1**:[4,15]

$$ZTO \rightarrow e^- + h^+ \quad (1)$$

$$e^- + h^+ \rightarrow energy \quad (2)$$

$$h^+ + H_2O \rightarrow H^+ + OH^{\cdot} \quad (3)$$

$$h^+ + OH^- \rightarrow OH^{\cdot} \quad (4)$$

$$e^- + O_2 \rightarrow O^{\cdot -}_2 \quad (5)$$

$$O^{\circ -}_2 + H^+ \rightarrow HO^{\cdot}_2 \quad (6)$$

$$(OH^{\circ}, O^{\circ -}_2, HO^{\circ}_2) + dye \rightarrow degradation\ products \quad (7)$$

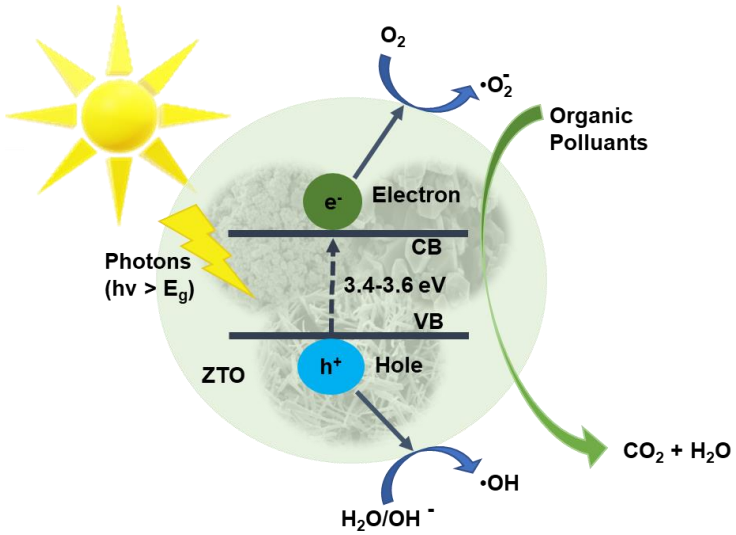

Figure 5.1. Schematic the reaction mechanism involved in the photocatalytic activity of ZTO nanomaterials.

Due to its multicomponent nature, two crystalline phases can be obtained for ZTO: Zn_2SnO_4 and $ZnSnO_3$, and both have been highly used as catalyst. The first is a n-type semiconductor with a A_2BO_4 cubic inverse spinel crystalline structure,[8,22] and it is known by its wide band gap (3.6 eV), good stability in adverse conditions, and high mobility already achieved for specific nanostructures (112 $cm^2 V^{-1} s^{-1}$).[32] The inverse spinel structures have some Zn^{2+} ions in tetrahedral A-sites, while other Zn^{2+} and the Sn^{4+} ions are located in the octahedral B sites. This ions inverted order leads to a non-stoichiometric material, resulting in important properties for catalyst applications such as low-visible absorption and high electron mobility.[35] $ZnSnO_3$ is a well-known ABO_3 perovskite material, essentially for its great piezoelectric and ferroelectric properties, with a reported a band gap of 3.9 eV.[36] Due to its piezoelectric properties, $ZnSnO_3$ has also been used as piezocatalyst for dyes degradation.[18–20] In ABO_3 perovskite structure, A-site tends to stabilize the active B-site transition metal ion. The presence of a corner-shared octahedral BO_6 network leads to a high electronic and oxygen mobility which can contribute to the oxygen non-stoichiometry. Besides, the B-site transition metal ion valence state is essential to the activity of perovskite oxide materials.[2] Moreover, recently, Chen *et al.* reviewed the role of piezoelectricity and ferroelectricity in photocatalysis and described that the photogeneration of electron-holes is improved due the dipole moment formed by the polarization electric field across the polar materials.[37]

Both ZTO phases have optical absorption in the UV region and for this reason ZTO has been mainly reported as catalyst under UV light irradiation.[16,38,39] Still, a few groups already reported the use of ZTO nanostructures as catalyst under visible-light.[8,40,41] Furthermore, for both ZTO phases, different shapes can be obtained and, in 2010, Firooz *et al.* showed the importance of the shape and morphology of the nanostructures for the photocatalytic activity, due to the available surface area.[7] In the last few years, several types of ZTO nanostructures (both phases) have then been used as catalysts, and even if $ZnSnO_3$ nanowires directly grown on a substrate were already used as catalyst, there are no reports employing these structures in powder form, due to the difficulty to produce this material.[22] Herein, the photocatalytic behavior of zinc-tin oxide nanostructures in the degradation of two dyes (methylene blue and rhodamine B) under both UV and visible lights was studied. Both phases Zn_2SnO_4 (nanoparticles, octahedrons) and $ZnSnO_3$ (nanowires) were tested. The nanostructures were synthesized by a low-cost and one-step seed-layer free hydrothermal synthesis at only 200 °C, being the $ZnSnO_3$ nanowires (in the powder form), to the authors best knowledge, applied for the first time as photocatalyst and revealing enhanced performance, leading to a complete degradation of both methylene blue and rhodamine B in only 90 minutes (under UV exposure). Furthermore, the ZTO nanostructures with the best performance were reused for both dyes, showing the potential to be used for multiple water treatments. ZTO nanostructures were also used as catalyst under visible-light irradiation, where although a lower performance was displayed the results are highly promising towards visible light photodegradation.

5.3. Experimental Section

5.3.1. Nanostructures' synthesis

$ZnSnO_3$ nanowires and Zn_2SnO_4 octahedrons were synthesized via hydrothermal method in a conventional oven, using the same methodologies and reagents reported in Chapter 2 and in published articles.[42,43] For the ZTO nanowires, the zinc (0.04 M of $ZnCl_2$) and tin (0.02 M of $SnCl_4 \cdot 5H_2O$) precursors were dissolved separately in 7.5 mL of deionized water and then mixed together. 7.5 mL of the surfactant ethylenediamine (EDA) were then added and the solution was left stirring for 30 minutes, after which the mineralizer sodium hydroxide (NaOH, 0.24 M) was added. Regarding the octahedrons' synthesis, the same reagents and procedure was used, with 15 mL of deionized water for solvent instead, and with no surfactant being added. Zn_2SnO_4 nanoparticles were also synthesized by a hydrothermal method in a conventional oven. For this synthesis the zinc and tin precursors used were: 0.34 g of zinc chloride ($ZnCl_2$ from Merck, 98%) and 0.44 g of tin tetrachloride ($SnCl_4 \cdot 5H_2O$ from Riedel-deHean, 98%), respectively, dissolved separately in 5 mL of distilled water each, and then the dissolved $SnCl_4 \cdot 5H_2O$ was added to the dissolved $ZnCl_2$. Next, sodium carbonate (Na_2CO_3 from Merck, 99.9%) solution (0.53 g in 5 mL of water) was added dropwise to the mixture under magnetic stirring and allowed to mix for 15 min.[44] For all synthesis, the mixtures were kept in the electric oven (Thermo Scientific) at 200 °C for 24 h, with a heating ramp of 200 °C/h, allowing the autoclave to cool to ambient temperature naturally. After the syntheses, the nanostructures (resultant precipitate) were centrifuged (high speed Neya 16) at 4000 rpm and washed several times with deionized water and isopropyl alcohol, alternately, and then were dried at 60 °C, in vacuum, for 2 h.

5.3.2. Nanostructures' characterization

The structural and morphological characterization was performed with the nanostructures in powder form. Structural characterization was performed by X-Ray diffraction (XRD) in a PANalytical's X'Pert PRO MRD diffractometer with Cu K_α radiation, with a data acquisition range of 10-90 ° 2θ range with a step size of 0.033 °. The morphology analysis of the nanostructures was carried out using scanning electron microscopy (SEM) inside a Carl Zeiss AURIGA CrossBeam workstation. X-ray photoelectron spectroscopy (XPS) was acquired by a Kratos Axis Supra, using monochromated Al Kα irradiation (1486.6 eV). The acquisition of the detailed scans was performed with an X-ray power of 225 W and a pass energy of 10 eV.

5.3.3. Photocatalytic activity experiments

The photocatalytic activity of the fabricated materials was evaluated at room temperature from the degradation of rhodamine B (RhB) and methylene blue (MB) from Sigma Aldrich. For each experiment, 40 mg of each powder containing the different nanostructures was dispersed in

50 mL of the RhB solution (5 mg/L) and MB (1.5 mg/L) and then stirred for 30 min in the dark to establish absorption-desorption equilibrium. The nanostructures were tested as photocatalysts under both UV and visible light. For the UV experiments 3 lamps aligned in parallel from Osram with 95 W and an emission wavelength of 254 nm (ozone free) were used. The solutions with the nanostructures were placed at a distance of 10 cm from the light source. The visible light exposure was performed using a LED solar simulator LSH-7320 (AM1.5 spectrum) with a power density of 100 $mW \cdot cm^{-2}$, at room temperature. The absorption spectra were carried out using a PerkinElmer lambda 950 UV/VIS/NIR spectrophotometer. The measurements were done in the 250–800 nm range every 30 minutes, after 5 min of centrifugation at 4000 rpm. The solution used for absorption measurement was then returned to the experimental recipient. In order to perform the reusability studies, the powder was washed several times with deionized water and isopropyl alcohol, alternately, collected by centrifugation at 4000 rpm and then dried again at 60 °C, in vacuum, for 2 h.

5.4. Results and analysis

5.4.1. Nanostructures characterization

In **Figure 5.2**, the XRD patterns and the SEM images of the $ZnSnO_3$ nanowires, Zn_2SnO_4 nanoparticles and Zn_2SnO_4 octahedrons are presented. Herein, the $ZnSnO_3$ phase is identified with #28-1486 ICDD card, which although was deleted from ICDD data base due to the similarities with the Zn_2SnO_4 and SnO_2 (tetragonal) phases, as explained in reference [42], clearly matches with the orthorhombic structure, thus being used here to identify $ZnSnO_3$.

The optical band gap of the $ZnSnO_3$ nanowires and Zn_2SnO_4 octahedrons was reported before, being 3.60 eV and 3.46 eV, respectively.[42] The optical band gap of the Zn_2SnO_4 nanoparticles was determined through the Tauc's plot, presented in **Figure 5.2**e, with 3.61 eV being obtained. The optical band gaps show that the ZTO nanostructures optical absorption is in the UV region, being more promisor as catalyst under UV light irradiation. These values are presented in **Figure 5.2**f.

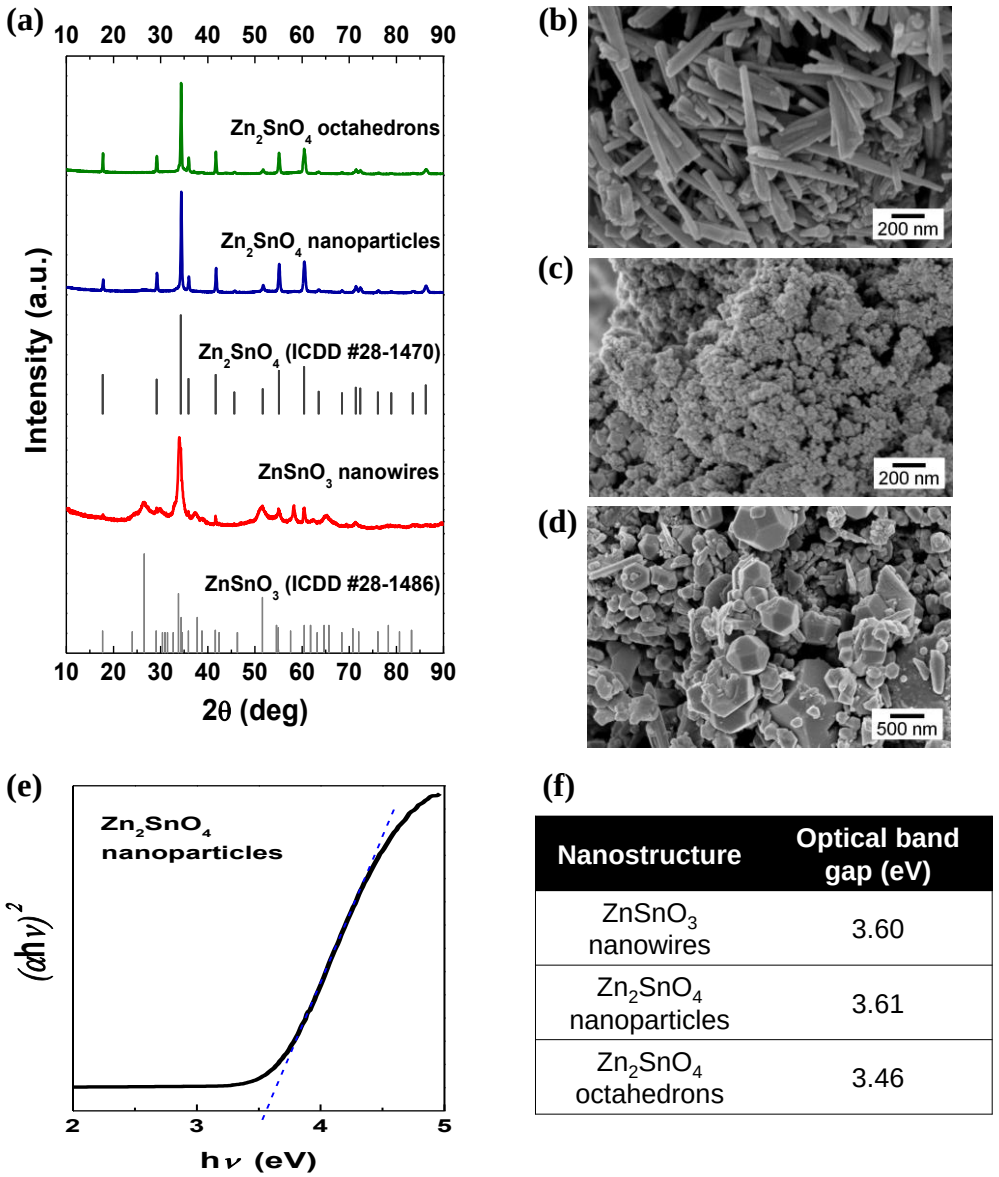

Nanostructure	Optical band gap (eV)
$ZnSnO_3$ nanowires	3.60
Zn_2SnO_4 nanoparticles	3.61
Zn_2SnO_4 octahedrons	3.46

Figure 5.2. (a) XRD patterns and SEM images of (b) $ZnSnO_3$ nanowires, and Zn_2SnO_4 (c) nanoparticles and (d) octahedrons. (e) Tauc's plot for Zn_2SnO_4 nanoparticles. (f) Optical band gaps of the ZTO nanostructures, where the values for $ZnSnO_3$ nanowires and Zn_2SnO_4 octahedrons are from reference [42].

Figure 5.3 shows the XPS spectra of the ZTO nanostructures and for all samples it is possible to identify Zn, Sn, O and C in the survey spectra. Besides adventitious carbon on the surface, there is possibly also a contribution from the carbon tape used to mount the powder samples for the XPS measurement. In **Figure 5.3**b detail scans of the of Zn $2p_{3/2}$ emissions at 1021 eV are presented, showing a zinc oxidation state of Zn^{2+} for all samples.[45] **Figure 5.3**c shows the Sn $3d_{5/2}$ peaks at 486 eV, characteristic of the Sn^{4+} oxidation state.[46] The peak at 530 eV, shown in **Figure 5.3**d, corresponds to O 1s.

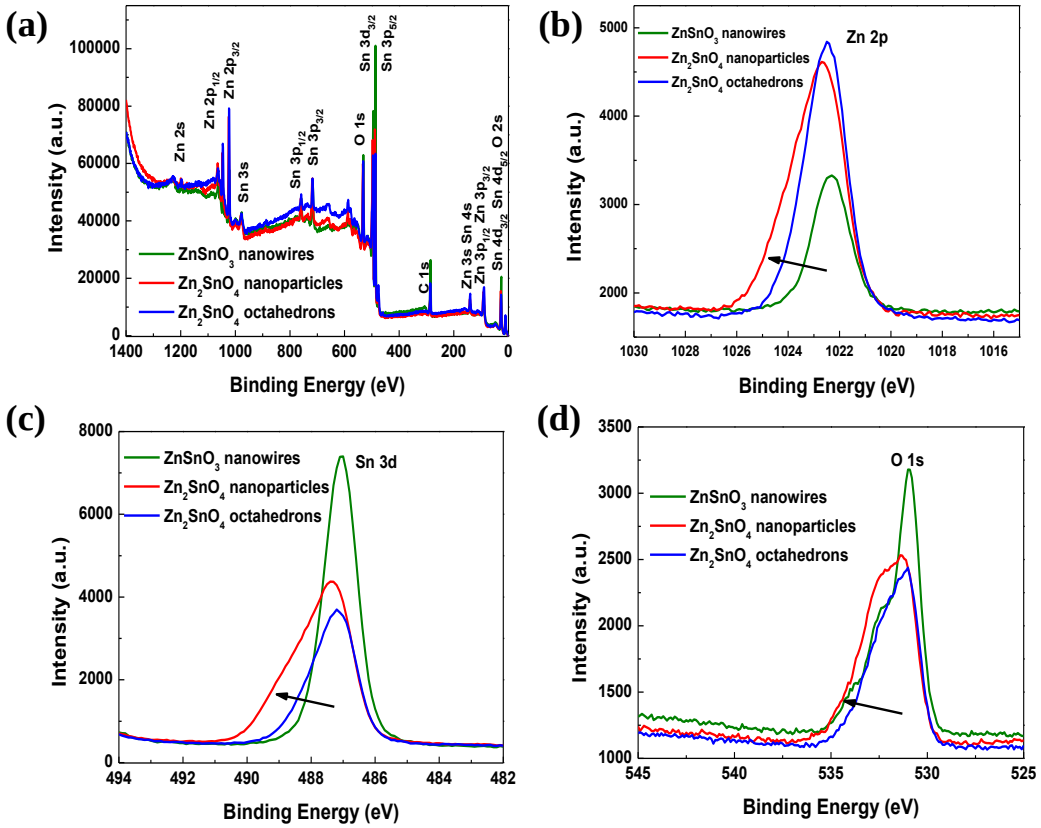

Figure 5.3. XPS spectra of ZTO nanostructures: (a) survey, (b) Zn 2p, (c) Sn 4d and (d) O1s.

The atomic ratios (Sn/Zn) calculated from the spectra for each sample are 2.71 ($ZnSnO_3$ nanowires), 0.72 (Zn_2SnO_4 octahedrons) and 0.99 (Zn_2SnO_4 nanoparticles). As previously discussed, while the identification of Zn_2SnO_4 by XRD is very clear, the $ZnSnO_3$ identification is not immediate since most of $ZnSnO_3$ peaks are common with either Zn_2SnO_4 or SnO_2, leaving always the possibility of these phases being mixed with the $ZnSnO_3$ nanowires. Nevertheless, EDS analysis (as shown in Chapter 2) of $ZnSnO_3$ nanowires shows a Sn/Zn atomic ratio of 1.29 (maximum),[42,43] which is much lower than that determined with XPS. While this value is slightly higher than 1, this can be attributed to either residual Sn or small SnO_2 nanoparticles, which are not visible at the nanowires' scale. This would be even more relevant regarding the XPS technique, since the detection depth is only approximately 8 nm, leading to higher Sn/Zn ratios, as was observed. Regarding the EDS analysis of Zn_2SnO_4 samples (**Figure 5.4**a and b), Sn/Zn atomic ratios of 0.56 and 0.50 are obtained for the Zn_2SnO_4 nanoparticles and Zn_2SnO_4 octahedrons, respectively. Concerning these Zn_2SnO_4 samples, an increased tin concentration deduced from the XPS analysis compared to the EDS results indicates that a tin surface segregation exists. Hence, the increased surface to volume ratio of the nanoparticles results in the detection of more tin, compared to the octahedrons. Higher tin concentrations in zinc-tin oxide increase the materials carrier concentration.[47] Thus, the higher asymmetry of all peaks originating from the Zn_2SnO_4 nanoparticles, compared to the octahedrons, is related to an increased carrier concentration, causing the typical plasmon loss structures of metallic degenerately doped materials.[48]

(a)

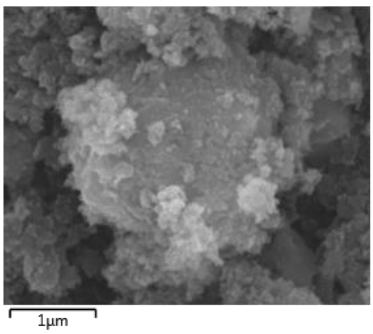

Element	Atomic concentration (%)
Zn	27
Sn	15
O	58

(b)

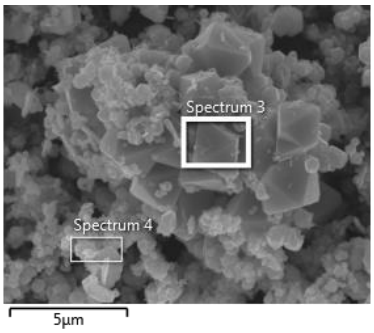

Element	Atomic concentration (%)
Zn	26
Sn	13
O	61

Figure 5.4. EDS analysis of (a) Zn_2SnO_4 nanoparticles and (b) Zn_2SnO_4 octahedrons.

5.4.2. Photocatalytic activity under UV light irradiation

The photocatalytic activity of three different ZTO nanostructures ($ZnSnO_3$ nanowires, and Zn_2SnO_4 nanoparticles and octahedrons) was investigated and compared under UV light irradiation on the discoloration of two aqueous solutions, one with MB (1.5 ppm) and another one with RhB (5 ppm). The power of the UV lamp was 200 W.

Methylene blue degradation using ZTO nanostructures

In **Figure 5.5** is presented the performance of ZTO nanostructures on the photocatalytic degradation of MB solution as well as the degradation of the MB solution without light and without ZTO nanostructures. Photocatalytic activity can be quantitatively evaluated by the photodegradation rate constant (k), using the pseudo-first order reaction kinetic model, represented by $ln\ (C_0/C) = kt$, being C_0 the initial concentration, ($mg.L^{-1}$).

The degradation of the MB over time (in dark and under UV light irradiation), presented in **Figure 5.5**e, shows that without any irradiation (with and without nanostructures) only a very small degradation is observed, (≈ 4 %). On the other hand, the MB solution without nanostructures but under UV light showed a degradation of ≈ 50 %, showing that this dye suffers a degradation over the time even without a catalyst. Nevertheless, a high performance was observed for all the nanostructures (showing significant degradation under 3 h). Using $ZnSnO_3$ nanowires a degradation of ≈ 96 % in only 90 min is obtained, corresponding to a degradation rate, k, of 0.0344 min^{-1}, significantly better than what is achieved using Zn_2SnO_4 nanoparticles and octahedrons, where 120 min (k = 0.0269 min^{-1}) and 180 min (k = 0.0179 min^{-1}) were required for

nearly full degradation, respectively. A photograph of the MB solution before and after the photocatalytic degradation with the different ZTO nanostructures, showing the discoloration of the solution, is shown in **Figure 5.5**g. A summary of the photodegradation rate constants obtained for the different nanostructures is presented in **Figure 5.5**h.

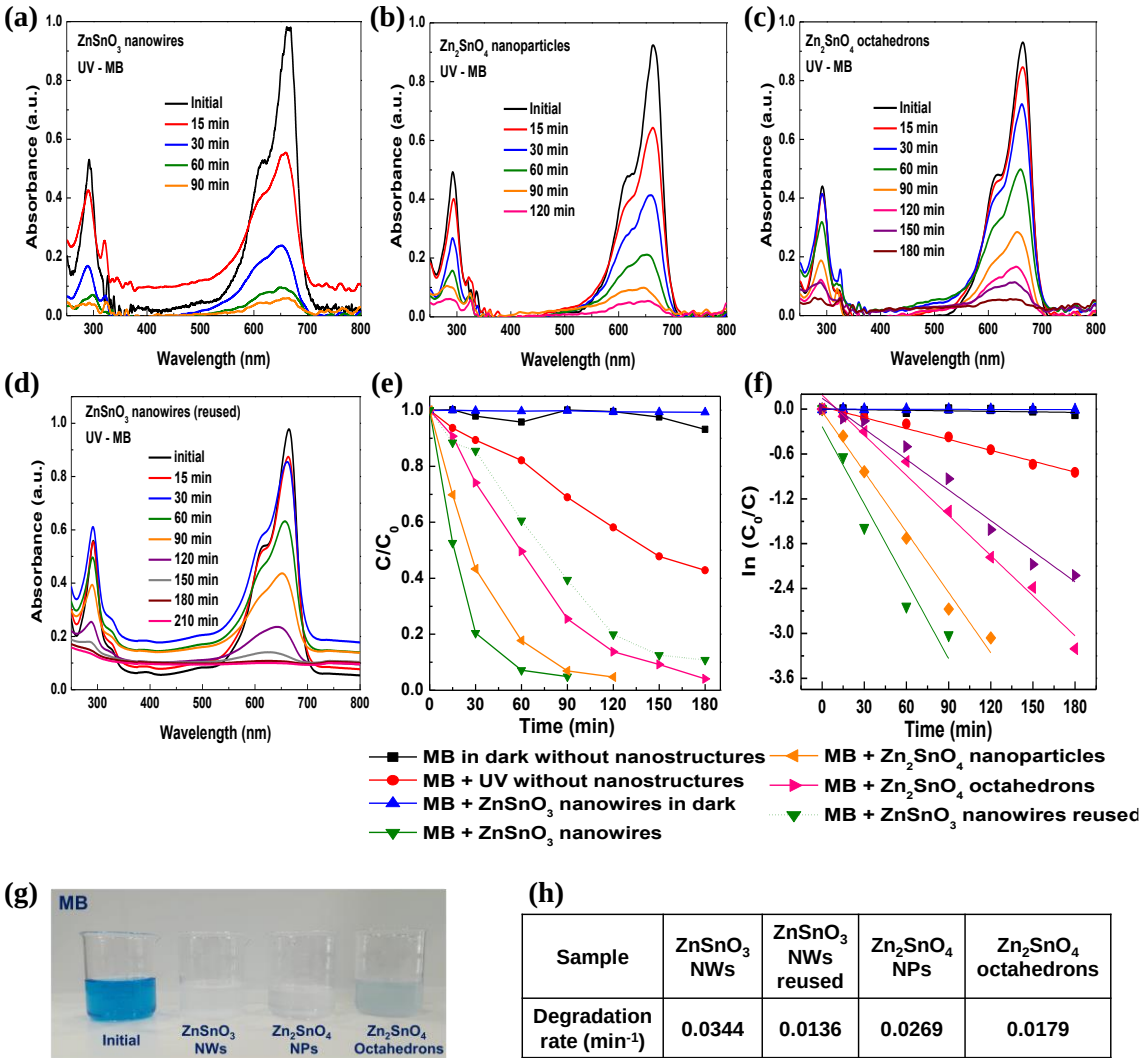

(g)

(h)

Sample	$ZnSnO_3$ NWs	$ZnSnO_3$ NWs reused	Zn_2SnO_4 NPs	Zn_2SnO_4 octahedrons
Degradation rate (min^{-1})	0.0344	0.0136	0.0269	0.0179

Figure 5.5. Absorbance spectra showing the photocatalytic degradation of MB in the presence of (a) $ZnSnO_3$ nanowires, (b) Zn_2SnO_4 nanoparticles, (c) Zn_2SnO_4 octahedrons, (d) reused $ZnSnO_3$ nanowires as catalysts. (e) C/C_0 comparison and (f) kinetic parameters of the MB degradation under UV light irradiation of the ZTO nanostructures. (g) Photograph of the initial MB solution and after degradation using each ZTO nanostructures. (h) Table with the degradation rates of MB using each ZTO nanostructures under UV light.

Due to the better performance of the $ZnSnO_3$ nanowires, they were reused to evaluate their photocatalytic activity. In **Figure 5.5**e the C_0/C of reused $ZnSnO_3$ nanowires is shown and while an increase of the degradation time to twice was observed, the photocatalytic activity is still very satisfactory, presenting a degradation rate of 0.0136 min^{-1}.[49] The decrease of performance could be related to a loss of the quantity of nanomaterial during the recovery and cleaning process. The possibility of recovery and reuse of the catalyst is very important in the photocatalytic processes, contributing to the decrease of the process costs, highlighting the importance of photocatalysis for wastewater treatment at industrial applications.

Additionally, **Figure 5.6**a shows that by reducing the power of the UV lamp to 95 W (1/3 of the initial power) the time for complete degradation increases only to 180 min (taking twice the time). Moreover, **Figure 5.6**b presents the degradation without stirring, showing that more 30 min are necessary to achieve a complete degradation, which can be attributed to a reduced surface area of the nanostructures in contact with the solution, since they precipitate in the cup base. Nevertheless, for both cases good performances are achieved.

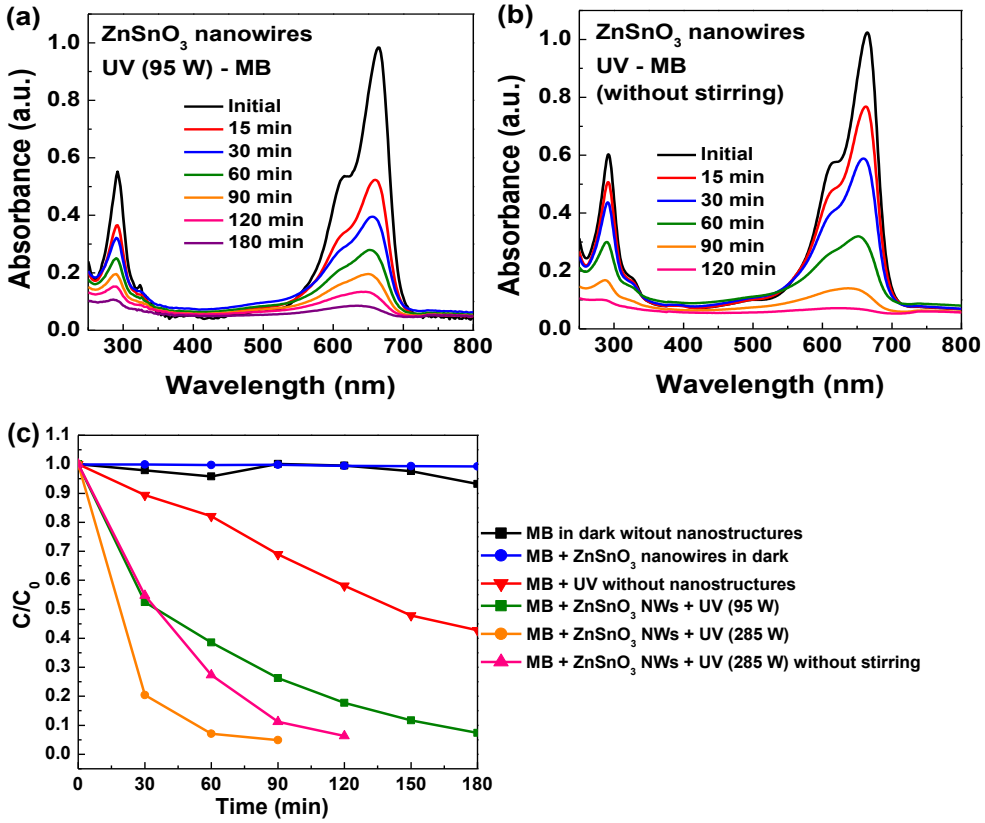

Figure 5.6. (a and b) Absorption measurements and (c) degradation ratio (C/C_0) over time for methylene blue under several conditions.

The photocatalytic response of the $ZnSnO_3$ nanowires in the MB degradation is very satisfactory when compared with the literature. Wu *et al.* showed the photocatalytic behavior of $ZnSnO_3$ nanowires, produced by thermal evaporation at 900 °C, in the degradation of MB solution, achieving 80 % of degradation after 1 h of exposure, whereas information on the employed lamp power was not provided, making it unfeasible to directly compare results.[50] Herein, ≈ 80 % of degradation was obtained in only 30' with stirring and a lamp power of 285 W, ≈ 90 % after 90 min with stirring and a lamp power of 95 W, while without stirring and with a lamp power of 285 W a degradation of ≈ 80 % was achieved after 120 min.

Rhodamine B degradation using ZTO nanostructures

Figure 5.7 shows the photocatalytic performance of ZTO nanostructures on RhB solution. For this dye, the catalytic activity of Zn_2SnO_4 nanoparticles and $ZnSnO_3$ nanowires was very

similar, reaching almost a completely degradation of RhB (≈ 96 %) in approximately 90 min, corresponding to degradation rates of 0.0362 min^{-1} and 0.0338 min^{-1}, respectively. Interestingly, these are similar to the rate found for the $ZnSnO_3$ nanowires for MB degradation. Concerning the Zn_2SnO_4 octahedrons, 210 min were necessary to reach the same level of RhB degradation, corresponding to a rather lower degradation rate of 0.0140 min^{-1}. Furthermore, as shown in **Figure 5.7**f, the RhB solution (without nanostructures) suffers significantly less degradation under UV light irradiation than MB, emphasizing the catalytic activity of the nanostructures, as the degradation is mostly due their activity. Therefore, both Zn_2SnO_4 nanoparticles and $ZnSnO_3$ nanowires were reused for degradation of RhB under UV light (shown in **Figure 5.7**d, e and g). As was observed for the MB solution, while the degradation time increased almost 50 %, these photocatalytic activities are still very satisfactory, with degradation rates of 0.0133 min^{-1} and 0.0131 min^{-1}, for $ZnSnO_3$ nanowires and Zn_2SnO_4 nanoparticles, respectively. To the author's best knowledge, there are no reports on the RhB photodegradation using $ZnSnO_3$ nanowires as catalyst, nevertheless, when comparing with Zn_2SnO_4 nanostructures the presented results are far from those reported by Zhao *et al.* where degradation rates of 0.1 min^{-1} were achieved, with a irradiation power of 300 W.[49]

In **Figure 5.7**i a photograph of the RhB solution, before and after the photocatalytic degradation with the different ZTO nanostructures, shows the discoloration of the solution where the nanostructures acted as catalysts. **Figure 5.7**j presents a resume of the photodegradation rate constants obtained for the different ZTO nanostructures

$ZnSnO_3$ nanowires showed a higher degradation rate for both dyes than the Zn_2SnO_4 nanostructures. This is most probably related to the geometry of the nanostructures, since numerous advantages are attributed to the 1D structures for photocatalytic applications such as: efficient charge transport; large surface area; and high length-to-diameter ratios that enhances the light absorption and scattering properties.[51] Concerning the performance of the Zn_2SnO_4 samples, the better performance achieved with the Zn_2SnO_4 nanoparticles, when compared to the octahedrons, can be related not only with geometry factors, but also with their higher carrier concentration, as observed trough the XPS analysis.

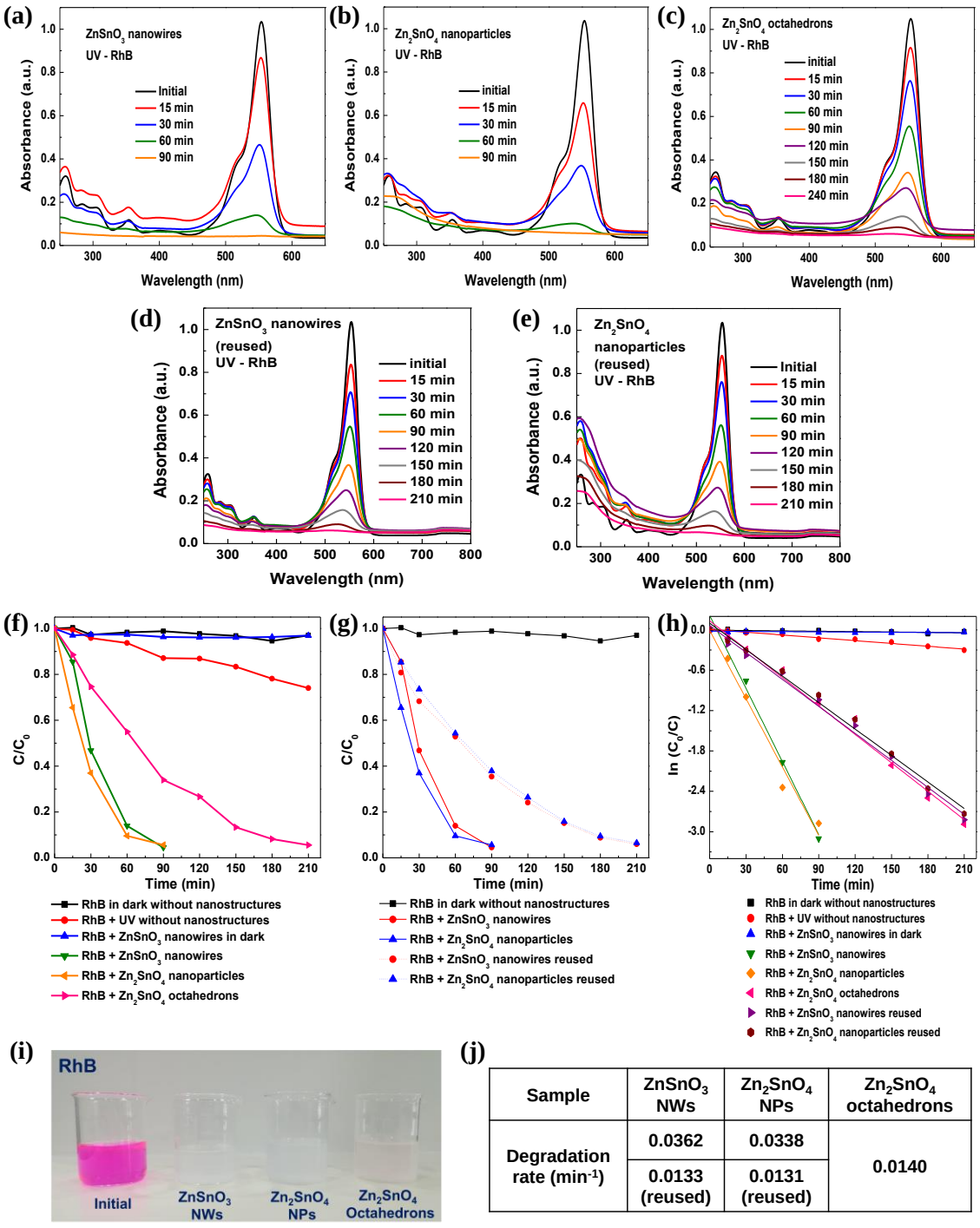

(j)

Sample	$ZnSnO_3$ NWs	Zn_2SnO_4 NPs	Zn_2SnO_4 octahedrons
Degradation rate (min^{-1})	0.0362	0.0338	0.0140
	0.0133 (reused)	0.0131 (reused)	

Figure 5.7. Absorbance spectra showing the photocatalytic degradation of RhB under UV-light in the presence of (a) $ZnSnO_3$ nanowires, (b) Zn_2SnO_4 nanoparticles, (c) Zn_2SnO_4 octahedrons, (d) reused $ZnSnO_3$ nanowires and (e) Zn_2SnO_4 nanoparticles as catalysts, under UV light irradiation (285 W). C/C_0 comparison between (f) all these nanostructures and (g) the reused $ZnSnO_3$ nanowires and Zn_2SnO_4 nanoparticles. (h) Kinetic parameters of the ZTO structures, with the respective fit curves. (i) Photograph of the initial MB solution and after degradation using each ZTO nanostructures. (j) Table with the degradation rates of MB using each ZTO nanostructures under UV light.

5.4.3. Photocatalytic activity under visible light irradiation

Both ZTO phases have optical absorption in UV region, being more promisor as catalyst under UV light irradiation. Still, herein, the photocatalytic activity of the three different ZTO nanostructures ($ZnSnO_3$ nanowires, and Zn_2SnO_4 nanoparticles and octahedrons), on the same RhB and MB aqueous solutions, was also investigated under visible light irradiation. The power of the visible light source used had a power density of 100 $mW \cdot cm^{-2}$. The absorbance measurements were all performed from 200 to 800 nm, every 2 h.

When using visible light irradiation, a complete degradation of MB using ZTO nanostructures was achieved in 10 h. However, when investigating the degradation of this dye without nanostructures under visible light it was found that the dye suffers the same degradation without nanostructures. These results are shown in **Figure 5.8**.

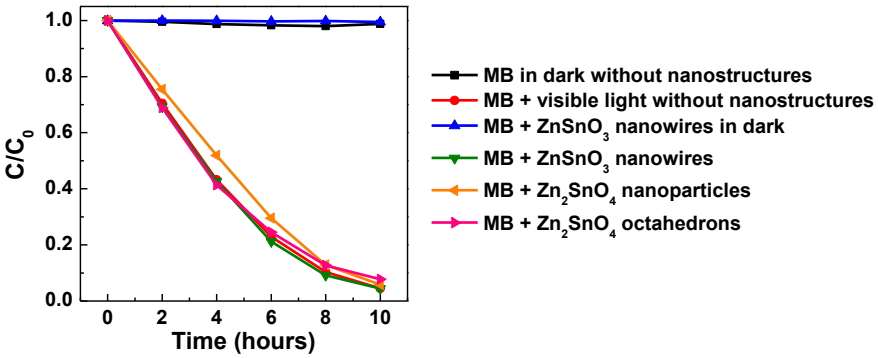

Figure 5.8. Degradation ratio (C/C_0) over time of methylene blue in dark without nanostructures, and under visible light irradiation without nanostructures and using $ZnSnO_3$ nanowires, and Zn_2SnO_4 nanoparticles and octahedrons as catalysts.

The photocatalytic degradation of RhB under visible light was measured for 12 h (**Figure 5.9**). A slight hypsochromic shift of RhB absorption bands can be observed after 4 h irradiation for all experiments due to the photooxidative N-de-ethylation of RhB.[52]

After 12 h of exposure RhB alone does not show significant change and in fact is similar to the control experiment performed in the dark. In the presence of ZTO nanostructures and after 12 h of exposure, the amount of RhB decreased by approximately 40 %, 50 % and 24 % when using $ZnSnO_3$ nanowires, Zn_2SnO_4 nanoparticles and Zn_2SnO_4 octahedrons, respectively. Thus, even under visible light a faster degradation of RhB is achieved due to the photocatalytic activity of the nanostructures, especially when using Zn_2SnO_4 nanoparticles. Concerning this material, while the measured performance was bellow the 90 % degradation in 120 min achieved by Ali *et al*., a 5 times higher irradiation power than the applied in this work was employed, making a direct comparison unreasonable.[41]

As expected, a much smaller degradation of RhB is achieved using the ZTO nanostructures under visible light, when compared to the UV irradiation. Nevertheless, concerning to the optical band gap of the ZTO nanostructures (3.4–3.6 eV), even when compared with TiO_2 (3.05 eV), the photocatalytic activity is quite satisfactory.[53]

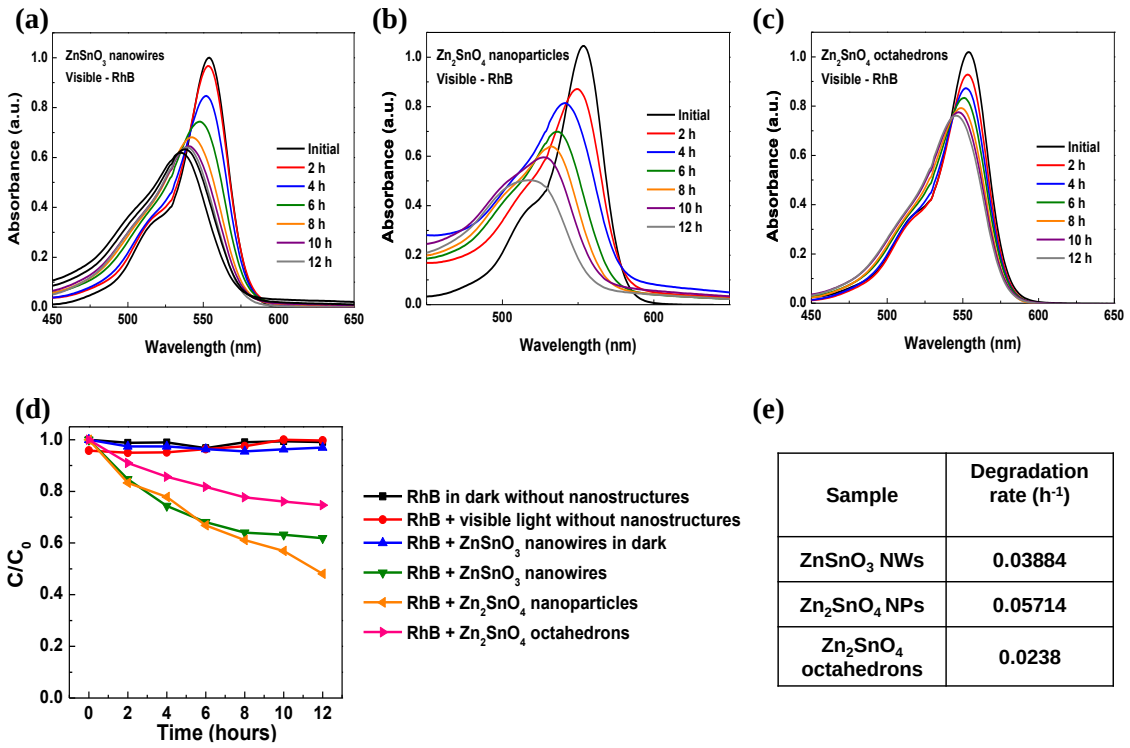

(e)

Sample	Degradation rate (h^{-1})
$ZnSnO_3$ NWs	0.03884
Zn_2SnO_4 NPs	0.05714
Zn_2SnO_4 octahedrons	0.0238

Figure 5.9. Absorbance spectra showing photocatalytic degradation of RhB under visible light in the presence of (a) $ZnSnO_3$ nanowires, and Zn_2SnO_4 (b) nanoparticles and (c) octahedrons. (d) C/C_0 comparison of the photocatalytic degradation between ZTO nanostructures. (e) Table with the degradation rates of RhB using each ZTO nanostructures under visible light.

5.5. Conclusions

In this paper $ZnSnO_3$ nanowires in powder form, produced by hydrothermal synthesis, were used as photocatalyst for the first time, to the best of our knowledge. This material showed a great performance in the photodegradation of two different dyes, methylene blue and rhodamine B, under both UV and visible light irradiations, when compared with Zn_2SnO_4 nanoparticles and octahedrons. $ZnSnO_3$ nanowires completely degraded both methylene blue and rhodamine B in only 90 min under 285 W of UV light irradiation. These results show the versatility of ZTO nanostructures to degrade different dyes. Moreover, the reusability of these materials was also demonstrated, which is a very important property. As expected, due to the wide band gap of the ZTO nanostructures, their photocatalytic activity under UV light is much higher than under visible light. Still, using $ZnSnO_3$ nanowires under visible light the amount of rhodamine B decreased by 40 % in 12 h and when using Zn_2SnO_4 nanoparticles 50 % of rhodamine B was degraded in 12 h, which is significantly better than what is reported for some TiO_2 nanostructures.

5.6. References

1. Kampouri, S. & Stylianou, K. C. Dual-Functional Photocatalysis for Simultaneous Hydrogen Production and Oxidation of Organic Substances. *ACS Catal.* **9**, 4247–4270 (2019).
2. Barrocas, B. *et al.* Characterization and electrochemical behaviour of nanostructured calcium samarium manganite electrodes fabricated by RF-Magnetron Sputtering. *Electrochim. Acta* **137**, 99–107 (2014).
3. Barrocas, B., Sério, S., Rovisco, A. & Melo Jorge, M. E. Visible-Light Photocatalysis in Ca0.6Ho0.4MnO3 Films Deposited by RF-Magnetron Sputtering Using Nanosized Powder Compacted Target. *J. Phys. Chem. C* **118**, 590–597 (2014).
4. Baruah, S. & Dutta, J. Zinc stannate nanostructures: hydrothermal synthesis. *Sci. Technol. Adv. Mater.* **12**, 013004 (2011).
5. Barrocas, B., Sério, S. & Melo Jorge, M. E. Hierarchically Grown CaMn3O6 Nanorods by RF Magnetron Sputtering for Enhanced Visible-Light-Driven Photocatalysis. *J. Phys. Chem. C* **118**, 24127–24135 (2014).
6. Michelin, C. & Hoffmann, N. Photosensitization and Photocatalysis—Perspectives in Organic Synthesis. *ACS Catal.* **8**, 12046–12055 (2018).
7. Firooz, A. A., Mahjoub, A. R., Khodadadi, A. A. & Movahedi, M. High photocatalytic activity of Zn2SnO4 among various nanostructures of Zn2xSn1-xO2 prepared by a hydrothermal method. *Chem. Eng. J.* **165**, 735–739 (2010).
8. Najam Khan, M., Al-Hinai, M., Al-Hinai, A. & Dutta, J. Visible light photocatalysis of mixed phase zinc stannate/zinc oxide nanostructures precipitated at room temperature in aqueous media. *Ceram. Int.* **40**, 8743–8752 (2014).
9. Nunes, D. *et al.* Photocatalytic TiO2 Nanorod Spheres and Arrays Compatible with Flexible Applications. *Catalysts* **7**, 60 (2017).
10. Barrocas, B., Monteiro, O. C., Jorge, M. E. M. & Sério, S. Photocatalytic activity and reusability study of nanocrystalline TiO2 films prepared by sputtering technique. *Appl. Surf. Sci.* **264**, 111–116 (2013).
11. Pimentel, A. *et al.* Synthesis of Long ZnO Nanorods under Microwave Irradiation or Conventional Heating. *J. Phys. Chem. C* **118**, 14629–14639 (2014).
12. Khan, M. N., Jaisai, M. & Dutta, J. Photocatalytic Inactivation of Escherichia Coli Using Zinc Stannate Nanostructures under Visible Light. *Adv. Mater. Res.* **1131**, 203–209 (2015).
13. Najam Khan, M. & Dutta, J. Comparison of photocatalytic activity of zinc stannate particles and zinc stannate/zinc oxide composites for the removal of phenol from water, and a study on the effect of pH on photocatalytic efficiency. *Mater. Sci. Semicond. Process.* **36**, 124–133 (2015).
14. Barrocas, B., Sério, S., Rovisco, A., Nunes, Y. & Jorge, M. E. E. M. Removal of rhodamine 6G dye contaminant by visible light driven immobilized Ca1-xLnxMnO3 (Ln=Sm, Ho; 0.1≤x≤0.4) photocatalysts. *Appl. Surf. Sci.* **360**, 798–806 (2015).
15. Zeng, J. *et al.* Transformation process and photocatalytic activities of hydrothermally synthesized Zn2SnO4 nanocrystals. *J. Phys. Chem. C* **112**, 4159–4167 (2008).
16. Fu, X. *et al.* Hydroxide ZnSn(OH)6: A promising new photocatalyst for benzene degradation. *Appl. Catal. B Environ.* **91**, 67–72 (2009).
17. Fu, X. *et al.* Hydrothermal synthesis, characterization, and photocatalytic properties of Zn2SnO4. *J. Solid State Chem.* **182**, 517–524 (2009).

18. Lo, M.-K., Lee, S.-Y. & Chang, K.-S. Study of ZnSnO3-Nanowire Piezophotocatalyst Using Two-Step Hydrothermal Synthesis. *J. Phys. Chem. C* **119**, 5218–5224 (2015).

19. Wang, Y.-T. & Chang, K.-S. Piezopotential-Induced Schottky Behavior of Zn1−xSnO3 Nanowire Arrays and Piezophotocatalytic Applications. *J. Am. Ceram. Soc.* **99**, 2593–2600 (2016).

20. Biswas, A., Saha, S. & Jana, N. R. ZnSnO3 Nanoparticle-Based Piezocatalysts for Ultrasound-Assisted Degradation of Organic Pollutants. *ACS Appl. Nano Mater.* **2**, 1120–1128 (2019).

21. Tobergte, D. R. & Curtis, S. Formation of Self-Assembled Defect-Free Zn2SnO4 Nanostructures from Binary Oxides without the Kirkendall Effect. *J. Chem. Inf. Model.* **53**, 1689–1699 (2013).

22. Sun, S. & Liang, S. Morphological zinc stannate: synthesis, fundamental properties and applications. *J. Mater. Chem. A* **5**, 20534–20560 (2017).

23. Chen, Z., Cao, M. & Hu, C. Novel Zn2SnO4 hierarchical nanostructures and their gas sensing properties toward ethanol. *J. Phys. Chem. C* **115**, 5522–5529 (2011).

24. Singh, R., Yadav, A. K. & Gautam, C. Synthesis and Humidity Sensing Investigations of Nanostructured ZnSnO3. *J. Sens. Technol.* **01**, 116–124 (2011).

25. Tharsika, T., Haseeb, A. S. M. a., Akbar, S. a., Sabri, M. F. M. & Wong, Y. H. Gas sensing properties of zinc stannate (Zn2SnO4) nanowires prepared by carbon assisted thermal evaporation process. *J. Alloys Compd.* **618**, 455–462 (2015).

26. Wu, J. M., Xu, C., Zhang, Y. & Wang, Z. L. Lead-free nanogenerator made from single ZnSnO3 microbelt. *ACS Nano* **6**, 4335–40 (2012).

27. Wu, J. M. *et al.* Ultrahigh Sensitive Piezotronic Strain Sensors Based on a ZnSnO3 Nanowire/Microwire. *ACS Nano* **6**, 4369–4374 (2012).

28. Wu, J. M. *et al.* Flexible and transparent nanogenerators based on a composite of lead-free ZnSnO3 triangular-belts. *Adv. Mater.* **24**, 6094–6099 (2012).

29. Guo, R., Guo, Y., Duan, H., Li, H. & Liu, H. Synthesis of Orthorhombic Perovskite-Type ZnSnO3 Single-Crystal Nanoplates and Their Application in Energy Harvesting. *ACS Appl. Mater. Interfaces* **9**, 8271–8279 (2017).

30. Hwang, J. K. *et al.* Direct nanoprinting by liquid-bridge-mediated nanotransfer moulding. *Nat. Nanotechnol.* **5**, 742–748 (2010).

31. Lim, T., Kim, H., Meyyappan, M. & Ju, S. Photostable Zn2SnO4 Nanowire Transistors for Transparent Displays. *ACS Nano* **6**, 4912–4920 (2012).

32. Kim, S., Kim, H., Janes, D. B. & Ju, S. Interface studies of N2 plasma-treated ZnSnO nanowire transistors using low-frequency noise measurements. *Nanotechnology* **24**, 305201 (2013).

33. Siddiqui, G. U., Rehman, M. M. & Choi, K. H. Enhanced resistive switching in all-printed, hybrid and flexible memory device based on perovskite ZnSnO3 via PVOH polymer. *Polymer (Guildf).* **100**, 102–110 (2016).

34. Yang, Y. J., Rehman, M. M., Siddiqui, G. U., Na, K. H. & Choi, K. H. Effect of adding a polymer and varying device size on the resistive switching characteristics of perovskite nanocubes heterojunction. *Curr. Appl. Phys.* **17**, 1733–1741 (2017).

35. Lei, M. *et al.* A novel self-catalytic route to zinc stannate nanowires and cathodoluminescence and electrical transport properties of a single nanowire. *J. Alloys Compd.* **657**, 394–399 (2016).

36. Miyauchi, M., Liu, Z., Zhao, Z.-G., Anandan, S. & Hara, K. Single crystalline zinc stannate nanoparticles for efficient photo-electrochemical devices. *Chem. Commun.* **46**, 1529–1531 (2010).

37. Chen, F., Huang, H., Guo, L., Zhang, Y. & Ma, T. The Role of Polarization in Photocatalysis. *Angew. Chemie Int. Ed.* **58**, 10061–10073 (2019).

38. Tian, Z., Liang, C., Liu, J., Zhang, H. & Zhang, L.-D. Zinc Stannate Nanocubes and Nanourchins with High Photocatalytic Activity for Methyl Orange and 2,5-DCP Degradation. *J. Mater. Chem.* **22**, 17210–17214 (2012).

39. Ivetić, T. B., Finčur, N. L., Đačanin, L. R., Abramović, B. F. & Lukić-Petrović, S. R. Ternary and coupled binary zinc tin oxide nanopowders: Synthesis, characterization, and potential application in photocatalytic processes. *Mater. Res. Bull.* **62**, 114–121 (2015).

40. Jia, T. *et al.* A Facile Approach for the Synthesis of Zn2SnO4/BiOBr Hybrid Nanocomposites with Improved Visible-Light Photocatalytic Performance. *Nanomaterials* **8**, 313 (2018).

41. Ben Ali, M. *et al.* Hydrothermal synthesis, phase structure, optical and photocatalytic properties of Zn2SnO4 nanoparticles. *J. Colloid Interface Sci.* **457**, 360–369 (2015).

42. Rovisco, A. *et al.* Seed-Layer Free Zinc Tin Oxide Tailored Nanostructures for Nanoelectronic Applications: Effect of Chemical Parameters. *ACS Appl. Nano Mater.* **1**, 3986–3997 (2018).

43. Rovisco, A. *et al.* Growth Mechanism of Seed-Layer Free ZnSnO3 Nanowires: Effect of Physical Parameters. *Nanomaterials* **9**, 1002 (2019).

44. Annamalai, A., Carvalho, D., Wilson, K. C. & Lee, M.-J. Properties of hydrothermally synthesized Zn2SnO4 nanoparticles using Na2CO3 as a novel mineralizer. *Mater. Charact.* **61**, 873–881 (2010).

45. Šepelák, V. *et al.* Nonequilibrium structure of Zn2SnO4 spinel nanoparticles. *J. Mater. Chem.* **22**, 3117 (2012).

46. Aragón, F. H. *et al.* Structural and Surface Study of Praseodymium-Doped SnO2 Nanoparticles Prepared by the Polymeric Precursor Method. *J. Phys. Chem. C* **119**, 8711–8717 (2015).

47. Bitter, S., Schlupp, P., von Wenckstern, H. & Grundmann, M. Vital Role of Oxygen for the Formation of Highly Rectifying Schottky Barrier Diodes on Amorphous Zinc–Tin–Oxide with Various Cation Compositions. *ACS Appl. Mater. Interfaces* **9**, 26574–26581 (2017).

48. Gassenbauer, Y. *et al.* Surface states, surface potentials, and segregation at surfaces of tin-doped In2 O3. *Phys. Rev. B - Condens. Matter Mater. Phys.* **73**, 1–11 (2006).

49. Zhao, Q. *et al.* Synthesis of hollow cubic Zn2SnO4 sub-microstructures with enhanced photocatalytic performance. *J. Alloys Compd.* **671**, 328–333 (2016).

50. Wu, J. M., Hsu, G. K., Yeh, H.-H. & Lin, H.-C. Metallic Zinc Nanowires Effect in High-Performance Photoresponsive and Photocatalytic Properties of Composite Zinc Stannate Nanowires. *J. Electrochem. Soc.* **159**, H497–H501 (2012).

51. Xiao, F. X. *et al.* One-dimensional hybrid nanostructures for heterogeneous photocatalysis and photoelectrocatalysis. *Small* **11**, 2115–2131 (2015).

52. Laatar, F. *et al.* CdSe nanorod/TiO 2 nanoparticle heterojunctions with enhanced solar- and visible-light photocatalytic activity. *Beilstein J. Nanotechnol.* **8**, 2741–2752 (2017).

53. Matias, M. L. *et al.* Paper-Based Nanoplatforms for Multifunctional Applications. *J. Nanomater.* **2019**, 1–16 (2019).

Chapter 6 – Electrodeposition for integration of ZTO-based nanostructures in devices

In Chapter 6 the application of ZTO and SnO_2 nanostructures for pH sensors is presented. To fabricate these devices the electrodeposition of the nanostructures was explored as a transfer method. The fabrication and characterization of the devices were performed in the clean room facilities and laboratory resources of CEMOP and CENIMAT. **Table 6.1** summarizes the syntheses' conditions of the nanostructures used in this chapter.

Table 6.1. Syntheses conditions of the Zn:Sn:O-based nanostructures used for pH sensors.

Nanostructures produced	Synthesis parameters	Heating system
$ZnSnO_3$ nanowires	$ZnCl_2$ / Zn:Sn – 2:1 / H_2O:EDA – 7.5:7.5 ml / 200 °C / 24 h (sub-sections 2.1 and 2.2)	conventional oven
Zn_2SnO_4 nanoparticles	$ZnCl_2$ / Zn:Sn – 2:1 / H_2O – 15 ml / 200 °C / 24 h (sub-section 3.1.4)	conventional oven
SnO_2 nanoparticles	H_2O:Ethanol – 6:10 ml / 140 °C / 4 h (sub-section 3.1.5)	conventional oven
SnO_2 nanoparticles	H_2O:Ethanol – 6:10 ml / 140 °C / 60' (sub-section 3.1.5)	microwave system

The contents of the section 6.2 are adapted from the following paper:

- **A. Rovisco**, J. Neto, R. Branquinho, J. Martins, E. Fortunato, R. Martins and P. Barquinha, pH sensors based on electrodeposited ZTO nanostructures, under preparation 2019

6.1. Abstract

In this work electrodeposition was employed as a transfer method for the integration of ZTO-based nanostructures synthesized by hydrothermal processes ($ZnSnO_3$ nanowires, Zn_2SnO_4 nanoparticles and SnO_2 nanoparticles). With this method the integration of the powder form nanostructures in pH sensors was achieved by a controlled deposition in specific substrate regions. pH sensors using zinc-tin oxide nanostructures were for the first time demonstrated, to the best of author's knowledge, reaching impressive sensitivities, especially those employing Zn_2SnO_4 nanoparticles for which the sensitivity (–58.6 mV/pH) was close to the theoretical maximum (–59 mV/pH). The performance of pH sensors using SnO_2 nanoparticles synthesized either in a conventional oven or in a microwave-system were found to be similar. Additionally, ZTO-based nanostructures were also deposited in carbon fibers through electrodeposition for future application in energy storage devices. The electrodeposition technique was shown to be a promising integration method for implementation of powder form nanostructures (as achieved by seed-layer free methods) in devices for different applications.

6.2. pH sensors based on electrodeposited ZTO nanostructures

6.2.1. Introduction

The concept of smart surfaces includes different kinds of devices, where (bio)sensors are some of the most interesting to integrate in this concept. For instance, for biomedical applications, flexible, wearable, biocompatible devices for patient monitoring could allow for early diagnosis or optimization along the medical treatment. In this kind of concepts, one of the highly important parameters for monitoring is the pH.[1,2]

pH sensors measure the hydrogen activity (a_H^+) being the pH given by $pH = -log\ a_H^+$.[2,3] The sensing in these devices can be categorized as electrochemical or spectrometric, with the electrochemical being divided into voltammetry (amperometry) or potentiometry.[1,2] While approaches as ion sensitive field-effect transistors and solid-state pH sensors have been widely used, due to its robustness and fast response, in general these sensors are cumbersome, complex and require high power consumption.[1] Potentiometry sensors however are very simple and efficient. These consist in measuring the potential between a pH sensitive electrode (swhich responds to the hydrogen activity in an electrolyte in solution) and a reference electrode (isolated from the solution) in an electrochemical cell. This measurement can be done under the condition of zero current making this an equilibrium method.[2] Moreover, using potentiometric microelectrodes offers a high sensitivity and selectivity for fine variation of pH measurements and allows the pH to be measured in small sample volumes.[2]

Particularly, pH sensors based on semiconductor oxides have been the target of high attention.[4] Similarly to what is observed for applications such as electronics and energy production/storage, these materials are advantageous compared to others due to the lower fabrications costs, high integration levels and high performance and sensitivity. Several oxide materials have been applied for pH sensors including ZnO and SnO_2.[4–7] Properties such as stability, insolubility and electro-catalytic behavior have made these materials very attractive for pH sensors.[8,9] Moreover, oxides are commonly amphoteric materials, enhancing their sensitivity. Multicomponent oxides have also been used as active layer in pH sensors, such as $HoTiO_3$ and $Eu_2Ti_2O_7$.[10–12] These materials present the advantage of having a better stability in aqueous solutions then binary oxides,[13] furthermore, the adjustment of their cationic ratio can be used to control their properties towards higher performances. While the ternary zinc-tin oxide (ZTO) has been widely used for sensor applications, especially for gas sensing, employment of this material for pH sensing is still quite limited, to the best of our knowledge. The employment of ZTO in these devices could benefit from its biosafety and its already known catalytic properties.

As high levels of integration for small size devices are desired, nanomaterials have been widely explored due their low dimensions. 1D materials are particularly interesting for this application: their large surface-to-volume ratio potentiate a short diffusion distance of the analyte towards the electrode surface which results in good signal-to-noise ratio, faster response and high sensitivity.[14] Furthermore, 1D materials typically have efficient charge transport, enabling a good electrical coupling with the working electrode.

Herein, pH sensors using two different ZTO nanostructures ($ZnSnO_3$ nanowires and Zn_2SnO_4 nanoparticles) are presented, being the first time these ternary nanostructures are implemented for this application, to the best of the author's knowledge. With excellent performances being achieved, especially in the case of Zn_2SnO_4 nanoparticles in which a sensitivity close to the theoretical maximum was almost reached, the potentiality of this material for sustainable, flexible and biocompatible pH sensors is clearly shown. The powder form of the ZTO nanostructures favors the use of a simple electrodeposition method, which again showcases the higher flexibility for application of the nanostructures given by the seed-layer free nature of the optimized syntheses. Other transfer methods such as spin coating, drop coating and printing were also possibly viable methods, however electrodeposition appears as a superior alternative due to its conformable coating capability.

6.2.2. Experimental details

Nanostructures synthesis

The $ZnSnO_3$ nanowires were produced by the optimized seed-layer free hydrothermal syntheses described in Chapter 2, while Zn_2SnO_4 nanoparticles were synthesized by the method presented in sub-section 3.1.4. SnO_2 nanoparticles were produced by both oven and microwave

hydrothermal synthesis. A summary of the conditions for the mentioned synthesis is presented in **Table 6.1**.

Devices fabrication

A shadow mask of polyethylene terephthalate (PET, from GoodFellow) was defined by a laser cutter (Universal Laser System ULS3.50) and was used to pattern the electrodes. Ti/Au electrodes with 6/60 nm thickness were deposited by e-beam evaporation on a polyethylene naphthalate (PEN, from Teonex) substrate. On each electrode, a sensing area (1 mm^2) was delimited using a wax printed layer (Xerox ColorQube 8570DNPS) on top of the Ti/Au connection line. The remaining electrode is thus insulated from the solution for the electrodeposition.

Electrodeposition

The nanostructures were dispersed in deionized water (1 mg/mL) and the solution was sonicated (HIELSHER M80) for 5 min before the electrodeposition process. A Gamry Instruments Reference 600 potentiostat/galvanostat was used to perform the electrodeposition of the nanostructures on the patterned electrodes. The electrodeposition process was performed in a constant current mode (20 µA) for 900 s with a three-electrode configuration, which consists on an Ag/AgCl reference electrode (BASi), a platinum wire counter electrode, and the patterned gold layer (the working electrode), resulting in the deposition of the nanostructures in solution onto the patterned area. Next, the electrodes were rinsed with deionized water and then dried at 50 °C for 1 h. A schematic representation of the electrodeposition is illustrated in **Figure 6.1**.

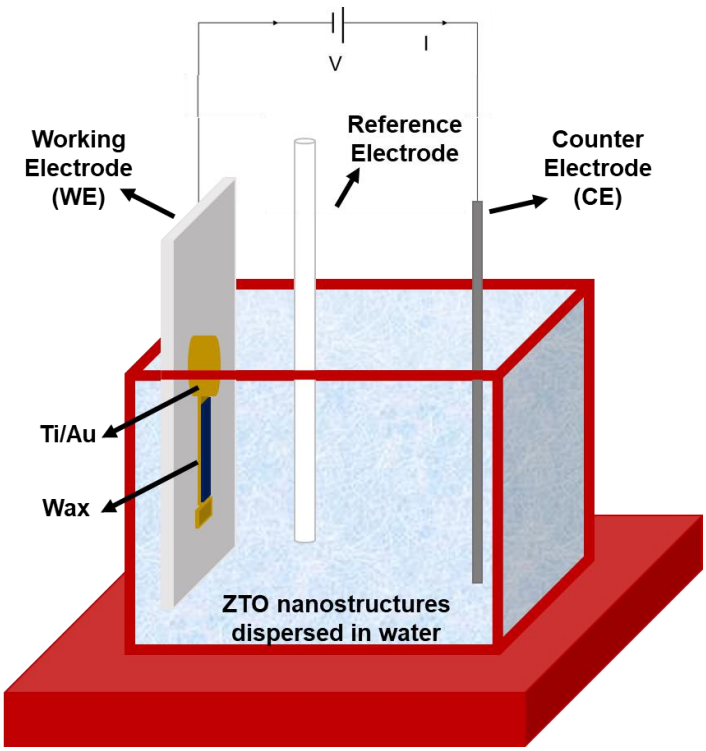

Figure 6.1. Schematic representation of the setup for the electrodeposition of the nanostructures onto the working electrode for the pH sensors.

pH sensor characterization

Employing the same three electrode cell configuration, electrochemical impedance spectroscopy (EIS) measurements were performed, in a frequency of 1 to 10^5 Hz, with an AC voltage of 10 mV. This was performed both before and after the electrodeposition of the nanostructures and was used to determine the depositions effectiveness. In the same configuration, and to determine the pH sensitivity of the sensors, the open circuit voltage variation was measured immersing the sensors in commercial buffer solutions with pH values of 4, 7 and 10 (buffer solutions, Roth) for 120 s at room temperature.

6.2.3. Results and discussion

ZTO nanostructures

Electrodeposition of the ZTO nanostructures

Two types of ZTO nanostructures were employed in the pH sensors production: $ZnSnO_3$ nanowires and Zn_2SnO_4 nanoparticles. Based on previous work with electrodeposition of nanostructures,[1] depositions under a constant current mode with 20 µA for 900 s were first tested. **Figure 6.2** shows the SEM images of the Ti/Au electrodes after electrodeposition of each ZTO nanostructures where it is possible to observe that a higher amount of Zn_2SnO_4 nanoparticles was deposited than for $ZnSnO_3$ nanowires. This can be related to the shape, size or even adhesion of each type of nanostructure, which can influence its deposition rate on the substrate.

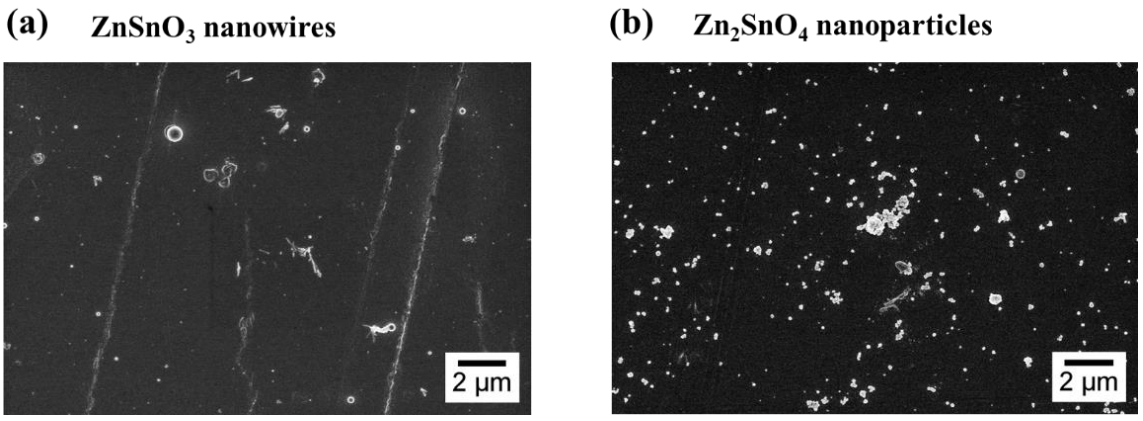

Figure 6.2. SEM images of the Ti/Au electrodes after the electrodeposition of (a) $ZnSnO_3$ nanowires and (b) Zn_2SnO_4 nanoparticles (20 µA for 900 s).

Electrochemical Characterization

In **Figure 6.3** the impedance modulus and phase angle measured by the EIS for the working electrodes before and after the electrodepositions (20 µA, 900 s) of the $ZnSnO_3$ nanowires and Zn_2SnO_4 nanoparticles are presented. The impedance, changing from capacitive to resistive

regimes from lower to higher frequencies, seems to be consistent with a series RC circuit. While the electrodeposition of $ZnSnO_3$ nanowires did not cause a significant change in the phase angle, an unexpected increase of the impedance was observed, which may arise from the nanowires' significant resistivity, which is probably dominating over an increase of the electrochemical surface area. For the case of Zn_2SnO_4 nanoparticles however, a significant decrease of the impedance is observed. This can be attributed to the increase of electrochemical surface area, which is also relevant for enhancing the sensor's sensitivity. Regarding the phase angle, in the low-frequency range, values close to - 90° indicate a capacitive regime for all measurements. However, the frequency range in which the phase is close to - 90° decreased with the Zn_2SnO_4 nanoparticles deposition. For higher frequencies (10^4-10^6 Hz), both for pristine electrodes and for electrodes with ZTO nanostructures, the impedance is mostly resistive (with a phase angle close to 0º) with the modulus of the impedance representing the series resistance of the measured system, which in this case should be determined by the impedance of the solution.[4]

The difference between the impedance curves induced by the deposition of the nanostructures was much higher for the Zn_2SnO_4 nanoparticles than for the $ZnSnO_3$ nanowires, which is in agreement with the difference in efficiency of deposition as observed in the SEM images.

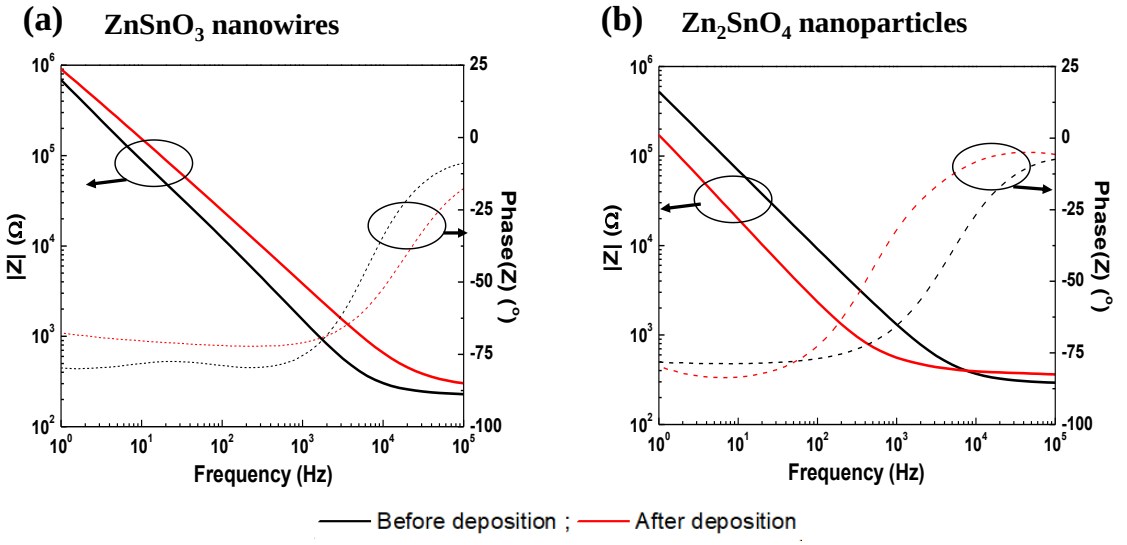

Figure 6.3. Bode impedance modulus and phase diagrams for the working electrodes before and after the electrodeposition of (a) $ZnSnO_3$ nanowires and (b) Zn_2SnO_4 nanoparticles.

pH sensitivity

In order to determine the pH sensitivity of the prepared samples, the measurement of the open circuit voltage (or potential) was performed, dipping the sensor (working electrode) in commercial buffer solutions with pH values of 10, 7 and 4 for 120 s, with the measured potential being dependent on the solutions' pH. Linear relations between pH and potential can be described by the Nernstian equation which at 25 ˚C is given by (1).

$$E = E^0 - (2.303RT/F)\,pH = E^0 - 0.05916\,pH \quad (1)$$

where E^0 is the standard electrode potential, T is the temperature, R is the gas constant and F is Faraday's constant, with the sensor's sensitivity being the slope of the E - pH straight line.[2] While sensitivities in the range of 50-70 mV/pH are considered to be acceptable for the desired application, it should be taken into account that the theoretical maximum sensitivity (Nernstian sensitivity) at 25 °C is −59 mV/pH. Ideal sensitivities correspond to a situation where all space charges are formed, due to the redox reaction, and indicate that the sensor is performing properly.

Figure 6.4 presents then the response measured for the Au electrode without nanostructures deposition and for the electrodes with the electrodeposited (20 µA, 900 s) $ZnSnO_3$ nanowires and Zn_2SnO_4 nanoparticles. The determined sensitivity when using Zn_2SnO_4 nanoparticles as sensitive material was −58.6 ± 2.7 mV/pH, being that this value is very close to the theoretical maximum, while using $ZnSnO_3$ nanowires yielded −54.0 ± 2.7 mV/pH. Furthermore, the low sensitivity (−9.7 ± 2.8 mV/pH) measured for the Au electrode without nanostructures emphasizes the role of the oxide nanostructures in the increase of pH sensitivity.

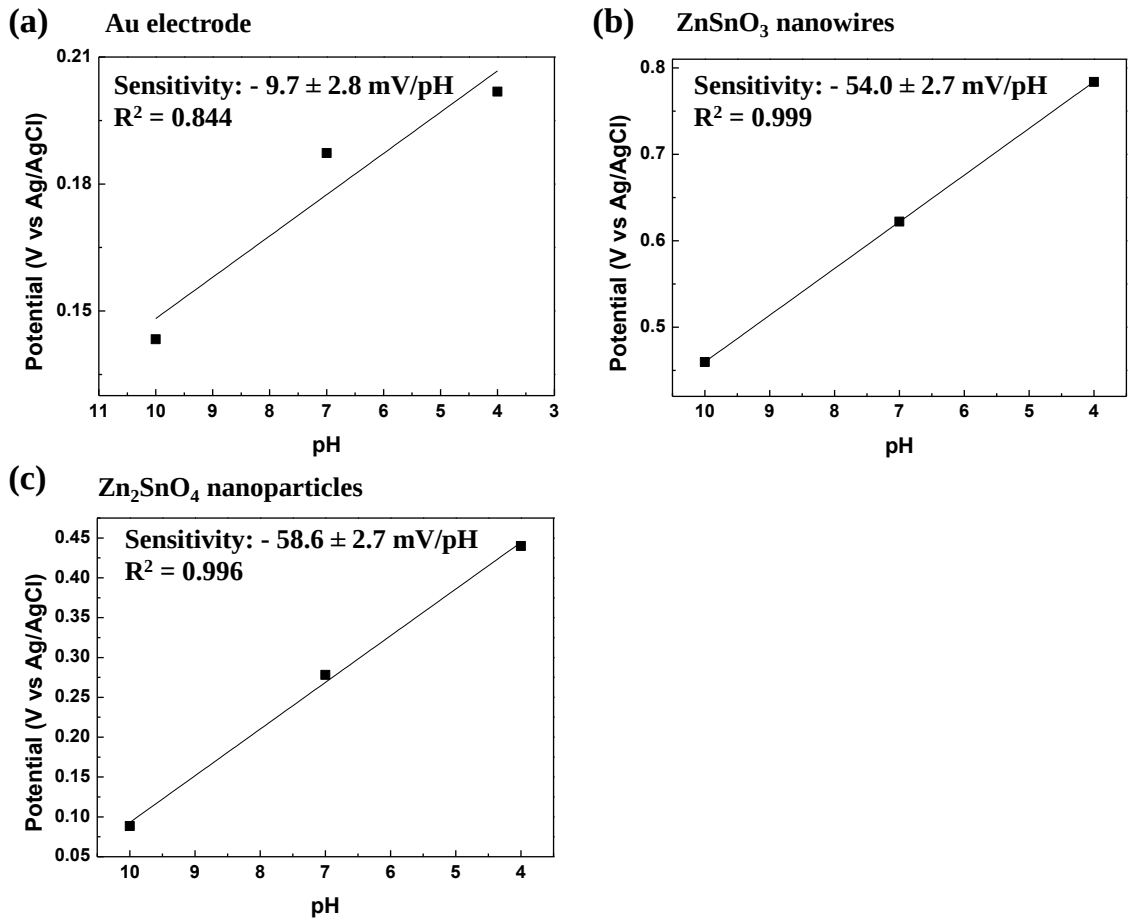

Figure 6.4. pH sensitivity measured from pH 10 to 4 of (a) Au electrode, (b) Au electrode with $ZnSnO_3$ nanowires and (c) Au electrode with Zn_2SnO_4 nanoparticles. The nanostructures were deposited by electrodeposition under a constant current of 20 µA for 900s. The uncertainty corresponds to the standard error from the linear regressions, and R^2 is the correlation coefficient.

These sensitivity values are much higher than those usually reported for the binary oxides ZnO and SnO_2,[4–6] which may be related to either their superior electrical properties or their improved stability. In fact, higher pH sensitivity has been reported for multicomponent oxides, such as $HoTiO_3$, and $Eu_2Ti_2O_7$. [10–12]

For the nanostructures' electrodeposition optimization, several current levels were tested. **Figure 6.5** shows the sensitivity values for the devices fabricated with respect to the different current levels applied during the electrodeposition of the ZTO nanostructures, for $ZnSnO_3$ nanowires and Zn_2SnO_4 nanoparticles.

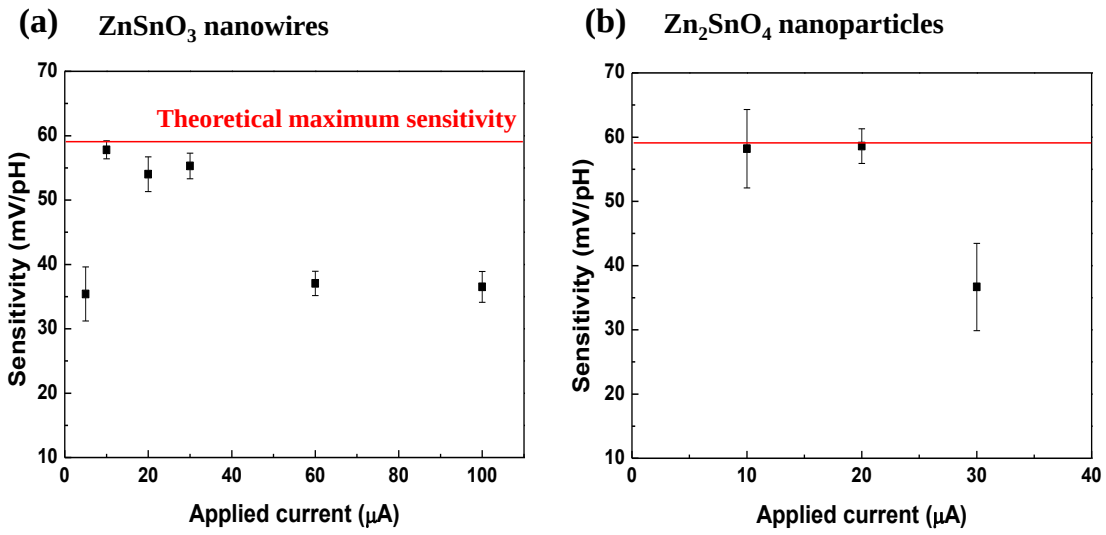

Figure 6.5. pH sensitivity values measured for devices using different applied current levels during the electrodeposition of (a) $ZnSnO_3$ nanowires and (b) Zn_2SnO_4 nanoparticles.

For $ZnSnO_3$ nanowires, the best device performance was obtained for depositions with a current value of 10 μA, in which a sensitivity of −57.8 ± 1.4 mV/pH was achieved. While slightly lower than the sensitivity reached using Zn_2SnO_4 nanoparticles, this value is still close to the theoretically maximum value. Regarding the devices with the Zn_2SnO_4 nanoparticles **Figure 6.5**b shows that higher sensitivity was obtained from the initial conditions, i.e. 20 μA and 900 s. In both cases, it was seen that the sensitivity decreases for electrodepositions with currents levels higher than approximately 30 μA, and it was in fact seen through SEM that a low concentration of nanostructures was present in the electrode for the higher currents. Current levels of 200 μA were also tested, but water electrolysis was observed under these conditions. While a dispersed distribution of nanostructures was observed in the electrodes, a very high performance was obtained with both ZTO nanomaterials, showing that even a low quantity of nanostructures is enough to obtain a high sensitivity, which implies that these are highly sensitive to pH variations.

For the establishment of these devices as viable alternatives, assessment of their reversibility and reproducibility is a key aspect. In this regard, further studies concerning the integration of the nanostructures in the electrodes are envisaged.

SnO_2 nanoparticles

Similar to the methodology used for devices with the ZTO nanostructures, a current of 20 µA was applied for 900 s for the electrodeposition of SnO_2 nanoparticles onto Ti/Au electrodes, and the same concentration (1 mg/mL) was used for the dispersion. This method was applied for both nanoparticles produced using conventional oven or a microwave system. The response measured from the corresponding devices, as well as their sensitivity, are shown in **Figure 6.6**. Only a slight difference in the sensitivity value was observed between these, with a higher sensitivity being obtained for the SnO_2 nanoparticles produced in a conventional oven (−47.7 ± 0.2 mV/pH) when compared to those produced in the microwave system (−45.4 ± 1.3 mV/pH). However, these values are still below those reported using SnO_2 nanoparticles in ISFET technology (−58 mV/pH).[7,15] Nevertheless, as in the case for the ZTO nanostructures, the electrodeposition conditions for the SnO_2 nanoparticles are not yet optimized, nevertheless not only was it possible to prove the promising application of this material, as it was shown that SnO_2 nanoparticles produced using a conventional oven or a microwave system have similar pH sensing properties.

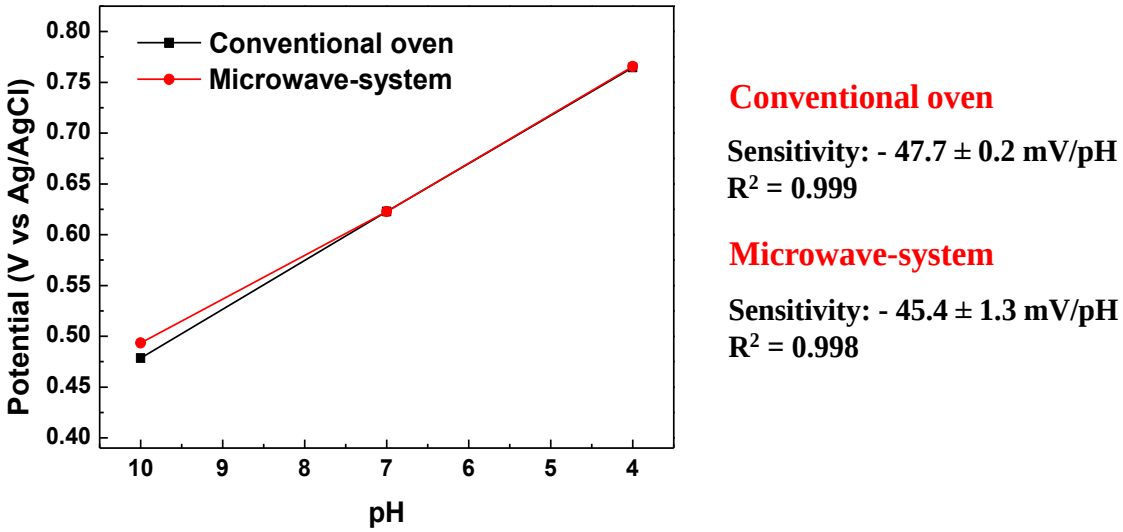

Figure 6.6. pH sensitivity measured from pH 10 to 4 for devices employing SnO_2 nanoparticles produced by hydrothermal method using a conventional oven and a microwave-system.

6.3. Carbon fibers covered by ZTO-based nanostructures

6.3.1. Introduction

Regarding energy storage and conversion, electrochemical capacitors (supercapacitors or SC) and rechargeable lithium-ion batteries are the most promising candidates. Depending on its charge store mechanism electrochemical capacitors can be considered electrical double layer capacitors (EDLC), in which charged ions are adsorbed-desorbed from an electrolyte onto high surface area electrodes, forming a double layer, or redox SCs where charge storage is given by fast redox reactions of active species on the surface of electroactive materials.[16] The electrodes control the properties of these devices by determining the capability, delivery rate and efficiency of energy storage. For EDLC, high surface area carbonaceous materials are employed as electrodes.[17] Regarding redox SCs, metal oxides have been widely used for these applications due to their high specific capacitance and energy density. Moreover, ternary metal oxides have shown higher supercapacitive performance than single component metal oxides due to their multiple oxidation states.[16] Similarly, for lithium-ion batteries, carbon-based anodes can also be employed, and it is largely reported that the inclusion of oxides nanostructures in these devices increases the capacity by increasing the surface area and reducing the Li^+ diffusion path length. Furthermore, addition of the nanostructures leads to the forming of stable solid electrolyte interphase layers that mitigate the mechanical stress during lithiation/delithiation enhancing the cyclability and battery lifetime.[18]

Depositing nanostructured metal oxides in carbon fibers can result in electrodes with good electronic conductivities, with the added benefits previously described for the use of metal oxide materials. Notably, the employment of nanomaterials will result in a very high specific surface area: the more efficient contact between electrolyte ions and electrodes increases the capacity while the decrease in the ions/electrons transport/diffusion lengths results in faster kinetics.[19,20] Specifically concerning ZTO nanostructures, several reports showed the great potential of these materials for both supercapacitors and batteries.[21–24] As so, although these applications were not yet explored in this work, we tested two approaches for implementation of ZTO nanostructures in carbon fibers, consisting in a direct growth method during the hydrothermal synthesis (which was described in Chapter 3) and in the electrodeposition of different ZTO-based nanostructures in the carbon fibers, which are described next.

6.3.2. Electrodeposition of ZTO nanostructures on carbon fibers

The same electrodeposition methodology used for pH sensors production, using a constant current of 20 μA for 900 s to deposit the nanostructures from a well dispersed suspension, was employed here however now the carbon fiber acted as the working electrode. After the

nanostructures' deposition, the carbon fibers were rinsed with deionized water and left to dry naturally. **Figure 6.7** shows the SEM images of the carbon fibers covered with the different nanostructures tested.

As it is possible to observe, the different nanostructures were successfully deposited onto carbon fiber electrodes, however Zn_2SnO_4 nanoparticles covered a higher area and resulted in a more homogeneous coverage. This can be due to either the higher homogeneity of the Zn_2SnO_4 nanoparticles or its smaller sizes when compared with the other structures. Interestingly, these nanostructures also presented a better electrodeposition on Ti/Au electrodes for the pH sensors. Figure 3.18a (Chapter 3) presented the SEM image of the fiber after direct growth of ZTO nanostructures using the hydrothermal synthesis parameters optimized to obtain $ZnSnO_3$ nanowires. It can be observed that a different $ZnSnO_3$ nanostructure ("nanoflower") is grown, due to the substrates influence during synthesis. This highlights the freedom given by employing a seed-layer free method in achieving the desired nanostructures, even if it does require a post-synthesis transfer method as electrodeposition.

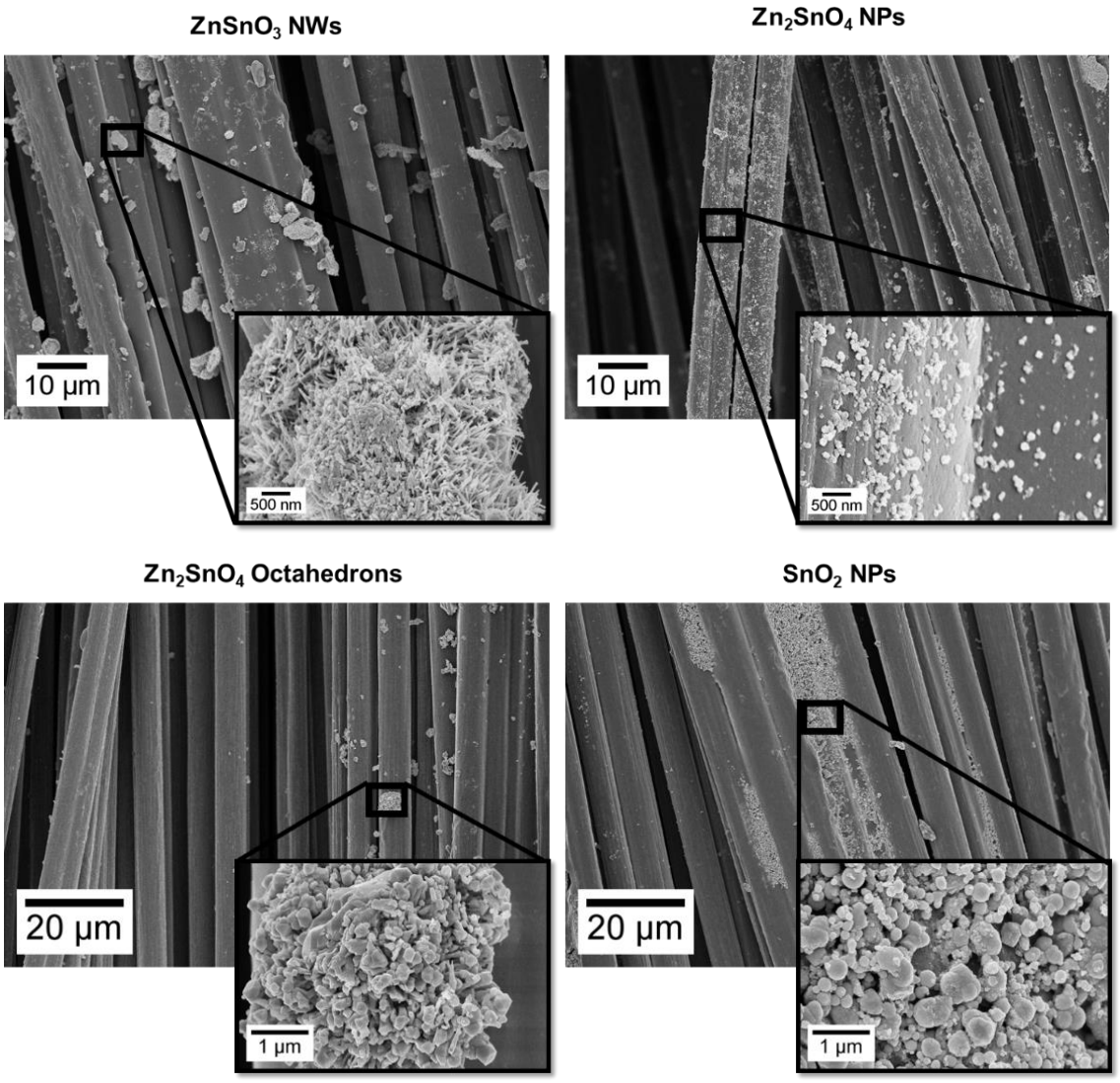

Figure 6.7. SEM images of different ZTO and SnO_2 nanostructures transferred to carbon fibers by electrodeposition.

6.4. Final remarks

In this chapter, electrodeposition was explored as a transfer method for employing the powder form nanostructures into devices. Namely, pH sensors were produced using three zinc and tin oxide-based nanostructures: $ZnSnO_3$ nanowires, Zn_2SnO_4 nanoparticles and SnO_2 nanoparticles. When using the ZTO nanostructures excellent results were obtained, with sensitivity being close to the theoretical maximum. To the best of our knowledge, this ternary material was used for the first time as sensitive layer in pH sensors and considering the achieved performance the potential of employing it for sensing in smart surfaces is clearly demonstrated, emphasizing the multifunctionality of this material system. Nevertheless, there is still room for optimization, with stability and reliability still needing to be accessed. Regarding the SnO_2 nanoparticles, even if the measured sensitivity is not as high as for the ZTO structures, the results for the nanostructures produced using a conventional oven and a microwave system were quite similar, implying that the different synthesis methods can result in nanostructures with very comparable properties.

The electrodeposition technique was also applied to transfer the ZTO-based nanostructures to carbon fibers for future application in batteries and supercapacitors. While still in a preliminary stage, effective coverage was observed, with Zn_2SnO_4 nanoparticles presenting a higher homogeneity on the carbon fibers.

Therefore, while there is still room for improvement, the electrodeposition method revealed to be a useful technique in transferring the powder form nanostructures onto the desired substrates.

6.5. References

1. Santos, L. *et al.* WO3 Nanoparticle-Based Conformable pH Sensor. *ACS Appl. Mater. Interfaces* **6**, 12226–12234 (2014).
2. Zhou, D. D. Microelectrodes for in-vivo determination of pH. in *Electrochemical Sensors, Biosensors and their Biomedical Applications* 261–305 (Elsevier, 2008).
3. Han, S. T. *et al.* An Overview of the Development of Flexible Sensors. *Adv. Mater.* **29**, 1–22 (2017).
4. Chiu, Y. S., Tseng, C. Y. & Lee, C. T. Nanostructured EGFET pH sensors with surface-passivated ZnO thin-film and nanorod array. *IEEE Sens. J.* **12**, 930–934 (2012).
5. Zhang, Q. *et al.* On-chip surface modified nanostructured ZnO as functional pH sensors. *Nanotechnology* **26**, 355202 (2015).
6. Cheng, Y. *et al.* Mechanism and Optimization of pH Sensing Using SnO2 Nanobelt Field Effect Transistors. *Nano Lett.* **8**, 4179–4184 (2008).
7. Chin, Y. L. *et al.* A novel SnO2/Al discrete gate ISFET pH sensor with CMOS standard process. *Sensors Actuators, B Chem.* **75**, 36–42 (2001).
8. Sardarinejad, A., Maurya, D. K. & Alameh, K. The effects of sensing electrode thickness on ruthenium oxide thin-film pH sensor. *Sensors Actuators, A Phys.* **214**, 15–19 (2014).

9. O'Hare, D., Parker, K. H. & Winlove, C. P. Metal-metal oxide pH sensors for physiological application. *Med. Eng. Phys.* **28**, 982–988 (2006).

10. Pan, T. M. & Liao, K. M. Comparison of structural and sensing characteristics of Pr2O3 and PrTiO3 sensing membrane for pH-ISFET application. *Sensors Actuators, B Chem.* **133**, 97–104 (2008).

11. Pan, T. M., Chang, K. Y., Lin, C. W., Tsai, S. W. & Wu, M. H. Label-free detection of uric acid using a disposable poly-N-isopropylacrylamide as an encapsulating enzyme material based on high-κ Eu2Ti2O7 electrolyte-insulator-semiconductor devices. *Sensors Actuators, B Chem.* **160**, 850–857 (2011).

12. Branquinho, R. M. M. S. Label-free detection of biomolecules with Ta2O5-based field effect devices (Doctoral Dissertation). (Faculdade de Ciências e Tecnologias, Universidade Nova de Lisboa, 2012).

13. Khan, M. N., Jaisai, M. & Dutta, J. Photocatalytic Inactivation of Escherichia Coli Using Zinc Stannate Nanostructures under Visible Light. *Adv. Mater. Res.* **1131**, 203–209 (2015).

14. Fulati, A. *et al.* Miniaturized pH sensors based on zinc oxide nanotubes/nanorods. *Sensors* **9**, 8911–8923 (2009).

15. Tsai, C. N., Chou, J. C., Sun, T. P. & Hsiung, S. K. Study on the sensing characteristics and hysteresis effect of the tin oxide pH electrode. *Sensors Actuators, B Chem.* **108**, 877–882 (2005).

16. Chen, D., Wang, Q. & Shen, G. Ternary oxide nanostructured materials for supercapacitors : a review. *J. Mater. Chem. A Mater. energy Sustain.* **3**, 10158–10173 (2015).

17. Dubey, R. & Guruviah, V. Review of carbon-based electrode materials for supercapacitor energy storage. *Ionics (Kiel).* **25**, 1419–1445 (2019).

18. Lim, Y. R. *et al.* Zn2GeO4 and Zn2SnO4 nanowires for high-capacity lithium- and sodium-ion batteries. *J. Mater. Chem. A* **4**, 10691–10699 (2016).

19. Chen, S., Xing, W., Duan, J., Hu, X. & Qiao, S. Z. Nanostructured morphology control for efficient supercapacitor electrodes. *J. Mater. Chem. A* **1**, 2941–2954 (2013).

20. Rakhi, R. B., Cha, D., Chen, W. & Alshareef, H. N. Electrochemical energy storage devices using electrodes incorporating carbon nanocoils and metal oxides nanoparticles. *J. Phys. Chem. C* **115**, 14392–14399 (2011).

21. Zhu, X. J., Geng, L. M., Zhang, F. Q., Liu, Y. X. & Cheng, L. B. Synthesis and performance of Zn2SnO4 as anode materials for lithium ion batteries by hydrothermal method. *J. Power Sources* **189**, 828–831 (2009).

22. Wang, X., Sumboja, A., Lin, M., Yan, J. & Lee, P. S. Enhancing electrochemical reaction sites in nickel-cobalt layered double hydroxides on zinc tin oxide nanowires: A hybrid material for an asymmetric supercapacitor device. *Nanoscale* **4**, 7266–7272 (2012).

23. Guo, X., Cai, M., Li, R. & Han, X. Secondary growth synthesis of ZnSn(OH)6 cube/Zn2SnO4 nanowire yolk–shell hierarchical structures with enhanced lithium ion storage properties. *CrystEngComm* **18**, 6608–6613 (2016).

24. Sun, S. & Liang, S. Morphological zinc stannate: synthesis, fundamental properties and applications. *J. Mater. Chem. A* **5**, 20534–20560 (2017).

Chapter 7 – Final conclusions and Future perspectives

The work presented in this dissertation showed the hydrothermal synthesis of ZTO nanostructures and their multifunctionality. In this last chapter a summary of the main conclusions drawn from this work is presented, followed by prospects and suggestions for future work, based not only on the present work but also on recent reports in literature.

7.1. Final conclusions

1) Hydrothermal synthesis of zinc-tin oxide-based nanostructures

The primary goal of this work was to achieve a well-controlled, low temperature (T < 200 º C), solution-based process to synthesize zinc-tin oxide nanostructures. While this material system allows for different types of structures with excellent properties, $ZnSnO_3$ nanowires were primarily pursued as this metastable material presents excellent properties for piezoelectric energy harvesters, gas sensors, resistive switching memories, batteries, and others. The synthesis of the nanostructures in a powder form was preferred to allow for a higher degree of freedom in its integration in devices (and to avoid contamination from the seed-layer materials). Under the proposed constraints to achieve this metastable phase, a one-step seed-layer free hydrothermal synthesis on a conventional oven was optimized regarding its physical and chemical conditions. The influence of each parameter in the synthesis was studied and the wide array of tested conditions resulted in the achievement of nanostructures with different morphologies and phases such as Zn_2SnO_4 octahedrons, Zn_2SnO_4 nanoparticles and SnO_2 nanoparticles. Nevertheless, the process conditions were optimized towards the synthesis of $ZnSnO_3$ nanowires, with a reproducible method for a homogenous production of these structures (without significant mixture of other phases) having been achieved.

This study has shown that the chemical parameters to achieve the metastable phase ($ZnSnO_3$ nanowires) were restricted to a specific range of values, showing that they play a critical role in the growth of these structures. The optimal conditions were a Zn:Sn molar ratio of 2:1 (1:1) using $ZnCl_2$ (ZnAc) as zinc precursor, a H_2O:EDA volume ratio of 7.5:7.5 ml:ml and a NaOH concentration of 0.240 M for syntheses at 200 ºC for 24 h.

The zinc precursors' solubility in the surfactant (EDA) in comparison to that of the tin precursor ($SnCl_4{\cdot}5H_2O$) resulted in the favoring of different types of structures for the synthesis: the lower solubility of ZnAc promotes tin-based structures while the higher solubility of $ZnCl_2$ results mostly in zinc-based structures. As such, for each of these two precursors, the Zn:Sn molar ratios presented different optimal values. Additionally, synthesis with the $ZnCl_2$ precursor resulted in larger and significantly more homogeneous nanostructures (less mixture of phases/structures) and more reproducible reactions, which can be attributed to its higher solubility, leading to a faster evolution of the species in synthesis.

The surfactant (EDA) was found to be crucial in directing the growth of the structures into the nanowire form. Additionally, and similarly to what is seen for the mineralizer (NaOH) concentration, its concentration influences the solution's pH which is known to favor the formation of either tin-based structures or zinc-based structures depending on its value. The formation of the desired metastable phase was achieved for intermediate values only, showing that both EDA and NaOH optimal concentrations are a balance between the role they play in the synthesis and their influence on the pH.

The physical parameters of the synthesis were found to be crucial for the achievement of the metastable phase. While lower energy levels favor the growth of the more energetically stable phases (Zn_2SnO_4 and SnO_2), the $ZnSnO_3$ is achievable for higher energy levels. Higher solution volumes (15 ml), corresponding to higher pressure in the synthesis, were found to be necessary for the obtention of the desired phase by supplying the necessary energy. It was observed that at least syntheses with 12 h at 200 ºC were necessary for a predominantly growth of nanowires but, interestingly, for very long synthesis (36 h), or at higher temperatures (220 ºC) the decomposition of the $ZnSnO_3$ phase into the more stable phases starts to occur. The optimal nanowires dimensions were found for 24 h synthesis at 200 ºC, and this emphasizes that while the hydrothermal process is a viable way to achieve the metastable phase at low temperatures, it requires a proper control and understanding of the synthesis parameters.

From this study a growth mechanism was proposed for the metastable $ZnSnO_3$ nanowires, which is schematically summarized in **Figure 7.1**.

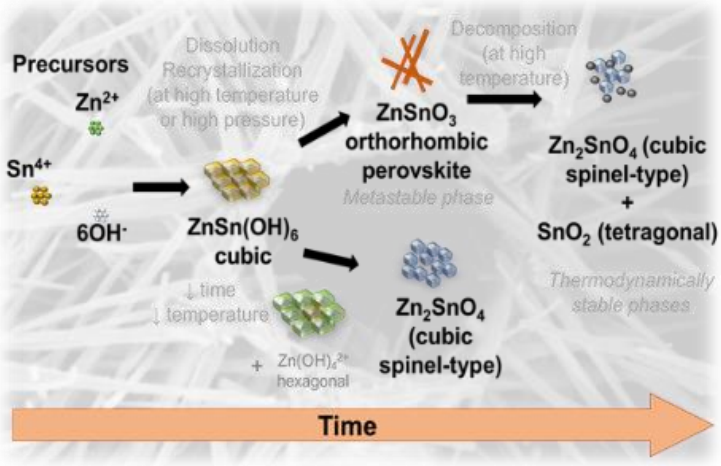

Figure 7.1. Growth mechanism of ZTO nanostructures: $ZnsnO_3$ nanowires and Zn_2SnO_4 nanoparticles.

To circumvent the inconveniently long durations of the conventional oven hydrothermal synthesis an alternative route of microwave heating assisted synthesis was explored to achieve accelerated chemical reactions. Based-on synthesis recipes for different types of nanostructures, nanostructures synthetized with both the conventional oven and the microwave method were compared and it was found that both methods could provide very similar results, whereas the microwave heating allowed for reductions of up to 20 h of synthesis time, while still yielding reproducible and homogeneous results. Although showing to potentially being able to replace the conventional oven, the microwave heating synthesis still requires further investigation, as the kinetics of the reaction are different thus requiring its own optimization.

From the wide array of conditions tested for the seed-layer free hydrothermal synthesis, several ZTO-based nanostructures were achieved. **Table 7.1** summarizes the synthesis conditions that were found to be reproducible and to efficiently result in nanostructures with a homogeneous distribution.

Table 7.1. Summary of the seed-layer free hydrothermal synthesis conditions for the different ZTO-based nanostructures achieved in this work. The syntheses presented in this table were found to be reproducible and to efficiently result in nanostructures with a homogeneous distribution. Note that, except for SnO_2 nanoparticles' synthesis, the Sn precursor was $SnCl_4.5H_2O$.

Nanostructure	Heating system	Zinc precursor / Zn:Sn molar concentration (M:M)	Mineralizer agent / Molar concentration (M)	Solvents / Volume (ml)	Temperature / Time
$ZnSnO_3$ nanowires	Conventional oven	$ZnCl_2$ / 0.040:0.020	NaOH / 0.240	H_2O:EDA / 7.5:7.5	200 °C / 24 h
		ZnAc / 0.020:0.020			
Zn_2SnO_4 octahedrons	Conventional oven	$ZnCl_2$ / 0.040:0.020	NaOH / 0.240	H_2O:EDA / 7.5:7.5	200 °C / 24 h
	Microwave				200 °C / 60'
Zn_2SnO_4 nanoplates	Conventional oven	$ZnCl_2$ / 0.040:0.020	NaOH / 0.240	H_2O:EDA / 7.5:7.5	200 °C / 12 h
	Microwave				200 °C / 30'
Zn_2SnO_4 nanoparticles	Conventional oven	$ZnCl_2$ / 0.040:0.020	NaOH / 0.240	H_2O:EDA / 7.5:7.5	200 °C / 24 h
		$ZnCl_2$ / 0.170:0.084	Na_2CO_3 / 0.330	H_2O / 15	200 °C / 24 h
	Microwave	$ZnCl_2$ / 0.040:0.020	NaOH / 0.240	H_2O:EDA / 7.5:7.5	200 °C / 20'
SnO_2 nanoparticles	Conventional oven	K_2SnO_3 / 0.073 ; Urea / 0.989		H_2O:Ethanol / 6:10	140 °C / 4 h
	Microwave				140 °C / 60'

The multifunctionality of the obtainable ZTO-based nanostructures permits for a wide array of applications to be envisaged and, naturally, for some devices, the employment of seed-layers can be mainly beneficial as they can integrate the device structure itself while also allowing to induce a specific type of structure in the grown nanomaterial. Attending to this, the hydrothermal synthesis employing seed-layers was explored for several types of seed-layers. While the identification of some of the obtained structures was not possible at this point, a correlation between the crystalline structure of the employed seed-layers and that of the grown nanostructures was still clearly seen. Seed-layers with hexagonal (ZnO and Ti), tetragonal (FTO and Sn) and amorphous (ZTO) structures resulted in the growth of nanosheets of unidentified phase. Cubic phase seed-layers (stainless steel and Cu) induced the growth of the Zn_2SnO_4 phase (with inverse spinel cubic structure). Zn_2SnO_4 nanowires were achieved through this method, being a very desirable structure for electronic applications, and that had not been previously synthesized successfully through the seed-layer free synthesis in this work. Cr and Ni seed-layers (both also having a cubic structure) resulted in nanograss structures of an unidentified phase. Cu nanowires as seed-layer were shown to be decorated with $ZnSnO_3$ nanowires (probably due to the monoclinic phase of native CuO), while carbon fibers were decorated with unidentified small flower-like nanostructures. Furthermore, it was observed that the employment of seed-layers not only influenced the type of grown nanostructures but also accelerated the growth process.

In summary, different approaches were explored regarding the hydrothermal synthesis method for the obtainment of ZTO-based nanostructures. These results show the versatility of this method to control the growth and morphology of the nanostructures. The use of nanomaterials in the devices contributes for the miniaturization and versatility demands in nanotechnology.

2) Properties of the ZTO nanostructures

Under the optimized conditions, several syntheses of the $ZnSnO_3$ nanowires were performed to prove its reproducibility. Statistical analysis of the nanowires' dimensions showed average lengths of 605 nm (± 72.8 nm) and average diameters of 65.8 nm (± 10.2 nm) resulting in an average aspect ratio of approximately 9.

Optical and electrical characterization was also conducted for some of the ZTO nanostructures synthetized in this work. The measured optical bandgaps for $ZnSnO_3$ nanowires (3.60 eV) and Zn_2SnO_4 octahedrons (3.46 eV) were found to be slightly lower than reported in the literature (3.9 and 3.6 eV, respectively), which can be attributed to a higher defect density arising from the low-temperature synthesis here employed, inducing subgap states. In the case of Zn_2SnO_4 nanoparticles, the measured optical bandgap was the same as reported in the literature (3.6 eV), suggesting that a good crystallinity is obtained through the hydrothermal method. The electrical characterization of the $ZnSnO_3$ nanowires was successfully performed inside an SEM tool. The shorter dimensions of the other types of nanostructures impeded their electrical characterization, even in the SEM tool. For the $ZnSnO_3$ nanowires an average resistivity of

7.80 ± 8.63 kΩ·cm was calculated which two orders of magnitude higher than the reported in the literature (≈ 73 Ω·cm) for these structures, probably deriving from a more defective structure due to the low-temperature solution-based process.

3) Applications of the ZTO nanostructures

Owing to the multifunctionality of the ZTO-based material system, several applications were explored under the scope of this work employing some of the synthesized nanostructures.

- ***Piezo/triboelectric nanogenerators***

Given the high piezoelectric polarization of the $ZnSnO_3$ nanowires, they were embedded in PDMS and the composite film was used for piezo/triboelectric nanogenerators. Comparison with similar devices employing either ZnO nanowires or no nanostructures at all showed that the piezoelectric polarization plays the major role in the output power generated by these devices. Furthermore, a micro-structured design of the PDMS film has shown to significantly enhance both the piezoelectric and the triboelectric properties of the devices. Whereas 6 V and 650 nA were achieved for a 10 N stimulus, for stimulus of ≈ 100 N outputs of 120 V and 13 μA were achieved, corresponding to a power density close to 230 $\mu W \cdot cm^{-2}$. The practical implementation of the devices was shown by lighting up several LEDs, showing the potential for energy harvesting in wearables.

- ***Memristive devices***

The $ZnSnO_3$ nanowires were also explored for integration in resistive switching devices. While a simple drop-casting method was used as a preliminary integration method, very good results were achieved. On/off ratio of the resistance states of the device was in the order of 10^7 and retention times were higher than 14 h. Additionally, the devices showed a very significant response under visible illumination, with an increase of 35 μA/s, which can be interesting for the implementation of optoelectronic memristors or for light sensing devices. Although further work is still required under the scope of these applications, these results already show these structures as permissible for the integration of memory on foil.

- ***Photocatalytic devices***

Synthetized ZTO nanostructures under the powder form, namely Zn_2SnO_4 nanoparticles and octahedrons, and $ZnSnO_3$ nanowires, were employed for photocatalysis. The $ZnSnO_3$ nanowires in the form of powder produced by solution-based synthesis were employed for this end for the first time (to the best of the author's knowledge), and this material showed a great performance, being close to or superior to the Zn_2SnO_4 nanostructures, completely degrading methylene blue and rhodamine B dies in only 90 min under 285 W of UV light irradiation. The reusability of the nanomaterials was also demonstrated, whereas degradation times increased to approximately 90 min. On the other hand, due to the wide bandgap of the ZTO nanostructures, the photocatalytic activity was much lower under visible light, with degradations of only ≈ 50 % for 12 h.

- **pH sensors**

pH sensors were produced using $ZnSnO_3$ nanowires, Zn_2SnO_4 nanoparticles and SnO_2 nanoparticles. The powder form nanostructures were implemented into the devices by the electrodeposition method. This proved as a valid transfer method by allowing some type of patterning and with a decent quantity of deposited nanostructures being achieved. The ternary material, ZTO, was for the first time used as sensitive layer in pH sensors, to the best of author's knowledge, and the measured sensitivities for both structures were close to the theoretical maximum. While devices employing the SnO_2 nanoparticles had lower sensibilities, it was interesting to demonstrate that whether employing SnO_2 nanoparticles produced by the conventional oven or by the microwave method, the results were very similar.

In summary, exciting results were shown for application in devices of the ZTO-based nanostructures produced by low-cost solution-based processes. The implementation of the nanostructures in these devices was facilitated by its powder form arising from the seed-layer free nature of the optimized synthesis. The multifunctionality of this material system is highlighted by its successful implementation in energy harvesters, resistive switching memories, photosensors, photocatalysts and pH sensors, being that further applications can certainly be envisaged. The work demonstrated thus show the great potential of ZTO nanostructures, especially $ZnSnO_3$ nanowires, for integration on environmentally friendly and self-sustainable smart surfaces.

7.2. Future Perspectives

Owing to the multifunctionality of ZTO nanostructures different fields of application were explored in this dissertation, opening a path for further investigation to be performed in the future.

Thus, in this section, recommendations and suggestions for future work are presented. These will encompass the different subjects covered in this work, from the hydrothermal synthesis of the nanostructures to the devices in which they are integrated, including also the nanostructures' characterization and transfer methods required for their integration.

1) Hydrothermal synthesis and post-treatments

Although a wide array of parameters was tested for the seed-layer free hydrothermal synthesis the focus was maintained predominantly on the obtention of the $ZnSnO_3$ nanowires. While it is likely that further tuning of this synthesis can be done to improve the achieved $ZnSnO_3$ nanowires' properties, there is also a significant room of optimization when envisaging the obtainment of other types of structures. For instance, it was seen that Zn_2SnO_4 nanostructures are achieved from the $ZnSnO_3$ phase at higher temperatures, meaning that there is an interesting investigation space for the achievement of these structures at higher temperatures than those tested in this work. These temperatures can also be achieved through post-synthesis treatments using different atmospheres, which can induce the phase transformation mentioned above and/or

tune the defect state density and crystalline quality of the material. Thermal annealing under different atmospheres can be performed with a rapid thermal annealing (RTA) technique available at our work group, providing a fast and well-controlled environment for these experiments. As the surface-to-volume ratio of the nanostructures is very high, the passivation of traps typically present at the surface by other means besides temperature can also be an important post-processing procedure. For this end, conformal techniques are very interesting as they can cover the exposed surface completely. Parylene CVD deposition is available in our group, and has been shown as being a viable passivation for ZnO-based active layers,[1,2] while an atomic layer deposition (ALD) tool is currently being installed in our clean room for highly conformable oxide coatings. It is expected that appropriate post-treatments of the nanostructures can enhance their properties not only for electronic applications, such as FETs, but for the generality of the possible applications

2) Microwave-assisted synthesis

The microwave-assisted synthesis was shown to result in nanostructures similar to those of the conventional oven, while significantly decreasing the synthesis time. Nevertheless, the synthesis conditions must be properly optimized when aiming to produce ZTO nanostructures, specially $ZnSnO_3$ nanowires, where some difference was observed between nanostructures synthesized with the different methods. The microwave-heating is faster and more homogeneous and thus can in theory provide nanostructures with superior properties, making the optimization of the synthesis conditions in this system a very interesting prospect for the future.

3) Transfer methods and integration processes

One of the main challenges regarding nanostructures is their controlled implementation in devices. Transfer methods bring the generic advantage of decoupling the synthesis steps from the nanowires' deposition on substrates, enabling a large degree of freedom during synthesis. Different transfer methods of nanowires to rigid and flexible substrates need to be studied in order to achieve precise alignment, positioning, high density and uniform nanowire distribution in large areas. The following techniques have been explored in CENIMAT, and can be applied for ZTO nanostructures, in the future:

- Dip, drop, spray and spin coating;[3]
- Film-applicator (Doctor blade);[4]
- Dielectrophoresis / electrodeposition;[5]
- Fluid flow in microfluidic channels;[6]
- Printing techniques.[7]

4) Direct growth of ZTO nanostructures on different substrates

In alternative to transfer methods, direct growth of the structures on a substrate can be advantageous in terms of yield, decrease of the total number of processing steps when considering device integration and preventing the damage of nanostructures during transfer

methods. The substrate material can influence the growth of the structures acting as a seed-layer, or alternatively, thin films can be deposited on catalytically inactive substrates and also act as seed-layers for nanostructure's growth. Several materials were explored as seed-layer in this work, which allowed to achieve different types of nanostructures. While these results revealed to be very promising for different applications there is still a large room for improvement. Firstly, these studies need further optimization for achieving a well-controlled, homogenous and reproducible synthesis of ZTO nanowires (both $ZnSnO_3$ and Zn_2SnO_4) in a vertical array, which has been reported in the literature for different applications such as solar cells, sensors, photocatalysis and also for electronics.[8–13] This will require the proper identification of the nanostructures grown in different seed-layer materials (in some cases unachieved in this work) which can benefit from the employment of TEM techniques. Horizontally grown nanowires would also be interesting to explore for planar integration, using catalytically inactive layers on top of patterned seeds to force the synthesis in planar direction.

High-resolution methods as nanoimprint lithography (NIL) and e-beam lithography (EBL) (both recently acquired in CENIMAT) will allow to achieve seed-layers patterned with lateral dimensions below 100 nm (as illustrated by first resolution tests performed at CENIMAT, **Figure 7.2**). Advanced methods as these will allow for large design flexibility, being of special interest for application of the nanomaterials for electronics, thus being fundamental to be explored in the future.

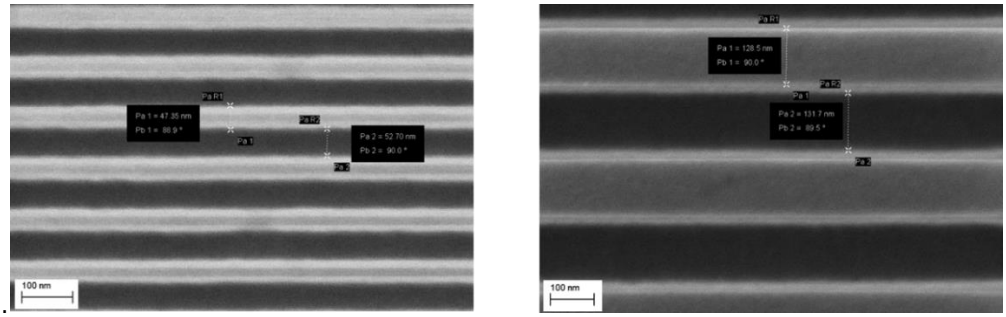

Figure 7.2. SEM images of lines/gaps with < 100 nm achieved using nanoimprint lithography (at CENIMAT).

5) Material characterization

Due to the small size of the nanostructures, the study of its properties is very challenging often involving high-resolution techniques or the implementation of complex setups for accessing the intrinsic properties of the materials. In specific, the crystalline, electrical and piezo/ferroelectric properties, need to be further investigated.

Concerning the crystalline structure of the synthesized nanostructures, TEM is a powerful tool that can provide detailed information on this regard, allowing for clarifying the identification of some nanostructures, for instance those grown on seed-layers which were not successfully identified at this point. While some TEM analysis attempts were done during this research work, issues with sample preparation and equipment failures always led to inconclusive results.

For the assessment of the piezoelectric properties of the nanowires the AFM tool should be used for the polarization of a single nanowire in the PFM mode to determine the piezoelectric constant (d_{33}). First steps were given in the last months towards this end, in collaboration with the Physics department of the University of Bologna, allowing to get initial measurements of d_{33} of $ZnSnO_3$ nanowires (≈ 20-25 pm/V) and verifying that this is at least 3-4 larger than the one measured for ZnO nanowires, also prepared by hydrothermal synthesis at CENIMAT.

The electrical characterization of single $ZnSnO_3$ nanowires was successfully performed in order to determine the resistivity in vacuum at room-temperature. Nevertheless, this process revealed to be very challenging and incompatible with smaller nanostructures due to resolution limitations of the e-beam assisted electrode deposition inside SEM. While standard electrical characterization can be performed inside SEM, for more complex circuits or for light/temperature/atmosphere dependent measurements a typical probe station needs to be used. For accessing nanostructures in a typical probe station, electrodes by standard lithographic processes can be used to contact Pt electrodes directly deposited inside the SEM tool on top of a desired nanostructure. This approach was tested with some preliminary results being shown in **Figure 7.3**. In some cases, the Pt deposition seems to be controlling the measured resistivity, as control structures without any nanowire between two Pt electrodes (**Figure 7.3**d) result in current levels comparable to that of structures employing nanowires (**Figure 7.3**b and c). This seems to indicate that some residual Pt is unintentionally deposited between the Pt electrodes, which is critical for the cases of smaller gaps.

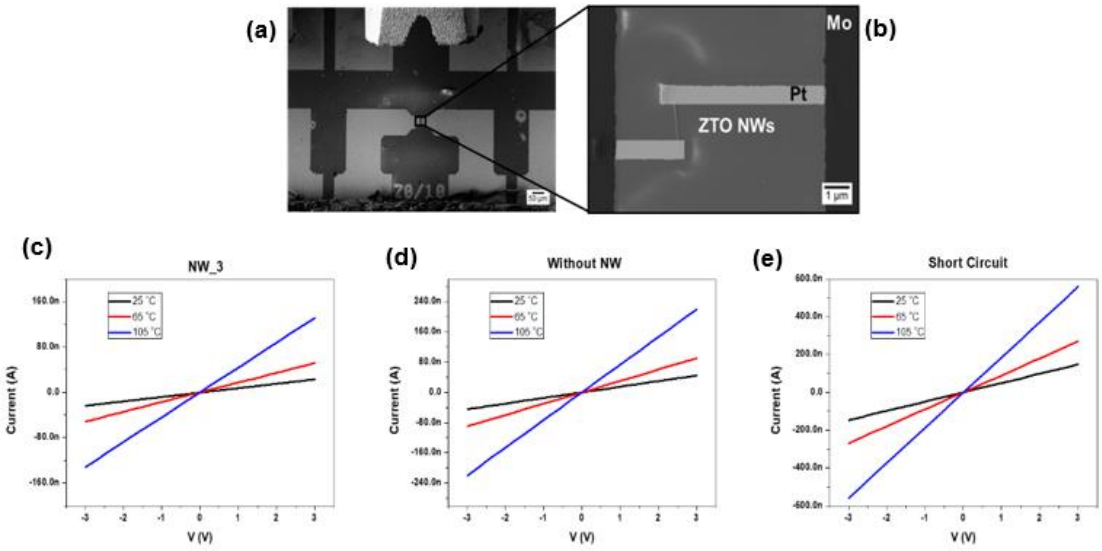

Figure 7.3. (a) SEM micrographs of the Mo electrodes patterned with lithography processes and (b) a zoom showing the Pt electrodes deposited inside SEM to contact the nanowire to the Mo electrodes. I-V measurements at different temperatures (25 °C, 65 °C and 105 °C) with the same type of structure (c) with a nanowire between electrodes, (d) without a nanowire between electrodes and (e) with the Pt electrodes intentionally short-circuited.

Additionally, these current levels are quite significant when compared to control structures where the Pt electrodes are intentionally short circuited (**Figure 7.3**e), showing that the contribution from the residual Pt is very significant. Optimization of the Pt deposition conditions is

required for both increasing its conductivity and, also, to decrease the deposition of residual Pt which severely limits the achievable gap resolution. An important step to accomplish this will be the use of a ns-resolution pattern generator recently installed in the SEM-FIB platform of CENIMAT.

On the other hand, the EBL technique provides the resolution required for defining the electrodes in small nanostructures. This technique can be used to achieve a nanolithography process that is then compatible with the employment of common electrode materials deposited in clean room by e-beam evaporation or sputtering.

6) Electronic applications: fabrication and integration on devices

Resistive switching memories

Although very interesting and promising results for the resistive switching devices were presented in this thesis, a significant amount of work is still required under this scope. First, the resistive change mechanism was not elucidated in the present work and understanding the devices' underlaying mechanisms is always indispensable for the maturing of the technology. This can be further investigated by conducting a set of experiments which include measurements under different temperatures, electrodes, ambient conditions, and device areas. Additionally, the set and reset process under illumination should also be investigated. Devices' cyclability must be significantly improved which should require optimization of the integration of the nanostructures in the devices. Integration methods to be explored include spin-coating, doctor blade, or even the employing of composites consisting in nanostructures and polymers.

Another very interesting approach is the fabrication of resistive switching memories with individual nanowires, which could be advantageous to infer on the intrinsic properties of the nanostructures. **Figure 7.4** presents several of these type of architectures that have been reported. This type of approaches can also be explored in the future in CENIMAT using the EBL tool.

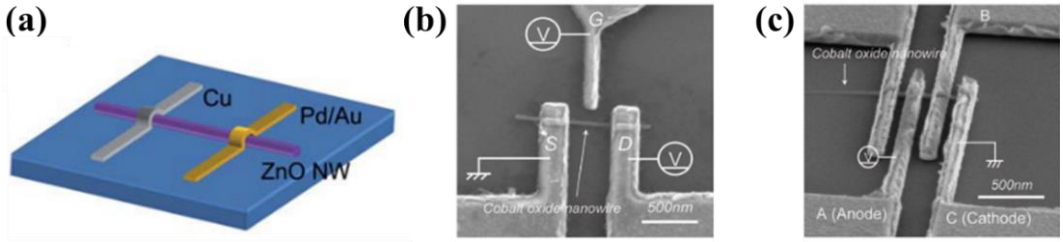

Figure 7.4. (a) Schematic illustration of the Cu/ZnO-NW/Pd memory device's structure from ref [14]. Field emission SEM images of (b) a nanowire side gate FET structure and of a (c) memristor device consisting on a single cobalt oxide nanowire device bridged between multielectrodes, both from ref [15]

Field effect transistors

Concerning FET applications, demonstrations of discrete Zn_2SnO_4 nanotransistors (with nanowires) were already reported in the literature.[16–18] However, to the author's best knowledge, there are no reports on $ZnSnO_3$ nanotransistors. Likewise, while the achievement of an on/off ratio ≈ 10^6 and a field effect mobility ≈ 112 $cm^2V^{-1}s^{-1}$ is a good demonstration of the ZTO's potential for this application, a combination of low temperatures, sustainable and scalable processes enabling good quality nanowires and controlled nanowire density over the device area (hence controlled electrical current) are yet to be shown. Moreover, transistors using ZTO nanostructures synthesized by solution processes were not reported yet.

Different approaches to fabricate nanotransistors with standard microlithography processes were explored under the scope of this work. In order to understand the reliability of these processes, ZnO commercial nanowires, from Sigma-Aldrich were used. **Figure 7.5**(a and b) shows the photograph and the schematic of the electrolyte-gate transistors with a random network of nanowires produced by combining a pick-and-place approach, microlithography processes and the electrolyte-gate methods described by Lídia *et al.* [19]. In **Figure 7.5**c the FETs' transfer curve can be observed, showing an on/off ratio of almost 4 orders of magnitude. While these results are far from what was already achieved using ZnO nanowires [20], they still show that this approach can be a valid tool in the characterization of the produced nanostructures, nanotransistors and even other nanodevices (such as memories). However, the same procedure was not yet successfully implemented for the synthesized ZTO nanostructures in this work.

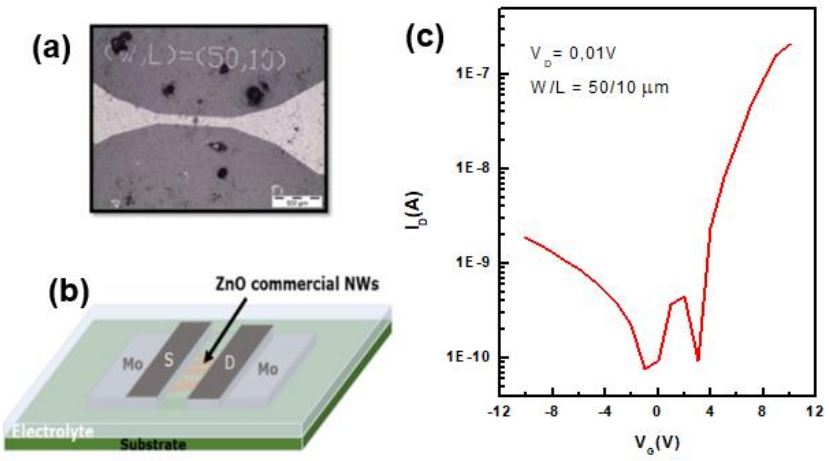

Figure 7.5. Electrolyte-gated transistor with ZnO commercial nanowires with 1 µm of length and 90 nm of diameter: (a) micrograph and (b) schematic. (c) I-V curve of a TFT with ZnO commercial nanowires annealed during 4 hours at 600 °C.

While this kind of approaches can be explored in the future for random networks of nanowires, the optimization of proper transfer methods and direct growth methods permits for additional device structures to be explored: single-wire structures by pick-and-place approaches (as was discussed before); TFTs with patterned random networks of ZTO nanowires replacing the conventional ZTO thin-films; and, finally, aligned multi-wire devices, enabling large integration levels and density-dependent output currents. These different structures can be used to

understand transistor operation at nanoscale level. Depending on the transfer or direct growth methodologies, both planar and vertical (gate-all-around transistors) structures can be studied.

The thin-film technology suitable for flexible substrates already available at CENIMAT will be fundamental to obtain the remaining materials of the transistors, such as electrodes (e.g., Mo/Al/IZO/GAZO) or insulators (e.g., Ta_2O_5-SiO_2/parylene).[1]

Circuit integration of the nanoelectronic devices

Finally, as a proof-of-concept of the developed technology, low-transistor count nanocircuits such as logic gates (e.g., inverter/NAND) and amplifiers should be demonstrated. After the optimization of the different compounds, it would be possible to integrate in the same circuit transistors, memristors, photosensors, etc.

7) Piezo and nanogenerators

Very good results were obtained for the energy harvesting applications, nevertheless, many improvements can still be performed, including:

- Vertical alignment of the $ZnSnO_3$ nanowires, aligning their z-axis with the pushing direction.
- Optimization of the concentration of the nanowires in the PDMS.
- Improvement of the electrodes.
- Annealing treatment of the nanowires to improve their crystallinity and piezoelectric properties by decreasing the defects in the crystalline structure.

8) Catalytic applications

A good performance of the powder form nanostructures was demonstrated for photocatalytic applications under UV light. As an interesting alternative, ZTO structures directly grown in different substrates can be explored for this application. This approach has the benefit of the nanostructures being fixated, thus not requiring their recollection after the catalysis. Additionally, it is expected that for appropriate combinations of seed-layers/nanostructures' materials the band-bending at the interface can lead to a reduction of the effective bandgap, which can be an interesting approach to increase the photocatalytic response under visible light.

9) pH sensors

In this thesis the potential of different zinc and tin oxide-based nanostructures for pH sensing was demonstrated. While electrodeposition was employed as it was the established method at our group, other methods of integration of the nanoparticles into the pH sensing devices can be explored for optimization of these devices. For example, microfluidic techniques can be used to localize nanoparticles onto specific areas and should result in a higher concentration of nanostructures than the electrodeposition method. Alternatively, when high areal resolution is not critical, and considering alternative inexpensive substrates such as paper which is one of the

focus in our work group, printing techniques can be employed.[7] Regarding the devices' performance, further investigation should be performed, namely cyclability, reversibility, and for a higher range of pH values than the employed in this work.

10) Other applications

In Chapter 6 it was presented the deposition of the nanostructures in carbon fibers. The field of electrochemical energy conversion and storage is starting to be developing in CENIMAT, as so, in the future electrochemical studies will be performed in these sample, in order to use it for batteries and supercapacitors.

7.3. References

1. Kiazadeh, A. *et al.* Improving positive and negative bias illumination stress stability in parylene passivated IGZO transistors. *Appl. Phys. Lett.* **109**, 051606 (2016).
2. Fernandes, C. *et al.* A Sustainable Approach to Flexible Electronics with Zinc-Tin Oxide Thin-Film Transistors. *Adv. Electron. Mater.* **4**, 1800032 (2018).
3. Rosa, J. *et al.* Memristors Using Solution-Based IGZO Nanoparticles. *ACS Omega* **2**, 8366–8372 (2017).
4. Santos, L. *et al.* Structure and morphologic influence of WO3 nanoparticles on the electrochromic performance of dual-phase a -WO3/WO3 inkjet printed films. *Adv. Electron. Mater.* **1**, 1–10 (2015).
5. Santos, L. *et al.* WO3 Nanoparticle-Based Conformable pH Sensor. *ACS Appl. Mater. Interfaces* **6**, 12226–12234 (2014).
6. Bernacka-Wojcik, I. *et al.* Bio-microfluidic platform for gold nanoprobe based DNA detection--application to Mycobacterium tuberculosis. *Biosens. Bioelectron.* **48**, 87–93 (2013).
7. Grey, P. *et al.* Handwritten Oxide Electronics on Paper. *Adv. Mater. Technol.* **2**, 1–7 (2017).
8. Chu, S., Li, D., Chang, P. & Lu, J. G. Flexible Dye-Sensitized Solar Cell Based on Vertical ZnO Nanowire Arrays. *Nanoscale Res Lett* **6**, 38 (2010).
9. Pimentel, A. *et al.* Microwave Synthesized ZnO Nanorod Arrays for UV Sensors: A Seed Layer Annealing Temperature Study. *Materials (Basel).* **9**, 299 (2016).
10. Lo, M.-K., Lee, S.-Y. & Chang, K.-S. Study of ZnSnO3-Nanowire Piezophotocatalyst Using Two-Step Hydrothermal Synthesis. *J. Phys. Chem. C* **119**, 5218–5224 (2015).
11. Ng, H. T. *et al.* Single Crystal Nanowire Vertical Surround-Gate Field-Effect Transistor.

Nano Lett. **4**, 1247–1252 (2004).

12. Schmidt, V. *et al.* Realization of a Silicon Nanowire Vertical Surround-Gate Field-Effect Transistor. *Small* **2**, 85–88 (2006).

13. Tomioka, K., Yoshimura, M. & Fukui, T. A III-V nanowire channel on silicon for high-performance vertical transistors. *Nature* **488**, 189–192 (2012).

14. Yang, Y. *et al.* Nonvolatile resistive switching in single crystalline ZnO nanowires. *Nanoscale* **3**, 1917–1921 (2011).

15. Nagashima, K. *et al.* Intrinsic mechanisms of memristive switching. *Nano Lett.* **11**, 2114–2118 (2011).

16. Hwang, J. K. *et al.* Direct nanoprinting by liquid-bridge-mediated nanotransfer moulding. *Nat. Nanotechnol.* **5**, 742–748 (2010).

17. Lim, T., Kim, H., Meyyappan, M. & Ju, S. Photostable Zn2SnO4 Nanowire Transistors for Transparent Displays. *ACS Nano* **6**, 4912–4920 (2012).

18. Kim, S., Kim, H., Janes, D. B. & Ju, S. Interface studies of N2 plasma-treated ZnSnO nanowire transistors using low-frequency noise measurements. *Nanotechnology* **24**, 305201 (2013).

19. Santos, L. *et al.* Solvothermal Synthesis of Gallium–Indium-Zinc-Oxide Nanoparticles for Electrolyte-Gated Transistors. *ACS Appl. Mater. Interfaces* **7**, 638–646 (2015).

20. Goldberger, J. *et al.* ZnO Nanowire Transistors. *J. Phys. Chem. B* **109**, 9–14 (2005).

Chapter 8 – Appendix

Two images obtained with this work won the Nano Today cover competition of 2018 and 2019, being the front cover of the volumes 21 and 26 of this journal, as shown in **Figures A1 and A2**.

Figure A 1. Front cover of the Volume 21 of Nano Today Journal, winner of the cover competition of 2018.

Figure A 2. Front cover of the Volume 26 of Nano Today Journal, winner of the cover competition of 2019.